Durham E-Theses

Solid-state NMR studies of inclusion compounds

Nordon, Alison

How to cite:

Nordon, Alison (1997) *Solid-state NMR studies of inclusion compounds*, Durham theses, Durham University. Available at Durham E-Theses Online: http://etheses.dur.ac.uk/4758/

Use policy

Solid-state NMR studies of inclusion

compounds

by

Alison Nordon, B.Sc. (Hons.)

College of St. Hild & St. Bede

University of Durham

A thesis submitted in partial fulfilment of the requirements for the

degree of Doctor of Philosophy

Department of Chemistry

University of Durham

1997

- 3 APR 1998

Solid-state NMR studies of inclusion compounds

Alison Nordon, B.Sc. (Hons.)
Submitted for the degree of Doctor of Philosophy
1997

Abstract

The work contained within this thesis is a study of inclusion compounds using solid-state NMR. Such compounds typically exhibit static and/or dynamic disorder, which precludes the use of diffraction-based techniques to obtain detailed structural information. Hence, due to its ability to probe local environments, solid-state NMR can be used to provide information which would otherwise be inaccessible. However, the dynamic nature of the guest molecules within inclusion compounds can yield unusual results for routinely applied experiments, such as cross polarisation, heteronuclear dipolar decoupling and dipolar dephasing. Therefore, some of the more fundamental aspects of solid-state NMR have first been explored.

The inclusion compounds of particular interest are those which contain urea or thiourea as the host species. The ordering of guest molecules and host dynamics have been investigated via both one- and two-dimensional ^{13}C and ^{1}H NMR experiments for the 2-hydroxyalkane/urea inclusion compounds. For the 1-fluorotetradecane/urea inclusion compound, an approach involving a combination of $^{1}H \rightarrow ^{13}C$ and $^{19}F \rightarrow ^{13}C$ cross-polarisation experiments, with both single-channel (^{1}H) and double-channel decoupling ($^{1}H, ^{19}F$) has been devised to assign ^{13}C resonances and hence deduce guest ordering. Steady-state and transient ^{19}F MAS NOE experiments have been used to probe the dynamics of the 1-fluorotetradecane/urea inclusion compound. Using the considerable sensitivity advantage of ^{19}F NMR, over that of ^{13}C, a detailed study of the conformational dynamics exhibited by fluorocyclohexane molecules included within thiourea has been performed via bandshape analysis, selective polarisation inversion and 2D exchange experiments. Intermolecular distance measurements have been determined for adjacent fluoroalkane molecules within urea tunnels using a series of static ^{19}F NMR experiments. From the results obtained, conclusions regarding the mutual orientations of adjacent end-groups in such compounds have been made.

Memorandum

The research presented in this thesis has been carried out in the Department of Chemistry, University of Durham, between October, 1994 and September, 1997. Unless otherwise stated it is the original work of the author. None of this work has been submitted for any other degree.

The copyright of this thesis rests with the author. No quotation from it may be published without her prior consent and information derived from it should be acknowledged.

Acknowledgements

To Mrs. Carol Carr

Abbreviations

NMR	nuclear magnetic resonance
MAS	magic-angle spinning
CP	cross polarisation
CRAMPS	combined rotation and multiple-pulse spectroscopy
BR-24	Burum-Rhim (pulse sequence)
MREV-8	Mansfield-Rhim-Elleman-Vaughan (pulse sequence)
WAHUHA	Waugh-Huber-Haeberlen (pulse sequence)
CPMG	Carr-Purcell-Meiboom-Gill (pulse sequence)
NOE	nuclear Overhauser effect
SPI	selective polarisation inversion
2D EXSY	two-dimensional exchange spectroscopy
SA	shielding anisotropy
MELODRAMA	melding of spin-locking and dipolar recovery at the magic angle (pulse sequence)
GAMMA	general approach to magnetic resonance mathematical analysis
BPP	Bloembergen-Purcell-Pound (theory)
FT	Fourier transform
WISE	wideline separation
TPPM	two-pulse phase-modulated (decoupling)
HH	head to head
HT	head to tail
TT	tail to tail
SIDE	simulated interrupted decoupling
PAS	principal axis system
rf	radio frequency
PDMSO	polydimethylsiloxane
TTMS	tetrakistrimethylsilylsilane
CYCLOPS	cyclically ordered phase sequence
TMS	tetramethylsilane
FID	free induction decay

Contents

Chapter 3 - Fundamental aspects of NMR explored using host-guest systems

Chapter 1

Introduction

1.1 Structural elucidation of disordered solids

The two most common techniques used to access structural information in the solid state are diffraction-based techniques and NMR. X-ray diffraction techniques rely on the existence of long-range order for structural elucidation. Therefore, in the study of solids which exhibit static and/or dynamic disorder, diffraction-based techniques can reveal the existence of disorder but cannot provide information of sufficient detail. In such cases, solid-state NMR is a particularly powerful tool due to its ability to probe local environments and study dynamic processes occurring at rates in the Hz to hundreds of MHz range.[1] The work contained within this thesis concentrates on a number of compounds, which are encompassed by the heading of disordered solids, that can be termed organic inclusion compounds.

1.2 Inclusion compounds

Inclusion compounds, or host/guest systems, can be considered as systems in which one species, the guest, is confined within another, the host, species. Some inclusion compounds exist only in the solid state, although the inclusion of guest molecules can occur in solution (but only if the host structure is retained in this medium). Inclusion compounds can typically be divided into two classes, with the division based upon whether the host structure consists of tunnels or cages. In order for a guest to be included within the host tunnels or cages, the guest must be of a suitable size and shape. Hence, inclusion compounds have applications in the separation and purification of molecules. It is also possible to stabilise molecules which are, for example, light or air sensitive, by inclusion into a suitable host structure. Therefore, it is important to be able to access and ultimately understand the

molecular interactions and dynamics which are present in inclusion compounds. Hence, those inclusion compounds which exist in the solid state are particularly interesting as they permit the study of such features in relatively controlled environments. The inclusion compounds which have been studied in this thesis, using solid-state NMR, are those formed by urea, thiourea and cyclodextrin.

1.2.1 Urea inclusion compounds[2-5]

In urea inclusion compounds, the urea is extensively hydrogen bonded to form linear, parallel tunnels (Figure 1.1b). The diameter of the tunnel varies from about 5.5 Å to 5.8 Å (Figure 1.2) and hence only guest molecules based on linear alkanes, of a sufficient length, and which possess a low degree of substitution can be included within the tunnels. Urea inclusion compounds can either be incommensurate, i.e. the periodicities of the host and guest structures cannot be related by a small integer, or commensurate. The compounds studied in this case are all incommensurate, and thus in principle each guest is in a different position with respect to the host. Upon removal of the guest molecules, the urea tunnel structure (hexagonal) collapses to form pure urea (tetragonal) and hence urea inclusion compounds exist only in the solid state. The study of urea inclusion compounds containing unsymmetric guests is an area of particular interest, due to the possibility of the existence of preferred guest orientations.[5-7] Such information may provide details regarding the mechanism of the crystal growth process.

Urea inclusion compounds can be used to separate, for example, linear alkanes from branched alkanes.[5] Polymers can be contained within the urea tunnels either via direct inclusion or by reaction of included monomers, and so this may help in the understanding of the behaviour of polymer chains in crystalline samples.[8,9] Urea can also be used to stabilise molecules such as diacyl peroxides and peroxy acids which are used in laundry products.[5] Due to the fact that the urea tunnels are chiral, these compounds have potential in the separation of racemic mixtures.[10-14]

1.2.2 Thiourea inclusion compounds[3-5]

In thiourea inclusion compounds, the thiourea is extensively hydrogen bonded to form linear, parallel tunnels (Figure 1.1a). However, unlike the urea tunnels (which are relatively smooth) the thiourea tunnel contains prominent constrictions and bulges, and hence the diameter varies from about 5.8 Å to 7.1 Å (Figure 1.2). Therefore, although strictly speaking, thiourea contains tunnels, it is perhaps more accurate to describe it as a cage structure. Thiourea can form inclusion compounds with much bulkier guest molecules than urea, such as cyclohexanes and organometallics. Thiourea inclusion compounds tend to be commensurate and so the guest molecules occupy preferred sites in the tunnels, centred on a 'bulge'. For guest molecules which are relatively isotropic in shape, the thiourea adopts a rhombohedral structure, which at low temperatures reverts to the monoclinic structure. The monoclinic structure, which permits the guest molecules to adopt a more ordered structure, is also formed at higher temperatures for planar guest molecules.

When guest molecules such as mono-substituted cyclohexanes are included within thiourea, their conformational behaviour can be markedly different from that in the pure phase or in solution.[15] Therefore, such guest molecules can provide sensitive probes for the study of host-guest interactions. As for urea, polymerisation reactions can also be performed in the thiourea tunnels. A Diels-Alder reaction has successfully been performed between maleic anhydride and cyclopentadiene in the thiourea tunnel with a high degree of diastereoselectivity being achieved.[5] It is also possible to form inclusion compounds between thiourea and some organometallic guest molecules that exhibit second harmonic generation, which could be used, for example, to extend the frequency range of lasers.[5]

a)

b)
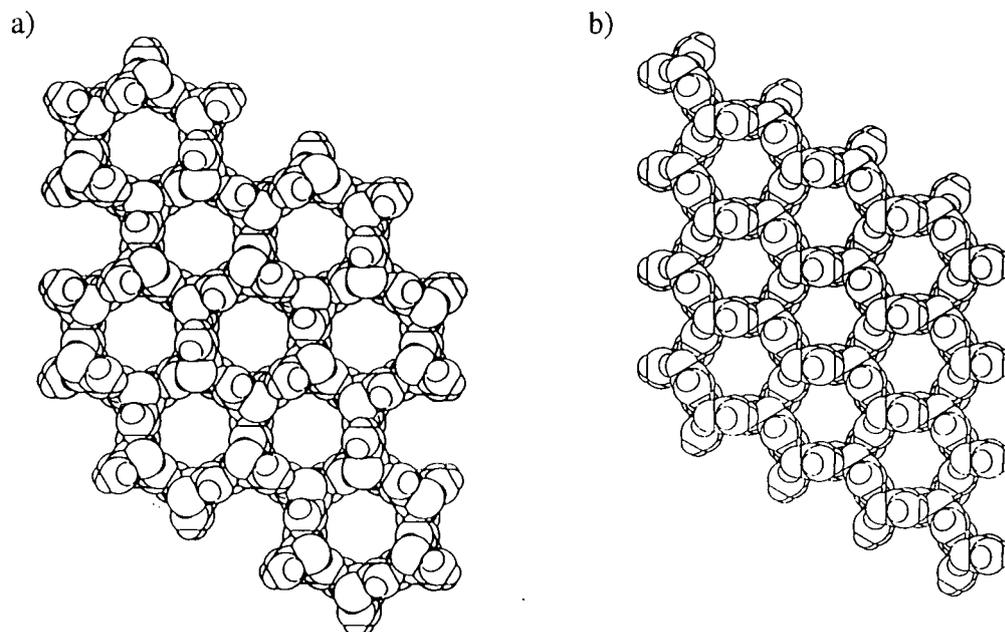
Figure 1.1. Host structure in a) a thiourea inclusion compound (rhombohedral) and b) a urea inclusion compound (hexagonal).[5]
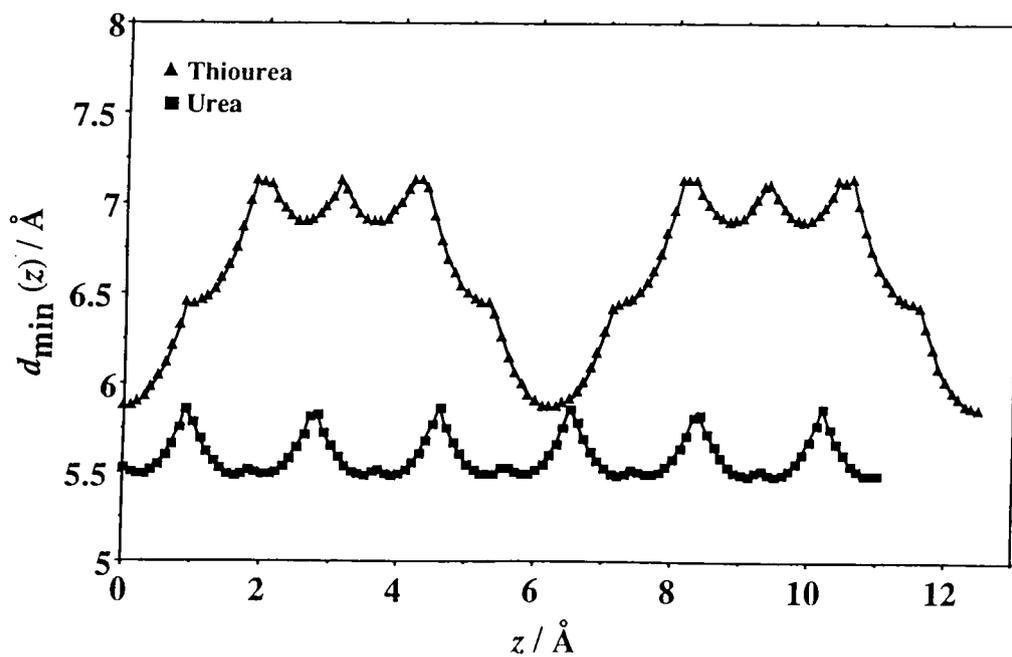
Figure 1.2. Variation in tunnel diameter (d/Å) along the tunnel axis (position is given by z/Å) for thiourea and urea.[5]

1.2.3 Cyclodextrin inclusion compounds[16-18]

Cyclodextrins are cyclic oligosaccharides that contain a hydrophobic cavity, in which a guest molecule can reside. Unlike urea and thiourea inclusion compounds, cyclodextrin inclusion compounds can exist both in solution and in the solid state. This is due to the fact that the conformation of the cyclodextrin ring is virtually the same in both phases. The most common cyclodextrins are made up of six (α-), seven (β-) or eight (γ-) glucose units, each in the chair conformation, connected to form a cone-shaped ring (Figure 1.3). The shape of the ring (Figure 1.4) is stabilised by intramolecular hydrogen bonding between secondary OH groups, and the cavities range from 5 Å in diameter for α-cyclodextrin to 8 Å in diameter for γ-cyclodextrin. Cyclodextrin inclusion compounds can be of the cage (herringbone and brick) or tunnel type.

Light- and/or air-sensitive substances or those with a particularly unpleasant odour can be included within cyclodextrin to enhance their stability or render them odourless, respectively. These features of the compounds are particularly attractive to the pharmaceutical industry as they allow the administration of otherwise unstable and/or unpleasant smelling substances.[19,20] The fact that cyclodextrins are soluble in water, yet possess a hydrophobic cavity, means that they can be used to dissolve substances which are only sparingly soluble in water. This property of cyclodextrins has found application in both the pharmaceutical and food industries.[17] By including substituted benzene molecules within the cyclodextrin cavity, it is possible to obtain regiospecific substitution, and thus cyclodextrins can be used as enzyme models.[17,21-23]
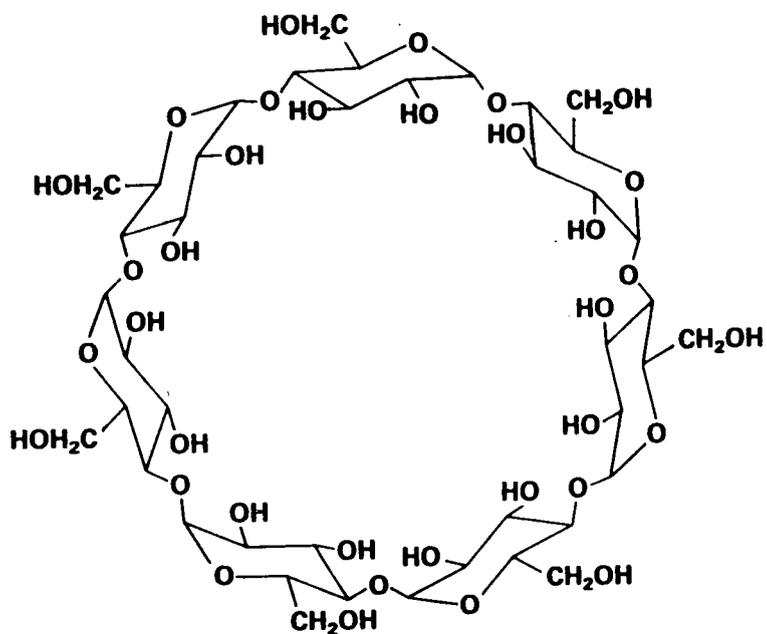
Figure 1.3. β-*cyclodextrin molecule showing how the glucose units, each in the chair conformation, connect to form a cone-shaped ring.*[24]
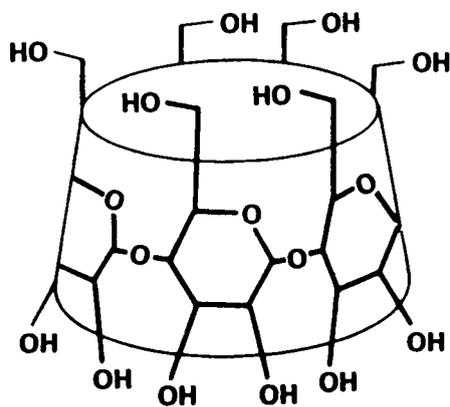
Figure 1.4. Schematic drawing of a cyclodextrin molecule depicting the cone shape adopted.[24]

1.3 Aims and objectives

The compounds which have been studied in depth are the fluoroalkane/urea, 2-hydroxyalkane/urea and fluorocyclohexane/thiourea inclusion compounds. However, prior to performing any specific experiments, some of the more fundamental aspects of NMR need to be explored. Standard experiments such as cross polarisation,[25] heteronuclear dipolar decoupling[26] and dipolar dephasing,[27] when applied to systems containing both mobile (guest) and rigid (host) components, have been examined. Potential aspects of interest for the urea inclusion compounds include guest ordering, hydrogen bonding, guest and host dynamics, and guest-guest intermolecular distances.[5] For the fluorocyclohexane/thiourea inclusion compound, the conformational dynamics and the possible existence of a well-defined distance between adjacent guest molecules are sources of great interest.[5]

In all of the compounds, at least two of the following NMR active nuclei are present: ^{13}C, ^1H, ^{19}F and ^2H. Nuclei such as ^{13}C and ^{19}F lend themselves well to the study of local environments, due to their large chemical shift range. Therefore, $^1H \rightarrow ^{13}C$ CP and/or ^{19}F single-pulse experiments, undertaken with high-power ^1H decoupling, will be used to probe guest ordering and dynamics. However, for those systems which contain both ^1H and ^{19}F, recent advances in probe technology are central to the study.[28-30] The considerable gain in sensitivity provided by the ability to acquire ^{19}F spectra, rather than ^{13}C, renders otherwise lengthy experiments, such as static and two-dimensional experiments, feasible. Therefore, the dynamics of the fluorocyclohexane molecules will be investigated by ^{19}F NMR. Particularly in the case of the fluoroalkane/urea inclusion compounds, the presence of ^{19}F nuclei at the end of guest molecules means that there are essentially isolated ^{19}F-^{19}F spin pairs. Hence, the use of static and/or MAS ^{19}F NMR experiments in the determination of ^{19}F-^{19}F intermolecular distances[31-33] will be investigated. CRAMPS experiments will be performed to investigate possible hydrogen bonding interactions.[34,35] For those compounds which contain both ^1H and ^{19}F, it is necessary to consider multiple-pulse sequences which simultaneously remove the homonuclear and heteronuclear dipolar interactions between the ^1H and ^{19}F.[36]

From the outline of some of the applications of inclusion compounds presented in the previous section, it is clear that an understanding of the molecular interactions and dynamics within such compounds is vital. However, as already mentioned, the structural information that can be provided by diffraction-based techniques is limited due the disordered nature of the inclusion compounds. Therefore, in the solid state, NMR is the technique of choice for the study of systems exhibiting static and/or dynamic disorder. The work presented in this thesis highlights the information that is accessible, using a range of solid-state NMR experiments, for a number of inclusion compounds.

1.4 References

1. J. Sandström, *Dynamic NMR Spectroscopy*, Academic Press, London, 1982.

2. K.D.M. Harris, *J. Solid State Chem.*, 1993, **106**, 83.

3. K. Takemoto and N. Sonoda, *Inclusion Compounds*, (Editors: J.L. Atwood, J.E.D. Davies and D.D. MacNicol), Academic Press, London, 1984, Volume 2, pp. 47-67.

4. K.D.M. Harris, *J. Mol. Struct.*, 1996, **374**, 241.

5. M.D. Hollingsworth, K.D.M. Harris, *Comprehensive Supramolecular Chemistry* (Editors: D.D. MacNicol, F. Toda, R. Bishop), 1996, Volume 6, Pergamon, pp. 177-237.

6. M.D. Hollingsworth and N. Cyr, *Mol. Cryst. Liq. Cryst.*, 1990, **187**, 135.

7. A. Nordon, R.K. Harris, L. Yeo and K.D.M. Harris, *Chem. Commun.*, 1997, 2045.

8. N. Vasanthan, I.D. Shin, C.P. Howe and A.E. Tonelli, *Magn. Reson. Chem.*, 1994, **32**, S61.

9. C. Howe, N. Vasanthan, C. MacClamrock, S. Sankar, I.D. Shin, I.K. Simonsen and A.E. Tonelli, *Macromolecules*, 1994, **27**, 7433.

10. W. Schlenk, *Justus Liebigs Ann. Chem.*, 1973, **7**, 1145.

11. W. Schlenk, *Justus Liebigs Ann. Chem.*, 1973, **7**, 1156.

12. W. Schlenk, *Justus Liebigs Ann. Chem.*, 1973, **7**, 1179.

13. W. Schlenk, *Justus Liebigs Ann. Chem.*, 1973, **7**, 1195.

14. L. Yeo and K.D.M. Harris, *Tetrahedron: Asymmetry*, 1996, **7**, 1891.

15. A.E. Aliev and K.D.M. Harris, *J. Am. Chem. Soc.*, 1993, **115**, 6369.

16. W. Saenger, *Inclusion Compounds*, (Editors: J.L. Atwood, J.E.D. Davies and D.D. MacNicol), Academic Press, London, 1984, Volume 2, pp. 231-259.

17. W. Saenger, *Angew. Chem. Int. Engl.*, 1980, **19**, 344.

18. G. Le Bas and N. Rysanek, *Structural Aspects of Cyclodextrins*, Edition de Santé, Paris, 1987.

19. T. Tanabe, S. Kishimoto, S. Maruyama, S. Kumon and E. Suzuki, *Supramol. Chem.*, 1994, **3**, 127.

20. F.H. Kuan, Y. Inoue and R. Chûjô, *J. Inclusion Phenom.*, 1986, **4**, 281.

21. Z.H. Qi, V. Mak, L. Diaz, D.M. Grant and C. Chang, *J. Org. Chem.*, 1991, **56**, 1537.

22. I. Tabushi, *Acc. Chem. Res.*, 1982, **15**, 66.

23. M. Komiyama and H. Hirai, *J. Am. Chem. Soc.*, 1984, **106**, 174.

24. J. March, *Advanced Organic Chemistry: Reactions, Mechanisms and Structure*, Wiley, 4th edition, 1992.

25. S.R. Hartmann and E.L. Hahn, *Phys. Rev.*, 1992, **128**, 2042.

26. K. Schmidt-Rohr and H.W. Spiess, *Multidimensional Solid-state NMR and Polymers*, Academic Press, London, 1994.

27. S.J. Opella and M.H. Frey, *J. Am. Chem. Soc.*, 1979, **101**, 5854.

28. U. Scheler, P. Holstein, S.A. Carss and R.K. Harris, *Chemagnetics Application Note*, May 1995.

29. S.A. Carss, U. Scheler, R.K. Harris, P. Holstein and R.A. Fletton, *Magn. Reson, Chem.*, 1996, **34**, 63.

30. S.C. Campbell, R.K. Harris, M.J. Hardy, D.C. Lee and D.J. Busby, *J. Chem. Soc., Perkin Trans. 2*, 1997, 193.

31. J.M. Griffiths and R.G. Griffin, *Anal. Chim. Acta*, 1993, **283**, 1081.

32. W.P. Power and R.E. Wasylishen, *Annual Reports NMR Spectroscopy*, 1991, **23**, 1.

33. J.M. Griffiths, A.E. Bennett and R.G. Griffin, 'Homonuclear Recoupling Schemes in MAS NMR', *Encyclopedia of NMR*, (Editors: D.M. Grant and R.K. Harris), Wiley, London, 1996, **4**, 2390.

34. R.K. Harris and P. Jackson, *J. Phys. Chem. Solids*, 1987, **48**, 813.

35. R.K. Harris, P. Jackson, L. H. Merwin, B.J. Say and G. Hägele, *J. Chem. Soc., Faraday Trans. 1*, 1988, **84**, 3649.

36. U. Haeberlen, *High Resolution NMR in Solids*, Academic Press, New York, 1976.

Chapter 2

Experimental

2.1 Spectrometer details

All the spectra contained within this thesis were acquired on a triple-channel Chemagnetics CMX spectrometer, operating at 200.13 MHz for ^{1}H. The spectrometer is operated using a Sun workstation which runs a software package called Spinsight. Data processing is also performed using Spinsight, although the version of software which is used for processing, i.e. the 'no acquisition' version, is located on a Sun Ultra Sparc workstation. The workstation actually controls the spectrometer through the digital card cage, which transmits all the pulse program details, e.g. timings, phase, frequency etc., to the synthesisers, transmitters, amplifiers and receiver. A schematic diagram of a spectrometer is shown in Figure 2.1. The synthesisers produce what is called the local oscillator (LO) signal, which is then mixed with the intermediate frequency (IF). The IF, which is 282 MHz on the CMX 200, can be considered as the 'working' frequency of the spectrometer and is generated from a 10 MHz reference signal. The reference frequency itself is generated by the DC power supply, which also provides power for the spectrometer. If for example a frequency of 200 MHz is required, the synthesisers produce a LO signal with a frequency of 482 MHz. Hence, from the difference of the IF and LO frequency, the required frequency of 200 MHz is generated. It is possible to alter the IF by ± 1 MHz, with the transmitters, using the frequency offset parameter in the pulse program. The transmitters also control the amplitude and phase of the pulse via the corresponding pulse program parameters.
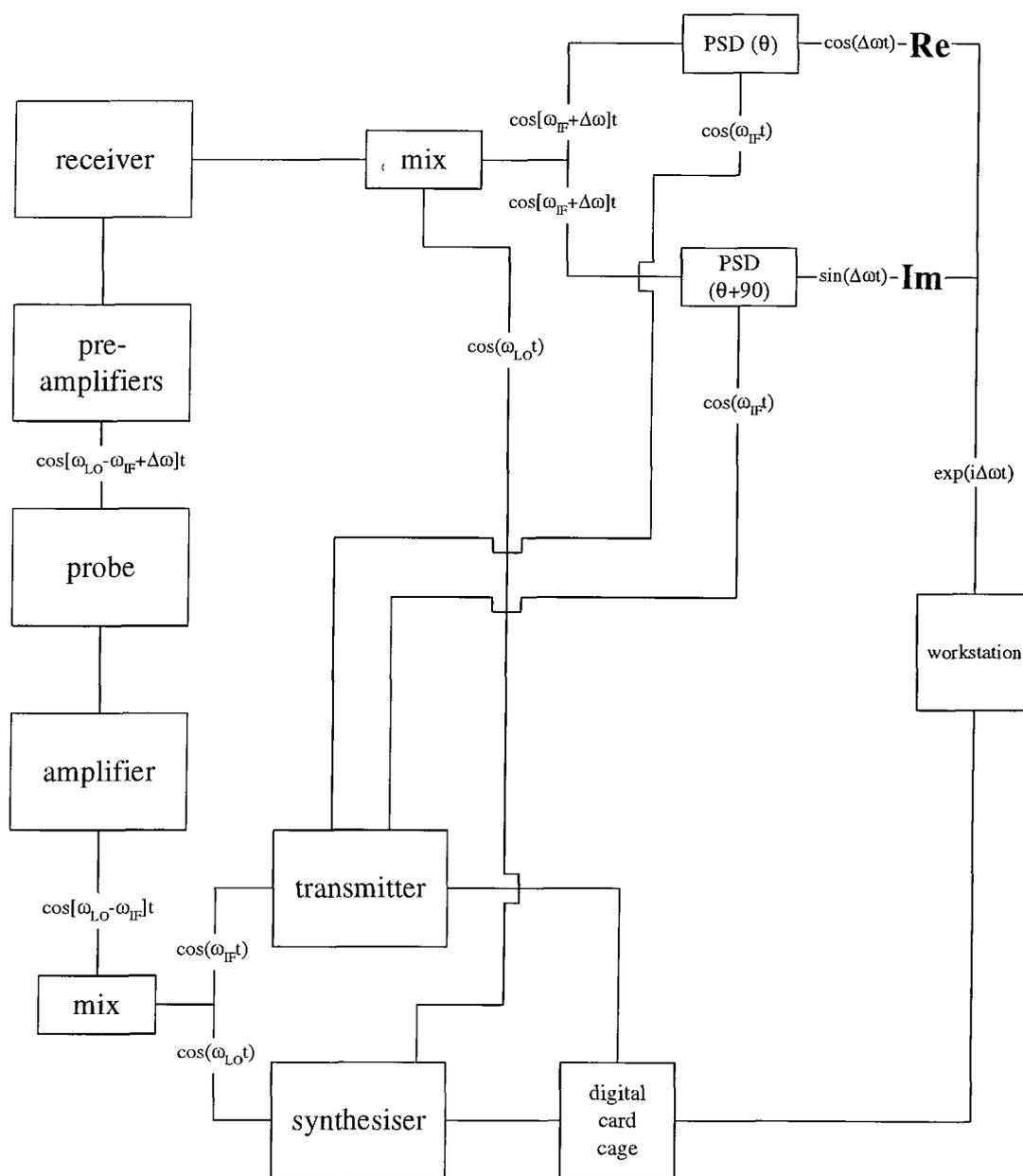
Figure 2.1. Schematic diagram of a spectrometer. The rf at different stages is given by cos(ωt), where ω denotes the frequency and θ denotes the phase.

The low-power rf from the transmitters then goes into the amplifiers. Assuming a simple single-pulse experiment, the high-power rf generated then passes through a set of crossed diodes, a high-power filter and bidirectional coupler before reaching the probe. The signal generated then goes back through the filter and down a λ/4 cable before going through two pre-amplifiers. The signal is then mixed with the LO frequency, generated by the synthesisers, in the receiver to give a frequency

which is equal to the IF plus the frequency difference between the Larmor frequency and the resonance frequency of the observe nucleus. This signal is then split into two channels, referred to as real and imaginary, with a phase-sensitive detector (PSD)[1] on each. The IF is mixed with the signal at the PSD stage, with the phase of the IF on one channel shifted by 90° with respect to that on the other. The difference between the IF and the signal frequency generates a frequency in the audio range, which is filtered and amplified before detection of the real and imaginary FIDs. The arrangement of two PSDs in parallel, with the output signal of one differing in phase by 90° from the other, is referred to as quadrature phase detection.[2] However, if, for example, the gain on the two channels differs slightly, then this results in a 'quadrature glitch' which manifests itself in the spectrum as a mirror image of the actual signal about the transmitter position. Although it is possible to rebalance the two receiver channels, for small imbalances application of CYCLOPS[3] phase cycling eliminates the unwanted signal.

Earlier it was mentioned that the signal goes down a λ/4 cable before being amplified and subsequently detected. The purpose of this particular, and adjoining, components is to separate the high-voltage rf going into the probe from the low-voltage rf signal coming out of the probe.[4] A schematic drawing of the circuitry required is given in Figure 2.2. The crossed diodes only conduct, i.e. allow rf through, when the rf is above a certain (low) voltage threshold. Consequently, the high-voltage rf generated by the amplifiers passes through the crossed diodes and into the probe. However, it is vital that the pre-amplifiers and receiver are protected from this high voltage, but yet are still able to detect the low-voltage signal. If any high voltage goes down the λ/4 cable, then the earthed crossed diodes conduct. Hence, at the end of the λ/4 cable which adjoins the earthed crossed diodes, the impedance is at a minimum. At the opposite end of the λ/4 cable, the impedance is at a maximum and so all the high-voltage rf is directed into the probe. The low-voltage signal then goes down the λ/4 cable and into the pre-amplifiers and receiver, since the crossed diodes do not conduct at this low voltage. The crossed diodes in between the amplifiers and the high-power filters, also prevent 'noise' from the amplifiers in their rest state from getting through into the detection circuitry.
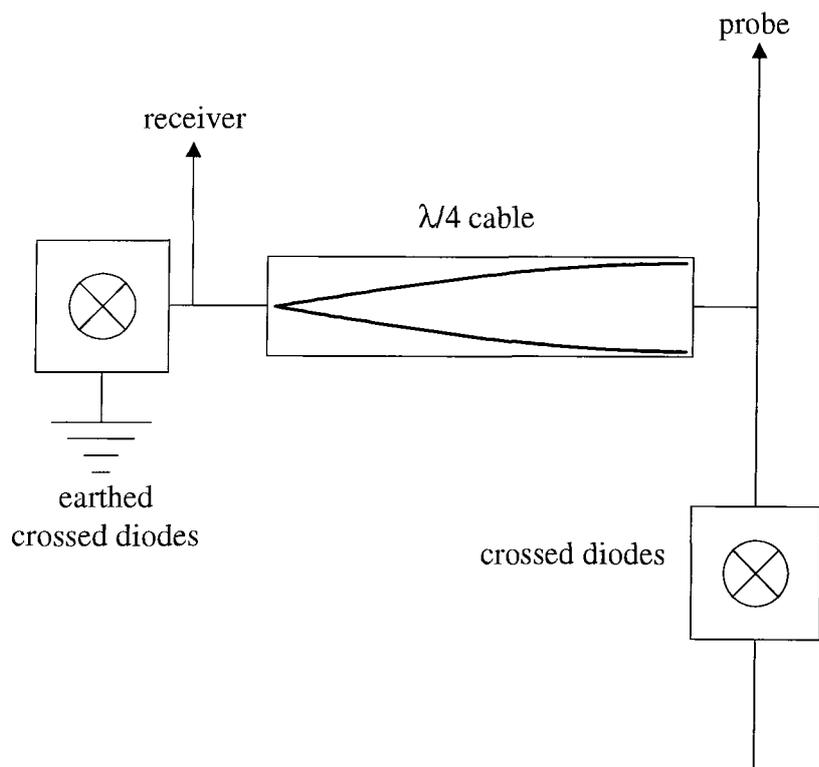
Figure 2.2. Circuitry used to detect low-voltage signals and protect the receiver from the high-power rf. A standing wave has been drawn inside the λ/4 cable to show how the voltage (and impedance) is at a minimum at one end and at a maximum at the other end when the wavelength of the rf is four times the length of the cable.

Having discussed the basic operation of a spectrometer, some of the components of the CMX and set-up procedures for particular experiments will now be discussed.

2.2 Probes

The nuclei which have been studied in this thesis are ^{1}H, ^{19}F, ^{13}C and ^{2}H, using a combination of three Chemagnetics MAS probes, HX, HF and HFX.

2.2.1 HX

The HX probe can be used to study ^{1}H and nuclei (X) in the 19.4-82.6 MHz frequency range. The frequency to which the X channel is to be tuned is changed by inserting 'top' and 'bottom' plug-in capacitors of a specific capacitance. The probe contains a spinning module which accepts 7.5 mm zirconia rotors. The drive tip for the rotor is made from Kel-F, with the endcap and spacers both being made from Teflon. It is possible to spin such rotors up to ~6.5 kHz and, for particularly slow spinning experiments such as magic-angle turning (MAT),[5] a 'smooth' drive tip is used. Typically, ^{1}H decoupling powers of the order of 60 kHz are possible using this probe.

2.2.2 HF

A purpose-built HF probe[6] is required, as opposed to a broadband HX probe, for the study of ^{1}H and ^{19}F due to the close proximity of their respective Larmor frequencies. Hence, it is not only necessary to tune and match each channel, but it is also necessary to tune a 'trap' on each channel. In practice, this is performed by connecting the output of the channel which is not being tuned, to an oscilloscope. The trap for the channel which is being tuned is then adjusted until a node, i.e. a minimum, is observed in the signal on the oscilloscope. Hence, when both traps are set, this corresponds to the condition where there is the minimum rf breakthrough between the two channels. It is best to set the ^{19}F trap first as this is most sensitive to the sample. In particular, the trap changes significantly when the sample is contained within a glass insert compared to when it is contained within a rotor. Having set the

^{19}F trap, one can then tune and match ^{19}F before performing the same procedure on ^{1}H, which is far less sensitive to the sample and its container. Isolation of the two channels is increased by using ^{1}H and ^{19}F high-power bandpass filters. Typically, ^{1}H decoupling powers of the order of 100 kHz are used. The probe contains a spinning module which accepts 4 mm zirconia rotors. The drive tip for the rotor is made from Vespel, with the endcap and spacers both being made from Teflon for ^{1}H observation or from Vespel for ^{19}F observation. It is possible to spin such rotors up to ~18 kHz and for slow-spinning (< 1000 Hz) experiments such as CRAMPS, a 'smooth' drive tip is used.

2.2.3 HFX

The HFX probe can be used to simultaneously decouple both ^{1}H and ^{19}F while observing an X nucleus in the 19.7-102.2 MHz frequency range. When the frequency of X is greater than 38.5 MHz, no 'top' or 'bottom' capacitor is required. However, for frequencies less than 38.5 MHz, a 'top' capacitor is required. The ^{1}H and ^{19}F frequencies are isolated via an adjustable ^{19}F trap and a fixed ^{1}H trap. The ^{19}F trap is set by minimising the output signal from the ^{1}H channel when tuning the ^{19}F channel. The ^{19}F trap is sensitive to the frequency to which the X channel is tuned. Therefore, when changing the probe from, for example, ^{31}P to ^{13}C, it is best to tune the X channel in 10 MHz intervals and at each stage set the ^{19}F trap. As this probe is not used to observe one of the high-frequency nuclei while simultaneously decoupling the other, it is only necessary to use the standard 200 MHz high-power bandpass filters on the ^{1}H and ^{19}F channels. As for the HX probe, a 100 MHz high-power low-pass filter is used on the X channel. With this probe, it is necessary to insert a 100 MHz low-power low-pass filter between the earthed crossed diodes and the first pre-amplifier to remove the ^{1}H and ^{19}F frequencies and their harmonics before detection of the signal. It should be noted that the ^{1}H and ^{19}F high-power bandpass filters used with the HF probe, cannot be used with the HFX probe to observe one of the nuclei while decoupling the other, due to their inability to handle the powers that are required for this probe.

The probe contains a spinning module which accepts 7.5 mm zirconia rotors and it is possible to spin such rotors up to ~6.5 kHz. The drive tip, endcap and spacers that are used in ^{13}C cross-polarisation experiments depend upon whether cross polarisation is from ^{1}H or ^{19}F. For ^{1}H→^{13}C cross-polarisation experiments, a Kel-F drive tip, boron nitride spacers and Kel-F endcaps are used. For ^{19}F→^{13}C cross-polarisation experiments, a Vespel drive tip, boron nitride spacers and Vespel endcaps are used. However, for ^{19}F→^{13}C cross-polarisation experiments where the Kel-F signal (~120 ppm) is removed from the region in which the signals of interest are present, and in ^{13}C single-pulse experiments, the choice of endcap and drivetip is irrelevant. Typically, ^{1}H and ^{19}F decoupling powers of the order of 56 kHz are used.

2.3 Magic-angle spinning (MAS)

2.3.1 Control of MAS rate

The majority of experiments have been performed using magic-angle spinning (MAS). The MAS rate is controlled using an automatic spinning-speed controller, which can be operated either using the software or via the controller itself. With this spinning-speed controller, it is possible to just input the required MAS rate, and the sample will spin up automatically with control over both the bearing and drive pressures. The spinning-speed controller allows control of the MAS rate typically to within ±1 Hz of the desired value, and it is also possible to set 'alarms' which are activated when the MAS rate goes outside a specified region. This then stops the sample from spinning and ends the acquisition process. These features of the spinning-speed controller are particularly desirable for long experiments, where stable spinning is required and for those experiments which are left unattended, where probe damage would be likely should the air pressure drop or the rotor spinning become unstable.

2.3.2 Setting the magic angle

For the HX and HFX probes, the magic angle is set by observing the ^{79}Br (50.143 MHz) signal from potassium bromide at a MAS rate of 2-3 kHz. Typically, the angle is set by maximising the number of rotational echoes in the FID. The rotational echoes arise from the effect of MAS on the quadrupolar interaction, which is only non-zero due to imperfections in the KBr (cubic) crystal lattice. It is also possible to use the lineshape of the nitrate peak in the ^{15}N spectrum of NH_4NO_3 to set the magic angle, though this is less convenient when performing ^{13}C experiments as capacitors and powers have to be changed. However, for the HF probe, it is not possible to observe ^{15}N or ^{79}Br, so the ^{1}H CRAMPS signal from $KHSO_4$ is observed.[7] The reason for using $KHSO_4$ is that the two ^{1}H signals are relatively well separated and both have a large shielding anisotropy (SA). Therefore, when the angle is not at 54.7°, the lines broaden due to this interaction, and hence the ^{1}H lineshape can be used to set the magic angle. Adjustment of the magic angle on all three of the probes is via a rod which is accessed from the base of the probe. It is only possible to change the angle by a few degrees on Chemagnetics MAS probes, and so for 'off-angle' experiments the probes need to be partially dismantled (see Chapter 7).

2.4 Power considerations

Before performing any actual experiments, it is necessary to consider which amplifiers are to be used and to check that the transmitters are connected to those required. Therefore, a brief discussion will follow which examines some of the important points concerning the amplifiers and the measurement of their output power.

2.4.1 Amplifiers

Although up to three amplifiers can be used at a time, there are in fact four amplifiers to choose from: a broadband (6-220 MHz) AMT amplifier, a low-

frequency (30-122 MHz) AMT amplifier, a CE narrowband (188.288-200.13 MHz) amplifier and a narrowband (188.288-200.13 MHz) Bruker amplifier. It is important to note that the CE and Bruker amplifiers both need to be tuned to the desired frequency. The two AMT amplifiers are relatively linear, whereas the CE amplifier can operate in either class A/B mode or class C mode. Again the CE amplifier needs to be tuned to give the maximum output possible in the required mode of operation. The output of the CE and AMT amplifiers can be adjusted by the rf output dial on the transmitters, or, in the case of the broadband AMT and the CE amplifiers, software control is possible using the 'amplitude' parameter in the pulse program. Hence, by changing the input voltage for linear amplifiers, it is possible to change the output voltage. The Bruker amplifier is a class C amplifier and the output is adjusted via coarse and fine gain dials. Unlike the other three amplifiers, this amplifier does not require any blanking and it is also necessary to have the rf output dial on the transmitter to be set at its maximum value for use for ^{1}H or ^{19}F. Similarly, when the CE amplifier is set to class C mode, the transmitter rf output dial needs to be set above a particular value (> 500) in order to drive the amplifier.

Typically, the CE and AMT amplifiers are capable of producing 500 W, with the maximum duration of continuous irradiation for the AMT amplifiers limited to ~ 20 ms. When using the low-frequency AMT amplifier, it is also necessary to blank the amplifier when it is not pulsing due to the manner in which it calculates its duty cycle. The Bruker amplifier is capable of producing 1000 W and, like the CE amplifier, can irradiate continuously for > 200 ms. The maximum power and the duration of pulses that are possible with the amplifiers, are quite capable of degrading probes and, as different probes have different power specifications, then the respective probe manual should always be consulted.

2.4.2 Measuring the power going into the probe

Prior to putting a pulse into the probe, it is important to know what the actual power going into the probe is, in order to avoid probe damage. The power going into the probe is measured by disconnecting the cable from the probe and connecting it to

a 30 dB attenuator which is then connected to an oscilloscope. A pulse, typically of 50 μs duration, is applied and subsequently observed on the oscilloscope. So that the pulse appears continuously on the oscilloscope, a recycle delay of 0.1s and an acquisition length of 8 points are used. The peak-to-peak voltage is read from the vertical scale, which is then converted into a power and multiplied by 1000 to allow for the 30 dB attenuation. The conversion of the peak-to-peak voltage to the actual power going into the probe is conveniently performed using a 'voltage/power/dbm' chart.

2.5 General set-up procedure

The majority of experiments performed have been either double- or triple-channel, i.e. involved both ^{1}H and either ^{19}F or ^{13}C, or all three nuclei. The set-up for single-pulse experiments is basically as described in section 2.5.1. For both the HF and HX probes, usually the CE amplifier in class A/B mode is used for ^{1}H while the broadband AMT is used for the observe nucleus, ^{19}F and ^{13}C. Similarly, for the HFX probe the CE and AMT amplifiers are used for ^{1}H and ^{13}C, respectively, with the Bruker amplifier being used for ^{19}F. The order in which the following subsections are presented corresponds to the order in which the operations are performed in practice.

2.5.1 Setting the ^{1}H channel power and shimming

First, it is necessary to set the power on the ^{1}H channel by performing a single-pulse experiment on polydimethylsiloxane (PDMSO). The power going into the probe is adjusted via the rf output dial on the transmitter until a pulse of the required duration rotates the magnetisation through an angle of 180°, such that a 'null' signal is observed. Typically, a 4-5 μs ^{1}H 90° pulse is set on the HX and HFX probes whereas a 3 μs ^{1}H 90° pulse is set on the HF probe. The probe is then shimmed by altering the current going into the shim coils that are positioned in the bore of the magnet, in order to compensate for inhomogeneities in B_0. When the

static field is inhomogeneous, this results in a range of precession frequencies and hence a broadened line is observed. The probe is properly shimmed when the PDMSO signal has the minimum linewidth (fwhh) possible.

2.5.2 Setting the magic angle

Usually a 90° pulse duration is not actually calibrated for ^{79}Br as to set the magic angle, only the single-pulse experiment is used. Instead, the rf output dial on the transmitter is turned down (~300) and a short pulse duration, typically 2 μs, is used, thus ensuring that an excessive amount of power is not going into the probe. Further details regarding this particular aspect of the general set-up, are given in section 2.3.2.

2.5.3 Setting the X-channel power

The method for setting the X-channel power depends upon whether the experiment to be performed is single pulse, usually with ^{1}H decoupling, or cross polarisation.

2.5.3.1 Single pulse

Typically, for ^{19}F experiments, acquisition was via single pulse rather than cross polarisation due to the sensitivity of the signal obtained to the matching condition (see Chapter 3). Therefore, a ^{19}F 90° pulse, usually of 3 μs in duration, was set, using hexafluorobenzene (C_6F_6), via the same method as for ^{1}H.

2.5.3.2 Cross polarisation

At the Hartmann-Hahn match, efficient transfer of magnetisation from ^1H to ^{13}C, in this case, can occur. The advantages of using cross polarisation rather than single pulse for acquisition of ^{13}C spectra, are that a shorter recycle delay can be used and there is a gain in sensitivity of up to a value given by γ_H/γ_C. To set the Hartmann-Hahn match for $^1H{\rightarrow}^{13}C$ CP, adamantane is used due to its relatively narrow matching profile at MAS rates in the 1.0-1.5 kHz range (at higher speeds the matching profile breaks up into sidebands). First, the rf output dial on the transmitter is reduced to a value below that typically used. Then by observing the ^{13}C FID, the ^{13}C CP power is increased until a maximum is observed in the signal intensity. It is at this maximum that the ^{13}C B_1 is four times that of ^1H and so the Hartmann-Hahn condition is met. For low frequency nuclei such as ^{15}N, it is necessary to reduce the ^1H CP power from ~60 kHz (^1H CP power used for ^{13}C CP experiments) to ~35 kHz when setting the Hartmann-Hahn match so that the ^{15}N CP power going into the probe is not too large.

2.6 Referencing

Chemical shifts for all the nuclei studied were referenced externally by rotor replacement with respect to the chemical shifts of the samples given in Table 2.1. These samples are also used to set the pulse duration for the corresponding nucleus.

Nucleus	Frequency/MHz at 4.7 T	Reference sample	Chemical shift/ppm
^1H	200.130	PDMSO	0 with respect to TMS
^{19}F	188.288	C_6F_6	-166.4 with respect to $CFCl_3$
^{13}C	50.329	adamantane	38.4 (high-frequency resonance) with respect to TMS
^2H	30.721	^2H_2O	0

Table 2.1. Reference samples used and their chemical shifts.

Particular attention must be paid to the referencing of ^{19}F spectra, when ^{1}H decoupling is applied, due to the Bloch-Siegert effect.[8] With a static magnetic field of 4.7 T and a ^{1}H decoupling power of the order of 100 kHz, a ^{19}F resonance shifts ~2.5 ppm to low frequency upon application of the ^{1}H rf field. This issue is of particular importance when quoting ^{19}F chemical shifts as the Bloch-Siegert shift, Δ (in ppm), is field and decoupling-power dependent,[8]

$$\Delta = \frac{\left(v_1 \frac{\gamma_0}{\gamma} \right)^2}{\left(v_0{}^2 - v^2 \right)} 10^6 \qquad \textit{Equation 2.1}$$

where v_0 is the Larmor frequency of the observed nucleus, v is the Larmor frequency of the nucleus to which decoupling is applied, v_1 is the decoupling power (expressed in Hz, i.e. $\gamma B_1/2\pi$), γ_0 is the magnetogyric ratio of the observed nucleus and γ is the magnetogyric ratio of the decoupled nucleus. Hence, at low magnetic fields the denominator in Equation 2.1 will be smaller than at high magnetic fields, and so larger Bloch-Siegert shifts are observed at lower magnetic fields. It can also be seen that the Bloch-Siegert shift will be larger when higher decoupling powers are used (Figure 2.3). The Bloch-Siegert shift can be to low or high frequency, depending on whether the Larmor frequency of the observed nucleus is less than or greater than that of the decoupled nucleus.

The source of the Bloch-Siegert shift can be understood by calculating the average Hamiltonian for one nucleus while a second off-resonance rf field is applied.[9] The Hamiltonian is given by,

$$H = -\omega_I I_z - \Delta\omega I_z - 2\omega_1 I_x \cos(\omega t + \varphi) \qquad \textit{Equation 2.2}$$

where the first term describes the Zeeman interaction (ω_I is the Larmor frequency and I_z is the spin operator), the second term describes off-resonance effects ($\Delta\omega$ is the difference between the Larmor frequency and the resonance frequency of the nucleus) and the final term describes application of an rf field (ω_1 is the rf power in rad s^{-1}, i.e. $\gamma_I B_1$ and ϕ denotes the phase).

In the rotating frame of the observe nucleus, Equation 2.2 is given by:

$$H(t) = -\Delta\omega I_z - 2\omega_1 \cos(\omega t + \varphi)\left[I_x \cos\omega_I t + I_y \sin\omega_I t\right]$$

$$= -\Delta\omega I_z - \omega_1\left\{I_x\left[\cos((\omega_I + \omega)t + \varphi) + \cos((\omega_I - \omega)t - \varphi)\right] + I_y\left[\sin((\omega_I + \omega)t + \varphi) + \sin((\omega_I - \omega)t - \varphi)\right]\right\}$$

Equation 2.3

The zero-order average Hamiltonian is given by,

$$\overline{H}^{(0)} = -\Delta\omega I_z \qquad \textit{Equation 2.4}$$

and the first-order average Hamiltonian is given by,

$$\overline{H}^{(1)} = -I_z \frac{1}{2}\omega_1{}^2 \left\{\frac{1}{\omega_I + \omega} + \frac{1}{\omega_I - \omega}\right\}$$

$$-I_x\omega_1\Delta\omega\left\{\frac{\cos\left[(\omega_I + \omega)\tau + \varphi\right]}{\omega_I + \omega} + \frac{\cos\left[(\omega_I - \omega)\tau - \varphi\right]}{\omega_I - \omega}\right\}$$

$$-I_y\omega_1\Delta\omega\left\{\frac{\sin\left[(\omega_I + \omega)\tau + \varphi\right]}{\omega_I + \omega} + \frac{\sin\left[(\omega_I - \omega)\tau - \varphi\right]}{\omega_I - \omega}\right\}$$

Equation 2.5

The Bloch-Siegert shift is given by the coefficient of $-I_z$ in $\overline{H}^{(1)}$ which is equivalent to that given by Equation 2.1.
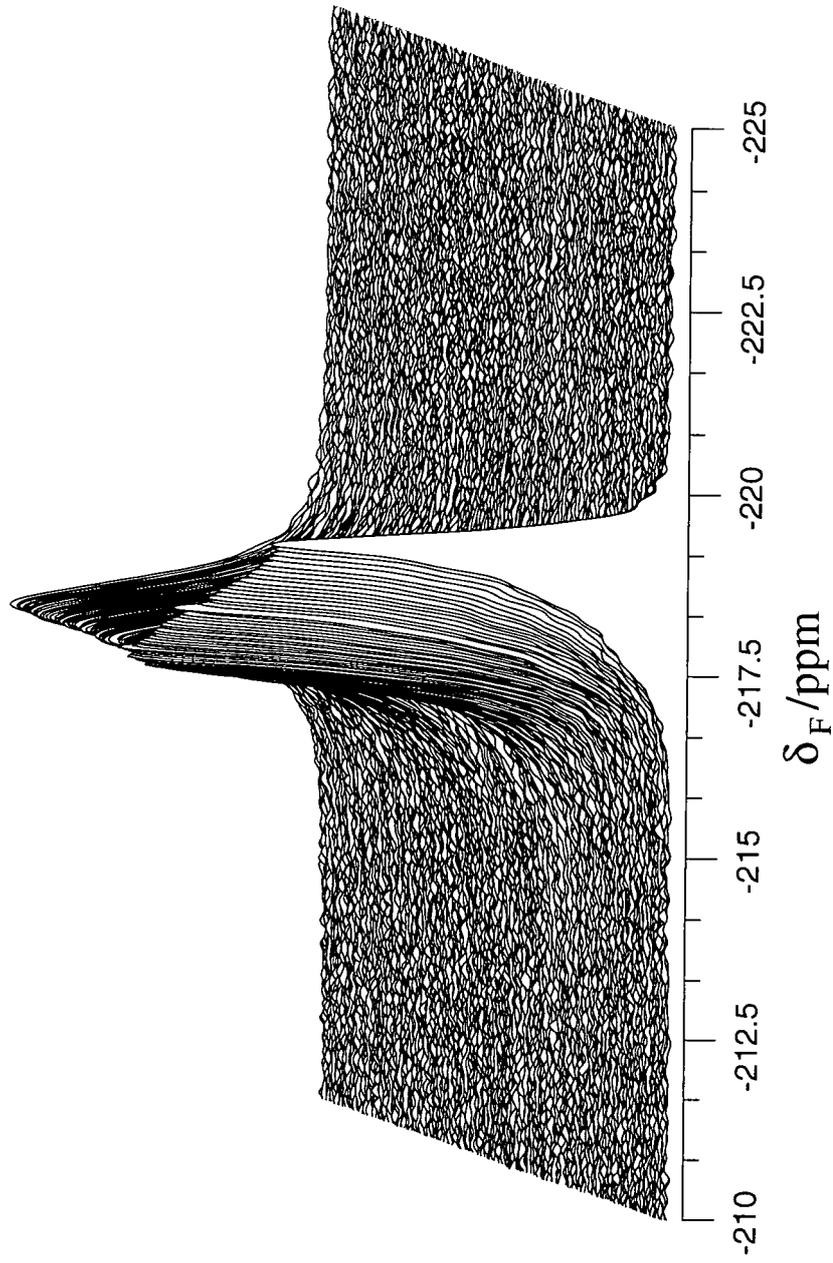
Figure 2.3. Variation in the Bloch-Siegert shift, as a function of ^1H decoupling power, observed in the ^{19}F spectra of the 1-fluorotetradecane/urea inclusion compound at 12 kHz. The decoupling power varies, from front to back, from ~100 kHz to 0 kHz.

δ_F/ppm

Hence, in order for ^{19}F chemical shifts to be universal when spectra are acquired under conditions of ^{1}H decoupling, the shift quoted should be corrected for the Bloch-Siegert shift. Due to the narrow lines in ^{19}F spectra obtained of the fluoroalkane/urea inclusion compounds, both with and without ^{1}H decoupling (see Chapter 5), the chemical shifts quoted are simply those taken from the spectra acquired without ^{1}H decoupling. However, for ^{1}H and ^{19}F containing compounds which have strong heteronuclear dipolar interactions, it is best to acquire two spectra of C_6F_6 (in separate buffers), one with and one without ^{1}H 'decoupling', and set the ^{19}F chemical shift in both cases to -166.4 ppm. Then any subsequent experiments, performed with and without ^{1}H decoupling, are acquired in the appropriate buffer, so that the Bloch-Siegert shift is removed from the chemical shifts obtained. However, for spectra acquired at different temperatures, it is important to note that although the same rf power levels may be put into the probe, the B_1 field generated will increase with decreasing temperature due to a decrease in the resistance of the coil. Therefore, the Bloch-Siegert shift will increase at lower temperatures and so, to correct for this effect at different temperatures, the variation in B_1 as a function of temperature should be determined. This could either be done by calibration of B_1 or comparing the ^{19}F chemical shifts obtained both with and without ^{1}H decoupling. The latter method was used in this case due to the relatively narrow linewidths obtained for the fluoroalkane/urea inclusion compounds in both experiments even at low temperatures.

2.7 Calibration of decoupling and cross-polarisation powers

In Chapter 3, experiments have been reported for which the ^{1}H decoupling and cross-polarisation powers have been varied. It is possible to change B_1 by either the rf output dial on the transmitters or by the software using the amplitude parameter in pulse programs. Obviously, for experiments in which a particular parameter is to be systematically varied over a period of several hours, it is particularly advantageous to use software control. The maximum B_1 is limited by the level at which the transmitters are set. However, it is possible to adjust B_1, using the amplitude

parameter in pulse programs, from 255 to 0 in minimum steps of one and where 255 corresponds to the level set at the transmitters. The maximum B_1 required is set using the method outlined in section 2.5.1 with an appropriate sample. As the experiments presented in Chapter 3 involved ^{1}H and ^{19}F, examples of calibration experiments will be discussed with respect to these two nuclei, although the method for calibrating B_1 is not specific to ^{1}H and ^{19}F. To determine B_1, at a given amplitude value, it is simply necessary to determine the pulse duration required to rotate the magnetisation through 180°. When calibrating B_1, in order to detect the signal, the circuitry is set up as shown in Figure 2.2. Therefore, the power determined in the calibration experiment will be the same as that for the observe channel in an actual experiment. The calibration curve for ^{19}F B_1 as a function of the amplitude value for the broadband AMT amplifier is shown in Figure 2.4. In the region shown, the experimental data (solid squares) can be fitted to

$$B_1 = 0.00202(F90a)^2 - 0.25511(F90a) + 11.31970 \quad \textit{Equation 2.6}$$

where F90a defines the amplitude parameter in the pulse program for a 90° pulse on the ^{19}F channel and B_1 is the rf field strength. Therefore, for any pulse on the observe channel, such as the ^{19}F cross-polarisation pulse, in which amplitude control is possible, B_1 can simply be determined from Equation 2.6. It can be seen that the amplifier behaves reasonably linearly in the 40-80 kHz range. However, as the power is reduced, i.e. the amplitude value is decreased, it becomes increasingly difficult to calibrate the power accurately. Hence, below about 5 kHz, which is equivalent to an amplitude value of ~90, B_1 cannot really be calibrated.
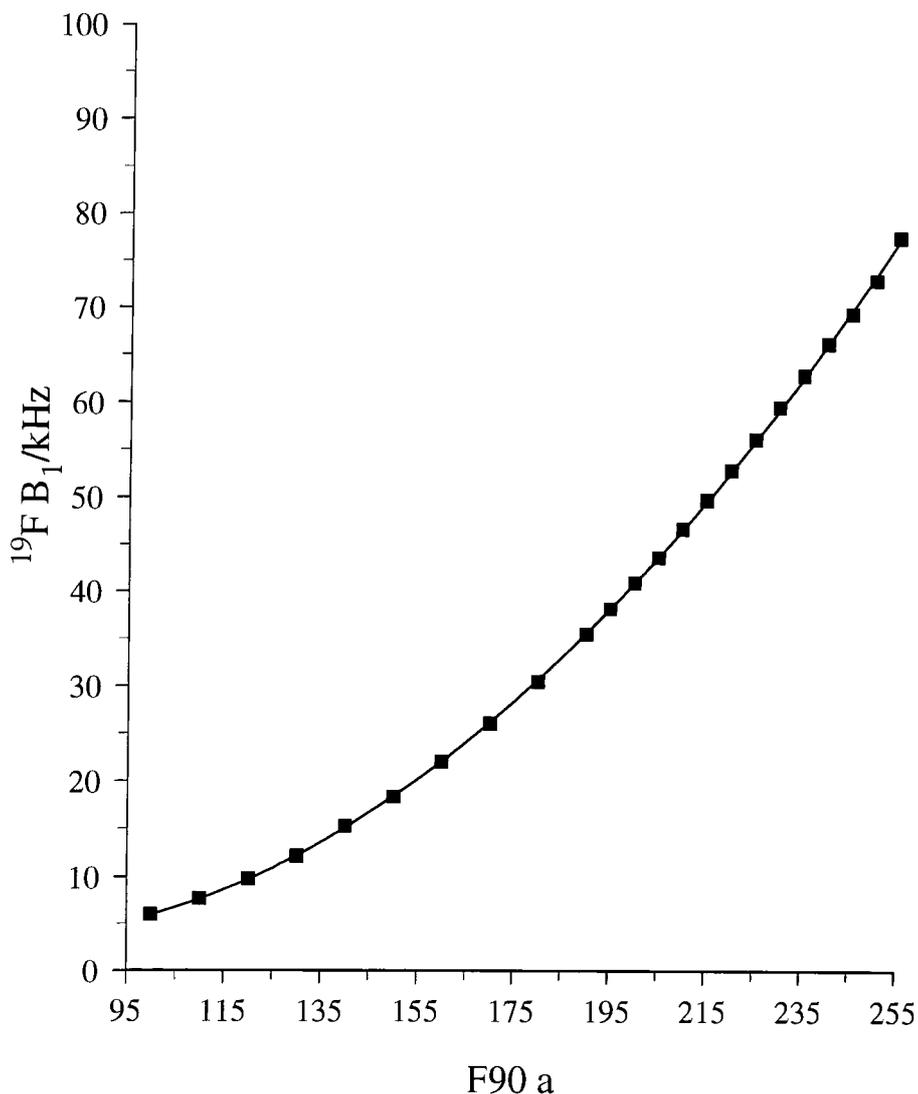
Figure 2.4. Graph plotting the ^{19}F B_1 power, for a given F90 a value, measured using C_6F_6.

However, the ^1H decoupling power cannot be determined directly from calibration of the ^1H 90° pulse durations. This arises from the fact that in the calibration experiment, the ^1H channel is the observe channel and hence the crossed diodes are present in the circuitry. However, in ^1H decoupling experiments, the crossed diodes are on the other (observe) channel and so more power will get into the probe, to give higher decoupling powers than that suggested by the calibration experiment. In order to see how much power the crossed diodes prevent from getting through into the probe, the peak-to-peak voltage was measured just before the probe, using the oscilloscope, for a number of amplitude values, with and without the crossed diodes in the circuitry, i.e. as set up for the calibration experiment and

decoupling, respectively. It was found that, upon conversion of the results obtained to powers, that the power going into the probe when the diodes were present was only ~70 % of that reaching the probe when the diodes were removed. Hence, allowing for the losses incurred by the diodes, it is then possible to determine the actual ^1H decoupling B_1. It is worth remembering that the Bloch-Siegert shift can also be used to determine the ^1H decoupling B_1.
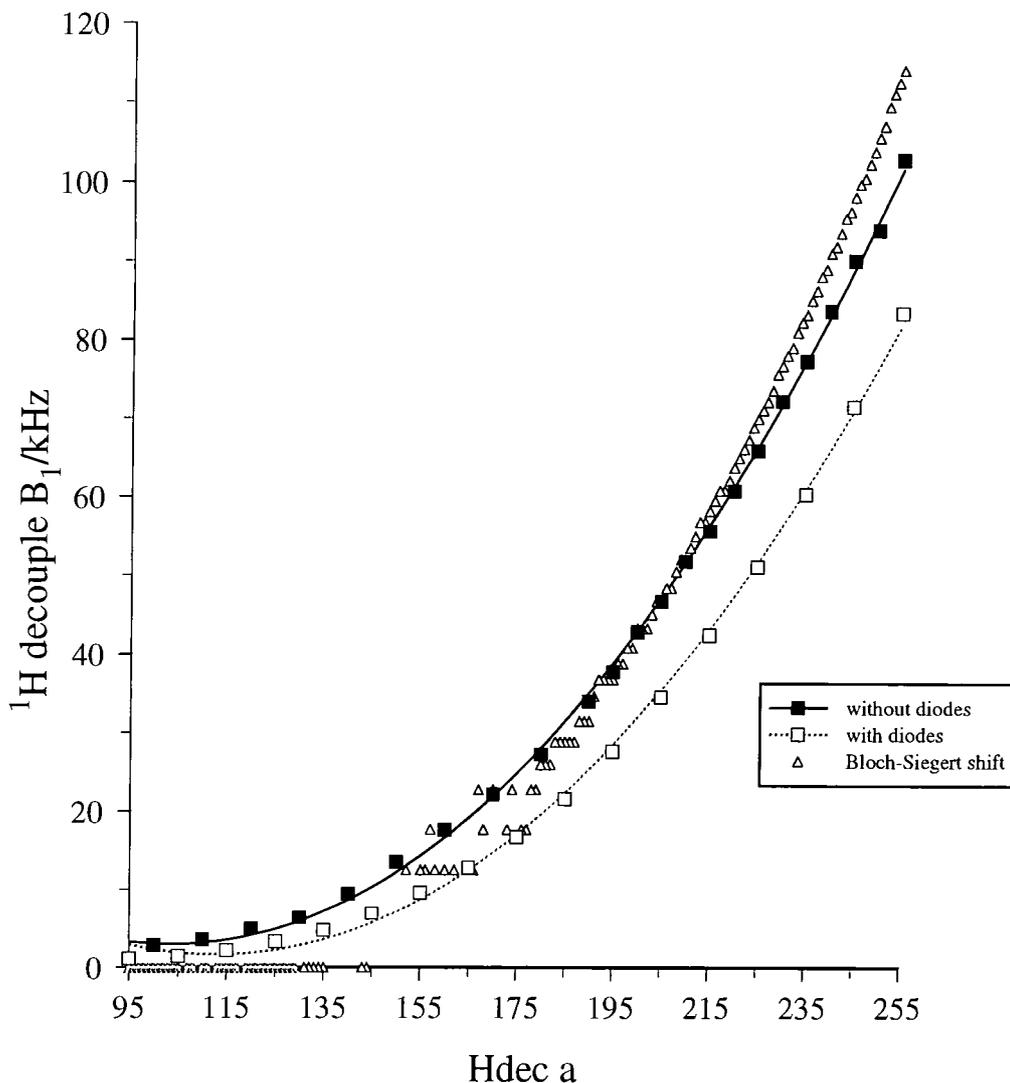
Figure 2.5. Graph comparing the ^1H decoupling power, for a given Hdec a value (Hdec a is the amplitude parameter in the pulse program for ^1H decoupling) measured with and without the diodes in the circuitry, and calculated from the Bloch-Siegert shift.

A comparison of the methods used to obtain the ^{1}H decoupling power as a function of amplitude value, is shown in Figure 2.5. Quite clearly, calculation of the ^{1}H decoupling power by direct measurement of the ^{1}H 90° pulse duration will underestimate that actually used. This is corroborated by the ^{1}H decoupling powers obtained from the Bloch-Siegert shift. However, it is noticeable that the values obtained from the Bloch-Siegert shift are not exactly the same as those obtained from the calibration experiments even after allowing for the crossed diodes. It is also difficult to use the Bloch-Siegert shift to calculate ^{1}H decoupling powers below ~35 kHz as the magnitude of the shift becomes too small, given the linewidths achievable in solid-state NMR. At low amplitude values, there is an appreciable amount of scatter observed in the decoupling powers obtained via the Bloch-Siegert shifts, as at this stage the shifts are comparable to the digital resolution (~6 Hz). However, an estimation of the ^{1}H decoupling power, shown by the solid line, can be obtained from the amplitude parameter by,

$$B_1(\text{decouple}) = 0.0043(\text{Hdeca})^2 - 0.8932(\text{Hdeca}) + 49.330 \qquad \textit{Equation 2.7}$$

The amplifier used in this case was the CE in class A/B mode and it can be seen that the amplifier behaves in a reasonably linear fashion from ~40-100 kHz.

The magnitude of B_1, at a particular hardware or software setting, will of course vary across the sample as it is inhomogeneous. Therefore, the position of the sample, within the rotor, is such that it will be in the most homogeneous part of the B_1 field, i.e. the centre of the coil, when placed in the stator. However, the sample which is packed at the extremities of the rotor, will still experience a different B_1 field to that packed in the centre of the rotor. For single-pulse and cross-polarisation experiments, inhomogeneities in B_1 from this source, have a negligible effect on the resolution of the spectra obtained. However, B_1 field inhomogeneities are critical in CRAMPS experiments where pulses of precise phase and duration are required to remove homonuclear dipolar interactions. To improve the homogeneity of B_1 over the sample, the sample volume can be restricted to the centre of the coil. It is possible to estimate the inhomogeneity in B_1 from the ^{19}F Bloch-Siegert shift observed in ^{1}H-decoupled spectra, in which the sample position is systematically varied along the length of a rotor.[8] Restriction of the sample size can improve the homogeneity of B_0

over the sample and hence an improvement in resolution can be observed if, for example, bulk susceptibility effects are a major source of line broadening.[10] However, if the sample volume is decreased, then spectra, particularly of insensitive nuclei such as ^{13}C and ^{15}N, will of course take much longer to acquire than for samples occupying the full volume.

2.8 CRAMPS

All CRAMPS experiments have been performed on the HF probe. Due to the requirement for MAS rates of the order of 1 kHz for CRAMPS experiments on a probe which is designed to spin at up to 18 kHz, a 'smooth' drive tip was used to permit slow, but stable spinning. To perform CRAMPS experiments, it is crucial that the pulse durations are set accurately. This is done using PDMSO and C_6F_6 for ^{1}H and ^{19}F, respectively, and good shimming is vital. First, the required pulse duration is set approximately by determining a 180° pulse with the transmitter positioned on resonance. Then, prior to performing the tune-up, all the signal is put into the real channel by altering the receiver phase. Accurate setting of pulse durations is then performed using the x, xx and tx tune-up sequences with typical results obtained for accurately-set pulse durations given in Figure 2.6. The x tune sequence is used to set the 90° pulse duration whereas the xx tune sequence is used to set the 180° pulse duration. The tx tune sequence is then used to check that as far as possible that 2×90° pulses are equal to a 180° pulse. To meet this condition, adjustments can be made to the output tuning of the amplifier or to the tuning of the CRAMPS diodes box to try and improve the sharpness of the pulse edges. Frequently, it is not possible to obtain the theoretical tune-up patterns due to factors such as inhomogeneities in B_1, detuning of the probe due to heating effects and amplifier power droop. (The setting of phases on all channels is not necessary on the CMX spectrometer, as it is equipped with digital phase shifters which have a settling time of 270 ns).
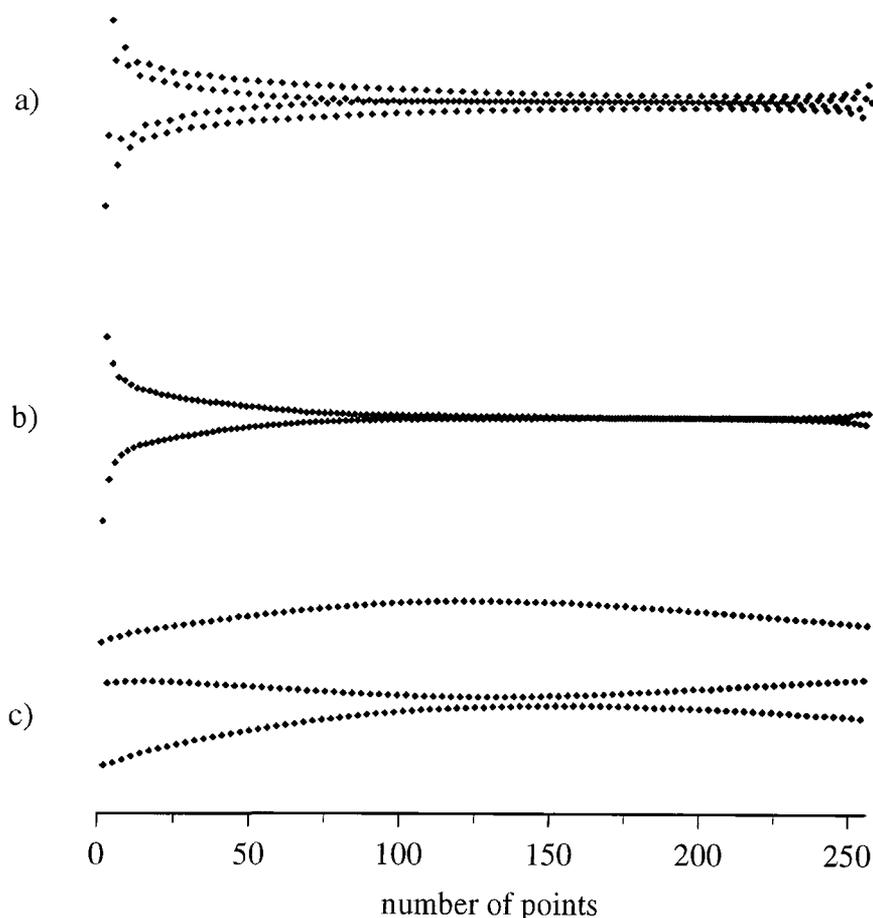
Figure 2.6. Typical tune-up patterns obtained on the HF probe for the a) x, b) xx and c) tx tune-up pulse sequences. In the example shown, the tune-up patterns are those observed for the ^1H signal of PDMSO.

For single-channel CRAMPS experiments, the Bruker amplifier was used, and for those experiments in which heteronuclear decoupling was also applied (see Chapter 3), the CE amplifier in class C mode was used on the channel which was not observed. The performance of the probe and the accuracy with which the pulse durations have been set is tested using adipic acid. A typical example of the resolution achievable in a ^1H CRAMP spectrum of this compound, acquired using BR-24, is shown in Figure 2.7. It is also possible to determine and/or check the scaling factor required to obtain the correct chemical shift scale and set the referencing using adipic acid. When processing CRAMPS data, it is usually necessary to left-shift the data by one point, and the re-scaling of the chemical shift can be performed by altering the dwell parameter.
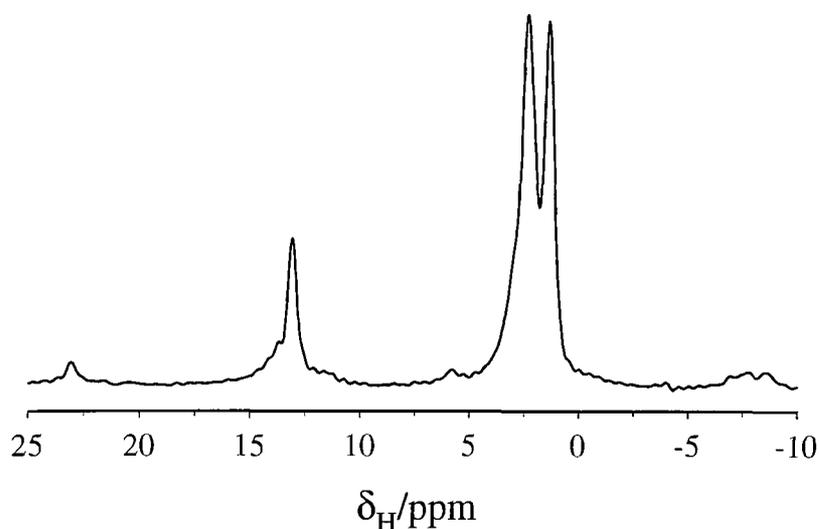
Figure 2.7. Typical ^1H CRAMP spectrum, obtained using BR-24, of adipic acid at a MAS rate of 800 Hz.

2.9 Variable-temperature operation

All of the Chemagnetics probes used are operable in the 123-523 K temperature range, although due to the instability of most of the compounds at elevated temperatures, only low-temperature experiments were performed. In order to lower the temperature of the sample, nitrogen gas is passed over the sample. The gas is cooled via passage through a copper coil immersed in liquid nitrogen and is then heated if necessary to the required temperature inside the variable-temperature stack. A thermocouple inside the stack is used to measure the temperature of the outlet gases, which obviously will not be the same as the actual sample temperature. Therefore, it is necessary to calibrate the temperature of the outlet gases against the actual sample temperature. Methods that are commonly used include monitoring changes in chemical shift as a function of temperature[11-13] and measuring phase transition temperatures.[14,15] However, calibration of the temperature in solid-state NMR is made difficult by possible heating and pressure effects induced by MAS.[16-18] With the Chemagnetics Pencil rotors, there is also the added complication of the existence of a temperature gradient[11,18] along the length of the rotor, which arises from the fact that the bearing and drive gases are at room temperature.[19]

The method chosen in this case involves measuring the ^{1}H chemical shift difference between CH_3 and OH of methanol absorbed on tetrakistrimethylsilylsilane (TTMS) as a function of temperature.[20] Preparation of the sample was performed in a glove box under a nitrogen atmosphere, before being subsequently sealed in a glass insert to ensure that moisture from the air could not affect the OH chemical shift. The glass inserts were packed tightly into rotors by wrapping in PTFE tape, to ensure stable spinning. However, the fact that the sample was sealed within a glass insert raises issues such as the glass insert having a different thermal conductivity to that of a sample. The primary reason for choosing this method is the fact that all the probes can easily be tuned to observe ^{1}H without the need for changing any capacitors, and with the HF probe the choice of nucleus is obviously limited. Experiments were performed at temperatures ranging from 173-313 K and at different MAS rates to examine the effects of sample heating induced by spinning.[21] For the HX probe, rotors 7.5 mm in o.d., it was found that at low temperatures the actual temperature (in °C) was about 25 % higher than that given by the thermocouple at a MAS rate of 1 kHz. However, upon spinning up to 5 kHz, significant heating of the sample was observed with the actual temperature measured of the order of 40-50 % higher than that given by the thermocouple. With the HF probe, rotors 4 mm in o.d., the actual temperature was only about 10 % higher than that given by the thermocouple at 6 kHz. Even upon increasing the MAS rate to 10 kHz, the actual temperature was still only about 15-20 % higher than that given by the thermocouple.

2.10 Sample preparation

The urea and thiourea inclusion compounds were prepared by Lily Yeo and Claire Bauer of the University of Birmingham and the cyclodextrin inclusion compounds were provided by Dr. J.R. Ascenso.

2.10.1 Fluorocyclohexane/thiourea

The fluorocyclohexane/thiourea inclusion compound was prepared by slowly cooling a solution containing fluorocyclohexane and thiourea in methanol. The crystals were collected and washed with 2,2,4-trimethylpentane to remove any fluorocyclohexane molecules adhering to their external surfaces. Powder X-ray diffraction studies at ambient temperature indicated that these crystals have the rhombohedral thiourea structure, as found for thiourea inclusion compounds containing other cyclohexane-based guest molecules.

2.10.2 1-fluorotetradecane/urea

The 1-fluorotetradecane/urea inclusion compound was prepared from commercially available reagents. An excess amount of 1-fluorotetradecane (excess with respect to the expected guest/host molar ratio in the inclusion compound) was added to a saturated solution of urea in methanol in a conical flask under ultrasonic agitation at ~55 °C. A sufficient amount of 2-methylbutan-2-ol was then added to render the liquid 1-fluorotetradecane completely miscible with the methanol. At this stage, crystals of the 1-fluorotetradecane/urea inclusion compound precipitated immediately and so these crystals were then dissolved by addition of a sufficient amount of methanol to establish a homogeneous solution. The flask was then transferred to an incubator, in which it was cooled systematically from 55 °C to 15 °C over a period of 24 hours. When sufficiently large crystals had grown (generally after a few days), they were collected and washed with 2,2,4-trimethylpentane. The crystals of the 1-fluorotetradecane/urea inclusion compound were long hexagonal needles, which behaved in the polarising microscope in a manner consistent with their assignment to the hexagonal crystal system. Powder X-ray diffraction indicated that the samples prepared had the conventional urea tunnel structure and did not contain significant amounts of pure-phase urea.

2.10.3 1,10-difluorodecane/urea and 1,12-difluorododecane/urea

The guest molecules, 1,10-difluorodecane and 1,12-difluorododecane, were synthesised by Dr. Paul Coe of the University of Birmingham. The inclusion compounds were then prepared by slow cooling of solutions containing the guest molecules and urea in either methanol or a mixture of methanol and tert-amyl alcohol.

2.10.4 2-dodecanol/urea, 2-pentadecanol/urea, 2-dodecanol/d₄-urea and 2-pentadecanol/d₄-urea

The 2-hydroxyalkane/urea inclusion compounds were prepared by slow cooling of solutions containing the guest molecules and urea in either methanol or a mixture of methanol and tert-amyl alcohol. The deuterium-containing inclusion compounds were prepared in a glove box under a nitrogen atmosphere, from solutions containing d_4-urea and the 2-hydroxyalkanes in d_1-methanol.

2.10.5 Cyclodextrin inclusion compounds

Cyclodextrin inclusion compounds can readily be prepared by adding guests, such as benzaldehyde, to saturated aqueous solutions of cyclodextrin.[22] After stirring the two solutions for approximately 24 hours, the precipitate formed is the inclusion compound.

2.11 References

1. D.D. Traficante, *Concepts Magn. Reson.*, 1990, **2**, 151.

2. D.D. Traficante, *Concepts Magn. Reson.*, 1990, **2**, 181.

3. D.I. Hoult, *Prog. NMR Spectrosc.*, 1978, **12**, 41.

4. D.D. Traficante, *Concepts Magn. Reson.*, 1993, **5**, 57.

5. J.Z. Hu, W. Wang, F. Lui, M.S. Solum, D.W. Alderman, R.J. Pugmire and D.M. Grant, *J. Magn. Reson., A*, 1995, **113**, 210.

6. U. Scheler, P. Holstein, S.A. Carss and R.K. Harris, *Chemagnetics Application Note*, May 1995.

7. P. Jackson and R.K. Harris, *Magn. Reson. Chem.*, 1988, **26**, 1003.

8. S.A. Vierkötter, *J. Magn. Reson., A*, 1996, **118**, 84.

9. U. Haeberlen, *High Resolution NMR in Solids*, Academic Press, New York, 1976.

10. D.L. Vanderhart, W.L. Earl and A.N. Garroway, *J. Magn. Reson.*, 1981, **44**, 361.

11. A. Bielecki and D.P. Burum, *J. Magn. Reson., A*, 1995, **116**, 215.

12. B. Wehrle, F. Aguilar-Parrilla and H.-H. Limbach, *J. Magn. Reson.*, 1990, **87**, 584.

13. G.C. Campbell, R.C. Crosby and J.F. Haw, *J. Magn. Reson.*, 1986, **69**, 191.

14. A.E. Aliev, K.D.M. Harris and D.C. Apperley, *Chem. Commun.*, 1993, 251.

15. A.N. Klymachyov and N.S. Dalal, *Solid State NMR*, 1996, **7**, 127.

16. T. Mildner, H. Ernst and D. Freude, *Solid State NMR*, 1995, **5**, 269.

17. L.C.M. van Gorkom, J.M. Hook, M.B. Logan, J.V. Hanna and R.E. Wasylishen, *Magn. Reson. Chem.*, 1995, **33**, 791.

18. F. Aguilar-Parrilla, B. Wehrle, H. Bräunling and H.-H. Limbach, *J. Magn. Reson.*, 1990, **87**, 592.

19. G. McGeorge, Summer school on NMR of solids, University of Durham, 1996.

20. A.E. Aliev and K.D.M. Harris, *Magn. Reson. Chem.*, 1994, **32**, 366.

21. S.C. Campbell, J.C. Cherryman, L.A. Crowe, A. Nordon and J.A. Shaw, unpublished work.

22. F.O. Garces, V. P. Rao, M.A. Garcia-Garibay and N.J. Turro, *Supramol. Chem.*, 1992, **1**, 65.

Chapter 3

Fundamental aspects of NMR explored using host-guest systems

3.1 Introduction

During the course of investigating structural and dynamic features of the inclusion compounds discussed in Chapter 1, many interesting results, which did not necessarily yield direct information concerning such features, were obtained. The structural and dynamic information derived is presented in the ensuing chapters. However, in this chapter the source of these interesting results has been explored, which has involved examining some of the more fundamental aspects of NMR. This chapter can be divided into three main sections which examine the topics of cross polarisation, decoupling and dipolar dephasing. Typically, spectra of dilute nuclei such as ^{13}C and ^{15}N, are acquired using cross polarisation. In the case of ^{19}F, cross polarisation has been employed not for sensitivity reasons, but to take advantage of the shorter T_1 of ^1H in comparison to that of ^{19}F.[1,2] However, as shown for $^1H \rightarrow ^{13}C$ cross-polarisation experiments, the dynamics of cross polarisation are greatly affected by mobility.[3] Hence, the dynamics of $^1H \rightarrow ^{19}F$ cross polarisation have been investigated for the 1,10-difluorodecane/urea inclusion compound. Heteronuclear ^1H-^{19}F dipolar decoupling has been examined using the 1-fluorotetradecane/urea inclusion compound. In particular, the variation in ^{19}F linewidth as a function of ^1H decoupling power at different temperatures has been examined. The application of TPPM[4] (two-pulse phase-modulated) decoupling to ^{19}F and ^{13}C NMR has been briefly studied.

Many solid-state NMR studies of inclusion compounds have focused upon the dynamic nature of the compounds. The dipolar dephasing experiment[5] has proven to be a powerful method for the separation of signals via the heteronuclear dipolar interaction. For many organic compounds, CH and CH_2 signals will have decayed to

zero within a typical dephasing time of 40 µs. The different rates at which signals decay within a compound, can yield motional information. For example, the different decay rates of benzaldehyde carbons were used to deduce that, within α-cyclodextrin cavities, such guest molecules are undergoing rotation about the C1-C4 axis.[6] In mobile systems or in those where there is a low abundance of protons, at longer dephasing times the ^{13}C signals may become negative.[2,7] In the β-cyclodextrin/benzaldehyde inclusion compound and also in β-cyclodextrin, it was possible to observe a negative peak at longer dephasing times. The dipolar dephasing experiment has been explored both theoretically and experimentally using β-cyclodextrin.

Many of the systems studied have contained both ^{1}H and ^{19}F and, due to recent advances in probe technology, ^{19}F spectra can be obtained with high-power ^{1}H decoupling and vice versa.[1,8] However, when the observe nucleus is present in high abundance, then either high-speed MAS and/or CRAMPS experiments can be performed. It is worth noting that recently CRAMPS sequences have been designed which remove homonuclear dipolar interactions even at high MAS rates.[9,10] However, in this study the application of CRAMPS experiments to systems containing both ^{1}H and ^{19}F has been investigated in relation to heteronuclear multiple-pulse decoupling schemes.[11]

3.2 Effect of MAS on ^{1}H spectra

The results presented in this chapter, which were introduced briefly in the previous section, arise, with the exception of the CRAMPS/heteronuclear decoupling schemes, primarily as a result of the mobility of the compounds studied. Although perhaps not immediately obvious at this stage, the effects of mobility and of MAS on ^{1}H spectra provide the key to the interpretation of the results obtained. For rigid organic solids, MAS has little effect on the ^{1}H spectrum due to the homogeneous[12] nature of homonuclear dipolar interactions. However, in cases where it is possible to attain MAS rates of the order of the average homonuclear dipolar coupling (due to motional averaging or where a high-speed MAS probe is available), the homonuclear

dipolar interactions can be partially suppressed. Hence, communication between protons, which proceeds via the flip-flop term in the homonuclear dipolar Hamiltonian, is reduced and the ^{1}H spectrum may start to break up into sidebands. Therefore, the effect of MAS upon the ^{1}H spectrum can have a dramatic effect upon decoupling, cross polarisation and dipolar dephasing experiments as will be demonstrated in the following sections.

3.3 Cross polarisation[13]

3.3.1 Introduction

In solid-state NMR, the study of rare-spin nuclei such as ^{13}C and ^{15}N by direct excitation of the nucleus in question is hampered by low sensitivity and the requirement for long recycle delays. However, cross polarisation (CP) combined with MAS (CP/MAS) and high-power ^{1}H decoupling (assuming that ^{1}H is the abundant spin nucleus) have made the acquisition of such spectra far more viable. In cross-polarisation experiments, the recycle delay is governed by $T_1(^1H)$, which is usually much shorter than $T_1(X)$, and the X signal is enhanced by a factor which is approximately equal to γ_H/γ_X. Hence, a combination of these two factors means that the system can be pulsed at a higher repetition rate, and in each transient the signal obtained will be greater than that obtained using direct excitation. Cross polarisation involves the transfer of ^{1}H magnetisation to the rare-spin nucleus using the pulse sequence shown in Figure 3.1. First a 90° pulse, with a phase of ±x,[14] is applied to ^{1}H, which places the magnetisation along the y-axis. Irradiation of ^{1}H is continued for a time denoted the 'contact time' with a phase of y (thus spin-locking the protons), while at the same time the X spins are irradiated. Magnetisation then develops along the axis of irradiation for the X nucleus, which is then observed under high-power ^{1}H decoupling conditions.
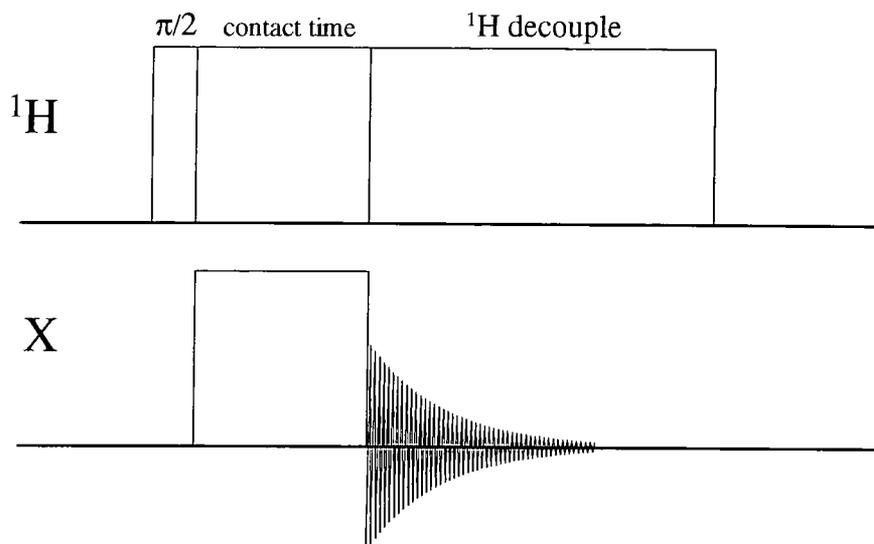
Figure 3.1. Standard single-amplitude cross-polarisation pulse sequence.

3.3.2 Theory[15]

In order for cross polarisation to occur, the rf fields of ^1H and X during the contact time must be matched according to the Hartmann-Hahn[16] condition,

$$\gamma_I B_{1I} = \gamma_S B_{1S} \qquad \textit{Equation 3.1}$$

where γ is the magnetogyric ratio of the nucleus and B_1 is the applied magnetic field. The reason for this can be understood by examining the Hamiltonian for a system containing I and S spins in the doubly rotating frame of reference,

$$\hat{H} = \omega_{1I}\hat{I}_y^j + \omega_{1S}\hat{S}_y^k + 2\beta_{IS}{}^{jk}\hat{I}_z^j\hat{S}_z^k \qquad \textit{Equation 3.2}$$

where ω_1 describes the rf frequency (assumed to be on resonance and applied along the x axis) and β_{IS} contains the spatial terms for the heteronuclear dipolar interaction. If the z axis is then redefined such that it is now parallel to B_1, i.e., so that the direction of quantisation is along z in the doubly rotating frame, then in this so-called tilted rotating frame,

$$\hat{H} = \omega_{1I}\hat{I}_z^j + \omega_{1S}\hat{S}_z^k + 2\beta_{IS}{}^{jk}\hat{I}_x^j\hat{S}_x^k \qquad \textit{Equation 3.3}$$

If one then transforms into the toggling frames of the I and S spins which have the same time dependence because $\omega_1 = \omega_{1I} = \omega_{1S}$, the heteronuclear dipolar interaction is given by,

$$\hat{H}_{IS} = 2\beta_{IS}{}^{jk}\left(\hat{I}_x^j\cos\omega_1 t + \hat{I}_y^j\sin\omega_1 t\right)\left(\hat{S}_x^k\cos\omega_1 t + \hat{S}_y^k\sin\omega_1 t\right) \qquad \textit{Equation 3.4}$$

Equation 3.4 can then be integrated between 0 and multiples of 2π to yield the average Hamiltonian for the heteronuclear dipolar interaction under conditions of simultaneous irradiation of the I and S spins with $\omega_{1I} = \omega_{1S}$, i.e. at the Hartmann-Hahn match,

$$\overline{H}_{IS} = \sum_{j,k} 2\beta_{IS}{}^{jk}\left(\hat{I}_x^j\hat{S}_x^k + \hat{I}_y^j\hat{S}_y^k\right) \qquad \textit{Equation 3.5}$$

which can be rewritten in terms of raising and lowering operators,

$$\overline{H}_{IS} = \sum_{j,k} \beta_{IS}{}^{jk}\left(\hat{I}_+^j\hat{S}_-^k + \hat{I}_-^j\hat{S}_+^k\right) \qquad \textit{Equation 3.6}$$

Hence, it can be seen that at the Hartmann-Hahn match polarisation transfer can occur between the I and S spins by mutual spin flips. Another way of looking at it is that in the rotating frame when $\omega_{1I} = \omega_{1S}$, the Zeeman energy levels of the I and S spins are 'matched' and therefore efficient energy transfer can occur between the two types of spins.

However, it is still possible for cross polarisation to occur even when $\omega_{1I} \neq \omega_{1S}$ as spin flips among the I spins broadens the Zeeman energy level of the I spins such that a range of matching conditions exists. So far the effect of MAS upon the cross-polarisation[17] process has been neglected. If the modulation of the I-S dipolar interaction by the flip-flop fluctuations among the I spins is dominant over the modulation of the I-S dipolar interaction by MAS, then the effects of MAS can be ignored. However, in cases where there is a low abundance of I spins or high mobility, then modulation of the I-S dipolar interaction by MAS must be taken into account. The spatial term in the expression for the heteronuclear dipolar interaction, β_{IS}, is given by,

$$\beta_{IS} = \frac{\mu_0 \gamma_j \gamma_k \hbar^2}{4\pi r^3} \frac{1}{2}\left(3\cos^2\theta_{jk} - 1\right) \quad \textit{Equation 3.7}$$

where θ_{jk} defines the angle between the I-S internuclear vector and B_0. Upon spinning the sample about an axis which makes an angle of θ_m with B_0, this imparts a time dependence (given by the MAS rate, ω_r) on θ_{jk}. The effect of MAS on the I-S dipolar interaction can be written in terms of its Fourier components, and it has been shown that cross polarisation can then only occur when,

$$\omega_{1I} = \omega_{1S} \pm n\omega_r \quad\quad \textit{Equation 3.8}$$

where n is an integer. Therefore, MAS has the effect of splitting the matching profile up into a series of matching sidebands[3] (separated by the MAS rate) and theory predicts that there should be no cross polarisation when $\omega_{1I} = \omega_{1S}$. However, in practice cross polarisation does occur at this matching condition, but is severely reduced in efficiency in comparison to that at the matching sidebands.

When the matching profile splits into sidebands, the precision with which the matching condition must be set for efficient cross polarisation to occur dramatically increases. The width of the matching sidebands, i.e. the range over which cross polarisation will occur about one of the conditions given in Equation 3.8, is governed by the dipolar interactions and the MAS rate. However, it is clear that if a discrete matching condition is to be maintained for the duration of an experiment (likely to be of the order of hours), it is vital to have stable, homogeneous rf fields and a stable spinning system. A number of methods have been proposed to try and restore a broader matching condition. Two methods which are effective, although they require special equipment, are variable-angle spinning[18] and 'stop and go'.[19] The former technique involves spinning the sample at an angle of, e.g., 90° during the contact time and then during the acquisition time the angle is set at the magic angle. In the latter technique, MAS is either stopped or the rate slowed during the contact time and then during the acquisition time the sample is spun up to the required rate. Both techniques decrease the sensitivity of the signal obtained upon the precise matching condition, but they are generally not viable experiments in most laboratories.

Other techniques have involved using rotor-synchronised pulse sequences[20-23] to restore a 'static' heteronuclear dipolar interaction during the contact time.

Although not as much of a problem now, with many modern-day spectrometers coming equipped with an automatic spinning-speed controller, such techniques still rely on stable MAS rates. However, there is a group of experiments which is based on the principle of providing a range of matching conditions within the contact time and is not critically dependent upon the MAS rate or the rf power levels. Experiments which come under this heading are those in which the amplitude of one of the rf fields is varied stepwise up and down,[24,25] increased in small steps to form a 'ramp'[26,27] or one in which the frequency of one of the rf fields is swept adiabatically[28,29] from an on-resonance to an off-resonance condition.[30] Recently, a method has been proposed that utilises a series of rotor-synchronised pulses which are varied in amplitude such that there is a slow adiabatic passage through the Hartmann-Hahn match.[31]

Due to the mobility of many of the guest molecules in the compounds studied, it was envisaged that cross polarisation to and between nuclei within these molecules could be affected by MAS. Therefore in the following section, the matching profile for ^{1}H→^{19}F cross polarisation in the 1,10-difluorodecane/urea inclusion compound at a MAS rate of 10 kHz has been determined. In the compound examined, the abundant spins are ^{1}H and the 'rare' spin, though not in the conventional sense, is ^{19}F. In the light of the results obtained, the ramped-amplitude cross-polarisation experiment was then applied to this compound.

3.3.3 Experimental results

To determine the matching profile in the following experiments, the ^{1}H spin-lock field was kept fixed at a value of 40 kHz with the ^{19}F B_1 field being varied to achieve the range of matching conditions. First, a matching profile was determined using the standard single-amplitude cross-polarisation sequence given in Figure 3.1. The ^{19}F spin-lock power was varied using the 'amplitude' parameter in the pulse program, which can have a value between 0 and 255, with 255 being the maximum B_1 possible at a given hardware setting. The pulse sequence was written so that independent software control of the spin-lock fields on both channels, of the

decoupling power and of the preparation pulse was possible. The calibration of the powers for both ^{1}H and ^{19}F was performed by determining the pulse duration required for a 180° pulse for a given 'amplitude' value using PDMSO and C_6F_6, respectively. Further details regarding the calibration of powers can be found in Chapter 2. Typical spectral conditions were: ^{1}H $\pi/2$ pulse duration, 3 μs; ^{1}H decoupling power, 100 kHz; ^{1}H spin-lock power, 40 kHz; ^{19}F spin-lock power, 28-50 kHz (^{19}F CP power 'amplitude' value varied from 176-215); contact time, 1 ms; number of transients, 64; MAS rate, 10 kHz; recycle delay, 5 s; acquisition time, 20.5 ms. The results obtained using the single-amplitude cross polarisation sequence are shown by the green (solid) squares in Figure 3.2.

The most noticeable feature of the matching profile obtained using the single-amplitude cross-polarisation sequence, is that it has split up into sidebands and hence cross polarisation is affected by MAS under the conditions employed. At approximately 10 kHz above and below the Hartmann-Hahn match, i.e., at the +1 and -1 matching conditions, the signal intensity obtained is greatest. In comparison, the signal intensity at the Hartmann-Hahn match is far less, implying that cross polarisation at this matching condition is very inefficient. It is also noticeable that the +1 matching sideband is more intense than the -1 matching sideband. This can be attributed to the lower spin-locking field used and the subsequent faster decay of the magnetisation parallel to B_1. Although the HF probe is quite capable of dealing with much higher spin-locking powers than those used, lower powers were actually employed so that ramped-amplitude cross-polarisation experiments, where the spin-lock power can be 20-30 kHz above the maximum used in the single-amplitude CP experiments, could be compared directly with the single-amplitude CP experiment. Other experiments have been performed in which higher spin-lock powers were used, and the matching profile obtained showed comparable features.
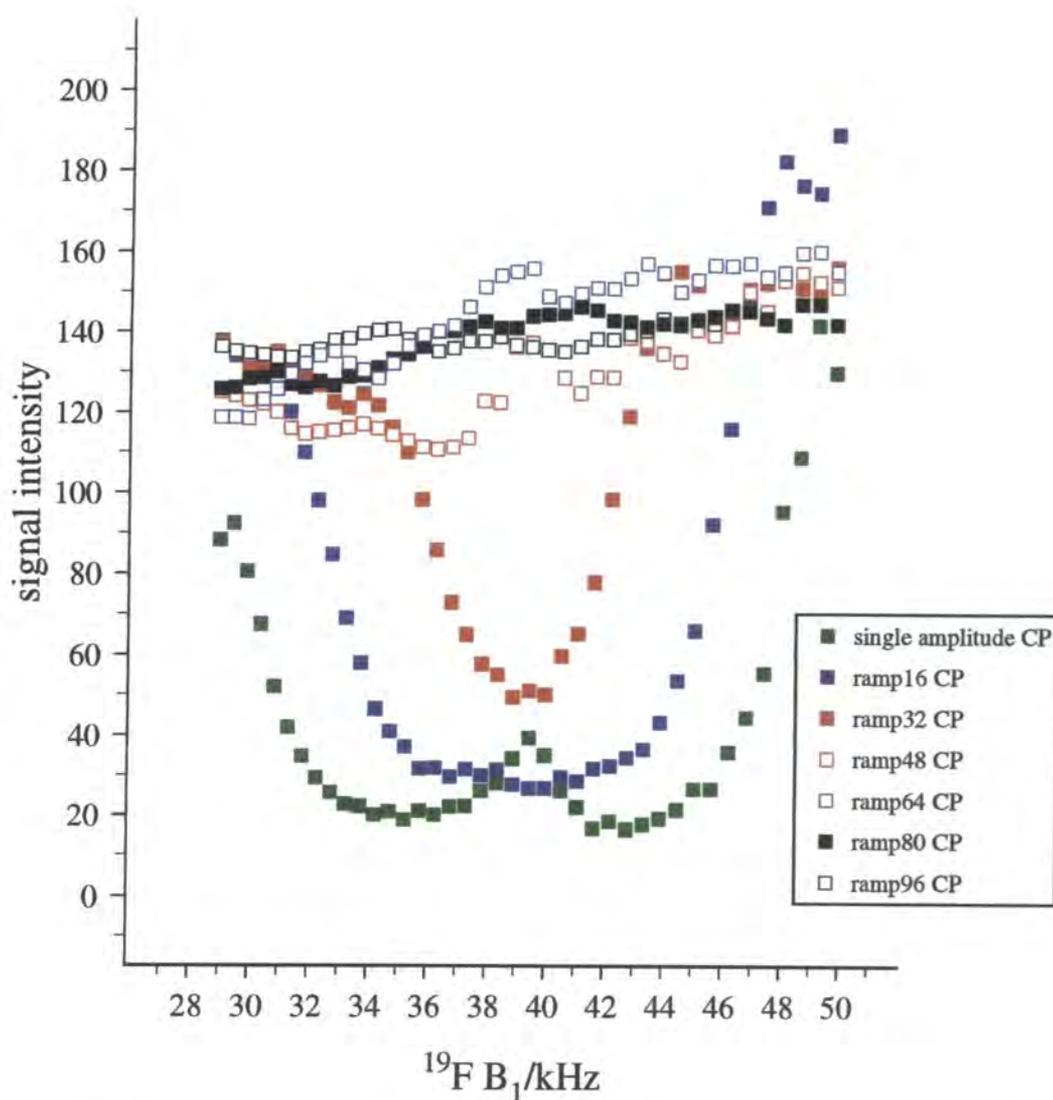
Figure 3.2. Variation of ^{19}F signal intensity for 1,10-difluorodecane/urea at 10 kHz as a function of matching condition acquired using single-amplitude and ramped-amplitude cross polarisation.

In an attempt to increase the efficiency of cross polarisation at the Hartmann-Hahn match and to in general decrease the sensitivity of the signal obtained to the matching condition, matching profiles were obtained using the ramped-amplitude cross-polarisation pulse sequence (Figure 3.3).
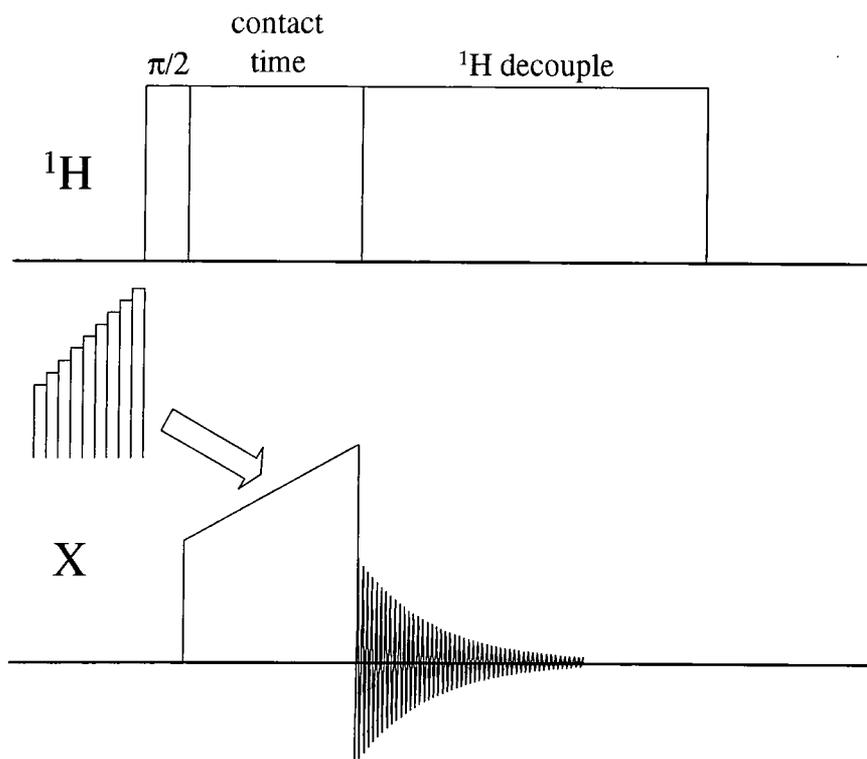
Figure 3.3. Ramped-amplitude cross-polarisation pulse sequence.

The sequence is the same as that shown in Figure 3.1, except the single-amplitude spin-locking field on the X channel has been replaced by a spin-locking field which gradually increases. In the pulse program used to create a ramped-amplitude pulse, the contact time pulse was divided into a number of smaller pulses, which differed in 'amplitude' value. The smallest step size that is possible on the CMX is given by a change in 'amplitude' value of one, which is equivalent to about 0.75 kHz. The change in rf field that occurs upon a change in the 'amplitude' value by one is reasonably linear at higher power levels, although it does start to vary at lower powers (see calibration plot in Chapter 2). Ramped-amplitude cross-polarisation experiments were performed with six different ramp sizes as shown in Figure 3.2. For ease and clarity, the pulse sequences have been named rampx CP, where x gives the number of amplitude values which make up the ramp. Hence, the larger the value of x, the greater the spin-lock power range that the ramp spans. The spectral conditions used to obtain the matching profiles with ramped-amplitude cross polarisation were the same as those used for the single-amplitude cross-polarisation experiment. In Figure 3.2, the ^{19}F B_1 power that is plotted against signal intensity for

the ramped CP sequences is in fact the central value of the ramp. Again due to non-linear effects at lower powers, the ramp spans a larger range of matching conditions at higher powers than it does at lower powers, although typically ramp16, ramp32, ramp48, ramp64, ramp80 and ramp96 covered power ranges of the order of 12 kHz, 24 kHz, 36 kHz, 48 kHz, 60 kHz and 72 kHz respectively. Therefore, when the ramp is centred at ~ 50 kHz, this corresponds to a maximum value of ~ 85 kHz for ^{19}F B_1 with the ramp96 sequence, which is within the power capability limits of the HF probe.

The smaller ramp sizes, < 25 kHz, do not give a broad, flat matching profile at the Hartmann-Hahn match, although they do broaden the width and increase the height of the matching sidebands and hence reduce the severity of the matching conditions. However, as the ramp size is increased and hence a wider range of matching conditions is covered, then it is possible to achieve efficient cross polarisation at all conditions between the +1 and -1 matching sidebands. It is noticeable that the signal intensity obtained using ramped CP is smaller at the -1 matching sideband than at the +1 sideband. Again this can be attributed to a more rapid decay of the magnetisation parallel to B_1 when using smaller spin-locking fields. In order to see how the dynamics of the CP process[32,33] using ramped CP compare to those with the single-amplitude cross-polarisation sequence, variable contact time experiments were performed at the Hartmann-Hahn match and the +1 matching sideband (Figure 3.4). It can immediately be seen that the ramped-amplitude CP sequence gives a much better signal at both matching conditions than single-amplitude CP. The results of the matching profile experiments shown in Figure 3.2 were obtained using a contact time of 1 ms, which was estimated to be the optimum value from a short variable contact time experiment conducted at the +1 matching sideband. However, in the light of the results presented in Figure 3.4, particularly for the ramped CP experiments, a contact time of 2 ms should give the best signal.
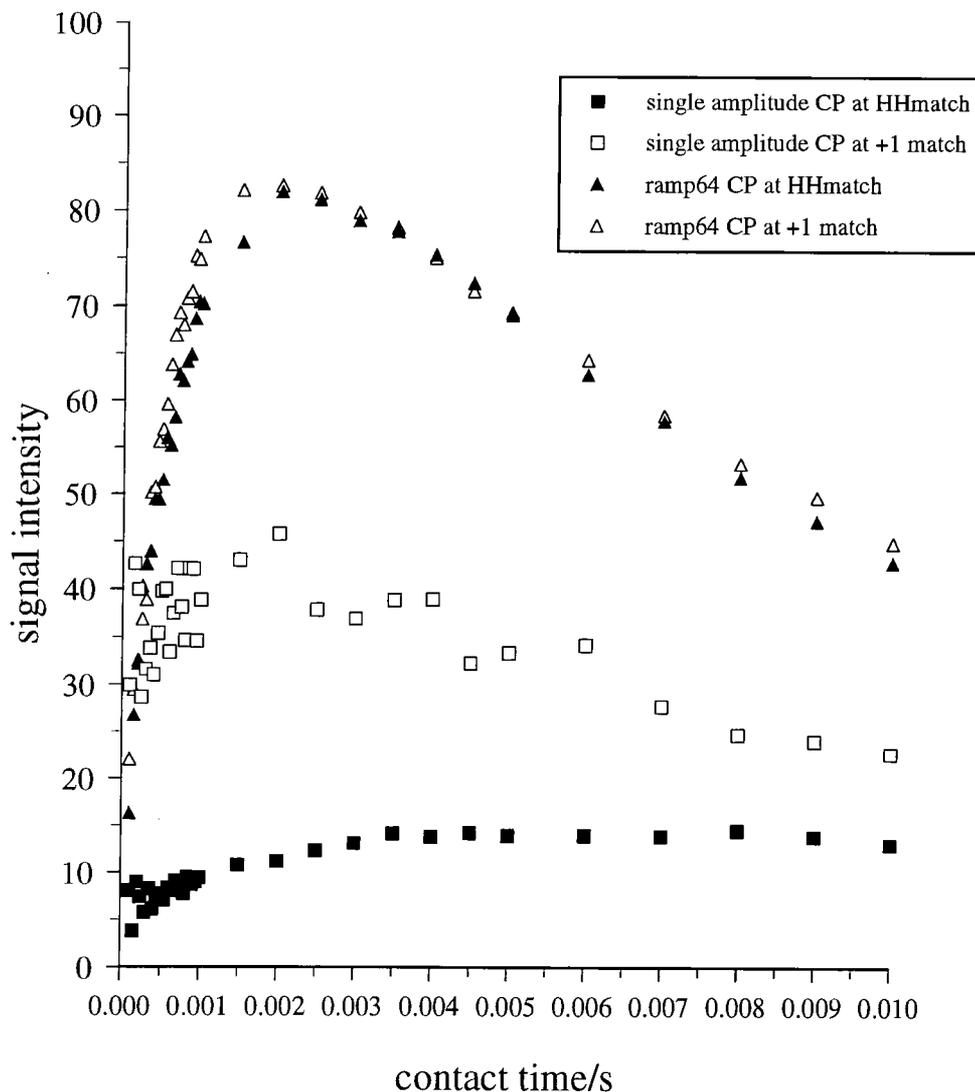
Figure 3.4. Graph plotting signal intensity against contact time obtained at the Hartmann-Hahn match and at the +1 matching sideband, using single-amplitude and ramped-amplitude cross polarisation.

For the single-amplitude cross-polarisation experiments, it is noticeable that there is an oscillatory build up (at short contact times) of signal observed at both matching conditions, and at the +1 matching condition the signal also decays in an oscillatory fashion but with a lower frequency. Oscillations in the CP build-up curve were first observed in $^1H \rightarrow {}^{13}C$ CP experiments performed on a single crystal of ferrocene.[34] This oscillatory build up of magnetisation was attributed to the fact that the ^1H-^{13}C spin pair can be considered as isolated. Similar oscillations have been observed for oriented samples[35,36] and also for powdered samples undergoing MAS.[37,38] Such dipolar oscillations are not normally visible in variable contact time

experiments, due to spin diffusion among the I spins. However, in the 1,10-difluorodecane/urea inclusion compound, it is clear that MAS modulates the I-I dipolar interactions and therefore it is reasonable to attribute the higher frequency oscillations at short contact times to the isolated nature of the ^{19}F-^{1}H spin pair. The reason for the lower frequency oscillations observed in the latter part of the CP profile is not clear.

For cross polarisation from abundant I spins to rare S spins, the kinetics of such a process can be given by,[14]

$$\frac{M(t)}{M(0)} = \left(\frac{1}{1 - \frac{T_{CP}}{T_{1\rho}}} \right) \left[1 - \exp \frac{-\left(1 - \frac{T_{CP}}{T_{1\rho}}\right)t}{T_{CP}} \right] \exp\left(\frac{-t}{T_{1\rho}} \right) \qquad \textit{Equation 3.9}$$

where T_{CP} defines the time for transfer of magnetisation from I to S spins, $T_{1\rho}$ defines the spin-lattice relaxation time in the rotating frame of I, and M gives the signal intensity. However, as a result of the oscillations observed in the single-amplitude cross-polarisation experiments, it is clear that the simple model described by Equation 3.9 cannot adequately describe the CP process. Other equations have been derived to describe more complex cases such as when $T_{1\rho}(S)$ is comparable to the cross-polarisation time, T_{CP},[39] although this is not true for the present case. Nevertheless, a value of $\sim 200 \mu s$ was estimated for T_{FH} at the Hartmann-Hahn match, although due to the fact that the signal is still increasing slightly at the longest contact time used, it is not possible to determine a value for $T_{1\rho}(^{1}H)$. At the +1 matching sideband, values of $\sim 15 \mu s$ and 13 ms were estimated for T_{FH} and $T_{1\rho}(^{1}H)$ respectively. These estimated values were obtained using the 'txh' function (Equation 3.9) in the XY panel of Spinsight, although as already stated, the CP process is more complex. However, this function appears to adequately describe the CP process using ramped CP. The values obtained for T_{FH} and $T_{1\rho}(^{1}H)$ at the Hartmann-Hahn match were 58 μs and 13 ms, respectively, and at the +1 matching sideband were 51 μs and 13 ms, respectively. It can be seen that the T_{FH} values obtained using ramped CP are in between those obtained using single-amplitude CP at the Hartmann-Hahn match and the +1 matching sideband. This is as expected

considering the fact that the ramp covers a range of matching conditions, and so an average value for T_{FH} should be obtained using ramped CP. Hence, it is also not surprising that the parameters describing the kinetics of the CP process using ramped CP are comparable at the Hartmann-Hahn match and +1 matching sideband.

The value determined for $T_{1\rho}(^1H)$ from the ramped CP experiment should be considerably more reliable than that determined from the single-amplitude CP experiments. It is clear that the ramped CP experiment results in a substantial increase in signal intensity compared to that obtained using single-amplitude CP. However, of greater importance is the fact that the signal obtained is virtually independent of the matching condition. This is a particularly desirable feature of the experiment and would be invaluable in 2D experiments which involve CP. This is because if the signal is critically dependent upon the matching condition, any variation in rf power levels and/or MAS rate would introduce an extra variable in the experiment. The only disadvantage with the ramped CP method as presented herein, is that for the initial part of the ramp, the spin-lock power might be insufficient. However, another way of altering B_1 other than via the 'amplitude' is by varying the offset frequency.[30] This would then mean that the initial value of the ramp could be set to the desired spin-lock power, with the power adjusted by using the effective spin-lock power at off-resonance conditions. As for the ramped-amplitude CP experiment, this would be very easy to implement on the CMX by virtue of the fact that the phase, frequency and amplitude of a pulse can all be controlled using the software.

3.4   Heteronuclear dipolar decoupling

3.4.1   Continuous irradiation versus phase-modulated heteronuclear decoupling

3.4.1.1   Theory of heteronuclear decoupling

A combination of MAS and high-power ^{1}H decoupling is used to obtain high-resolution spectra of dilute (S) nuclei in the solid state. MAS removes line broadening due to SA whereas high-power ^{1}H decoupling is required to remove heteronuclear dipolar interactions. The most common and most simple method for removing heteronuclear dipolar interactions involves continuous irradiation of the abundant (I) spin nuclei. Average Hamiltonian theory[11] can be used to provide a simple explanation of how such a method removes the heteronuclear (I-S) dipolar interactions.[40] The heteronuclear dipolar interaction can be described by,

$$\hat{H}_{IS} = 2\beta_{IS}\hat{I}_z{}^j\hat{S}_z{}^k \qquad \qquad \textit{Equation 3.10}$$

where β_{IS} defines the spatial terms, $\hat{I}_z$ and $\hat{S}_z$ define the spin terms. For continuous irradiation of the I spins such that $\hat{I}_z$ precesses about the x axis in the rotating frame, viewed in a frame rotating about the x axis, i.e. a toggling frame,

$$\hat{I}_z{}^j = \hat{I}_z{}^j\cos\omega_1 t + \hat{I}_y{}^j\sin\omega_1 t \qquad \qquad \textit{Equation 3.11}$$

where ω_1 denotes the angular frequency of the decoupling field and t defines time. Therefore, the average Hamiltonian for the heteronuclear dipolar interaction under continuous irradiation of the I spins is given by,

$$\overline{\hat{H}}_{IS} = \sum_{j,k} 2\beta_{IS}{}^{jk}\hat{S}_z{}^k \int_0^{\omega_1 t_p} \frac{d(\omega_1 t)}{\omega_1 t_p}\left(\hat{I}_z{}^j\cos\omega_1 t + \hat{I}_y{}^j\sin\omega_1 t\right) \qquad \textit{Equation 3.12}$$

where $\omega_1 t_p$ denotes the angle through which the I spins precess. Hence, it can be seen that when $\omega_1 t_p$ is equal to a multiple of 2π, $\overline{H}_{IS} = 0$ and for long irradiation times, t_p, such that $t_p \gg \dfrac{2\pi}{\omega_1}$, then $\overline{H}_{IS} \rightarrow 0$.

In Equation 3.12, homonuclear dipolar interactions between the I spins have been neglected. However, even ignoring such interactions, for the average Hamiltonian approach to be valid, the cycle time, i.e. the time required for the I spins to precess through an angle of 2π, must be short and hence a sufficiently large decoupling field is required. The criterion for efficient heteronuclear decoupling is that the decoupling power, ω_1, must be larger than both the heteronuclear (I-S) and homonuclear (I-I) dipolar interactions. The latter requirement arises because homonuclear dipolar interactions between the I spins cannot normally be neglected in organic solids since flip-flop fluctuations of the I spins cause modulation of the I-S dipolar interaction. For Equation 3.12 to be equally valid when dipolar interactions between I spins are included, the I spins must appear 'static' over a complete cycle. For this to be the case, ω_1 must be at least equal to the rate of the flip-flop fluctuations of the I spins. The flip-flop fluctuations of the I spins, through the resultant modulation of the I-S dipolar interaction, can help reduce line broadening due to heteronuclear dipolar interactions. Although it is impossible to irradiate all the I spins at any one time on resonance, such interactions between the I spins serve to remove any possible inefficiencies in the removal of I-S dipolar interactions introduced via off-resonance effects. For static samples in the absence of heteronuclear decoupling, it has been shown that the flip-flop fluctuations of the I spins can reduce the S spin linewidth via a process termed self-decoupling.[41,42]

Most experiments are performed using MAS to remove broadening due to SA and so the effects of MAS upon the spin system must then be considered. For rigid organic solids, in the presence of I-I spin interactions (homogeneous), I-S dipolar interactions can effectively be removed using high-power decoupling. In such cases, normal MAS rates have little if any effect on the I-I dipolar interactions and hence their contribution to heteronuclear dipolar decoupling is unaffected. However, at high MAS rates or at lower MAS rates for more mobile solids, the homonuclear I-I dipolar

interactions can be partially averaged. Hence, the flip-flop fluctuation rate of the I spins is reduced and consequently off-resonance effects can broaden the S spin linewidth. The slowing down of flip-flop fluctuations at higher MAS rates and the resultant increase in S spin linewidth has been illustrated using ferrocene.[43] Commercial probes are now available which can routinely achieve MAS rates of the order of 15-25 kHz, further accentuating the problem.

3.4.1.2 Improved heteronuclear decoupling

It was stated earlier that the decoupling power must be at least equal to the rate of flip-flop fluctuations. In cases where the decoupling power required cannot be achieved, clearly 'new' heteronuclear decoupling schemes are necessary to remove residual broadening in order to achieve the narrowest lines possible. Consideration has only been given to residual broadening arising from heteronuclear dipolar interactions although other sources are of course possible.[44,45] Given the effect of MAS upon particularly mobile compounds or those in which the I spins are sparse, then decoupling schemes are required which can reintroduce the I-I dipolar interactions.

For compounds such as adamantane, in which MAS slows down spin exchange among the I spins, a low-frequency phase-modulated decoupling scheme[46] has shown substantial improvements in decoupling efficiency over continuous irradiation. Moreover, a two-pulse phase-modulated (TPPM) decoupling scheme[4] has proved to be more efficient than continuous irradiation for compounds in which the I spins are weakly coupled and also in those which are strongly coupled. In the original study,[4] it was claimed that there is an optimum combination of pulse duration and modulation angle for a given MAS rate, rf power and compound. The TPPM decoupling scheme is illustrated in Figure 3.5 with the modulation angle and the pulse duration denoted by ϕ and $\tau/2$, respectively.
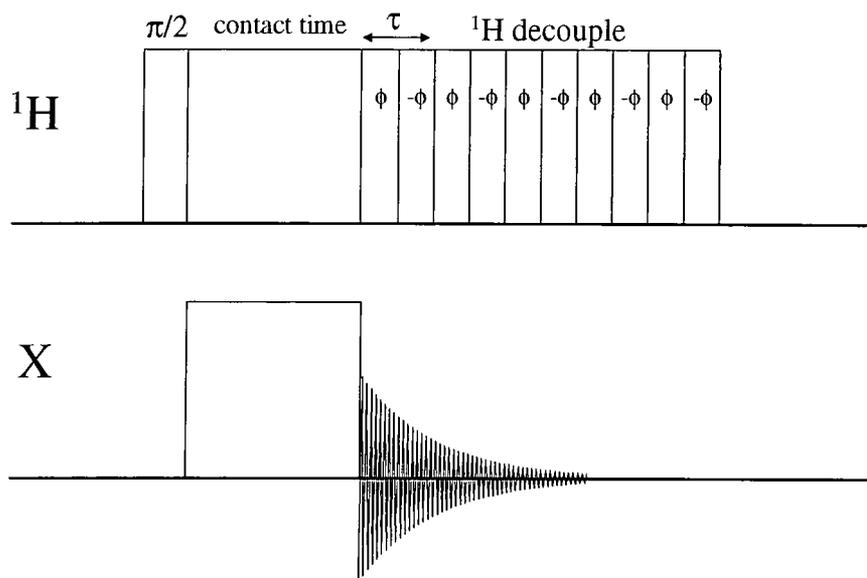
Figure 3.5. $^1H \rightarrow X$ cross polarisation with TPPM ^1H decoupling.

In a recent study[47] which examined the mechanism of decoupling with TPPM, it was shown that optimum decoupling is achieved when the modulation frequency, ω_m, matches the nutation frequency about the x axis, ω_x (assuming that the decoupling field is applied along the x axis). The modulation frequency of the TPPM sequence can be given by,

$$\omega_m = \frac{2\pi}{\tau} \qquad \textit{Equation 3.13}$$

and the nutation frequency about the x axis can be given by,

$$\omega_x = \omega_1 \cos\phi \qquad \textit{Equation 3.14}$$

where ω_1 is the decoupling power expressed in frequency terms (γB_1). Hence, if only a small modulation angle is used, then $\omega_x \approx \omega_1$ and so the pulse duration, $\tau/2$, required corresponds to a 180° tip angle. The improvement in decoupling efficiency of TPPM, when $\omega_m = \omega_x$, over continuous irradiation is due to a secondary resonance effect. If one imagines that B_1 in the rotating frame is the same as B_0 in the laboratory frame, then ω_m can be envisaged as being the 'rf' irradiation in the rotating frame.[48] Then when ω_m is equal to the precession frequency of the spins about B_1, ω_x, then a second nutation of the I spins occurs about a direction which is perpendicular to the nutation in the rotating frame. It is the averaging by this second

nutation that removes terms not removed by the first, and therefore more efficient heteronuclear decoupling is achieved. In the following section, the performance of TPPM decoupling has been compared with that of continuous irradiation in the acquisition of ^{13}C and ^{19}F spectra with ^{1}H decoupling in two fluoroalkane/urea inclusion compounds.

3.4.1.3 Experimental results

3.4.1.3.1 Proton spectra

The effect of MAS on the ^{1}H spectra of the 1-fluorotetradecane/urea inclusion compound is shown in Figure 3.6. At the MAS rate used to acquire ^{13}C spectra (3 kHz), the ^{1}H spectrum has already started to split up into sidebands.
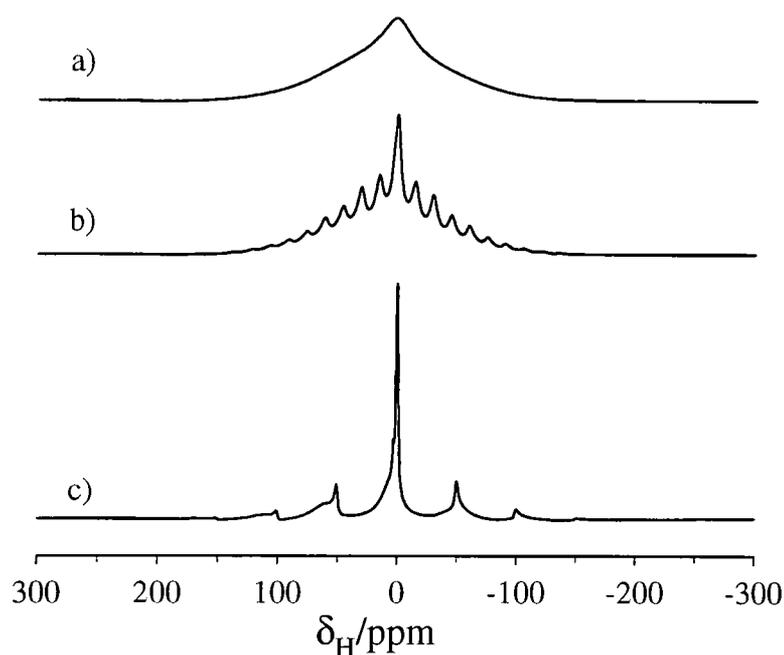
Figure 3.6. Single-pulse ^{1}H spectra of 1-fluorotetradecane/urea acquired at a) 0 kHz, b) 3 kHz and c) 10 kHz. c) is plotted on a different vertical scale to that of a) and b).

However, at 10 kHz, which is the MAS rate used to acquire ^{19}F spectra, one would expect communication between the I spins to be severely hampered,[46] and hence a

reduction in ^{1}H decoupling efficiency to be observed. Therefore, TPPM ^{1}H decoupling has been used in the acquisition of ^{13}C spectra, at 3 kHz, and of ^{19}F spectra, at 10 kHz.

3.4.1.3.2 Carbon-13 spectra

For the acquisition of ^{13}C spectra typically MAS rates of the order of 3 kHz have been used and linewidths of the order of 10-20 Hz have readily been achieved for the urea inclusion compounds. However, for those ^{13}C in close proximity to ^{19}F in the fluoroalkane/urea inclusion compounds, very broad and in some cases barely discernible resonances can be found in ^{1}H→^{13}C CP spectra, acquired with only ^{1}H decoupling. This behaviour is exhibited by those resonances even where one might have expected MAS to average the ^{13}C-^{19}F dipolar interaction. However, in cases where ^{1}H decoupling is insufficient, the whole spin system can be rendered homogeneous and hence it is not possible to spin out the ^{13}C-^{19}F dipolar interaction. As TPPM ^{1}H decoupling has been shown to give substantially better decoupling than continuous irradiation in strongly ^{1}H-coupled systems, ^{13}C spectra have been obtained of 1-fluorotetradecane/urea using continuous irradiation (Figure 3.7a) and TPPM (Figure 3.7b) ^{1}H decoupling, with no ^{19}F decoupling. The spectral conditions used were: ^{1}H π/2 pulse duration, 4.4 μs; contact time, 1.0 ms; recycle delay, 10 s; number of transients, 184; acquisition time, 102.4 ms; MAS rate, 3 kHz, ^{1}H decoupling power, 57 kHz; TPPM ^{1}H pulse duration, 8.7 μs; TPPM phase angle, ±7.0°.

Further experimental details and results regarding the 1-fluorotetradecane/urea inclusion compound are presented in Chapter 5. However, the most visible difference between the two spectra is that the resonances in Figure 3.7b are narrower than in Figure 3.7a, and also extra peaks are visible in Figure 3.7b. In particular, peaks at 14.4 ppm (CH_3 adjacent to a CH_2F), 27.6 ppm ($CH_2CH_2CH_2F$) and 84.1 ppm (CH_2F - $^1J_{CF}$ ~ -160 Hz) are more visible using TPPM than with continuous irradiation decoupling. Therefore, it can be assumed that TPPM decoupling is more efficient than continuous irradiation by virtue of the decrease in

linewidth observed. As a result, carbons which possess a dipolar interaction with ^{19}F are more visible in only ^{1}H-decoupled spectra as the interaction is more 'isolated' and hence can be averaged by MAS.
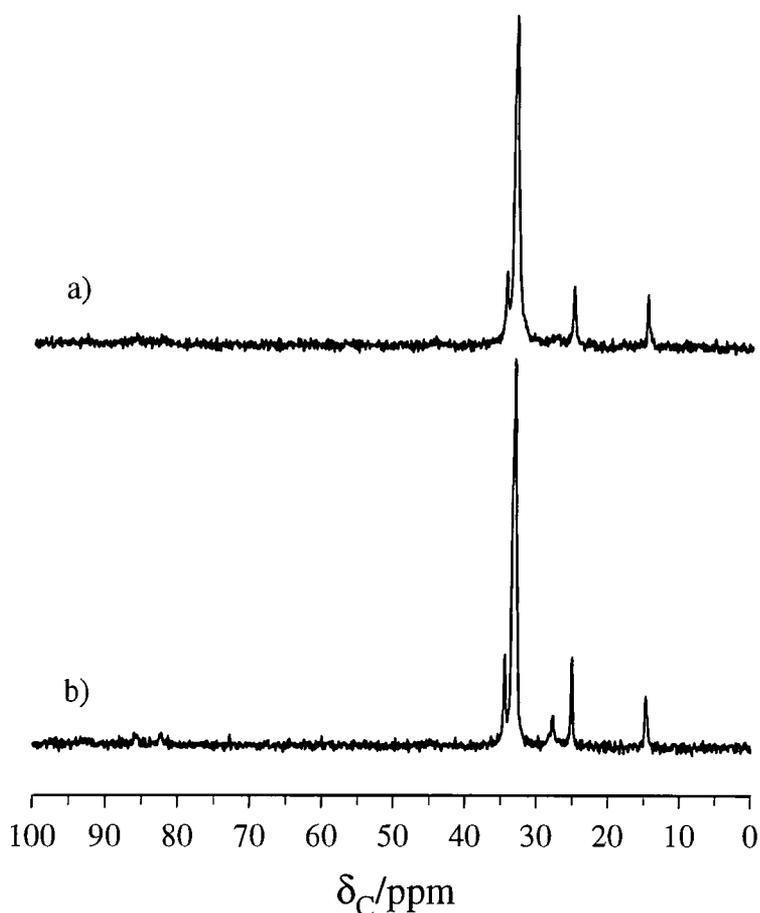
Figure 3.7. $^1H\rightarrow^{13}C$ CP spectra of 1-fluorotetradecane/urea acquired at 3 kHz with a) continuous irradiation ^1H decoupling and b) TPPM ^1H decoupling.

3.4.1.3.3   Fluorine-19 spectra

As shown by the ^{1}H spectra of 1-fluorotetradecane/urea (Figure 3.6), spinning at 10 kHz may have a dramatic effect upon the efficiency of ^{1}H decoupling in ^{19}F NMR experiments. In ^{1}H$\rightarrow^{19}$F CP spectra acquired with ^{1}H decoupling of fluoroalkane/urea inclusion compounds, the 'shape' of the ^{19}F peak and its intensity are dependent upon the matching condition (see earlier section and also Chapter 5). Therefore, in order to try and obtain more information regarding the ^{19}F peak,

experiments have been performed on the 1,10-difluorodecane/urea inclusion compound across a range of matching conditions, with continuous irradiation (Figure 3.8a) and TPPM (Figure 3.8b) ^{1}H decoupling. The spectral conditions used were: ^{1}H $\pi/2$ pulse duration 3 μs, contact time, 1.0 ms; recycle delay, 5 s; number of transients, 32; ^{1}H decoupling power, 100 kHz; ^{1}H CP power, 100 kHz; ^{19}F CP power, 85-25 kHz; acquisition time, 81.9 ms; MAS rate, 10 kHz, TPPM ^{1}H pulse duration, 5.64 μs; TPPM phase angle, $\pm 7.0°$. Again with TPPM ^{1}H decoupling, narrower lines result in the ^{19}F spectrum at all the matching conditions studied than with continuous irradiation. Unfortunately, the improvement in ^{1}H decoupling is not sufficient to yield any further information regarding the composition of the peak.
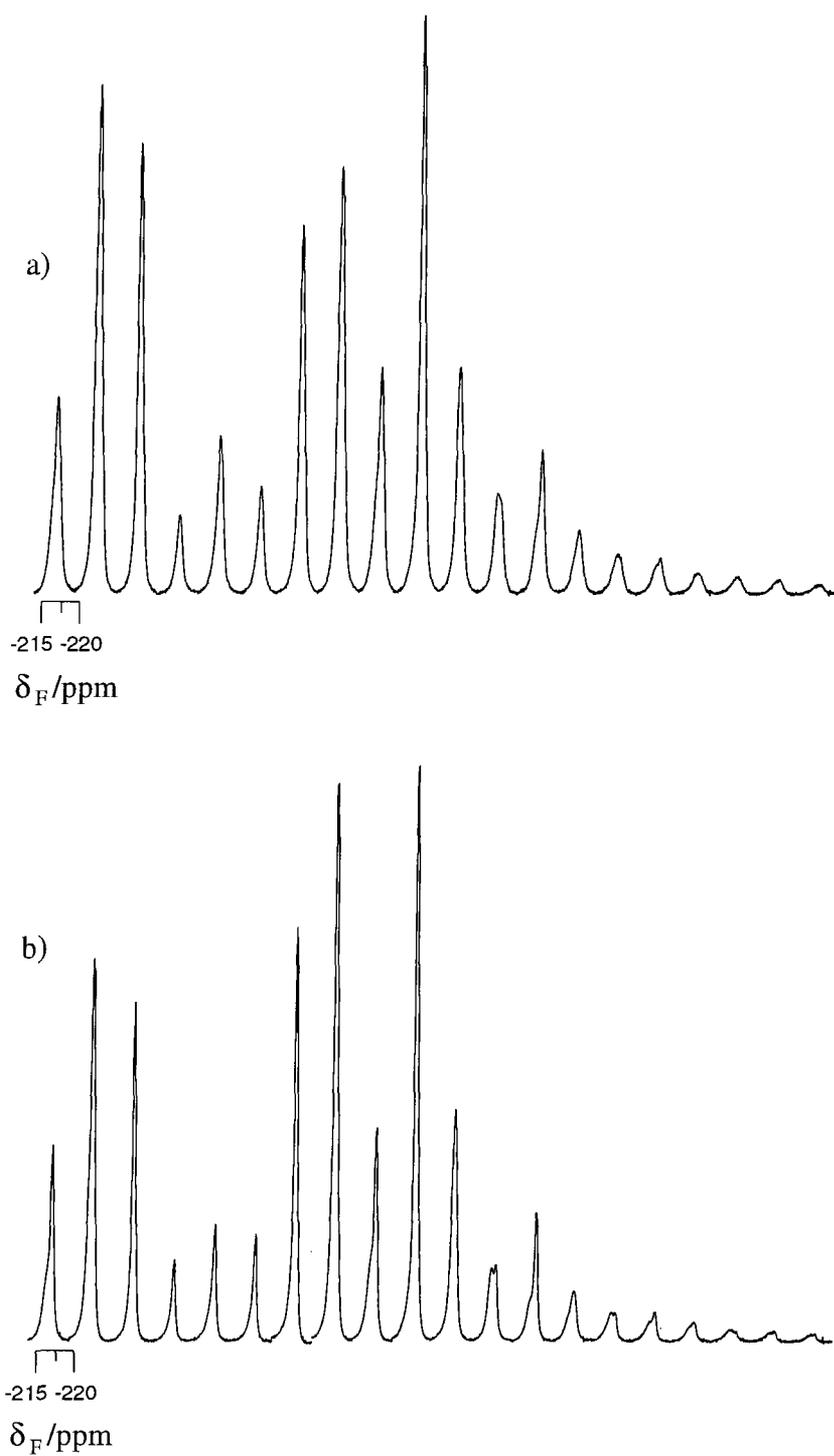
Figure 3.8. Fluorine-19 spectra acquired at different matching conditions with a) continuous irradiation and b) TPPM ^1H decoupling. The ^1H CP power used was 100 kHz and the ^{19}F CP power was varied, from left to right, from 85 kHz to 25 kHz.

3.4.2 Heteronuclear rotational resonance recoupling

3.4.2.1 Rotational resonance

The most well-known rotational resonance experiment is that in which the MAS rate is set equal to an integer multiple of the chemical shift separation between two dipolar coupled spins (R^2).[49] If the two spins are not dipolar coupled, then the lineshapes of the two peaks remains unchanged at the R^2 condition. However, if they are dipolar coupled with one another then their lineshapes change dramatically at the R^2 condition. Within such lineshapes is contained information regarding SA, relative orientations of the two SA tensors with respect to the dipolar principal axis system (PAS), isotropic chemical shift differences, scalar coupling and dipolar coupling. Due to the complexity of this lineshape and the subsequent difficulty in extracting an accurate distance measurement, usually the rotational-resonance spin-exchange experiment[49] is preferred. Rotational resonance can also occur when the magnitude of an applied rf field, given by $\gamma B_1/2\pi$, is equal to a multiple of the MAS rate. In cases where the MAS rate is set equal to a multiple of the spin-lock field, the resulting oscillation observed in the signal[48] contains information concerning SA. This experiment can be extended to two dimensions in which it is then possible to correlate SA with isotropic chemical shifts.[50] It is also possible to selectively excite a single sideband in a spectrum by setting the MAS rate equal to a multiple of a spin-locking field.[51]

However, of relevance to this work is the heteronuclear rotational resonance experiment (R^3).[52,53] Heteronuclear rotational resonance recoupling occurs between two spins, denoted I and S, when the MAS rate is equal to a multiple of the decoupling field expressed in frequency terms (Figure 3.9).

I decouple

I

$\omega_1 = n\omega_r$

$\pi/2$

S
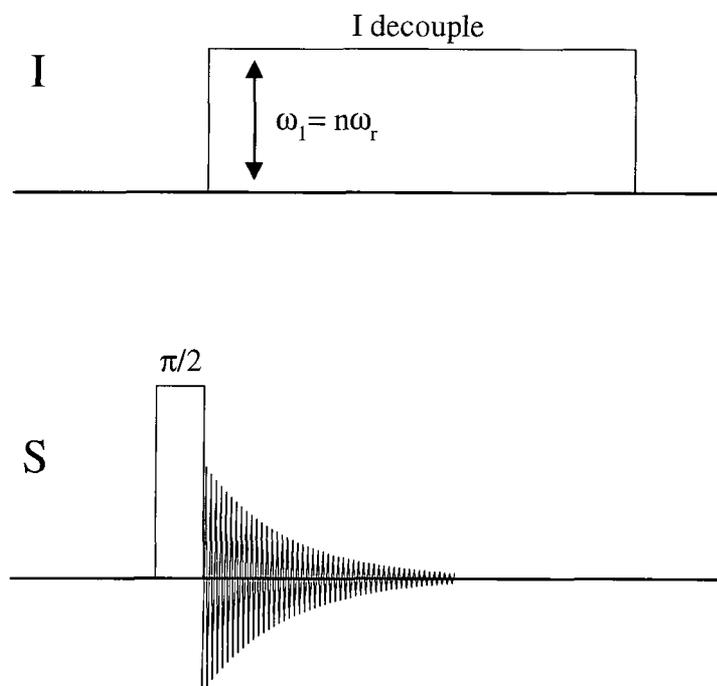
Figure 3.9. Single-pulse with I decoupling pulse sequence. When the I decoupling power, ω_1 (where ω_1 is equal to γB_1), is a multiple of the MAS rate, ω_r (given in rad s^{-1}), then heteronuclear rotational resonance recoupling occurs.

When the I spins are irradiated, they precess about B_1 with a frequency of ω_{1I}. However, the I-S heteronuclear dipolar interaction is modulated by MAS, which introduces frequency components of ω_r and $2\omega_r$ into the spatial term, β_{IS}, for this interaction. Again, if one imagines that B_1 in the rotating frame acts in the same way as B_0 in the laboratory frame, then the modulation of I-S with frequency components of ω_r and $2\omega_r$ can be envisaged as being the 'rf' irradiation in the rotating frame. Hence, when $\omega_{1I} = n\omega_r$, the time-dependence imposed by the rf field on the spin part of the heteronuclear dipolar interaction is the same as that imposed by MAS on the spatial part. Therefore, the S spin evolves under the heteronuclear dipolar interaction as if it were static and consequently there is a recoupling of the heteronuclear dipolar interaction. For an isolated I-S spin pair, continuous irradiation or MAS can result in the decoupling of the two spins, but in combination recoupling can occur.

In principle, it should be possible to extract distance information from the resulting spectrum. Recoupling of the ^{31}P-^{15}N dipolar interaction in ^{31}P spectra of a

[15]N-labelled N-methyldiphenylphosphoranidate compound has been reported.[52-55] At the rotational resonance condition, the spinning sidebands and the isotropic peak in the ^{31}P spectrum split to resemble Pake-like powder patterns. However, this experiment has not been extensively used to measure heteronuclear dipolar interactions, due to the complexity of the information contained within the lineshape, its extreme sensitivity to inhomogeneities in the rf field intensity and variations in the direction of the rf field across the sample.[52,53] More recently, a variation of this experiment in which the amplitude of the decoupling field is modulated, has been reported for 2-^{13}C/^{15}N doubly labelled glycine.[56] In this experiment the heteronuclear dipolar interaction is reintroduced when the MAS rate is equal to a multiple of the amplitude-modulation frequency of the decoupling field. This version of the experiment holds far more potential than the first version, as it is insensitive to inhomogeneities in the rf field.

In the example discussed above, a triple-channel probe is required to decouple the ^{1}H spins and to be able to recouple the I and S spins. In such a case, the I-S spin pair is essentially isolated when ^{1}H decoupling is applied and hence can be modulated by MAS (inhomogeneous). It is also possible to achieve heteronuclear rotational resonance recoupling between ^{1}H and ^{13}C in mobile systems such as adamantane.[57] However, it is not possible to extract distance information from the spectra due to the multi-spin nature of the heteronuclear dipolar interaction in this particular case. Heteronuclear rotational resonance recoupling has also been observed between ^{1}H and ^{19}F in some fluorinated steroids.[2] Due to the results observed in the cross polarisation and decoupling experiments described in earlier sections, it was thought that the fluoroalkane/urea inclusion compounds might exhibit [1]H-^{19}F rotational resonance recoupling.

3.4.2.2 Experimental results

Fluorine-19 spectra of the 1-fluorotetradecane/urea inclusion compound have been acquired as a function of ^{1}H decoupling power at MAS rates of 12 kHz, 10 kHz, 8 kHz, 6 kHz, 4 kHz and 1 kHz. The ^{1}H decoupling power was altered using the 'amplitude' parameter which was varied from 255 to 0 in steps of 1. Calibration of the ^{1}H decoupling power was performed by determining the pulse duration required for a 180° pulse for a given 'amplitude' value using PDMSO. However, this does not give the actual decoupling power used, as the calibration experiment is performed with the crossed diodes and λ/4 cable present in the circuitry, whereas for decoupling they are absent. This fact has been taken into account in the results presented, although further details regarding this point are discussed in Chapter 2. Typical spectral conditions were: ^{19}F π/2 pulse duration, 3 µs; recycle delay, 10 s, number of transients, 4; acquisition time, 20.5 ms; ^{1}H decoupling 'amplitude', 255-0. An example of the results obtained at 12 kHz is shown in Figure 3.10. In the slices extracted from the stacked plot in Figure 3.10, it is particularly noticeable that the ^{19}F chemical shift moves to higher frequencies as the ^{1}H decoupling power is reduced. This can be attributed to the Bloch-Siegert shift,[58] which is of particular importance when quoting ^{19}F chemical shifts and can also be used to determine the ^{1}H decoupling power (see Chapter 2).

It can also been seen that at specific ^{1}H decoupling fields, the ^{19}F resonance is severely broadened (Figure 3.10e and Figure 3.10g) particularly in comparison to that obtained when no decoupling is applied (Figure 3.10a). When the MAS rate is decreased, the maxima observed in the linewidths occur at lower ^{1}H decoupling powers and the number of maxima observable becomes fewer (Figure 3.11). The variation of the maxima positions, in relation to ^{1}H decoupling power, with MAS rate suggests that there is an interference between MAS rate and decoupling power. Variable decoupling power experiments were then performed at a single MAS rate, 6 kHz, and at different temperatures (Figure 3.12). It can be seen that as the temperature is decreased, there is no shift observed in the decoupling power at which the maxima occur, but they do become less well defined. The lack of variation of

maxima positions further suggests that there is an interference between MAS rate and decoupling power.

In order to rationalise these results, one must first consider the nature of the ^{19}F-^{1}H dipolar interaction and the effect of MAS upon this and on the ^{1}H-^{1}H dipolar interactions. At MAS rates of the order of 10 kHz, from the appearance of the ^{1}H spectrum of 1-fluorotetradecane/urea (Figure 3.6), one would expect the I-I flip-flop fluctuations to be reduced in rate in comparison to those at lower MAS rates. Hence, at such MAS rates, the ^{19}F-^{1}H dipolar interaction can be considered as being inhomogeneous and so it is possible for MAS to modulate the interaction. However, at lower spin rates, flip-flop fluctuations between the I spins are more prevalent and hence they tend to dominate the modulation of the I-S dipolar interaction rather than MAS. Similarly, at low temperatures flip-flop fluctuations between the I spins are the dominant modulating factor on the I-S dipolar interaction. Therefore, in order to observe heteronuclear rotational resonance recoupling in which one of the spins is ^{1}H, MAS must split the ^{1}H spectrum into sidebands and hence slow down the I-I dipolar fluctuations. Then the I-S spin pair can be considered to be relatively isolated and so modulation of the interaction by MAS is possible. Hence recoupling of the heteronuclear dipolar interaction can occur at the rotational resonance condition. However, it is worth remembering that it will be very difficult to extract any meaningful distance measurements from ^{1}H-^{19}F systems due to the multi-spin nature of the protons.
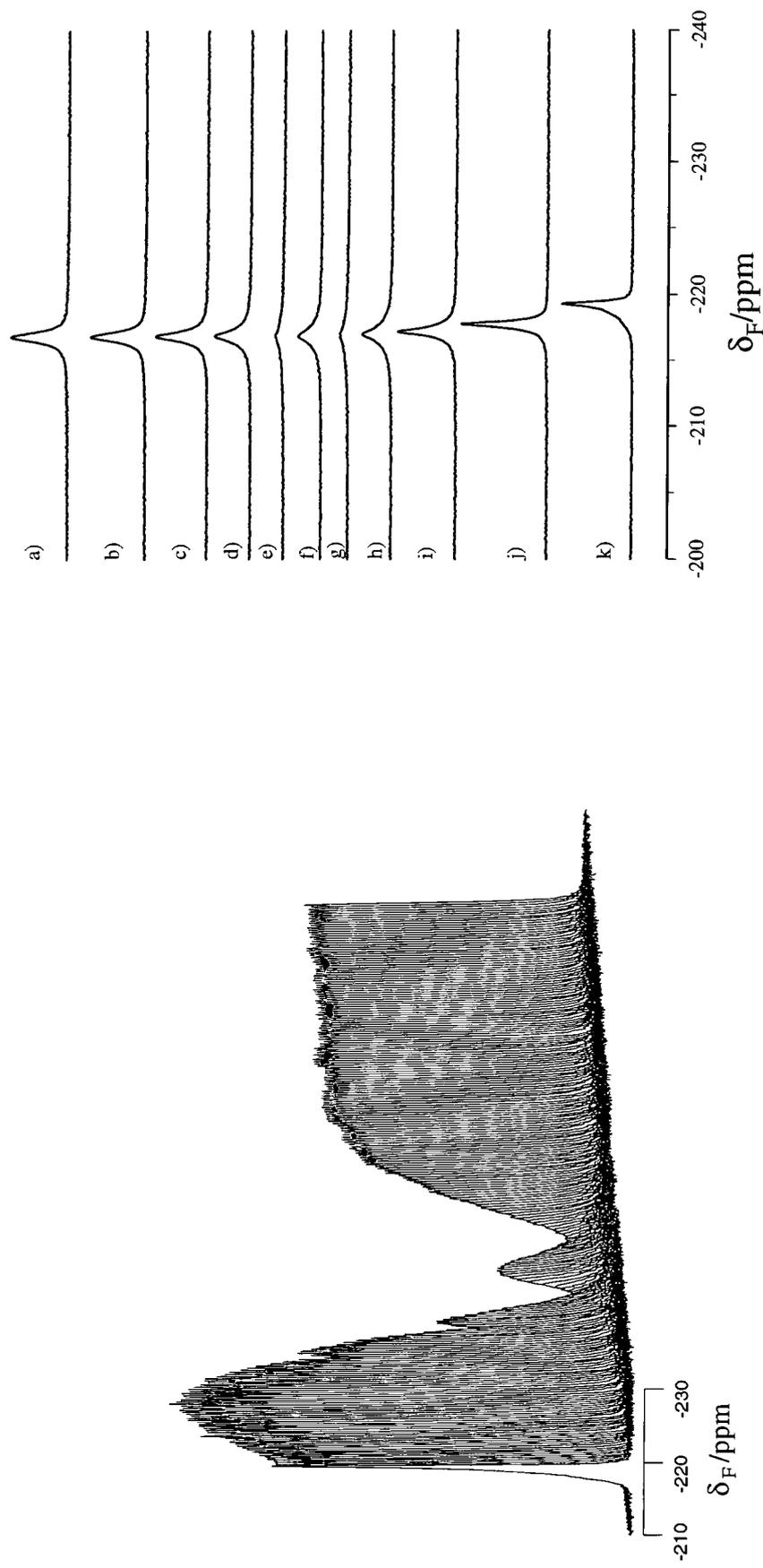
Figure 3.10. Variable ^1H decoupling power experiment performed on 1-fluorotetradecane/urea at 12 kHz. The decoupling power varies, from front to back in the stacked plot, from 100 kHz to 0 kHz with the minimum signal intensities (or maximum linewidths) observed at decoupling powers of 44 kHz, 33 kHz, 22 kHz and 11 kHz. Slices on the right hand side correspond to decoupling powers of a) 0 kHz, b) ~0 kHz, c) 3 kHz, d) 5 kHz, e) 11 kHz, f) 17 kHz, g) 22 kHz, h) 33 kHz, i) 44 kHz, j) 66 kHz and k) 100 kHz.
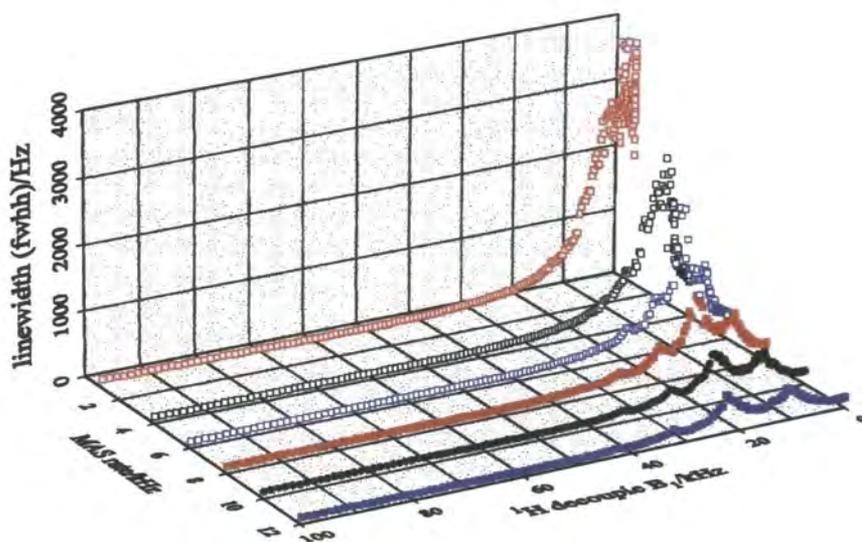
Figure 3.11. Graph plotting ^{19}F linewidth as a function of ^{1}H decoupling power at MAS rates (from back to front) of 1 kHz, 4 kHz, 6 kHz, 8 kHz, 10 kHz and 12 kHz. All experiments were performed at 300 K.
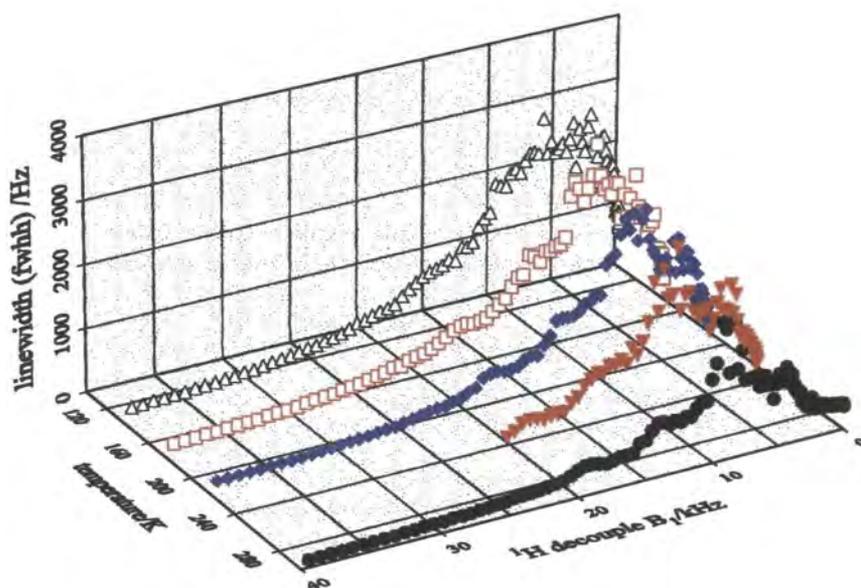
Figure 3.12. Graph plotting ^{19}F linewidth as a function of ^{1}H decoupling power at temperatures (from back to front) of 137 K, 177 K, 217 K, 258 K and 300 K. The MAS rate used was 6 kHz.

3.4.3 Multiple-pulse heteronuclear dipolar decoupling in CRAMPS experiments

3.4.3.1 Introduction

To observe either ^1H or ^{19}F in the solid state, when such nuclei are present in high abundance, multiple-pulse sequences such as WAHUHA,[59] MREV-8[60,61] or BR-24[62] along with MAS (CRAMPS[63]) are used to remove homonuclear dipolar interactions and SA, respectively. However, in systems containing both nuclei, it is then necessary to consider the ^1H-^{19}F (heteronuclear) dipolar interactions. Although the pulse sequences applied to remove homonuclear dipolar interactions scale the heteronuclear dipolar interaction, they also scale to the same extent the chemical shift and hence it may still be difficult to access the desired information. Typically, heteronuclear decoupling is achieved in solid-state NMR experiments by irradiating the appropriate spins at their Larmor frequency. However, for continuous irradiation of the S spins, as shown in Equation 3.12, $\overline{H}_{IS} = 0$ only when $\omega_1 t_p$ is equal to a multiple of 2π. Therefore, in order to remove the heteronuclear dipolar interaction, the S spins must precess through an angle equal to a multiple of 2π during the so-called 'large' windows in the homonuclear multiple-pulse averaging sequence. If the large windows, of duration 2τ, are typically $6\,\mu s$, then for this condition to be met, S-decoupling powers of $167\,kHz$ would be necessary.

Hence, removal of I-S dipolar interactions by continuous irradiation would require a relatively robust probe. External filters would also be needed to isolate the frequencies, which, in the case considered here, would need to be of a particularly high specification in order to isolate the ^1H and ^{19}F frequencies. The addition of filters to the circuitry means that higher powers are needed to achieve the same pulse durations as when no filters are in place. However, of perhaps greater significance is the effect of the filters upon the shape of the pulse. The filters that are used to isolate the ^1H and ^{19}F frequencies are bandpass filters, i.e. they only permit a small range of frequencies either side of a specific frequency through. For effective averaging of the homonuclear dipolar interactions, the pulse edges need to be as sharp possible and so the pulse will have to 'contain' all frequencies. However, the very purpose of

bandpass filters is to remove higher and lower frequencies around a specific frequency, and thus filters can degrade the averaging performance of multiple-pulse sequences.

It is worth remembering that filters are only needed if rf is to be applied on the decoupling channel while the FID is being simultaneously observed. Therefore, if decoupling pulses can be applied in different 'large windows' to that in which an FID point is acquired, i.e. an 'observation window', then simultaneous removal of both homonuclear and heteronuclear dipolar interactions is possible without filters. This was first realised for the WAHUHA pulse sequence via the application of a 180° pulse (to the S spins) in either of the two 'large windows'.[64] The removal of the heteronuclear dipolar interaction using this approach is still possible even when the pulse duration is finite and so the whole of the window is available for the pulse. The evolution of the S spins during the 180° pulse can easily be calculated by evaluating the integral in Equation 3.12 between π and 0. Hence, if the phase of the 180° pulse is always x, then the state of S_z in the toggling frame will always be proportional to $|S_y|$, as will be shown later.

However, upon determination of the average Hamiltonian for the heteronuclear dipolar interaction $\left(\overline{\overline{H}}_{IS}\right)$, two WAHUHA sequences and hence $2\times180°$ pulses are required to constitute a cycle over which $\overline{\overline{H}}_{IS} = 0$. To improve the averaging efficiency of the heteronuclear dipolar interaction, 180° pulses can in fact be applied in every 'large window', but the phase of alternate pulses must be reversed in order for $\overline{\overline{H}}_{IS} = 0$. The application of 180° pulses in alternate 'large windows' to remove heteronuclear dipolar interactions while simultaneously removing homonuclear dipolar interactions via the MREV-8 pulse sequence has also been demonstrated.[65] As BR-24 is considered to be superior to MREV-8, in terms of its ability to eliminate higher-order terms in the average Hamiltonian, and is frequently the pulse sequence of choice for obtaining CRAMP spectra, the simultaneous removal of I-S dipolar interactions when I-I dipolar interactions are averaged by BR-24 has been investigated.

Due to the greater chemical shift range of ^{19}F, then CRAMPS sequences such as BR-24 may limit the spectral width too much. In fact in a static ^{19}F CRAMPS study,[65] the MREV-8 sequence was only just able to provide a large enough spectral width for the spectrum. The cycle time could always be reduced by decreasing tau and/or the pulse durations, but experiments tend to be run at the limits of the technology available, so this option is not really feasible. In conventional CRAMPS experiments, the transmitter is placed to one side of the spectrum so that only one half of the spectral width is in fact available. However, CRAMPS sequences are now available which average the unwanted signals on the other side of the transmitter and hence allow the whole spectral width to be utilised.[66] Such sequences will be useful in ^{19}F NMR and in particular in the acquisition of static spectra.[67] Therefore, in all of the pulse sequences presented in section 3.4.3.3.2, the quadrature detection versions of BR-24 have been used.

3.4.3.2 Homonuclear decoupling via BR-24 with simultaneous heteronuclear decoupling

3.4.3.2.1 Removal of heteronuclear dipolar interactions via 180° pulses in alternate windows of BR-24

The compound used to test the heteronuclear averaging ability of the sequences devised was NH_4PF_6, with ^{19}F being the observed nucleus. The ^{19}F CRAMP spectrum of this compound, acquired using the BR-24 pulse sequence, shows a very broad peak without ^{1}H decoupling (Figure 3.13b). The spectral conditions used were: ^{19}F $\pi/2$ pulse duration, 1.5 µs; tau, 3.0 µs; recycle delay, 20 s; number of points acquired, 512; MAS rate, 1146 Hz; number of transients, 16. However, upon applying ^{1}H decoupling with MREV-8 in the manner described previously,[65] two sharp peaks (fwhh ~ 100 Hz) are present in the spectrum. Hence, this compound was deemed to provide a sensitive test of the I-S decoupling efficiency of the proposed sequences. Based upon previous heteronuclear decoupling sequences with the WAHUHA and MREV-8 homonuclear decoupling sequences,

180° pulses (of fixed phase and with a duration of 2.47 µs) were first applied to the S spins in every alternate window of the BR-24 pulse sequence (Figure 3.14). It is obvious from the linewidths of the two peaks in Figure 3.13a, fwhh ~ 280 Hz, that although there is some degree of averaging of I-S dipolar interactions, this pulse sequence is inferior to the MREV-8 sequence with 2×180° decoupling pulses per cycle.
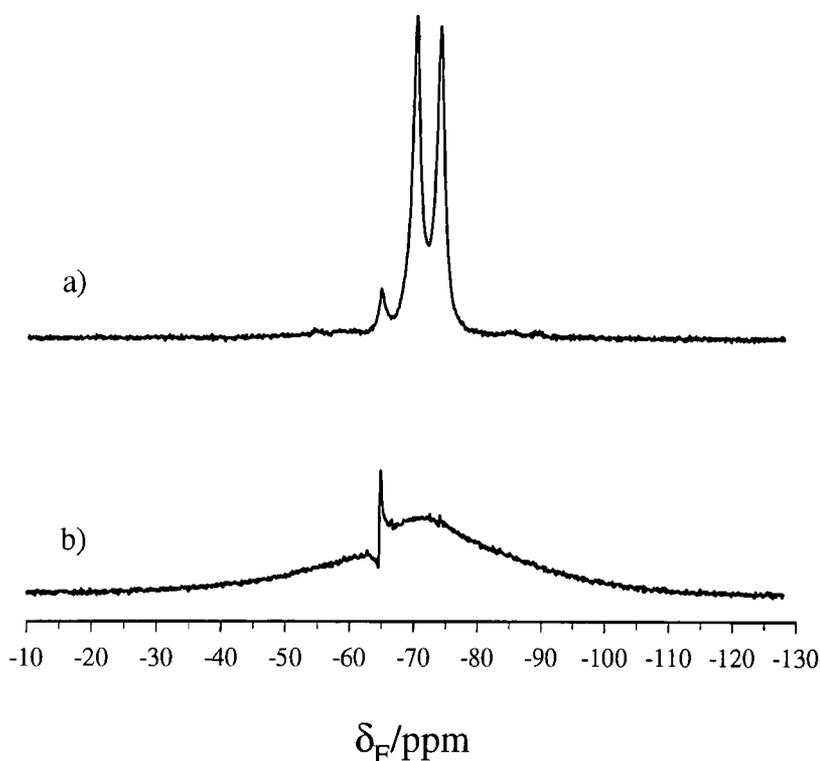
Figure 3.13. Comparison of ^{19}F CRAMP spectra obtained using a) BR-24 with ^1H decoupling via the sequence in Figure 3.14 and b) BR-24 alone. The 'peak' at -65 ppm is an artefact arising from transmitter positioning.

The reason for this can be seen by determining the heteronuclear dipolar interaction term in the toggling frame for the two pulse sequences. Upon summing all the $\tilde{I}_z\tilde{S}_z$ terms, to yield the average Hamiltonian for the I-S dipolar interaction over the BR-24 sequence, $\overline{\hat{H}}_{IS} \propto 4\hat{I}_z\hat{S}_z$. However, upon performing the same procedure for the MREV-8 sequence, $\overline{\hat{H}}_{IS} = 0$. Hence, the poorer performance of the BR-24/heteronuclear decoupling sequence in relation to the MREV-8/heteronuclear decoupling sequence can be attributed to this residual term. This result may at first

sight be unexpected, but this residual term arises as a result of the construction of the BR-24 pulse sequence which is necessary for the removal of higher-order terms in the average Hamiltonian. For the same reason as for the WAHUHA sequence, with BR-24 it is not possible for $\overline{\hat{H}}_{IS}$ to be zero over one cycle and so I-S decoupling schemes have been devised where one cycle comprises 2×BR-24 sequences.

time	BR-24	$I_z(t)$	Xdec	$S_z(t)$	$I_zS_z(t)$
0		z			zz
τ	x	z		z	zz
2τ	y	x			xz
3τ		y	x	2y	yy
4τ	-y				-xz
5τ	-x	x			
6τ		z		-z	-zz
7τ	-x				
8τ	y	-x			xz
9τ		y	x	-2y	-yy
10τ	-y				
11τ	x	-x			-xz
12τ		z		z	zz
13τ	y				
14τ	x	y			yz
15τ		x	x	2y	xy
16τ	-x				
17τ	-y	y			-yz
18τ		z		-z	-zz
19τ	-y				
20τ	x	-y			yz
21τ		x	x	-2y	-xy
22τ	y				
23τ	x	z			zz
24τ		y		z	yz
25τ	-x	z			zz
26τ	-y				
27τ		x	x	2y	xy
28τ	-y				
29τ	x	-z			zz
30τ		y		-z	-yz
31τ	-x				
32τ	y	-z			zz
33τ		x	x	-2y	-xy
34τ	-x				
35τ	y	-y		z	-yz
36τ		z			zz

Figure 3.14. Evolution of the I-S dipolar coupling term in the effective Hamiltonian while applying the BR-24 sequence to the I spins.

3.4.3.3 Design of pulse sequences for the elimination of heteronuclear dipolar interactions in CRAMPS experiments

3.4.3.3.1 Subcycles for homonuclear and heteronuclear decoupling

The basic building block for the WAHUHA, MREV-8 and BR-24 pulse sequences is the solid echo[68] pulse sequence (Figure 3.15).
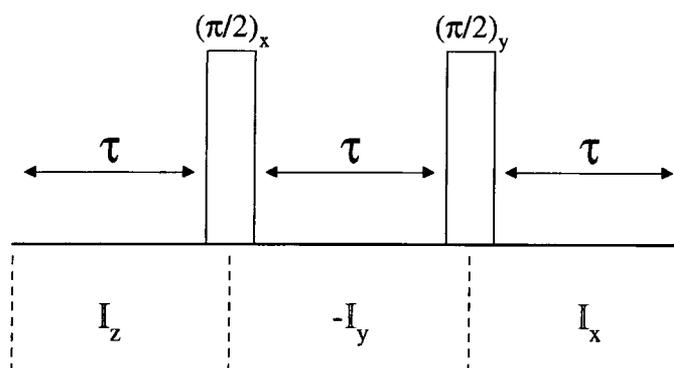
Figure 3.15. Solid echo pulse sequence.

Assuming δ pulses, it can be seen that at a time $t = 3\tau$, the chemical shift of I,

$\overline{\hat{H}}_I \propto \frac{1}{3}\left(\hat{I}_z - \hat{I}_y + \hat{I}_x\right)$ and the homonuclear dipolar interaction, $\overline{\hat{H}}_{II}^0 = 0$. As the

Hamiltonian which determines the toggling frame, $\hat{H}_{rf}$, has to be cyclic, then two more 90° pulses with phases of -x and -y are required. This results in a four-pulse sequence with an overall cycle time of 6τ, which is in fact the WAHUHA pulse sequence. By evaluation of higher order and cross terms of the Hamiltonians, it is possible to use the 'pulse cycle decoupling' approach[62] to arrive at the MREV-8 and BR-24 pulse sequences which eliminate such undesirable terms.

Similarly, the basic building block for the removal of heteronuclear dipolar interactions is the Hahn echo[69] (Figure 3.16). It is worth noting that application of 180° pulses to the S spins has no effect upon the averaging efficiency of the homonuclear (I-I) dipolar interactions. Again assuming δ pulses, it can be seen that at

a time $t = 2\tau$, the chemical shift of S, $\overline{H}_S = 0$ and the heteronuclear dipolar interaction, $\overline{H}_{IS}^0 = \hat{I}_z\hat{S}_z - \hat{I}_z\hat{S}_z = 0$.
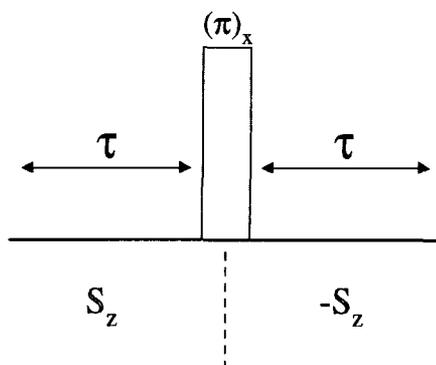
Figure 3.16. Hahn echo pulse sequence.

Hence, the subcycle for heteronuclear decoupling consists of two 180° pulses separated by a time denoted 2τ with an overall cycle time of 4τ (Figure 3.17).
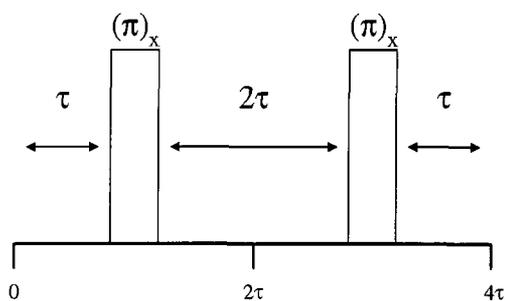
Figure 3.17. Basic cycle for heteronuclear decoupling.

Larger cycles can be constructed by simply putting subcycles next to each other or by placing one subcycle within other subcycles in a similar manner to which the BR-24 sequence is constructed from 3×MREV-8 sequences.[62] However, if pulses are applied to the I spins as in homonuclear decoupling sequences such as BR-24, then when constructing homonuclear/heteronuclear decoupling schemes, both the S and I spins must be considered. Hence, the construction of the decoupling scheme must take into account the symmetry[70] of the homonuclear decoupling sequence. In sequences such as BR-24 which are not symmetric, two sequences must be combined

in order that the sign of $\tilde{I}_z\tilde{S}_z$ in the first cycle is equal and opposite to the $\tilde{I}_z\tilde{S}_z$ term at the same position in the second cycle. If there are 'extra' pulses or windows in the sequences which do not belong to a subcycle,[62] even when all the $\tilde{I}_z\tilde{S}_z$ terms are summed and $\overline{\hat{H}}_{IS} = 0$, the heteronuclear dipolar interaction will not be removed. To illustrate this point, two versions of a heteronuclear decoupling sequence which both contain ten 180° pulses per cycle are shown in Figure 3.18, one of which works (Figure 3.18a) and the other does not (Figure 3.18b). The dashed lines indicate how the heteronuclear decoupling scheme is made up from the basic Hahn echo sequences, with the numbers then indicating which Hahn echo sequences are 'partners' in each subcycle.
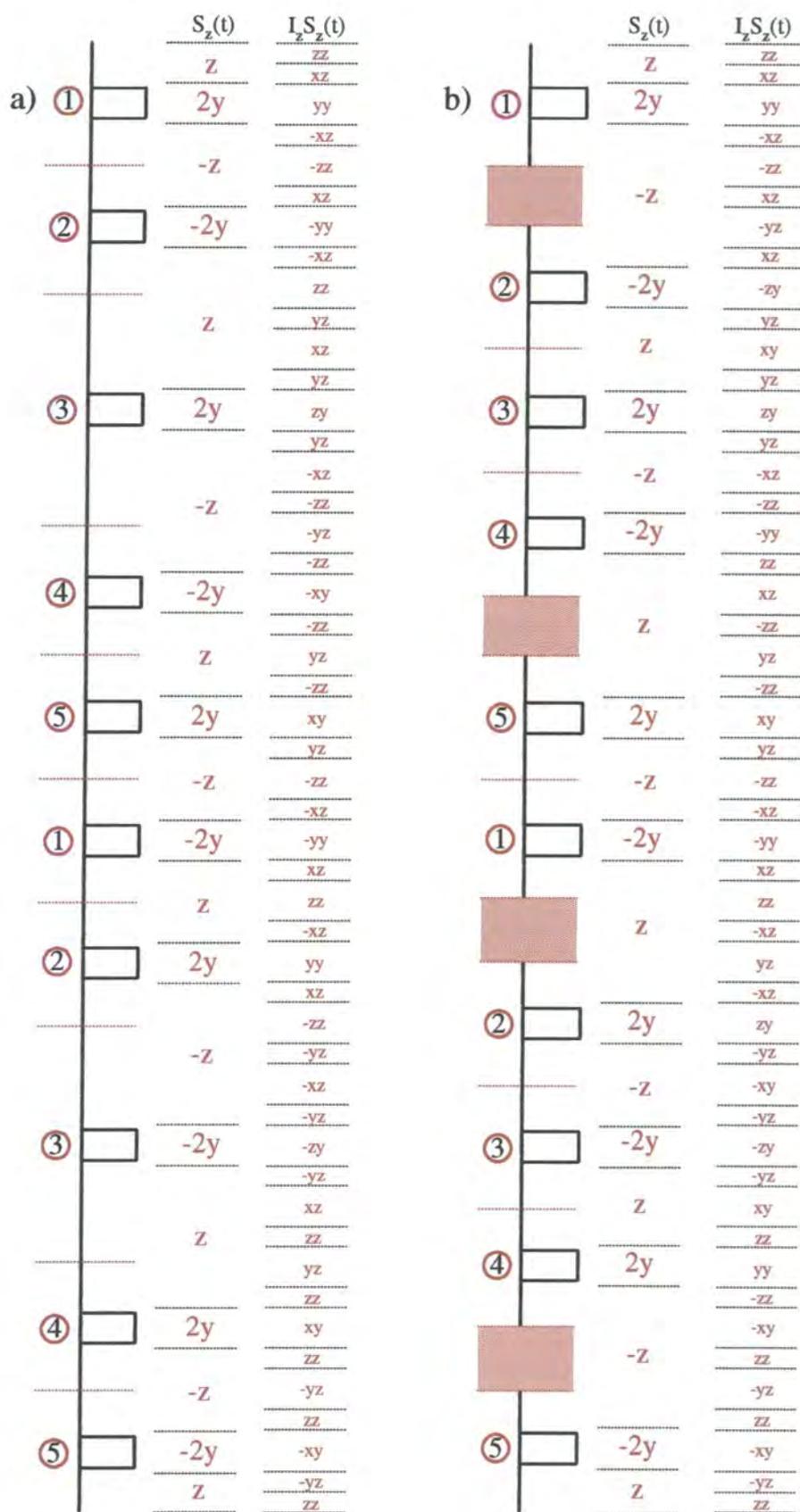
Figure 3.18. Heteronuclear decoupling schemes using 10×180° pulses. The sequence in a) works where as that in b) does not. The hatched areas in b) do not belong to any of the subcycles.

3.4.3.3.2 Pulse sequences

To ensure that when all the $\tilde{I}_z\tilde{S}_z$ terms are summed, $\overline{\hat{H}}_{IS} = 0$ and hence the heteronuclear dipolar interaction is removed, the decoupling sequence must obey the principles discussed in the previous section, and so overall must contain an even number of 180° pulses as in the sequences proposed in Figure 3.19. The evolution of the $\tilde{I}_z$, $\tilde{S}_z$ and $\tilde{I}_z\tilde{S}_z$ terms over the course of a complete cycle for the dec2x, dec6x, dec10x and dec22x pulse sequences are shown in Figure 3.20 and Figure 3.21. Typical examples of the spectra obtained using the 2×BR-24/dec2x, dec6x and dec22x pulse sequences are shown in Figure 3.22. It can be seen that as the number of 180° pulses increases, the efficiency of heteronuclear decoupling increases. The linewidths (fwhh) obtained using 2×BR-24/dec2x, dec6x and dec22x pulse sequences were 500 Hz, 170 Hz and 120 Hz. Hence, the decoupling efficiency achieved using the 'best' of the new heteronuclear decoupling sequences, dec22x, is at least comparable to that obtained using the MREV-8 sequence with 2×180° pulses per cycle. To increase the efficiency of decoupling with MREV-8, without having to acquire an FID point and apply a pulse in the same large window, an MREV-8 sequence has been written in which one cycle is made up of 2×MREV-8 sequences and 6×180° pulses.[71] This pulse sequence has been tested, again observing ^{19}F, on 2,4,6-trifluoromethylbenzoic acid, and a slight improvement in resolution was obtained.[72]
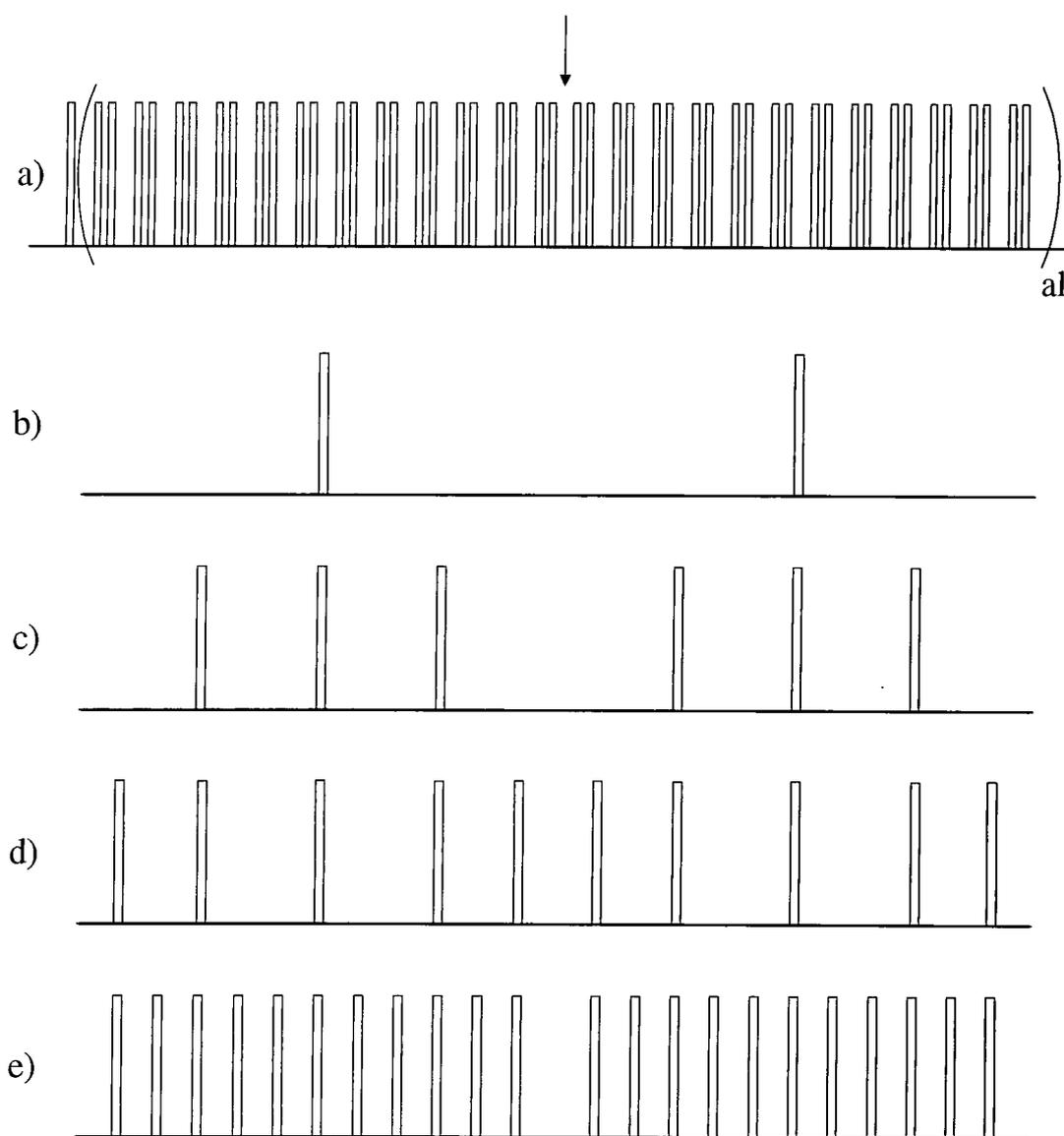
Figure 3.19. Pulse sequences for homonuclear/heteronuclear decoupling. Homonuclear dipolar interactions are averaged via a) two BR-24 sequences with the arrow indicating the sampling point. Simultaneous heteronuclear decoupling is achieved using b) dec2x, c) dec6x, d) dec10x and e) dec22x, where the number preceding x indicates the number of 180° pulses.
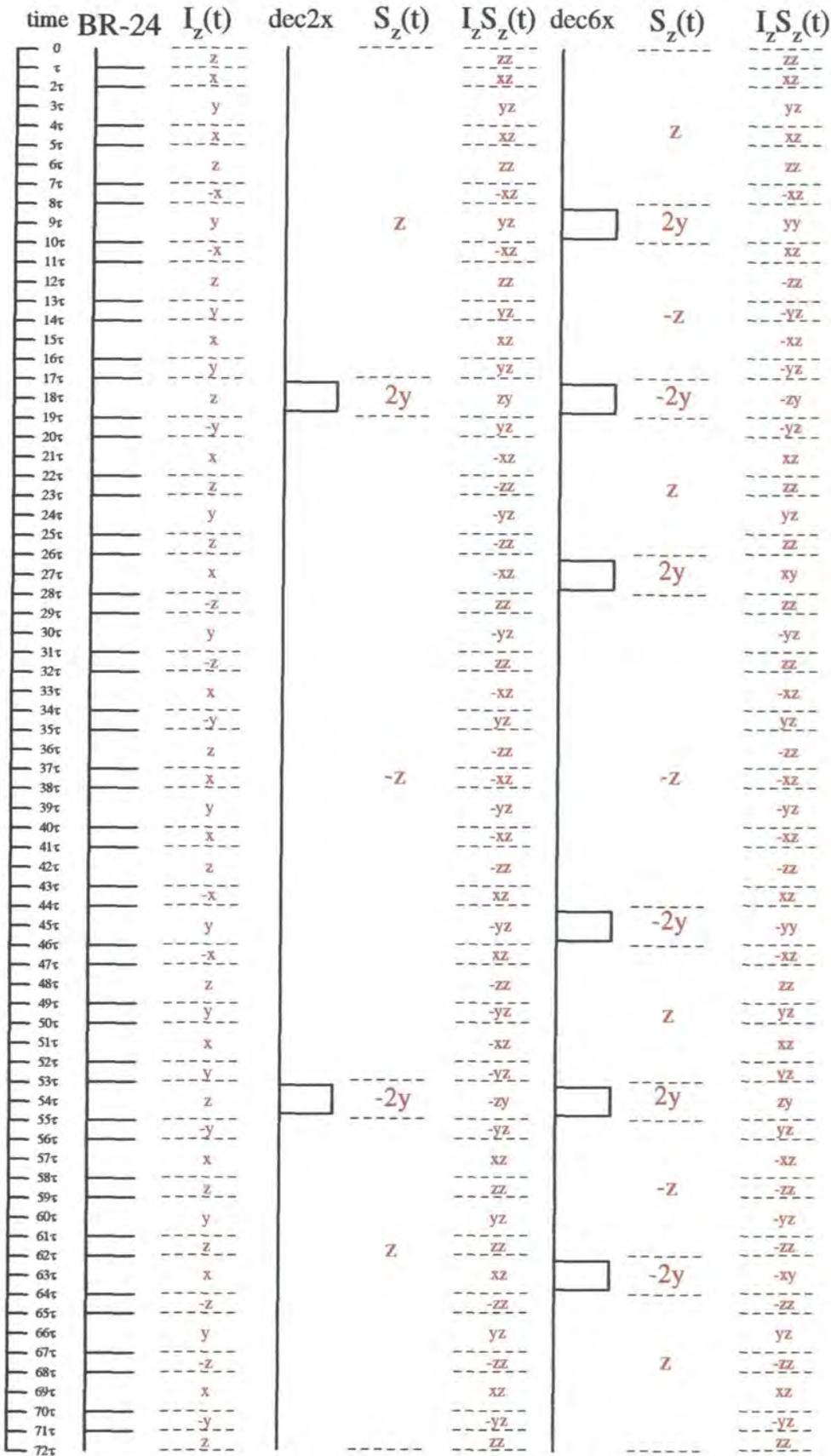
Figure 3.20. Evolution of I-S dipolar coupling term in the effective Hamiltonian using dec2x and dec6x heteronuclear decoupling schemes.

time	BR-24	$I_z(t)$	dec10x	$S_z(t)$	$I_zS_z(t)$	dec22x	$S_z(t)$	$I_zS_z(t)$
0								
τ		z		z	zz		z	zz
2τ		x			xz			xz
3τ		y		2y	yy		2y	yy
4τ		x					-z	-xz
5τ		x			-xz			-xz
6τ		z		-z	-zz		-2y	-zy
7τ		-x			xz		z	-xz
8τ		-x					z	-xz
9τ		y		-2y	-yy		2y	yy
10τ		-x			-xz		-z	xz
11τ					-xz			xz
12τ		z			zz		-2y	-zy
13τ							z	
14τ		y		z	yz		z	yz
15τ		x			xz		2y	xy
16τ								
17τ		y			yz		-z	-yz
18τ		z		2y	zy		-2y	-zy
19τ		-y					z	
20τ		-y			yz		z	-yz
21τ		x			-xz		2y	xy
22τ		z						
23τ		z		-z	-zz		-z	-zz
24τ		y			-yz		-2y	-yy
25τ		z			-zz		z	zz
26τ								
27τ		x		-2y	-xy		2y	xy
28τ					-zz		-z	zz
29τ		-z			-zz			zz
30τ		y		z	yz		-2y	-yz
31τ							z	
32τ		-z			-zz		z	-zz
33τ		x		2y	xy		2y	xy
34τ		y			yz			
35τ		-y			yz			yz
36τ		z		-z	-zz		-z	-zz
37τ								
38τ		x			-xz			-xz
39τ		y		-2y	-yy		-2y	-yy
40τ		x			xz		z	xz
41τ							z	
42τ		z		z	zz		2y	zy
43τ		-x					-z	
44τ		-x			-xz		-z	xz
45τ		y		2y	yy		-2y	-yy
46τ					xz		z	-xz
47τ		-x					z	
48τ		z			-zz		2y	zy
49τ		y			-yz			
50τ		y		-z	-yz		-z	-yz
51τ		x			-xz		-2y	-xy
52τ		y			-yz		z	
53τ		y						yz
54τ		z		-2y	-zy		2y	zy
55τ		-y			-yz		-z	yz
56τ		-y						
57τ		x			xz		-2y	-xy
58τ		z		z	zz		z	zz
59τ								
60τ		y			yz		2y	yy
61τ		z			zz		-z	-zz
62τ		z						
63τ		x		2y	xy		-2y	-xy
64τ					zz		z	-zz
65τ		-z			zz			-zz
66τ		y		-z	-yz		2y	yy
67τ								
68τ		-z			zz		-z	zz
69τ		x		2y	xy		-2y	-xy
70τ		y						
71τ		-y		z	-yz		z	-yz
72τ		z			zz			zz

Figure 3.21. Evolution of I-S dipolar coupling term in the effective Hamiltonian using dec10x and dec22x heteronuclear decoupling schemes.
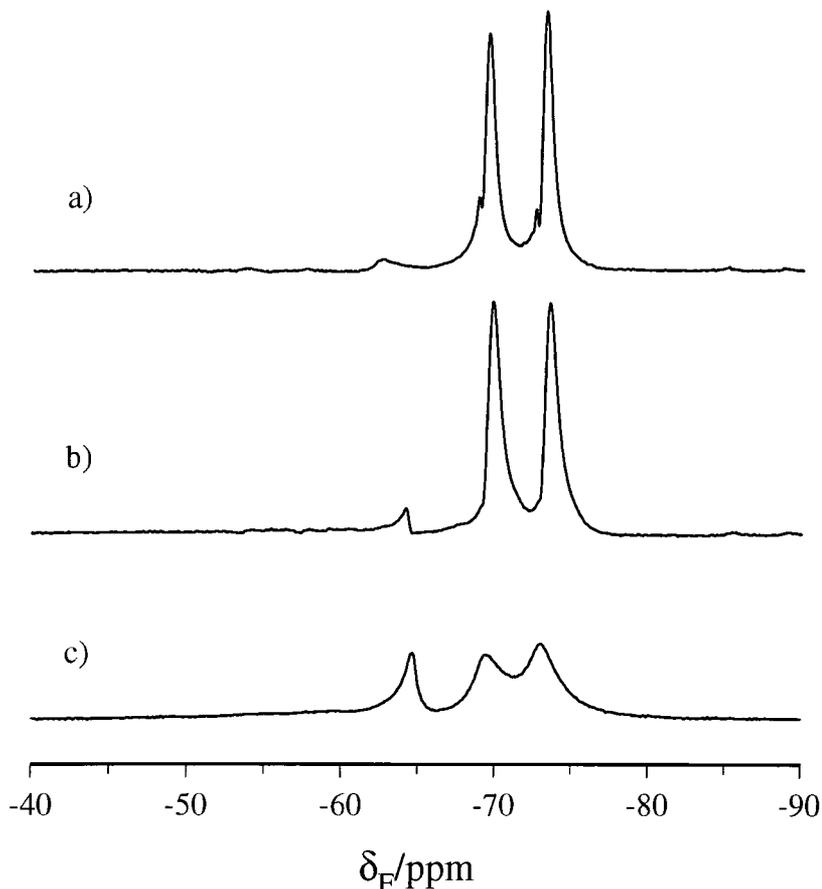
Figure 3.22. Fluorine-19 CRAMP spectra of NH₄PF₆ acquired using a) 2×BR-24 on
^{19}F *and 22×180° pulses on* ^{1}H *(dec22x), b) 2×BR-24 on* ^{19}F *and 6×180° pulses on* ^{1}H
(dec6x), and c) 2×BR-24 on ^{19}F *and 2×180° pulses on* ^{1}H *(dec2x). The 'peak' at*
-65 ppm is an artefact arising from transmitter positioning.

The major disadvantage of the 2×BR-24/heteronuclear decoupling sequences, particularly in their application to ^{19}F NMR, is that they drastically reduce the spectral width. This could be a big problem for static work or compounds which exhibit a wide range of chemical shifts. However, the improved 2×MREV-8/heteronuclear decoupling sequence in combination with sequences which allow the transmitter to be placed in the centre of the spectrum (quadrature detection),[66] as opposed to one side in conventional CRAMPS experiments, could have more potential in ^{19}F NMR. Due to the much narrower chemical shift range exhibited by ^{1}H, and hence the smaller spectral width required, the 2×BR-24/heteronuclear decoupling sequences (particularly in combination with quadrature detection) could have more application in ^{1}H NMR. The BR-24 sequences have been used to acquire

^{1}H CRAMP spectra of a ^{1}H- and ^{19}F- containing organic compound, with the resultant spectra being of higher resolution than those previously obtained using MREV-8.[73]

3.5 Dipolar dephasing

3.5.1 Spectral editing

The dipolar dephasing experiment in solid-state ^{13}C NMR, sometimes referred to as interrupted decoupling or non-quaternary suppression, is most frequently used as a spectral editing technique.[5] In its simplest form the pulse sequence is similar to the standard cross-polarisation sequence, except that a delay on both channels, in which no rf is applied, is inserted between the contact time and acquisition (Figure 3.23). Typically a delay, denoted tau, of 40 μs is used to remove signals arising from carbons which have strong dipolar interaction with protons, e.g. CH and CH_2. In contrast, signals from those carbons which have weak dipolar interactions with protons, e.g., CH_3 and quaternary carbons, are still present after tau. Hence, the evolution of the ^{13}C spins during tau under the heteronuclear dipolar interaction can be used to simplify complex spectra. Although further spectral editing sequences have been proposed[74-78] to distinguish between, for example, CH and CH_2, the dipolar dephasing experiment is the only one that is routinely used in most laboratories.

The duration of tau required in order for the signal of a particular nucleus to decay to zero is dependent upon the magnitude of the heteronuclear dipolar interaction. For host-guest compounds, due to the mobility of the guest molecules, carbon signals arising from these molecules take much longer to dephase than host signals. Similarly, longer dephasing times are needed to dephase non-bonded heteronuclear dipolar spin pairs than directly bonded. An example of this was found for ^{1}H-^{19}F spin pairs in which significantly longer dephasing times were required than that for directly bonded ^{13}C-^{1}H spin pairs. This was attributed to the fact that the distance dependent term was more dominant than the magnetogyric ratio term in the

expression for the heteronuclear dipolar interaction.[1] It has also been shown both experimentally and theoretically that for high-speed MAS experiments, the dipolar dephasing experiment may fail to give a null signal.[79]
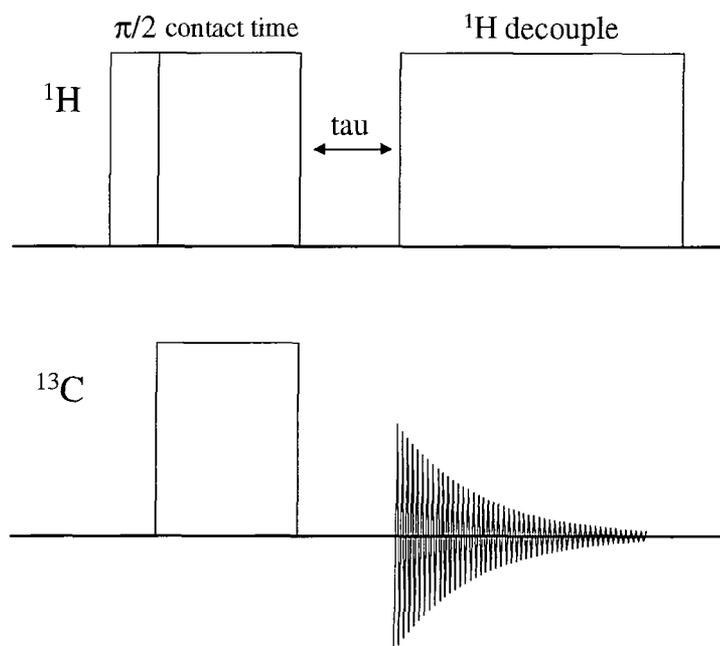
Figure 3.23. Dipolar dephasing pulse sequence.

So far it has been assumed that signals decay approximately exponentially to zero as a function of dephasing time. However, for some compounds at certain dephasing times the signal can become negative.[2,7] The reason for this can be explained if one considers a variable dephasing time experiment performed on an isolated I-S spin pair. During t_1 (tau) of such an experiment, the FID of the S spin is monitored under dipolar-coupled conditions. Therefore, if a negative signal is observed this means that on Fourier transformation, there will be a discernible dipolar splitting in the resultant spectrum.

3.5.2 Evolution of I-S dipolar interaction during tau

Typically in variable dephasing time experiments, the pulse sequence used is that illustrated in Figure 3.23, except that a rotor-synchronised 180° refocusing pulse

is applied to the S spins. If the sequence in Figure 3.23 is used, acquisition of the FID will start at a time tau after the contact time. Assuming quadrature detection, the complex FID for a single resonance can be described by,[80]

$$v(t) = A \exp[-i(\omega t + \theta)] \qquad\qquad Equation\ 3.15$$

where A is an amplitude parameter, ω describes the frequency, t defines time and θ describes the phase of the resonance. A zero-order phase correction can then be applied by,

$$v(t) = A \exp[-i(\omega t + \theta)] \exp[i\theta]$$

$$= A \exp[-i\omega t] \qquad\qquad Equation\ 3.16$$

However, for spectra containing many resonances, then the phase of each resonance is linearly dependent upon its frequency and so at time t, a first-order phase correction will also need to be applied. As acquisition starts at a different time t for each point in the second dimension with the pulse sequence in Figure 3.23, then a different first-order phase correction will need to be applied to each slice. However, if acquisition starts at time t=0, then only a zero-order phase correction needs to be applied. This condition can be met if a 180° pulse is applied to the S spins at a multiple of a rotor period (denoted t_m), which refocuses the evolution of the S spins under the chemical shifts and hence removes the frequency-dependent phase correction term (Figure 3.24). Importantly, the heteronuclear dipolar interaction is not refocused at time t=0 by virtue of the existence of the decoupling window.
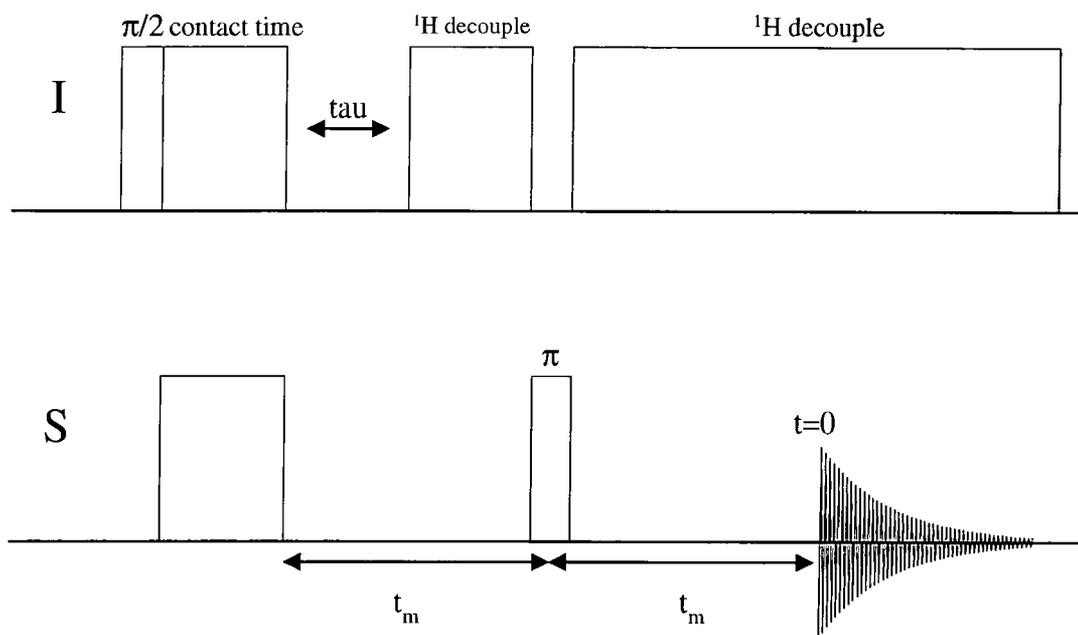
Figure 3.24. Dipolar dephasing pulse sequence with a 180° refocusing pulse applied to the S spins.

When the 180° pulse is applied to the S spins, no ^{1}H decoupling is applied as this would otherwise lead to cross polarisation and hence the information concerning the heteronuclear dipolar interaction encoded in the S spin may be lost. Another version of the pulse sequence in Figure 3.24 can be used in which the dephasing window is split either side of the 180° pulse.[81] This doubles the evolution time available without having to increase t_m in which signal loss occurs due to T_2 relaxation. However, the heteronuclear dipolar interaction would be refocused in this case and so a 180° pulse also has to be applied to the I spins at the same time as a 180° pulse is applied to the S spins. To prevent cross polarisation from occurring when the 180° pulses are applied simultaneously on both channels, their powers should be mismatched.

In the time denoted tau, the S spins evolve under their chemical shifts and heteronuclear dipolar interactions. As already stated, the chemical shift is refocused at time t=0, so in the following discussion chemical shift will be ignored. For an isolated I-S dipolar-coupled spin pair at a single orientation, θ, with respect to B_0, a doublet results in the S spin spectrum, due to coupling with an I spin which is parallel and antiparallel to B_0 ($m_I = +\frac{1}{2}$ and $m_I = -\frac{1}{2}$), at,

$$\nu = \nu_S \pm \frac{1}{2}D\left(1 - 3\cos^2\theta\right) \qquad \textit{Equation 3.17}$$

where ν_S is the frequency of the uncoupled S spin and D is the dipolar coupling constant. Therefore, in the rotating frame of the S spin, half of the S spins rotate clockwise and half anticlockwise which results in a net oscillation of the S spin magnetisation. However, for an S spin in the presence of a large number of I spins as for ^{13}C in an organic compound, usually this oscillation is not seen as the S spin magnetisation is lost to the proton spin bath.[82-84] However, in compounds in which the ^1H-^1H dipolar interactions are weakened, it may be possible to observe some oscillation in the S spin signal before its signal is lost to the protons. For MAS experiments, the angle θ and hence the heteronuclear dipolar interaction is time dependent. However, at multiples of a rotor period, this time dependence is removed and hence the heteronuclear dipolar interaction is refocused which results in the formation of rotational echoes.[81,85] Therefore, by varying tau, it is possible to obtain in F_2, S-spin spectra which contain information regarding the evolution of such spins under the heteronuclear dipolar interaction. Fourier transformation of t_1, yields heteronuclear dipolar spectra which are split into sidebands.

In order to obtain, for example, accurate ^{13}C-^1H[81,85] and ^{15}N-^1H[86,87] distance measurements in organic compounds, such a spin pair can be rendered isolated by suppressing the ^1H-^1H dipolar interactions during tau by Lee-Goldberg[88] decoupling or multiple-pulse sequences such as MREV-8.[60,61] Such homonuclear decoupling techniques also scale the heteronuclear dipolar interaction, and so this must be allowed for when calculating a distance parameter. This type of two-dimensional experiment in which chemical shift information is contained in F_2 and heteronuclear dipolar information is contained in F_1 is often known as separated local-field spectroscopy.[81,85-87]

3.5.3 Computer simulation of variable dephasing time experiments

The simulation of variable dephasing time experiments has been performed using the 'SIDE' computer program (see Appendix), which has been used in two

previous studies that looked at the effects of high-speed MAS[79] and SA[89] in dipolar-dephasing experiments. The 'SIDE' program is written in Turbo Pascal and simulates the dephasing of a ^{13}C-^{1}H spin pair in a powder sample undergoing MAS. The program works by first creating an array which describes 256 initial orientations of a ^{13}C-^{1}H vector with respect to the MAS axis. The dipolar splitting for each element in the array is calculated using Equation 3.17 and then the phase angle accumulated by each vector is determined, typically at 5 μs intervals, during the dephasing time. The magnitude of each vector is calculated and the resulting values are weighted to allow for a statistical distribution of ^{13}C-^{1}H orientations in a powder. Finally, the ^{13}C signal intensity is obtained at a given dephasing time by summing over all 256 initial orientations. The effect of spin diffusion between protons during the dephasing time can readily be incorporated by changing the sign of D with the application of 180° pulses. In the simulations presented in this chapter, the signal intensity as a function of dephasing time and each of the three important variables has been plotted. Such plots can be considered as showing data which have been Fourier transformed in one dimension only, i.e. F_2.

In many variable dephasing time experiments, it is not possible to see any oscillation of the signal during tau. Instead, the signal simply decays to zero due to flip-flop fluctuations among the I spins. The effect of spin diffusion can be simulated using the 'SIDE' program by varying the number of sign changes that occur during the dephasing time. The 'position' of the sign changes, and hence the time at which a 180° pulse is applied, during the dephasing time is input from a table of random numbers. A larger number of sign changes equates to greater spin diffusion among the proton spins. In the simulation shown in Figure 3.25, the typical parameters used were: MAS rate, 4 kHz; ^{13}C-^{1}H bond length, 1.1 Å; step size, 5 μs; number of steps, 256; number of runs, 250; number of sign changes, 0-32. It can be seen that with no spin diffusion, i.e. zero sign changes per run, the signal clearly oscillates and at multiples of a rotor period, every 250 μs, the signal is refocused. With no spin diffusion, the signal should still decay due to T_2 relaxation during the dephasing time, although such an effect is not included within the simulation. As the number of sign changes increases, the number of observable rotor echoes decreases due to loss of signal to the proton spin bath. With the maximum number of sign changes allowed

using 'SIDE', no rotational echo can be observed because of rapid loss of magnetisation to the surrounding protons.

The effect of MAS on the dephasing of the signal has been considered by varying the MAS rate with a fixed spin diffusion rate and bond length. In the simulation shown in Figure 3.26, the typical parameters used were: MAS rate, 0-20 kHz; ^{13}C-^{1}H bond length, 1.1 Å; step size, 5 μs; number of steps, 256; number of runs, 250; number of sign changes, 8. Obviously, as the MAS rate increases, rotor echoes occur at shorter dephasing times. Therefore, at higher MAS rates, it is possible to see more rotational echoes, before the ^{13}C magnetisation is lost to the protons via spin diffusion, than at lower MAS rates. The effect of bond length upon dephasing has been examined in Figure 3.27 using typical parameters of: MAS rate, 4 kHz; ^{13}C-^{1}H bond length, 0.2-2.0 Å; step size, 5 μs; number of steps, 256; number of runs, 250; number of sign changes, 8. It can clearly be seen that as the bond length is increased the rate of signal decay decreases to such an extent that spin diffusion becomes the dominating factor and so no rotational echoes are observable.

using 'SIDE', no rotational echo can be observed because of rapid loss of magnetisation to the surrounding protons.

The effect of MAS on the dephasing of the signal has been considered by varying the MAS rate with a fixed spin diffusion rate and bond length. In the simulation shown in Figure 3.26, the typical parameters used were: MAS rate, 0-20 kHz; ^{13}C-^{1}H bond length, 1.1 Å; step size, 5 μs; number of steps, 256; number of runs, 250; number of sign changes, 8. Obviously, as the MAS rate increases, rotor echoes occur at shorter dephasing times. Therefore, at higher MAS rates, it is possible to see more rotational echoes, before the ^{13}C magnetisation is lost to the protons via spin diffusion, than at lower MAS rates. The effect of bond length upon dephasing has been examined in Figure 3.27 using typical parameters of: MAS rate, 4 kHz; ^{13}C-^{1}H bond length, 0.2-2.0 Å; step size, 5 μs; number of steps, 256; number of runs, 250; number of sign changes, 8. It can clearly be seen that as the bond length is increased the rate of signal decay decreases to such an extent that spin diffusion becomes the dominating factor and so no rotational echoes are observable.

Figure 3.25. Variable dephasing time experiment as a function of spin diffusion at a MAS rate of 4 kHz.
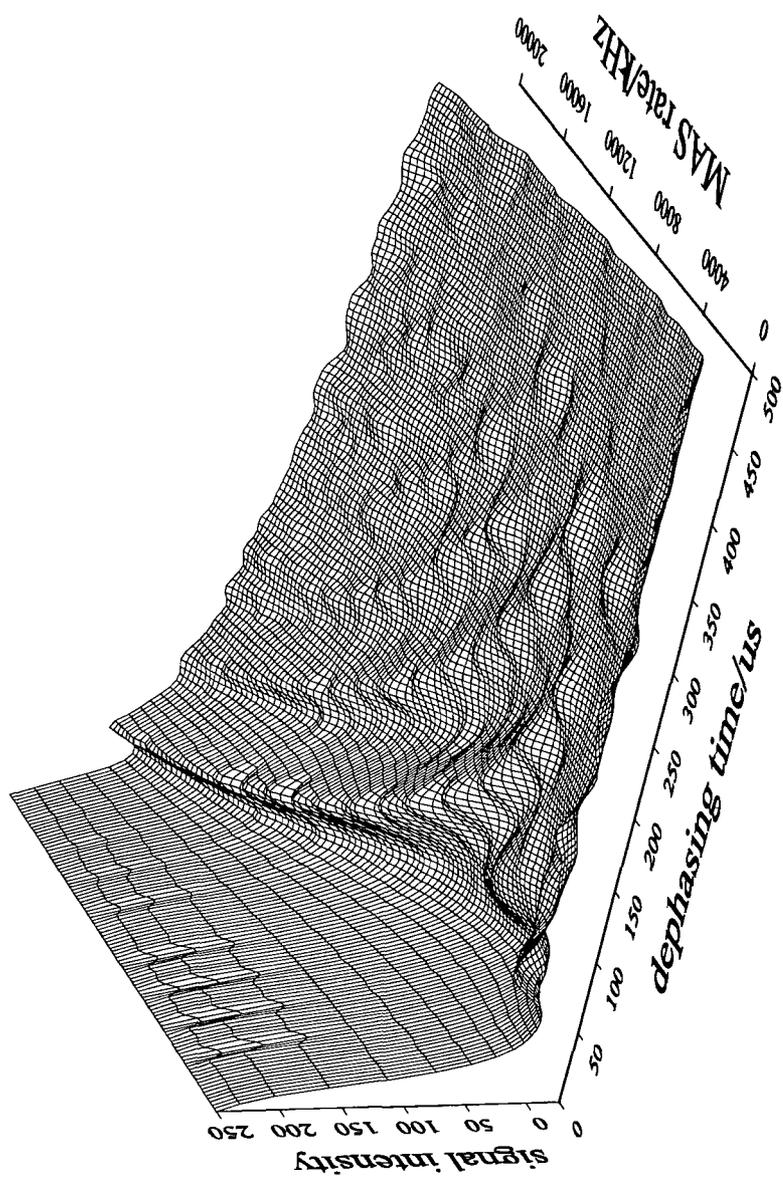
Figure 3.26. Variable dephasing time experiment as a function of MAS rate.
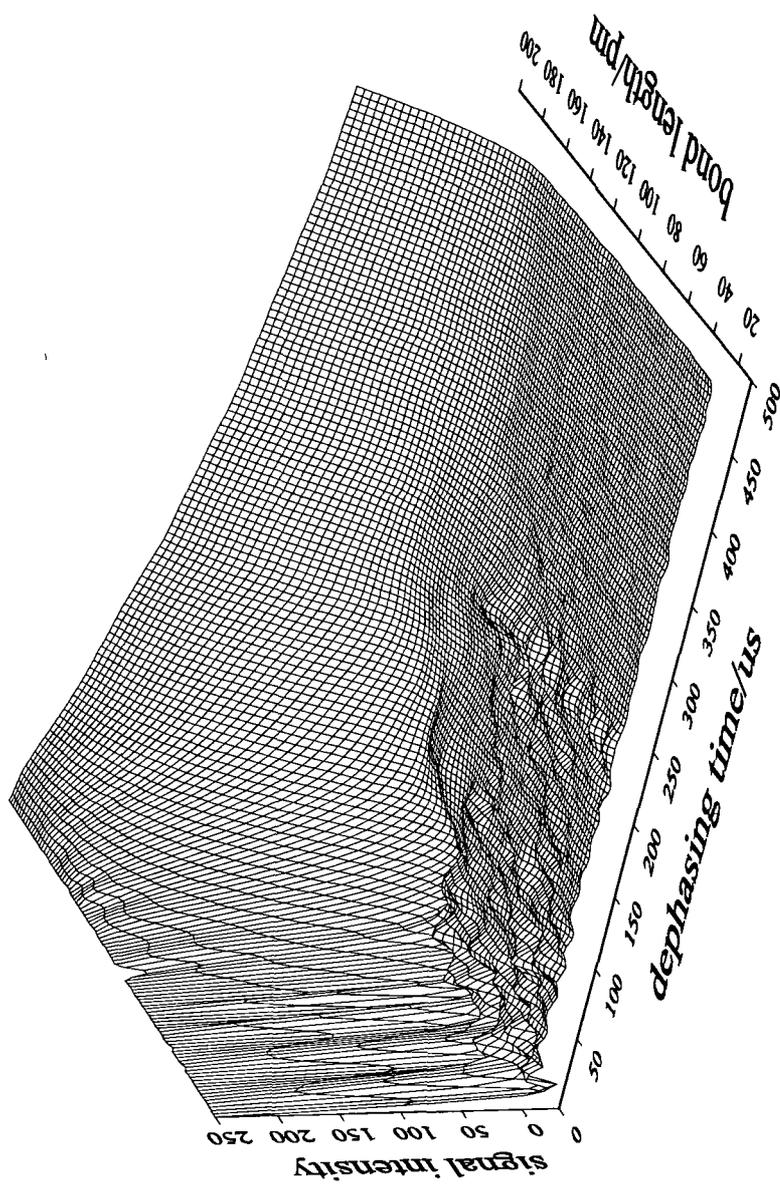
Figure 3.27. Variable dephasing time experiment as a function of ^{13}C-^{1}H bond length.

3.5.4 Variable dephasing time experiment performed on β-cyclodextrin

A variable dephasing time experiment was first performed on the β-cyclodextrin/benzaldehyde inclusion compound. It was found that at certain dephasing times, some of the host signals were negative. To investigate this further, a variable dephasing time experiment was performed on the host compound, β-cyclodextrin (Figure 3.28), although it is likely that the cavity does in fact contain water.
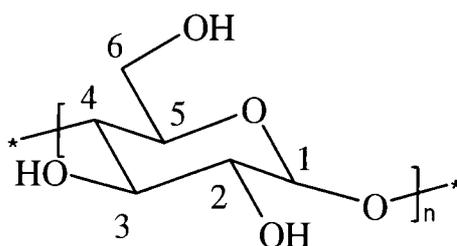
Figure 3.28. Numbering used to identify carbons in a single glucose unit. Seven of these units form a β-cyclodextrin ring.

The ^{13}C CP/MAS spectrum of β-cyclodextrin is shown in Figure 3.29. The spectral conditions used were: π/2 pulse duration, 5 μs; contact time, 2 ms; recycle delay, 2 s; ^{1}H decoupling power, 50 kHz; MAS rate, 4 kHz; number of transients, 512; acquisition time, 102.4 ms. The peaks in the region of 60-64 ppm, 79-84 ppm and 102-104 ppm can be attributed to C6, C4 and C1 respectively. The most intense group of peaks in the 72-76 ppm region can be attributed to C2, C3 and C5. In principle, if there is only one β-cyclodextrin molecule in the crystallographic unit cell, then one might expect to observe up to seven signals per carbon. However, as chemical shift differences are small relative to the linewidths achieved, then not all signals are visible.
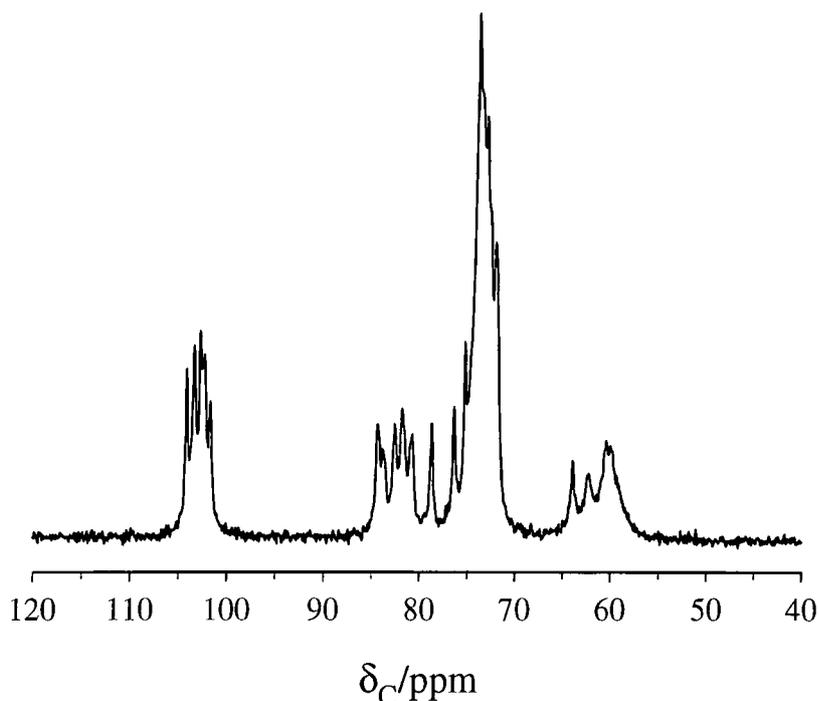
Figure 3.29. $^1H \rightarrow ^{13}C$ CP/MAS spectrum of β-cyclodextrin at 4 kHz.

A variable dephasing time experiment was then performed using the pulse sequence shown in Figure 3.24. The same spectral conditions were used as in the acquisition of Figure 3.29 except: number of transients per slice, 1728; ^{13}C π pulse duration, 7.6 μs; initial value of tau, 0.1 μs; dwell in the 2nd dimension, 10 μs; t_m, 500 μs; number of slices, 50. Stacked plots of the data obtained after Fourier transformation of t_2 and of both t_2 and t_1 are shown in Figure 3.30 and Figure 3.31, respectively. In order to obtain the pure absorption lineshape (see Chapter 6 for a more detailed discussion) in Figure 3.31, the t_2 dimension was first Fourier transformed and phased to give,[90]

$$S(t_1, \omega_2) = \frac{1}{2}\left[\exp(i\Omega_1 t_1) + \exp(-i\Omega_1 t_1)\right]\left[A_2 + iD_2\right] \qquad Equation\ 3.18$$

where A and D are absorption and dispersive Lorentzians, Ω denotes the angular frequency, t denotes time and the subscript denotes the dimension. The imaginary part of the spectrum was then replaced with zeros (using the 'Zero Imag' command in the processing panel of Spinsight), such that

$$S(t_1, \omega_2) = \frac{1}{2}\left[\exp(i\Omega_1 t_1) + \exp(-i\Omega_1 t_1)\right]A_2 \qquad Equation\ 3.19$$

and a complex Fourier transform was applied to t_1 to give,

$$S(\omega_1,\omega_2) = \frac{1}{2}\left[A_1^+ + iD_1^+ + A_1^- + iD_1^-\right]A_2 \qquad \text{Equation 3.20}$$

The real part of the spectrum can then be described by,

$$Re\left[S(\omega_1,\omega_2)\right] = \frac{1}{2}\left[A_1^+ A_2 + A_1^- A_2\right] \qquad \text{Equation 3.21}$$

which represents a pure absorption lineshape but with the spectrum symmetrical about $\omega_1=0$. An alternative method to symmetrising the spectrum to obtain pure absorption lineshapes involves acquiring a 'normal' data set and a second 'time reversed' data set.[91]
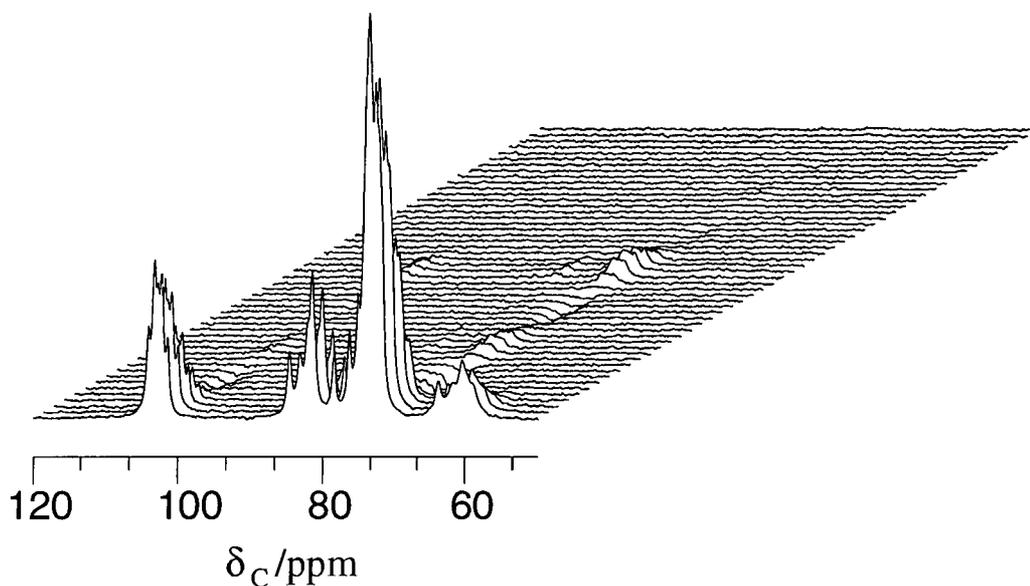
Figure 3.30. Variable dephasing time experiment (t_1, F_2) performed on β-cyclodextrin with the ^{13}C chemical shift spectrum and the ^{13}C-^1H dipolar FID given in the F_2 and t_1 dimensions, respectively. The dephasing time varies, from front to back, from 0.1 μs to 500.1 μs with slices plotted at 10 μs intervals.
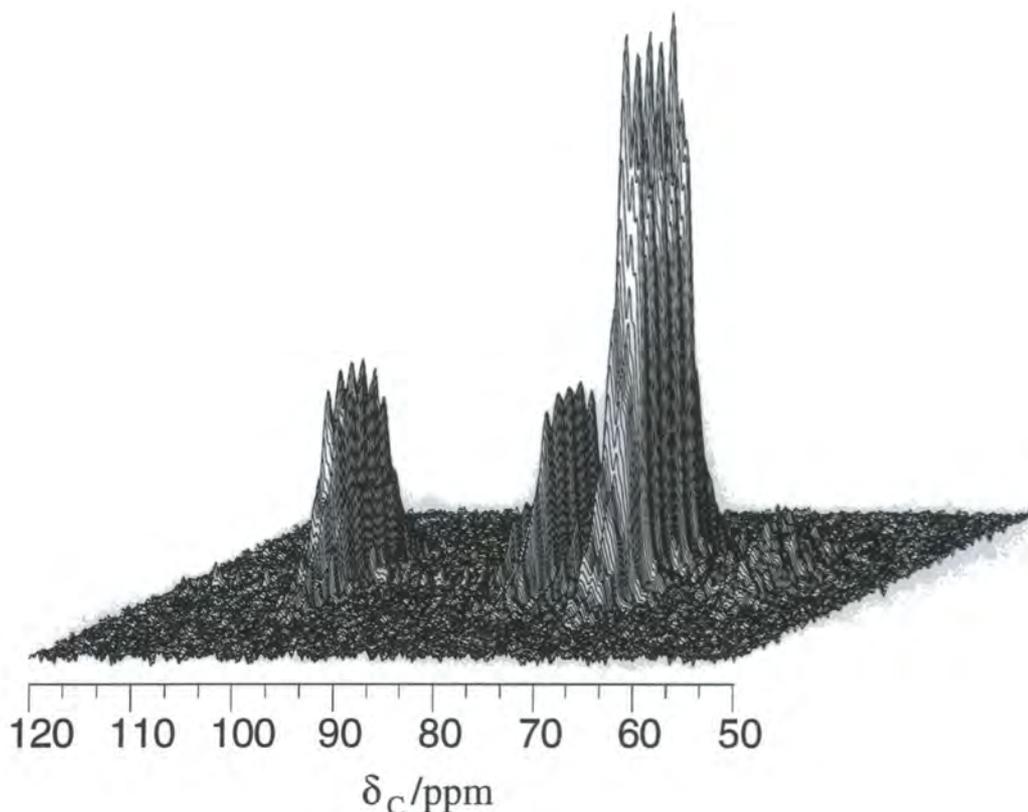
Figure 3.31. Variable dephasing time experiment (F_1, F_2) performed on β-cyclodextrin with the ^{13}C chemical shift and ^{13}C-^1H dipolar spectra given in the F_2 and F_1 dimensions, respectively.

In Figure 3.30, rotational echoes are observable for all carbon signals except for the C6 signal. This signal arises from a CH_2 and therefore it is not surprising that this signal has decayed to zero, due to the effects of spin diffusion among the protons, before a rotational echo can be observed. However, it is not possible to see any signs of the appearance of a second rotational echo in the last slice (tau=500.1 μs), as a result of the effects of spin diffusion among the protons. For all the CH carbons in β-cyclodextrin, it is possible to see a damped dipolar oscillation. This can be attributed to the rather isolated nature of ^1H-^{13}C spin pairs, which is presumably contributed to by the ring shape of the molecule. A ^1H spectrum of β-cyclodextrin is shown in Figure 3.32 and it can be seen that there is a relatively

narrow (fwhh of central peak ~ 1.5 kHz) peak superimposed on a much broader signal. The spectral conditions used were: ^{1}H $\pi/2$ pulse duration, 5.0 μs; recycle delay, 2 s; MAS rate, 4 kHz; number of transients; 128; acquisition time, 10.2 ms. However, in a ^{1}H-^{13}C WISE[92] spectrum obtained of β-cyclodextrin,[93] there was no narrow peak present in the ^{1}H dimension, suggesting that the source of this peak is water. On summing all the slices in the ^{1}H dimension, a broad featureless peak (fwhh ~ 40 kHz), comparable to the broad peak in Figure 3.32, was obtained suggesting that the source of this peak is β-cyclodextrin. This implies that the ^{1}H-^{1}H dipolar interactions are relatively strong, although the flip-flop fluctuations among the protons are obviously not so rapid such that no ^{13}C-^{1}H dipolar splittings can be observed.

250   200   150   100   50   0   -50   -100   -150   -200   -250

δ_H/ppm
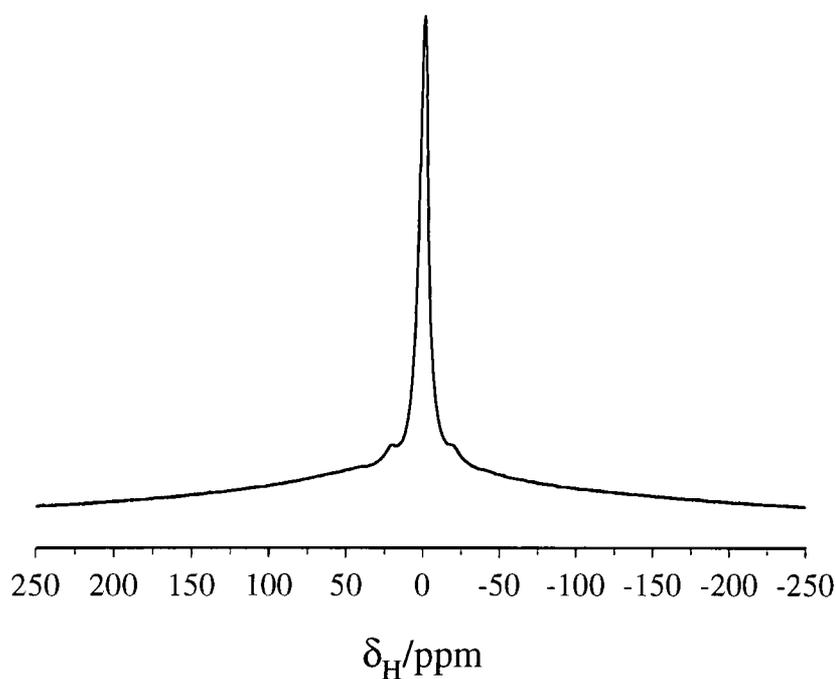
Figure 3.32. ^{1}H MAS spectrum of β-cyclodextrin acquired at 4 kHz.

In principle, it is possible to obtain distance information from slices of Figure 3.31 taken parallel to F_1. Due to the number of peaks associated with a particular carbon, spectra were obtained by summing slices over the range of chemical shifts exhibited by a particular carbon. The spectra obtained experimentally, which are not plotted on the same vertical expansion, are shown on the left in Figure 3.33.

Simulated spectra were obtained by importing the FID created by the 'SIDE' program into a Mathcad[94] sheet and Fourier transforming these data. The experimental data were then 'fitted' by comparing them with simulated data 'by eye'. The 'fitting' of such data is complex as spin diffusion effects must be included into the simulations. As the dominant heteronuclear dipolar interaction will be between directly bonded spin pairs, the ^{13}C-^1H bond length in the simulations was set at 1.1 Å. Therefore, the main parameters that were varied were the number of sign changes and the amount of line broadening applied. Not surprisingly, the dipolar spectrum of C6 shows the least structure and, in order to 'fit' the spectrum, the maximum possible number of sign changes was needed, i.e. 32, and line broadening of ~ 400 Hz was applied. Clearly, there will be loss of signal due to the ^1H-^1H dipolar interactions and also it is worth remembering that the program only allows for dephasing of the ^{13}C signal by one ^1H and so it is not surprising that such large dampening factors were needed. It would have been possible to 'fit' the experimental data using a shorter bond length, but this would have had little meaning in reality. The dipolar spectra of C1 and C4 are comparable, which is not surprising considering that their sites in the glucose ring are quite similar. The best 'fit' spectrum was obtained with 10 sign changes and of the order of 800 Hz line broadening was applied. It is the dipolar spectrum of the C2, C3, C5 carbons which contains the most structure as a result of the clearly visible dipolar oscillation and rotational echo in Figure 3.30. Dipolar sidebands are also present which are separated by the MAS rate (4 kHz). The best 'fit' was obtained using 16 sign changes and 100 Hz of line broadening was applied.

It is difficult to obtain anything quantitative regarding the precise number of sign changes required to 'fit' the experimental data. The effect of applying line broadening and increasing the number of sign changes has the same effect on the dipolar FID, in that they both increase the decay rate of the signal. However, of the two parameters varied it is the number of sign changes which has the major effect on the appearance of the spectrum and hence qualitative conclusions can be drawn from the results. It can be seen that there are three basic lineshapes for the dipolar spectra. The CH_2 spectrum (C6) shows the least structure and consequently required the most sign changes per run. The C2, C3, C5 CH dipolar spectrum and the C1/C4 spectra required far fewer sign changes, which is as expected for CH's compared to a CH_2.

The dipolar spectra of the C1/C4 CH required more sign changes than the C2, C3, C5 dipolar spectra and hence although the former show some evidence of dipolar sidebands they are not as evident as in the C2, C3, C5 dipolar spectrum.

a)

b)

c)

d)

50 30 10 -10 -30 -50   50 30 10 -10 -30 -50
      /kHz   /kHz
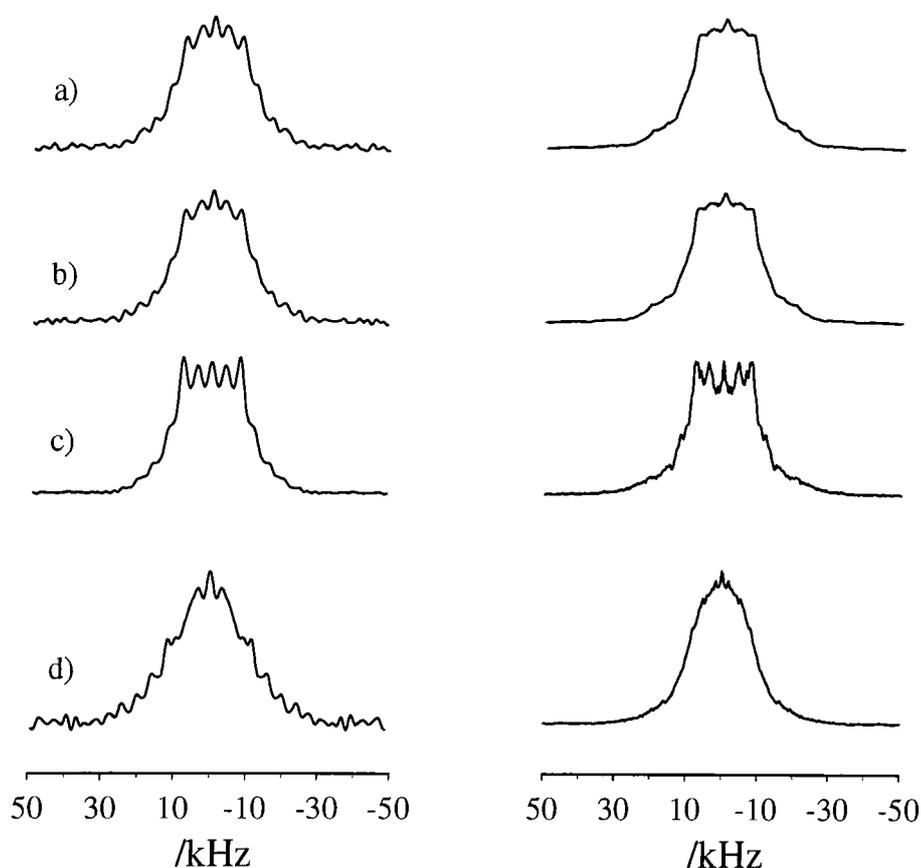
Figure 3.33. Comparison of experimental (left) and simulated (right) heteronuclear dipolar spectra for a) C1, b) C4, c) C2, C3, C5 and d) C6.

However, if spin diffusion among the protons could be eliminated, by for example application of homonuclear multiple-pulse decoupling during the dephasing time, then the validity of assuming a bond length of 1.1 Å could be checked. It would also be worth altering the 'SIDE' program, such that dephasing from more than one proton could be allowed for. Although 'SIDE' has been used to examine the dephasing of a ^{13}C-^{1}H spin pair in this case, it could very easily be altered to look at the dephasing of spin pairs such as ^{19}F-^{1}H and ^{15}N-^{1}H.

3.6 Conclusions

From the results presented, it is clear that the mobility of the guest molecules can affect routinely applied techniques such as cross polarisation, dipolar decoupling and dipolar dephasing. Therefore, it is important to understand the results obtained before performing more complicated experiments, for example, to obtain structural information. In cases where efficient cross polarisation can occur only at discrete matching conditions, it has been demonstrated that the ramped-amplitude cross polarisation experiment is more favourable than the single-amplitude cross polarisation experiment. The TPPM decoupling sequence can reduce the linewidths obtained, compared to those attainable via continuous irradiation techniques, when the decoupling efficiency is reduced by mobility or the required decoupling powers cannot be achieved. It is also important to note that for systems in which there exists essentially isolated heteronuclear dipolar interactions, the decoupling power should not be set to a multiple of the MAS rate in order to avoid the possibility of rotational resonance recoupling.

Dipolar dephasing experiments are most frequently used as a spectral editing technique to remove, for example, CH and CH_2 signals from a ^{13}C spectrum. However, as demonstrated for β-cyclodextrin, signals may become negative rather than simply decay to zero and in such cases, structural information may be attainable. In the acquisition of spectra of abundant spins, such as ^{1}H or ^{19}F, which exhibit both homonuclear and heteronuclear dipolar couplings, it has been shown that the BR-24 sequence can be used in combination with 180° pulses to remove both interactions simultaneously.

3.7 References

1. S.A. Carss, U. Scheler, R.K. Harris, P. Holstein and R.A. Fletton, *Magn. Reson. Chem.*, 1996, **34**, 63.

2. S.A. Carss, *Ph.D. Thesis*, University of Durham, 1995.

3. E.O. Stejskal, J. Schaefer and J.S. Waugh, *J. Magn. Reson.*, 1977, **28**, 105.

4. A.E. Bennett, C.M. Rienstra, M. Auger, K.V. Lakshmi and R.G. Griffin, *J. Chem. Phys.*, 1995, **103**, 6951.

5. S.J. Opella and M.H. Frey, *J. Am. Chem. Soc.*, 1979, **101**, 5854.

6. J.A. Ripmeester, *J. Inclusion Phenomena*, 1988, **6**, 31.

7. L.B. Alemany, D.M. Grant, T.D. Alger and R.J. Pugmire, *J. Am. Chem. Soc.*, 1983, **105**, 6697.

8. U. Scheler, P. Holstein, S.A. Carss and R.K. Harris, *Chemagnetics Application Note*, May 1995.

9. S. Hafner and H.W. Spiess, *J. Magn. Reson., A*, 1996, **121**, 160.

10. D.E. Demco, S. Hafner and H.W. Spiess, *J. Magn. Reson., A*, 1995, **116**, 36.

11. U. Haeberlen, *High Resolution NMR in Solids*, Academic Press, New York, 1976.

12. M.M. Maricq and J.S. Waugh, *J. Chem. Phys.*, 1979, **70**, 3300.

13. A. Pines, M.G. Gibby and J.S. Waugh, *J. Chem. Phys.*, 1973, **59**, 569.

14. R.K. Harris, *Multinuclear Magnetic Resonance in Liquids and Solids - Chemical Applications*, (Editors: P. Granger and R.K. Harris), NATO ASI, Maratea, 1988.

15. D.P. Burum, 'Cross Polarisation in Solids', *Encylopedia of NMR*, (Editors: D.M. Grant and R.K. Harris), Wiley, London, 1996, **3**, 1535.

16. S.R. Hartmann and E.L. Hahn, *Phys. Rev.*, 1992, **128**, 2042.

17. F. Engeke, 'Cross Polarisation in Rotating Solids: Spin-½ Nuclei', *Encylopedia of NMR*, (Editors: D.M. Grant and R.K. Harris), Wiley, London, 1996, **3**, 1529.

18. M. Sardashti and G.E. Maciel, *J. Magn. Reson.*, 1987, **72**, 467.

19. R.C. Zeigler, R.A. Wind and G.E. Maciel, *J. Magn. Reson.*, 1988, **79**, 299.

20. S. Hediger, B.H. Meier and R.R. Ernst, *Chem. Phys. Lett.*, 1993, **213**, 627.

21. X. Wu and K.W. Zilm, *J. Magn. Reson., A*, 1993, **104**, 154.

22. H. Geen, J.J. Titman and H.W. Spiess, *Chem. Phys. Lett.*, 1993, **213**, 145.

23. S. Hediger, B.H. Meier and R.R. Ernst, *J. Chem. Phys.*, 1995, **102**, 4000.

24. O.B. Peersen, X. Wu, I. Kustanovich and S.O. Smith, *J. Magn. Reson., A*, 1993, **104**, 334.

25. O.B. Peersen, X. Wu and S.O. Smith, *J. Magn. Reson., A*, 1994, **106**, 127.

26. G. Metz, X. Wu and S.O. Smith, *J. Magn. Reson., A*, 1994, **110**, 219.

27. G. Metz, M. Ziliox and S.O. Smith, *Solid State NMR*, 1996, **7**, 155.

28. S. Hediger, B.H. Meier, N.D. Kurur, G. Bodenhausen and R.R. Ernst, *Chem. Phys. Lett.*, 1994, **223**, 283.

29. S. Hediger, B.H. Meier and R.R. Ernst, *Chem. Phys. Lett.*, 1995, **240**, 449.

30. A.C. Kolbert and A. Bielecki, *J. Magn. Reson., A*, 1995, **116**, 29.

31. S. Hediger, P. Signer, M. Tomaselli, R.R. Ernst and B.H. Meier, *J. Magn. Reson.*, 1997, **125**, 291.

32. D. Marks and S. Vega, *J. Magn. Reson., A*, 1996, **118**, 157.

33. S. Ding, C.A. McDowell and C. Ye, *J. Magn. Reson., A*, 1994, **109**, 6.

34. L. Müller, A. Kumar, T. Baumann and R.R. Ernst, *Phys. Rev. Lett.*, 1974, **32**, 1402.

35. R. Pratima and K.V. Ramanathan, *J. Magn. Reson., A*, 1996, **118**, 7.

36. F. Tian and T.A. Cross, *J. Magn. Reson.*, 1997, **125**, 220.

37. G.E. Hawkes, M.D. Mantle, K.D. Sales, S. Aime, R. Gobetto and C.J. Groombridge, *J. Magn. Reson., A*, 1995, **116**, 251.

38. J.V. Hanna and M.A. Wilson, *J. Phys. Chem.*, 1992, **96**, 6518.

39. M. Mehring, *High Resolution NMR in Solids*, (Editors: P.Diehl, E. Fluck and R. Kosfeld), Springer-Verlag, New York, 1976.

40. K. Schmidt-Rohr and H.W. Spiess, *Multidimensional Solid-state NMR and Polymers*, Academic Press, London, 1994.

41. M. Mehring and G. Sinning, *Phys. Rev. B*, 1977, **15**, 2519.

42. G. Sinning, M. Mehring and A. Pines, *Chem. Phys. Lett.*, 1976, **43**, 382.

43. I.J. Shannon, K.D.M. Harris and S. Arumugam, *Chem. Phys. Lett.*, 1992, **196**, 588.

44. D.L. Vanderhart, W.L. Earl and A.N. Garroway, *J. Magn. Reson.*, 1981, **44**, 361.

45. A.N. Garroway, D.L. Vanderhart and W.L. Earl, *Phil. Trans. R. Lond. A*, 1981, **299**, 609.

46. P. Tekely, P. Palmas and D. Canet, *J. Magn. Reson., A*, 1994, **107**, 129.

47. Z. Gan and R.R. Ernst, *Solid State NMR*, 1997, **8**, 153.

48. Z. Gan and D.M. Grant, *Chem. Phys. Lett.*, 1990, **168**, 304.

49. D.P. Raleigh, M.H. Levitt and R.G. Griffin, *Chem. Phys. Lett.*, 1988, **146**, 71.

50. Z. Gan, D.M. Grant and R.R. Ernst, *Chem. Phys. Lett.*, 1996, **254**, 349.

51. A.C. Kolbert, D.P. Raleigh, R.G. Griffin and M.H. Levitt, *J. Magn. Reson.*, 1990, **89**, 133.

52. T.G. Oas, R.G. Griffin and M.H. Levitt, *J. Chem. Phys.*, 1988, **89**, 692.

53. M.H. Levitt, T.G. Oas and R.G. Griffin, *Israel J. Chem.*, 1988, **28**, 271.

54. D.P Raleigh, A.C. Kolbert, T.G. Oas, M.H. Levitt and R.G. Griffin, *J. Chem. Soc., Faraday Trans. 1*, 1988, **84**, 3691.

55. J.R. Garbow and T. Gullion, *Carbon-13 NMR Spectroscopy of Biological Systems*, (Editor: N. Beckmann), Academic Press, London, 1995, Chapter 3.

56. K. Takegoshi, K. Takeda and T. Terao, *Chem. Phys. Lett.*, 1996, **260**, 331.

57. T. Nakai and C.A. McDowell, *Chem. Phys. Lett.*, 1994, **227**, 639.

58. S.A. Vierkötter, *J. Magn. Reson., A*, 1996, **118**, 84.

59. J.S. Waugh, L.M. Huber and U. Haeberlen, *Phys. Rev. Lett.*, 1968, **20**, 180.

60. P. Mansfield, *J. Phys. C; Solid State Phys.*, 1971, **4**, 1444.

61. W.K. Rhim, D.D. Elleman, R.W. Vaughan, *J. Chem. Phys.*, 1973, **59**, 3740.

62. D.P. Burum and W.K. Rhim, *J. Chem. Phys.*, 1979, **71**, 944.

63. B.C. Gerstein, *Phil. Trans. R. Soc. Lond. A*, 1981, **299**, 521.

64. P. Van Hecke, H.W. Spiess and U. Haeberlen, *J. Magn. Reson.*, 1976, **22**, 103.

65. U. Scheler and R.K. Harris, *Chem. Phys. Lett.*, 1996, **262**, 137.

66. D.P. Burum, D.G. Cory, K.K. Gleason, D. Levy and A. Bielecki, *J. Magn. Reson., A*, 1993, **104**, 347.

67. E. Hughes, unpublished work.

68. J.G. Powles and J.H. Strange, *Proc. Phys. Soc.*, 1963, **82**, 60.

69. E.L. Hahn, *Phys. Rev.*, 1950, **80**, 580.

70. P. Mansfield, *Phil. Trans. R. Soc. Lond. A*, 1981, **299**, 479.

71. E. Hughes and A. Nordon, unpublished work.

72. E. Hughes, personal communication.

73. S.C. Campbell, personal communication.

74. J.S. Hartman and J.A. Ripmeester, *Chem. Phys. Lett.*, 1990, **168**, 219.

75. R.H. Newman and L.M. Condron, *Solid State NMR*, 1995, **4**, 259.

76. D.P. Burum and A. Bielecki, *J. Magn. Reson.*, 1991, **95**, 184.

77. R. Sangill, N. Rastrup-Andersen, H. Bildsøe, H.J. Jakobsen and N.C. Nielsen, *J. Magn. Reson., A*, 1994, **107**, 67.

78. X. Wu, S.T. Burns and K.W. Zilm, *J. Magn. Reson., A*, 1994, **111**, 29.

79. R.H. Newman, *J. Magn. Reson.*, 1990, **86**, 176.

80. D.D. Traficante, *Concepts Magn. Reson.*, 1990, **2**, 151.

81. M.G. Munowitz, R.G. Griffin, G. Bodenhausen and T.H. Huang, *J. Am. Chem. Soc.*, 1981, **103**, 2529.

82. R.K. Hester, J.L. Ackerman, B.L. Neff and J.S. Waugh, *Phys. Rev. Lett.*, 1976, **36**, 1081.

83. R.K. Hester, J.L. Ackerman, V.R. Cross and J.S. Waugh, *Phys. Rev. Lett.*, 1975, **34**, 993.

84. R.K. Hester, V.R. Cross, J.L. Ackeramn and J.S. Waugh, *J. Chem. Phys.*, 1975, **63**, 3606.

85. R.G. Griffin, G. Bodenhausen, R.A. Haberkorn, T.H. Huang, M. Munowitz, R. Osredkar, D.J. Ruben, R.E. Stark and H. Van Willigen, *Phil. Trans. R. Soc. Lond. A*, 1981, **299**, 547.

86. J.A. DiVerdi and S.J. Opella, *J. Am. Chem. Soc.*, 1982, **104**, 1761.

87. J.E. Roberts, G.S. Harbison, M.G. Munowitz, J. Herzfeld and R.G. Griffin, *J. Am. Chem. Soc.*, 1987, **109**, 4163.

88. M. Lee and W.I. Goldberg, *Phys. Rev.*, 1965, **140**, 1261.

89. R.H. Newman, *J. Magn. Reson.*, 1992, **96**, 370.

90. J. Keeler and D. Neuhaus, *J. Magn. Reson.*, 1985, **63**, 454.

91. M.G. Munowitz and R.G. Griffin, *J. Chem. Phys.*, 1983, **78**, 613.

92. K. Schmidt-Rohr, J. Clauss and H.W. Spiess, *Macromolecules*, 1992, **25**, 3273.

93. A. Nordon and U. Scheler, unpublished work.

94. Mathcad PLUS 6.0, Mathsoft Inc., USA.

Chapter 4

Solid-state NMR studies of 2-hydroxyalkane/urea inclusion compounds

4.1 Introduction

In urea inclusion compounds, the urea (host) is extensively hydrogen-bonded to form linear, parallel tunnels.[1-3] The tunnels are wide enough, 5.5-5.8 Å in diameter, to contain guest molecules[4] such as alkanes and substituted alkanes of a sufficient length and with minimal branching. The stability of the hexagonal tunnel structure relies upon the presence of guest molecules, which are normally packed within van der Waals contact of each other. If the guest molecules escape from the tunnels, the host reverts to a tetragonal structure. At low temperatures, the compounds are known to undergo a phase transition in which the host structure changes from being hexagonal to orthorhombic. In certain cases, the conventional urea tunnel structure can distort to accommodate guest molecules with bulky functional groups. The host structure in most cases does not significantly hinder the motion of the guest molecules. However, in alkanedione/urea inclusion compounds there are significant host-guest interactions,[1] which compensate for the resultant weaker host-host interactions.

It is possible to describe, separately, the structures of both the host and guest molecules, in spite of the fact that they exhibit considerable dynamic disorder, in terms of a three-dimensional lattice. Of particular importance is the relationship between the periodicities of the guest (c_g) and host (c_h) structures along the tunnel axis. Inclusion compounds in which $pc_g \approx qc_h$ where p and q are reasonably small integers, can be described as being commensurate. In comparison, when this relationship cannot be satisfied, such compounds are described as being incommensurate. The majority of urea inclusion compounds, and, in particular, the

systems studied in this and the ensuing chapter, are incommensurate. The periodicities of the guest and host structures can be determined using X-ray diffraction.[1,5] Such studies of inclusion compounds have revealed that c_g for linear alkanes is about 0.5 Å shorter than the value corresponding to the minimum guest-guest interaction energy, thus suggesting that the interaction between adjacent guest molecules is repulsive. A theoretical model has been developed to predict and understand the one-dimensional structure of urea inclusion compounds.[6] However, in some urea inclusion compounds, there is three-dimensional ordering of the guest molecules.[7] This interchannel ordering of guests is dependent upon functional group[2] and can be described via c_g and an additional parameter, Δ_g, which describes the offset along the tunnel axis between guests in adjacent tunnels.

In addition to studies concerning the periodic structural properties of urea inclusion compounds, there have been a number of investigations which have focused on local structural properties. In particular, the dynamics and conformation of guest molecules, end-group interactions between guests within the urea tunnels and the dynamics of the host molecules have been examined. Methods used to determine the dynamic properties of guest molecules are $T_1(^1H)$ measurements,[8] neutron scattering experiments,[1,2] residual dipolar coupling[9] measurements[10] and ^2H NMR lineshape studies.[11] Guest motions that have been identified for alkanes include reorientation about their long axis, torsional libration about the penultimate C-C bond, and rapid rotation of end methyl groups. Conformational properties of guest molecules have been studied via ^2H NMR lineshape analysis,[12-14] ^{13}C NMR chemical shifts,[15,16] ^1H-coupled ^{13}C MAS NMR,[17] ^{13}C-^1H dipolar spectra[18] and Raman spectroscopy.[19] The last-mentioned study will be discussed in more detail in Chapter 7 in relation to the results presented therein. However, the results from the aforementioned studies are somewhat in disagreement over whether the central part of the alkane chain adopts an all trans conformation or contains defects. There is also some debate over the proportion of guest end-groups adopting a gauche conformation.

Of particular interest is the ordering of unsymmetric guest molecules in the urea tunnels. When an unsymmetric guest molecule, $X(CH_2)_nY$, is included within the urea tunnels, the guest molecules can be oriented X---X, head to head (HH),

Y---Y, tail to tail (TT), or X---Y, head to tail (HT), as shown in Figure 4.2. With a purely statistical distribution of end-group interactions, the ratio of (HH+TT) to 2(HT) will be one. In perhydrotriphenylene (PHTP) inclusion compounds,[20] which contain tunnels with a wider diameter than urea, it is possible for rapid end-over-end exchange of some guest molecules to occur.[21] Therefore, the preference for a particular ordering of two adjacent molecules can provide a method of determining interaction energies. In comparison, in urea inclusion compounds, once the guest molecules are in the tunnels there is no possibility of guest reorientation with respect to end-group interactions between adjacent molecules. Therefore, the ordering of guest molecules in the urea tunnels may reveal information concerning the crystal growth process of such compounds. The ordering of guest molecules can be determined experimentally via solid-state NMR, due to its ability to probe local environments. Hence, in disordered solids, where the use of diffraction-based techniques is precluded from providing detailed structural information, NMR is the technique of choice. Theoretical models[22] based on the introduction of guest molecules sequentially and simultaneously into the urea tunnels have been developed to rationalise experimental results.

The dynamics of the urea molecules have been the subject of far fewer studies in comparison to the vast number focusing on guest dynamics. However, it is known that the urea molecules undergo 180° flips about the C=O bond (Figure 4.1), with a frequency of the order of MHz at ambient temperatures, from ^{2}H NMR studies.[23] It is believed that the host and guest motions are uncorrelated.
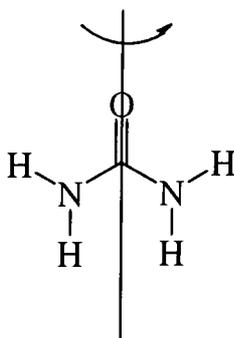
Figure 4.1. Illustration of the dynamic behaviour exhibited by urea.
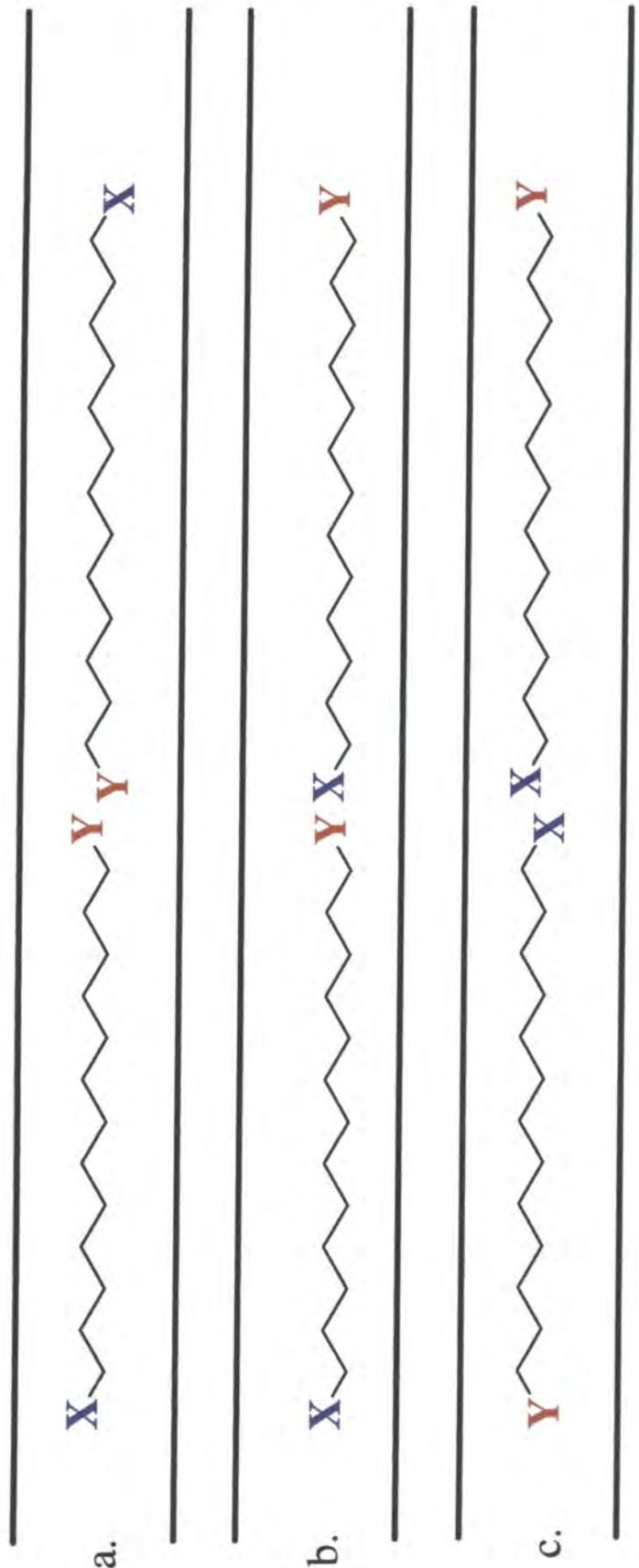
Figure 4.2. Schematic diagram showing unsymmetric guest molecules oriented a) tail to tail (TT), b) head to tail (HT) and c) head to head (HH) in the urea tunnels.

4.2 Determination of guest molecule ordering via solid-state ^{13}C NMR

Solid-state NMR can be used to determine the ordering of unsymmetric guest molecules in the urea tunnels. This is because end-groups in different environments can have different chemical shifts. Thus, for example, a head-to-tail orientation may have a different chemical shift in the 'head' region of the spectrum to a head-to-head orientation. However, for the two different intermolecular interactions to be distinguishable, the nucleus of choice must have a relatively large chemical shift range in comparison to the linewidth of the resulting peak. In previous ^{13}C NMR studies of unsymmetric guest molecules,[1,24] those resonances arising from end-group and adjacent carbons were doubled in number in comparison to those arising from inner carbons. Assuming that the resonance doubling arises from different end-group interactions rather than conformational inequivalencies, then the intensities of such end-group resonances can be used to quantitatively determine the orientational preference of a particular guest. To assign particular end-group interactions, one strategy that has been used involves comparing the spectra of unsymmetric X-Y molecules with that of the corresponding symmetric guest molecules (X-X and/or Y-Y) and/or comparing spectra of compounds containing mixtures of guest molecules (X-Y/X-X) and/or (X-Y/Y-Y).[1,21,24]

Before examining examples of guest preferences, it is worth mentioning how the peak intensities give quantitative orientational information. As already stated, for a purely random distribution of guest molecules, the number of HT interactions will be equal to the number of HH+TT interactions. Therefore, the number of HT interactions will be twice the number of HH interactions. However, a resonance arising from a HH interaction has double the number of 'head' end-groups contributing to its intensity in comparison to a HT interaction. Therefore, in the spectrum of a guest which exhibits no particular orientational preference, in both of the end-group regions (i.e., 'head' and 'tail' regions), the two components of the doublet will be equal in intensity. It is also worth mentioning that it is not always possible to see doublets in both the X and Y regions of the spectrum.[22] In the ^{13}C spectrum of the 1-cycanodecane/urea inclusion compound, it was not possible to see

the CH$_3$ end-group in its two different environments.[1] A reason cited for this observation is that the CH$_3$ is not a particularly polarisable group and hence the ^{13}C chemical shift is virtually identical in the two environments.

In a study of a series of 1-cyanoalkane/PHTP inclusion compounds,[24] the guest molecules prefer to be ordered HH/TT, i.e., CN---NC and CH$_3$---H$_3$C, rather than HT, i.e., CN---H$_3$C. Similarly, in the 1-cyanodecane/urea inclusion compound, the preferred orientation of the guest molecules was found to be HH/TT.[1] In contrast, in the methyl undecanoate/urea inclusion compound[24] there is a preference for HT ordering of the guest molecules. This result suggests that during formation of the compound, the ester group is preferentially absorbed onto the crystal growth surface. However, it is important to note that there are many other factors which can influence the crystal growth process other than the end-group interactions.[24]

4.3 Determination of guest ordering in 2-hydroxyalkane/urea inclusion compounds

The two compounds studied were 2-dodecanol/urea and 2-pentadecanol/urea. Results from powder and single-crystal X-ray diffraction studies,[25] performed at room temperature, reveal that both compounds possess the conventional urea tunnel structure and that they are incommensurate. Some guests such as alkanediones can form hydrogen bonds with the urea,[1] which involves a rotation of some of the urea molecules about the C=O bond to yield a distorted tunnel structure. However, at room temperature, the host tunnels are not distorted in the 2-dodecanol or 2-pentadecanol inclusion compounds. Hence, it is presumed that any host-guest interactions are weak in comparison to those observed in alkanedione/urea inclusion compounds. The ordering of the 2-hydroxyalkane guest molecules (Figure 4.3) has been examined using ^{13}C NMR experiments. To help in the assignment of the end-group interactions, two mixed-guest urea inclusion compounds, 2-dodecanol/dodecane and 2-pentadecanol/pentadecane, have also been studied. However, from their ^{13}C spectra (Figure 4.5b and Figure 4.6b), it can be deduced that although the mixed-guest compounds were prepared from the corresponding alkane

and alcohol, in a ratio of 1:3, the alkane is included within the urea tunnels whereas the alcohol prefers to remain in the methanol, which is the solvent used in the preparation of the inclusion compounds.
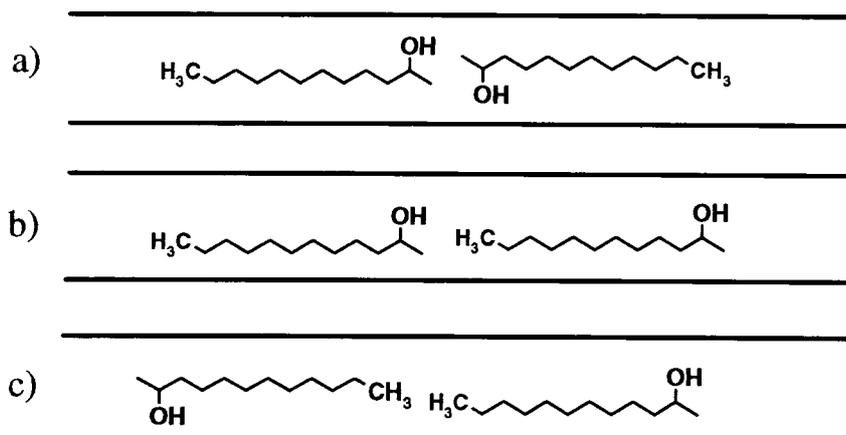
Figure 4.3. Possible ordering of 2-hydroxyalkanes, a) head to head (HH), b) head to tail (HT) and c) tail to tail (TT).

4.3.1 Experimental results

The $^1H \rightarrow ^{13}C$ CP spectra obtained for the 2-dodecanol and 2-pentadecanol inclusion compounds are shown in Figure 4.5 and Figure 4.6, respectively. Typical spectral conditions were: ^1H $\pi/2$ pulse duration, 4.2 µs; contact time, 1.0 ms; recycle delay, 10 s; ^1H decoupling power, 60 kHz; MAS rate, 3 kHz; number of transients, 512; acquisition time, 204.8 ms. As expected for such mobile molecules, the typical ^{13}C linewidth (fwhh) of the guest peaks is small, i.e. ~ 14 Hz. A general assignment (Table 4.1) of the ^{13}C spectra can be made from solution-state ^{13}C NMR data[26,27] and a previous study of alkane/urea inclusion compounds.[16] The nomenclature used to identify a particular carbon in a 2-hydroxyalkane is shown in Figure 4.4.
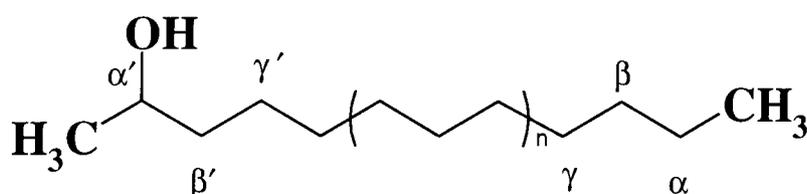
Figure 4.4. Nomenclature used to assign ^{13}C spectra (n=1 for 2-dodecanol and n=2 for 2-pentadecanol).
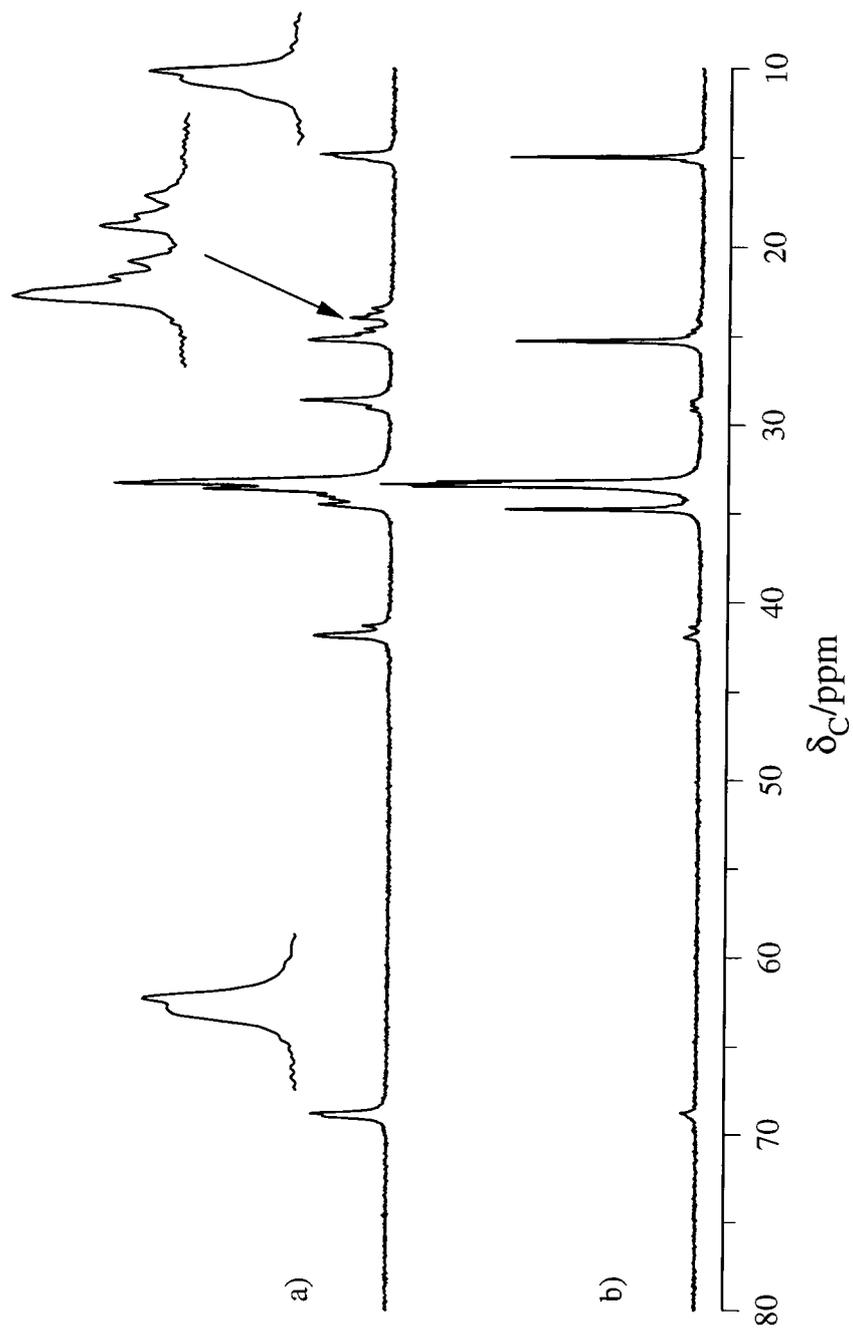
Figure 4.5. $^1H \rightarrow ^{13}C$ CP spectra of a) 2-dodecanol and b) 2-dodecane urea inclusion compounds.
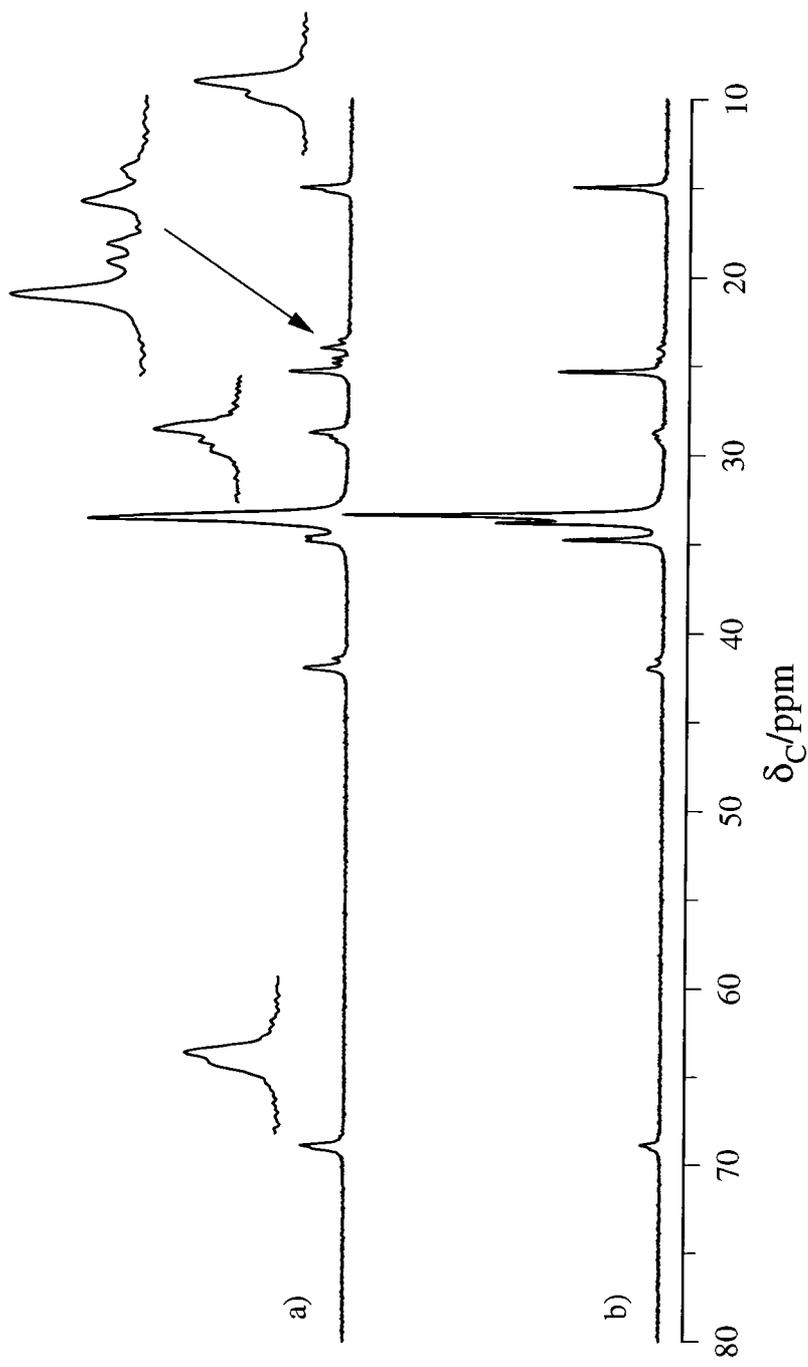
Figure 4.6. $^1H \rightarrow {}^{13}C$ CP spectra of a) 2-pentadecanol and b) 2-pentadecanol/pentadecane urea inclusion compounds.

	2-dodecanol/urea	2-pentadecanol/urea
Carbon	δ/ppm	δ/ppm
-CH₂**CH₃**	14.9, 15.0, 15.2	15.0, 15.2
α-CH₂	25.2	25.3
β-CH₂	34.6	34.6, 34.9
'inner' CH₂	33.3, 33.6, 34.0,[††] 34.2[††]	33.6
γ′-CH₂	28.6, 29.1	28.8, 29.0, 29.3
β′-CH₂	41.4, 41.9	41.4, 41.9
α′-CHOH	68.8, 68.9	68.9, 69.1
-**CHOH**CH₃	23.5, 23.8, 24.0, 24.6,[†] 24.9[†]	23.5, 23.6, 24.0, 24.6, 24.8

Table 4.1. Assignment of ^{13}C spectra of 2-dodecanol (Figure 4.5) and 2-pentadecanol (Figure 4.6) urea inclusion compounds. The chemical shifts marked with [†] and [††] could alternatively be assigned as α-CH₂ and β-CH₂, respectively.

For some of the carbons, it is possible to see at least three resonances which complicates their assignment, particularly in the 23.0-25.5 ppm region of ^{13}C spectra of the 2-hydroxyalkane/urea inclusion compounds. However, it is possible to assign the resonances at 25.2 ppm and 25.3 ppm in ^{13}C spectra of the 2-dodecanol and 2-pentadecanol compounds, respectively as α-CH₂ from ^{13}C spectra of their corresponding alkane/urea inclusion compounds. In previous studies of monosubstituted alkane/urea inclusion compounds,[1,28] there was only one resonance for the α-CH₂ (i.e., adjacent to the CH₃). Hence, the other peaks in the 23.0-25.5 ppm region have tentatively been assigned as **CH₃CHOH**. A comparison of the integral of this group of peaks with, for example, that of the α′-CHOH peak indicates that two carbons, α-CH₂ and **CH₃CHOH**, contribute to this region in the spectrum. Typically, ^{13}C spectra of urea inclusion compounds containing unsymmetric guests have double the number of resonances for end-group carbons, and in some cases for those adjacent, compared to other carbons. Therefore, the multiplicities observed for some carbons cannot be accounted for solely by different end-group interactions. Thus, in

the following section, other possible sources for the number of resonances observed will be examined.

4.4 Chiral recognition

In conventional inclusion compounds, the urea molecules are hydrogen bonded to one another to form helical ribbons which are woven together to form tunnels. In a single crystal of a urea inclusion compound, the helical ribbons can either be right-handed ($P6_122$) or left-handed ($P6_522$). When the guest molecules are also chiral, as in the case of 2-dodecanol and 2-pentadecanol, it is possible that a particular enantiomeric form of the guest could be preferred in a particular enantiomeric form of the host. The degree to which such chiral recognition can be achieved depends upon the difference between host-guest interactions for different enantiomeric combinations of the two species.[29] As well as the existence of different enantiomeric forms of the guests (R and S), it is also possible for the end-groups of the guest molecules to adopt different conformations (trans and gauche), as shown in Figure 4.7. (The question of end-group conformation will be discussed at greater length in Chapter 7 for fluoroalkane/urea inclusion compounds). Therefore, if one considers the fact that for a particular enantiomer with a particular end-group conformation, it is also possible for such a molecule to be oriented head to head or head to tail with respect to a neighbouring molecule, then clearly there are a large number of complex factors affecting the number of resonances observed for end-group carbons and those adjacent.

In a computational study of 2-bromoalkane/urea inclusion compounds,[29] the conformation and chiral preferences of the guest molecules were examined. It was demonstrated that the preferred conformation of the guest molecules is with the bromine trans and the methyl gauche and that, given this conformation, there will be an excess of the R enantiomer in the $P6_122$ urea tunnels. In studies of urea inclusion compounds containing chiral guests, it was shown that such compounds do exhibit some degree of chiral recognition.[30-33] For a series of esters, it was suggested that the oxygen, proton and methyl group adjacent to the chiral centre dictate the chiral

preference exhibited by such compounds.[32] From the limited amount of data concerning this interesting feature of urea inclusion compounds, it is not unreasonable to assume that the chirality of the guests contributes to the complexity of the ^{13}C spectra in comparison to spectra of achiral guest/urea inclusion compounds.[1,21,24,28]
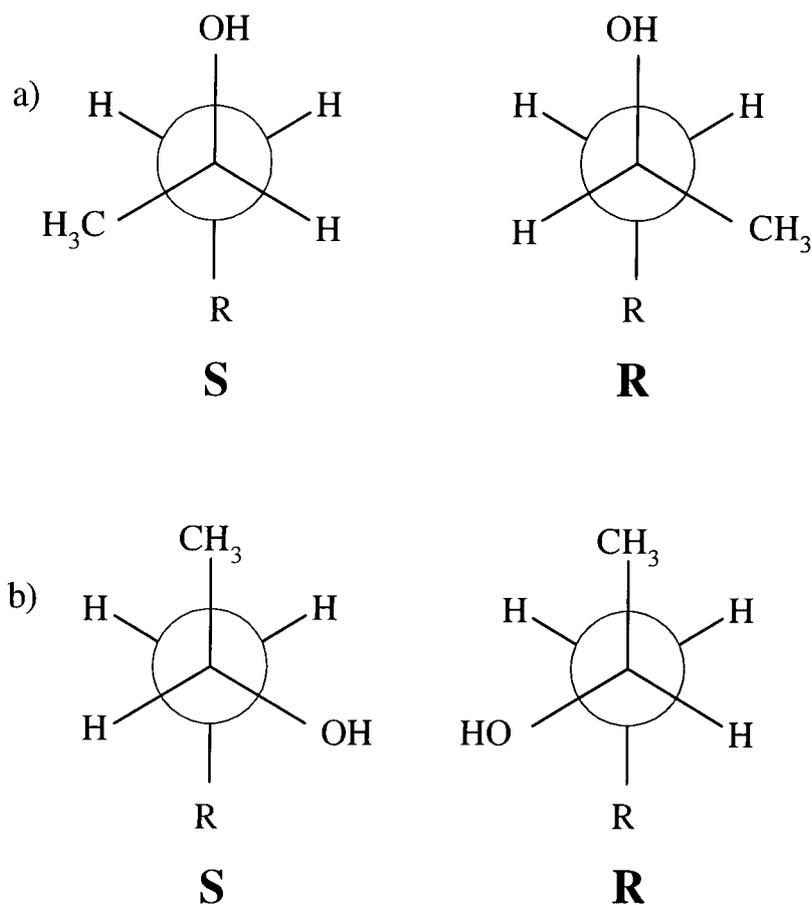
Figure 4.7. R and S enantiomeric forms of 2-hydroxyalkanes with a) OH trans and b) OH gauche to the alkyl chain.

4.5 Variable-temperature ^1H CRAMPS experiments

Because of the narrow chemical shift range of ^1H, the use of ^1H CRAMPS as a tool for the structural elucidation of organic solids has mainly been confined to those systems which exhibit hydrogen bonding.[34-37] In the 2-hydroxyalkane/urea inclusion compounds, although there are no significant host-guest interactions, it is

possible that there could be some hydrogen bonding between the guest molecules. The ^{1}H CRAMP spectrum (acquired using BR-24) obtained at 20 °C of the 2-dodecanol/urea inclusion compound is shown in Figure 4.8. Typical spectral conditions were: $\pi/2$ pulse duration, 1.75 µs; tau, 3.0 µs; recycle delay, 10 s; acquisition length, 512 points; MAS rate, 1.1 kHz; number of transients, 16. Using solution-state ^{1}H NMR data,[27] the spectrum can be assigned as shown in Table 4.2.
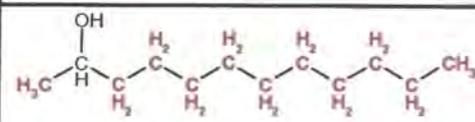
δ_H/ppm	^{1}H
1.8	
4.2	
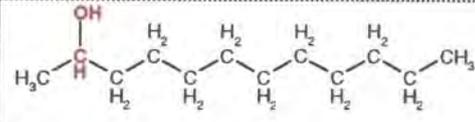
Table 4.2. Assignment of ^{1}H CRAMP spectrum (shown in red) obtained at 20 °C.

However, at 20 °C there appears to be no resonance which can be attributed to the urea ^{1}H. Given the fact that these protons are involved in hydrogen bonding, it is unlikely that they are hidden within the range covered by the guest ^{1}H signals.

    Variable-temperature ^{1}H CRAMPS experiments were then performed with the results obtained shown in Figure 4.8. The same spectral conditions as for the room temperature experiment were employed, except that a MAS rate of 1.8 kHz was used. As the temperature is lowered, the peaks at 1.8 ppm and 4.2 ppm broaden due to a reduction in mobility of the guest molecules. Given the resolution of the ^{1}H CRAMP spectra, particularly at lower temperatures, it is not possible to deduce whether there are any significant interactions between the guest molecules. However, another peak, which presumably arises from the urea ^{1}H, gradually appears at 9.9 ppm and sharpens as the temperature is decreased. Before considering why this peak behaves as it does with temperature, confirmation of the assignment was first required. This can easily be achieved by comparing spectra of a particular inclusion compound made from h_4-urea and d_4-urea.
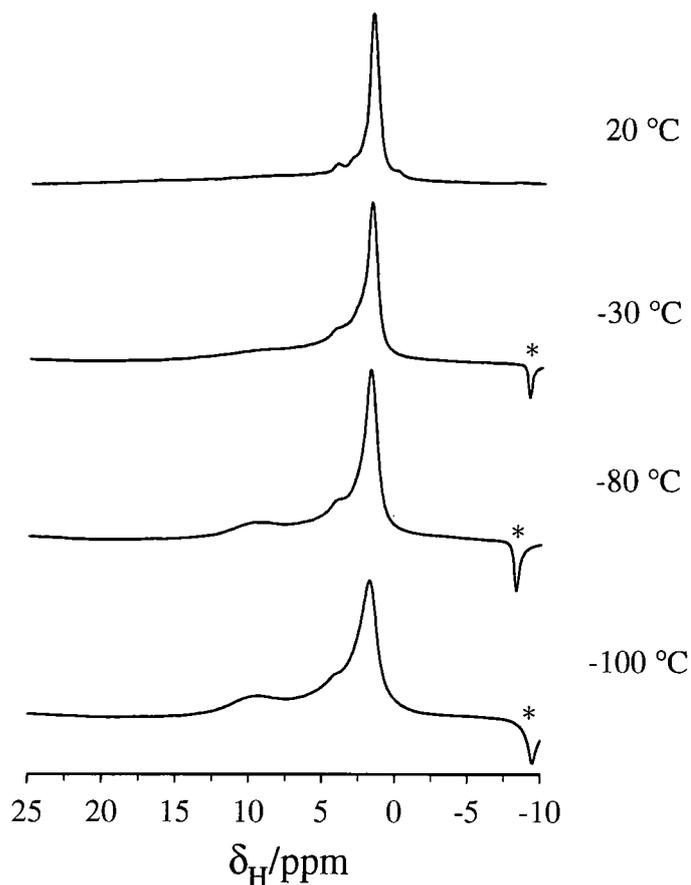
Figure 4.8. Variable-temperature ^1H CRAMP spectra of 2-dodecanol/urea inclusion compound. The 'peak' denoted by the asterisk is an artefact arising from the transmitter positioning.

4.6 Variable-temperature ^1H CRAMPS studies of the 2-pentadecanol/h$_4$-urea and d$_4$-urea inclusion compounds.

Proton CRAMP spectra were obtained for both the h$_4$-urea and d$_4$-urea compounds at room temperature (Figure 4.9a) and at -100°C (Figure 4.9b). It can be seen that the 2-dodecanol and 2-pentadecanol/h$_4$-urea inclusion compounds behave similarly as a function of temperature. To ensure that the d$_4$-urea sample did not undergo ^1H exchange with moisture in the air, the rotor was packed in a glove box. As it would have been particularly difficult to seal the sample in a glass ampoule, due to the nature of the sample and the small rotor size (4 mm diameter), in an attempt to keep the rotor air tight the usual Teflon endcap was replaced with a spacer. The room temperature spectra of the h$_4$-urea and d$_4$-urea compounds are comparable, except in

the higher frequency region (~ 9 ppm) of the h_4-urea spectrum, where it is just possible to see a very broad underlying peak. However, at -100°C the peak at 9.4 ppm, which is clearly visible in the h_4-urea spectrum, is barely visible in the corresponding d_4-urea spectrum.
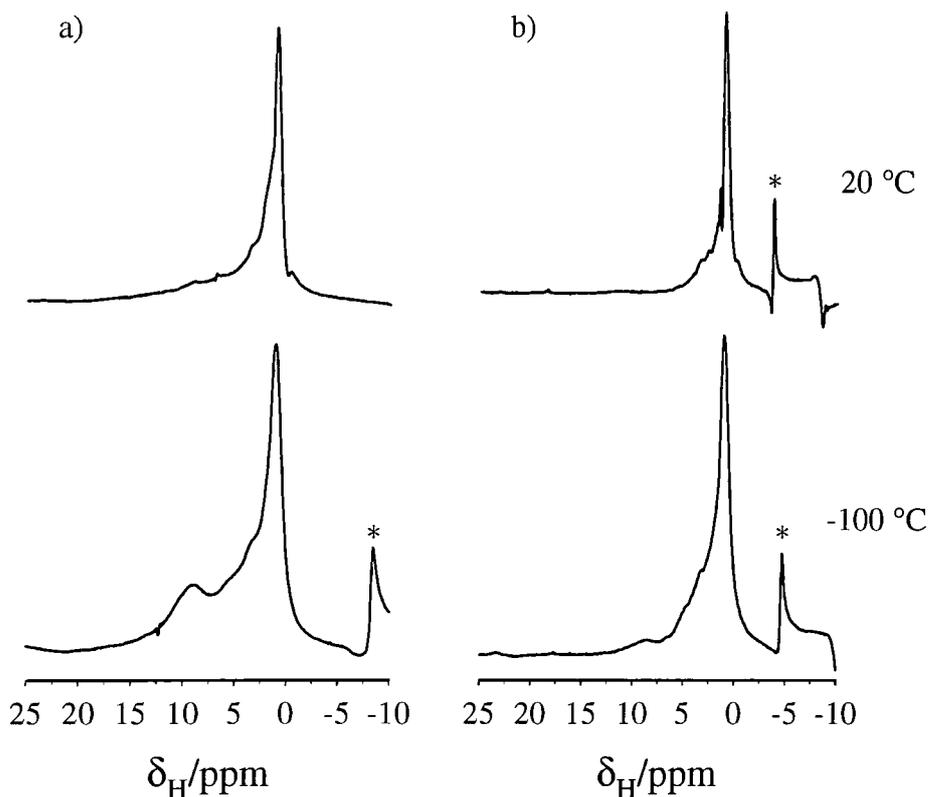
Figure 4.9. Comparison of ^1H CRAMP spectra of a) 2-pentadecanol/h_4-urea and b) 2-pentadecanol/d_4-urea. The asterisks indicate artefacts due to the transmitter.

This corroborates the assignment of the broad peaks at 9.4 ppm and 9.9 ppm in the 2-pentadecanol and 2-dodecanol inclusion compounds, respectively, as being those arising from the urea ^1H. The ^1H chemical shift of the urea signal fits in with the notion that the urea host structure is extensively hydrogen bonded. It is just possible to detect a very small peak in the d_4-urea spectrum, which can probably be attributed to residual ^1H in the urea. To see if any ^1H exchange had occurred on the timescale of the duration of the experiment, the d_4-urea sample was deliberately exposed to the air for about an hour. Another spectrum was then acquired, at -100°C, of the d_4-urea sample which appeared the same as the spectrum of the d_4-urea sample

in Figure 4.9b, where contact with the air was minimised. Therefore, it is unlikely that the sample changed much in terms of ^{2}H content during the course of the experiments. However, to provide conclusive evidence that the host molecules in the 2-pentadecanol/d$_4$-urea inclusion compound were actually deuterated, a ^{2}H MAS NMR experiment was performed.

4.6.1 ^{2}H MAS experiments

Typically in ^{2}H NMR studies,[38] static spectra are obtained using a quadrupole echo sequence[39] and a short π/2 pulse duration (~ 2 μs). These experimental features are necessary to minimise spectral distortions arising from not starting acquisition of the FID at an echo maximum and an insufficiently wide excitation profile respectively. Previous static ^{2}H NMR studies of urea inclusion compounds[23,40] required a spectral width of the order of 500 kHz. As only a 7.5 mm HX probe was available for this work, and so the necessary pulse excitation width was not possible using a 90° pulse angle, the appearance of static ^{2}H spectra would have been severely distorted. The spectrum was acquired using MAS and to achieve the same degree of excitation across the entire spectral width, a small tip angle pulse was used. Typical spectral conditions were: π/2 pulse duration, 5 μs; duration of excitation pulse, 0.5 μs; recycle delay, 0.5 s; number of transients, 65536; MAS rate, 4 kHz; acquisition time, 16.4 ms. The resulting spectrum is shown in Figure 4.10.
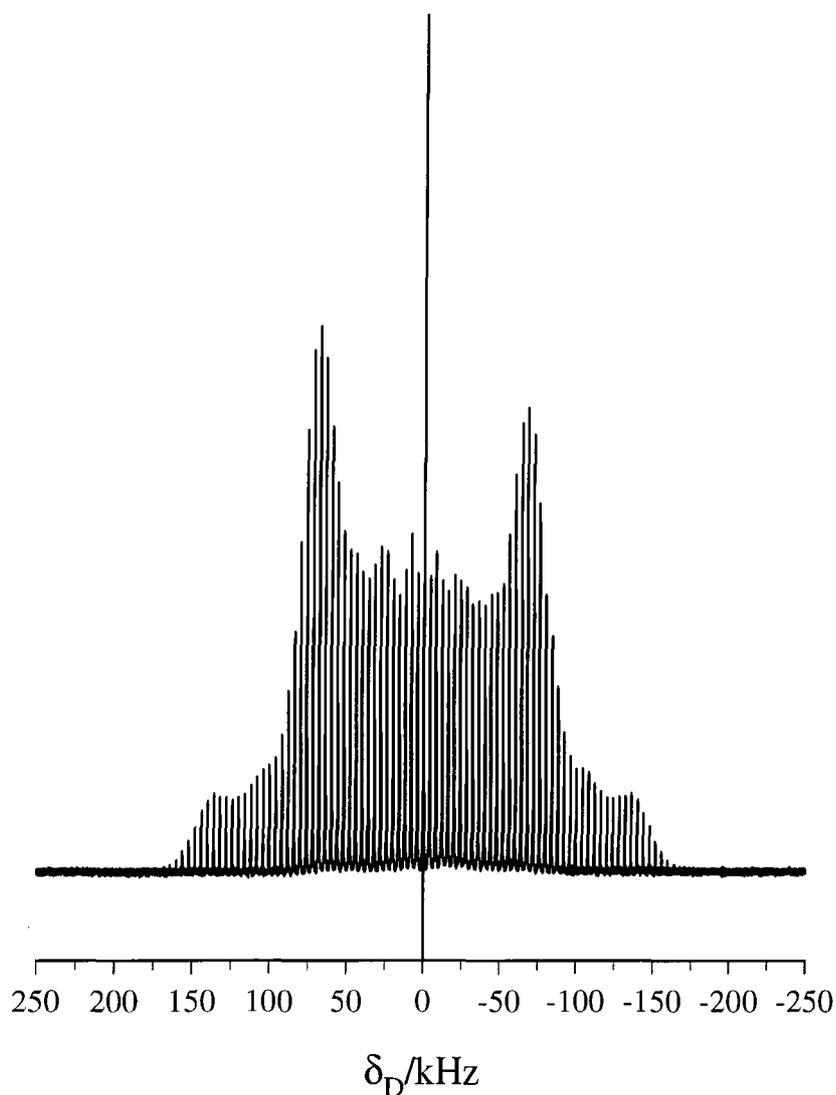
Figure 4.10. ^2H NMR spectrum of 2-pentadecanol/d₄-urea acquired with a MAS rate of 4 kHz. The large central 'spike' is an artefact.

The spectrum is slightly distorted, although its general outline and major splitting (~ 135 kHz) are comparable to those of previously reported static ^2H NMR spectra of d₄-urea inclusion compounds.[23,40] Such spectra revealed that there are two different types of deuterons in urea which give rise to two overlapping spectra, one of which exhibits considerable motional narrowing and the other which appears to arise from a 'rigid' site. The 'mobile' component gives rise to two small peaks at ±8 kHz and two only just observable shoulders at ±95 kHz, which are superimposed on a 'full-width' spectrum arising from the 'rigid' component. The reason for the two-component appearance of the spectrum lies in the orientation of the quadrupolar

tensor for the two deuterons in relation to the motional axis. Unfortunately, due to spectral distortions, it is only just possible to observe the features of the 'mobile' component in Figure 4.10. However, the purpose of this spectrum was merely to check that the sample and, in particular, that the urea was deuterated. Hence, from the signal obtained and the general appearance of the spectrum, it can be concluded that the sample does contain d_4-urea. The motion of the urea molecules will be discussed in the following section, where the effects on the CRAMP spectra will be examined.

4.7 Urea dynamics

The motion of the host molecules in the n-nonadecane/d_4-urea inclusion compound has been studied via ^{2}H NMR.[23] At room temperature (303 K), the urea molecules were shown to undergo 180° jumps about their C=O bonds at a rate of 2×10^6 Hz. On lowering the temperature to 258 K, the rate slowed to 4×10^5 Hz. The guest and host dynamics occur on completely different timescales, but the possibility of different types of guest (different with regard to functionality and chain length) having an effect upon the urea motion has been considered. For the 1,10-dibromodecane/urea compound,[40] the rate of the jump motion of urea was comparable to that found in the n-nonadecane/d_4-urea inclusion compound. However, it has been shown that when there is a higher density of bulky, polarisable groups present, the rate of motion of the host may be slowed.[1,41]

4.7.1 Dynamic broadening in CRAMP spectra[42]

In the variable-temperature ^{1}H CRAMP spectra of the 2-dodecanol and 2-pentadecanol/urea inclusion compounds, as the temperature is lowered, a broad peak appears at 9.9 ppm (Figure 4.8) and 9.4 ppm (Figure 4.9a), respectively. This peak was attributed to the urea molecules, based on ^{1}H CRAMP spectra (Figure 4.9b) obtained of the 2-pentadecanol/d_4-urea inclusion compound. Therefore, at 20 °C, the urea peak is so broad that it is barely discernible from the baseline. As the protons are

directly bonded to ^{14}N in urea, it might be thought that the nature of the broadening is the ^{1}H-^{14}N dipolar/quadrupolar interaction.[35,43] However, one would expect the peak to increase in width at lower temperatures, rather than decrease, due to a decrease in the rate of motion. However, in a variable-temperature ^{1}H CRAMPS study of L-alanine and L-[^{15}N]-alanine,[42] the source of line broadening was shown to be from the dynamic nature of the compound rather than the ^{1}H-^{14}N dipolar/quadrupolar interaction. The linewidth (given by $1/T_2^*$ in Equation 4.1) obtained in a CRAMPS experiment is dependent on the inter-pulse time tau and the motional correlation time. For the WAHUHA sequence, it can be described by,[44]

$$\frac{1}{T_2^*} = M_2 \tau \frac{2}{3\alpha} \left[1 - \frac{(5\cosh\alpha - 2)\sinh^2\alpha}{\alpha\sinh 3\alpha} \right] \qquad \textit{Equation 4.1}$$

where $\alpha = \dfrac{\tau}{\tau_c}$, M_2 is the second moment, τ is the pulse spacing and τ_c is the motional correlation time. It has been shown[42] that, with typical pulse spacings of 1-3 μs, CRAMPS linewidths are sensitive to motions in the 100s of kHz to MHz range.

Hence, in this case there must be some kind of interference[45-47] of the averaging of SA by MAS and/or the averaging of ^{1}H-^{1}H dipolar interactions by the BR-24 sequence, with the motion of the urea molecules at the higher temperatures. Considering the rate of motion of the urea molecules obtained via ^{2}H NMR studies,[40,41] this suggests that the latter is the case.[42,47] Experiments were also performed on the 2-pentadecanol/urea inclusion compound using the MREV-8 pulse sequence. Although the general appearance of the MREV-8 spectra were comparable to those obtained using BR-24, the urea peak at room temperature is not as broad and hence more visible using the MREV-8 pulse sequence. This is because the expression for the linewidth obtained using CRAMPS is dependent upon the pulse sequence used.[44] Therefore, in order to obtain a urea peak with a much narrower linewidth, CRAMPS experiments would have to be performed at either much lower or higher temperatures than has been in this case. However, the probe and sample respectively limit the minimum and maximum temperature at which experiments can be performed.

4.8 Single-pulse ^1H MAS NMR

Single-pulse ^{1}H MAS NMR experiments have been performed on the 2-pentadecanol/h$_4$-urea and d$_4$-urea inclusion compounds (Figure 4.11) at room temperature. Typical spectral conditions were: π/2 pulse duration, 1.75 μs; recycle delay, 10 s; MAS rate, 10.0 kHz; acquisition time, 20.5 ms; spectral width, 200 kHz; number of transients, 64. The linewidth of the central peak in Figure 4.11a is ~ 1 kHz, which compares to that of 300 Hz for Figure 4.11b. The only difference between the spectra of the compounds in Figure 4.11a and Figure 4.11b is that in the former the urea must give rise to a signal whereas in the latter it cannot. Therefore, the urea must make the major contribution to the broadness of the ^{1}H spectrum in Figure 4.11a. Isotopic substitution of ^{1}H by ^{2}H has been a strategy used to obtain chemical shift information from ^{1}H 'wideline' experiments.[48] It has also been possible to obtain such information from compounds in which there is partial averaging of the ^{1}H-^{1}H dipolar interactions by motion.[49] However, isotopic substitution can be costly and inconvenient, and most typical organic solids have ^{1}H linewidths of the order of tens of kHz. In a solid-state ^{1}H NMR study, in which CRAMPS and MAS-only techniques were compared,[50] caution was urged in the interpretation of intensities and fine structure observed in ^{1}H MAS spectra unless CRAMP spectra were available for comparison. The fine structure observed in ^{1}H MAS spectra has been studied using the delayed-acquisition experiment.[51-53] However, unlike the CRAMPS technique, the delayed-acquisition experiment is sensitive to both temperature and moisture.[54] It has also been suggested that the peaks observed in such experiments are only from a small fraction of molecules moving virtually isotropically. Hence, the intensities of the peaks cannot be interpreted quantitatively.[54,55] For the 2-hydroxyalkane/urea inclusion compounds, subjection to the heating and drying conditions necessary to eliminate problems caused by moisture would actually degrade the samples. However, another method for interpreting ^{1}H MAS spectra involves separating out the components which make up the overall line using another nucleus via a 2D experiment.
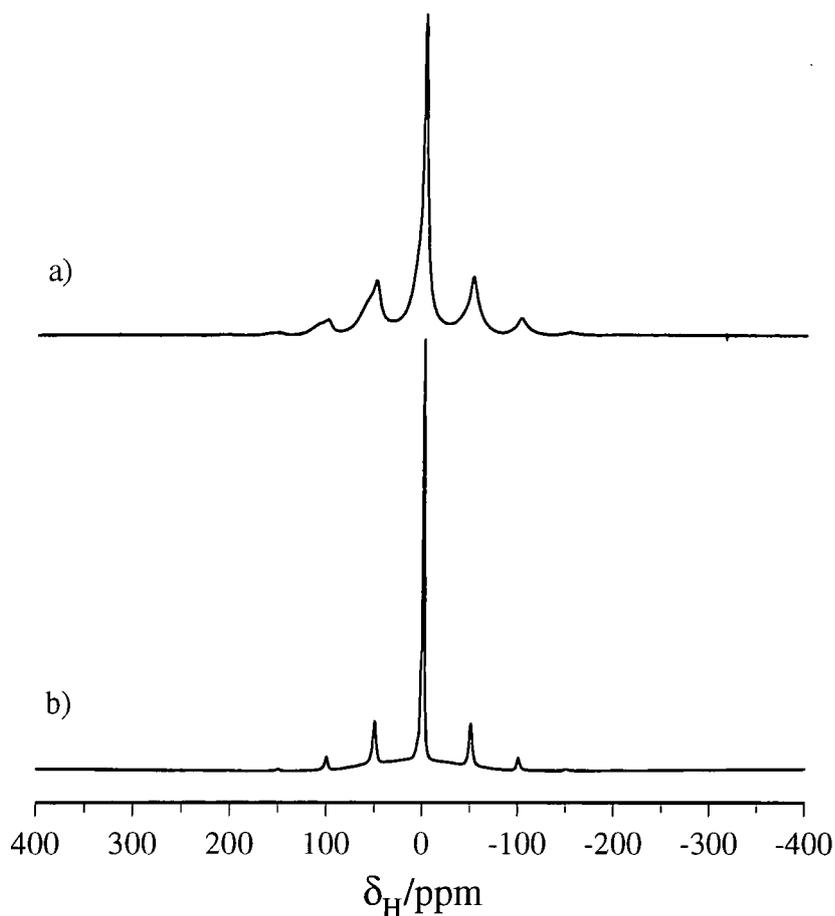
Figure 4.11. Single-pulse ^1H MAS spectra of a) 2-pentadecanol/h$_4$-urea and b) 2-pentadecanol/d$_4$-urea at 10 kHz.

4.9 Two-dimensional correlation experiments

Two-dimensional experiments can formally be defined as correlation, separation or exchange experiments.[56] However, the actual assignment of an experiment to a particular class appears to be in some cases quite subjective.[38] All two-dimensional experiments correlate one particular interaction with another, but some can more accurately be described as separation experiments. In this section, the experiments discussed will be referred to as being of the correlation type, although they can also be described as separation experiments. The two-dimensional heteronuclear correlation experiment involves allowing one type of nucleus (I) to

evolve during t_1, then transferral of this information to a second type of nucleus (S), which then evolves during t_2.
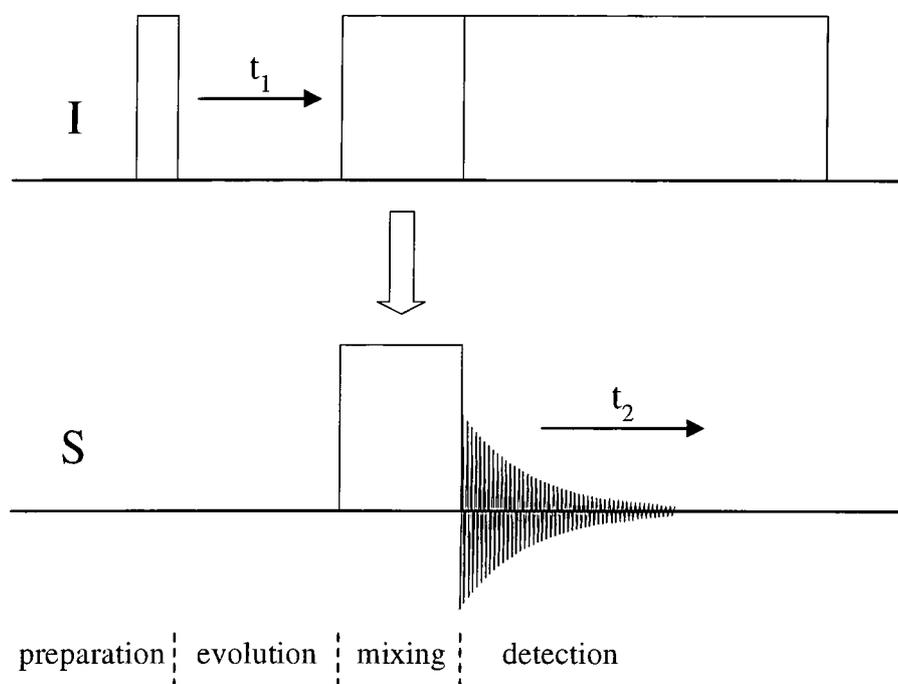
Figure 4.12. Schematic diagram of the two-dimensional I-S correlation experiment.

Examples of nuclei which have been the subject of heteronuclear chemical shift correlation experiments include ^1H-^{13}C,[57,58] ^1H-^{19}F,[59] ^{19}F-^{119}Sn,[60] ^{15}N-^{13}C[61] and ^{19}F-^{13}C.[62] The basic pulse sequence, as illustrated in Figure 4.12, gives rise to homonuclear and heteronuclear dipolar coupled I spins in the F_1 dimension. However, these interactions can be removed during t_1 by homonuclear multiple-pulse decoupling, e.g. MREV-8[63] or BLEW-48[64] applied to the I spins and/or heteronuclear decoupling, e.g. 180° pulse applied to the S spins[65] or BB-48.[58] The evolution of the I spins is then transferred to the S spins. However, it is important that the evolution undergone by individual I spins is not 'lost' via spin diffusion during this time. This can be achieved via cross polarisation using a short contact time or multiple-pulse sequences, such as WIM-24,[66,67] which remove the I-I interactions, but maintain the I-S interactions. The S spins are then allowed to evolve during t_2, typically under high-power proton decoupling (I-S decoupling). Hence, by acquiring spectra as a function of t_1, the evolution undergone by the I spins during t_1 can effectively be

transferred to the S spin spectra. Upon Fourier transformation of both t_2 and t_1, with the appropriate data manipulation, a two-dimensional correlation spectrum results.

It is also possible to perform homonuclear correlation experiments. Examples of such experiments include those which correlate isotropic with anisotropic chemical shifts,[68,69] isotropic chemical shifts with quadrupolar interactions[70] and isotropic chemical shifts with heteronuclear dipolar interactions[71] or homonuclear dipolar interactions.[72,73] Using a two-dimensional version of the delayed-acquisition experiment,[74] it has been possible to correlate ^1H chemical shifts in the same manner as in the solution-state COSY experiment.[75]

In the ^1H MAS spectrum of the 2-pentadecanol compound and (more especially) of the 2-dodecanol/urea inclusion compound (Figure 4.13), it is possible to see some very narrow peaks as well as a broader component which splits up into sidebands at 10 kHz. To probe the origin of such peaks and also to study the mobility of the 2-dodecanol/urea inclusion compound, two-dimensional experiments have been performed in which the wideline ^1H MAS spectrum has been correlated with ^{13}C chemical shifts[57] and, in a second experiment, with the ^1H CRAMP spectrum.[73]
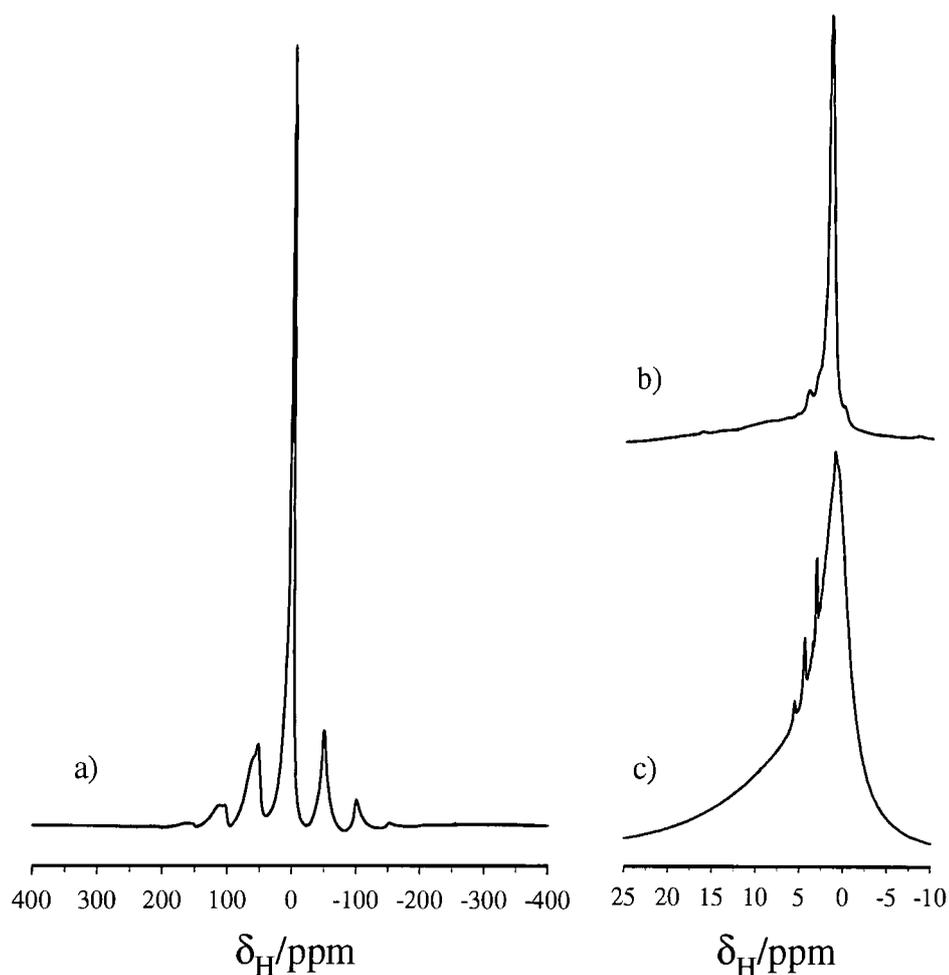
Figure 4.13. ^1H MAS spectra of 2-dodecanol/urea inclusion compound acquired using a) single pulse at 10 kHz and b) CRAMPS at 1.1 kHz. c) is an expansion of a) for comparison with b).

4.9.1 Proton-carbon correlation experiment

Although the ^{1}H MAS spectra are relatively narrow in comparison to those of less mobile organic solids, it is still virtually impossible to extract any detailed information from such spectra. However, it is possible to separate out the components which make up the overall ^{1}H MAS spectra using the ^{13}C chemical shifts in a ^{1}H-^{13}C wideline separation (WISE) experiment.[57] This experiment and various modifications of it,[76] have been used to determine mobility and domain sizes in polymers.[57,77] The pulse sequence used for the correlation of ^{1}H MAS spectra with ^{13}C chemical shifts is shown in Figure 4.12. Transverse ^{1}H magnetisation is first

created via a π/2 pulse, and is then allowed to evolve during t_1 under chemical shift and both the homonuclear and heteronuclear dipolar interactions. To avoid transfer of the evolution undergone by individual ^1H spins to other ^1H spins via spin diffusion during polarisation transfer to ^{13}C, a short contact time of 0.1 ms was used. Then, during t_2, the ^{13}C spins evolve under their chemical shifts.

The phase cycling for the WISE sequence is exactly the same as that for the standard cross-polarisation pulse sequence. The ^{13}C contact pulse has a phase cycle of four to remove artefacts from imperfect quadrature detection and the dc offset.[78] As the ^1H π/2 preparation pulse has a phase cycle of two for spin temperature inversion,[79] this results in a total phase cycle of eight. In order to obtain pure absorption lineshapes and frequency discrimination in F_1, two data sets are acquired in which the phase of the ^1H π/2 preparation pulse is shifted by 90° in the second experiment with respect to that in the first. The data sets are then combined in a manner described in Chapter 6. The results of the ^1H-^{13}C WISE experiment are shown in Figure 4.14 and Figure 4.15.
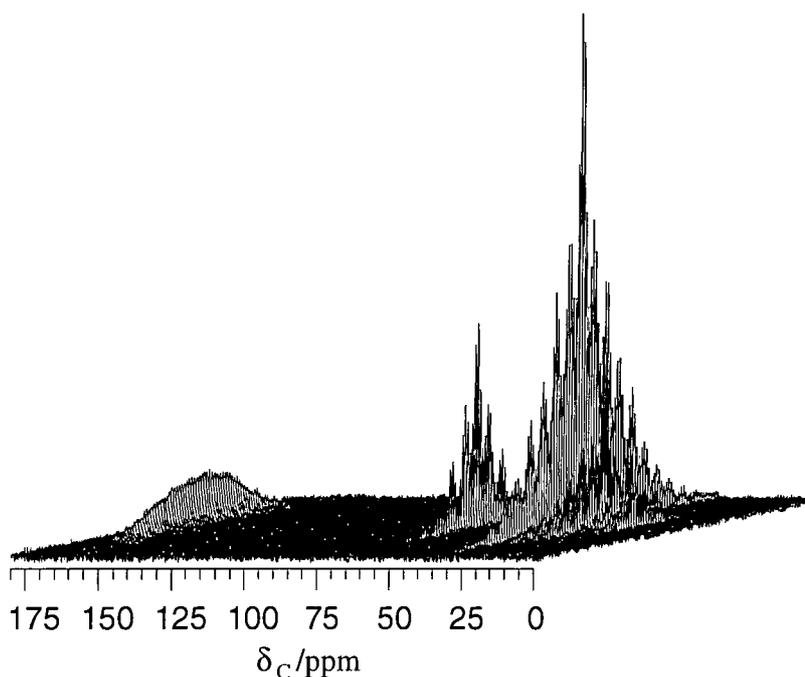
Figure 4.14. Stacked plot of ^1H-^{13}C WISE spectrum of the 2-dodecanol/urea inclusion compound at 4 kHz.

The spectral conditions used were: ^1H $\pi/2$ pulse duration, 4.0 µs; contact time, 0.1 ms; recycle delay, 2.0 s; number of transients per slice, 464; number of slices in t_1, 80; dwell time in t_1, 5.0 µs; acquisition time, 102.4 ms; MAS rate, 4.0 kHz.
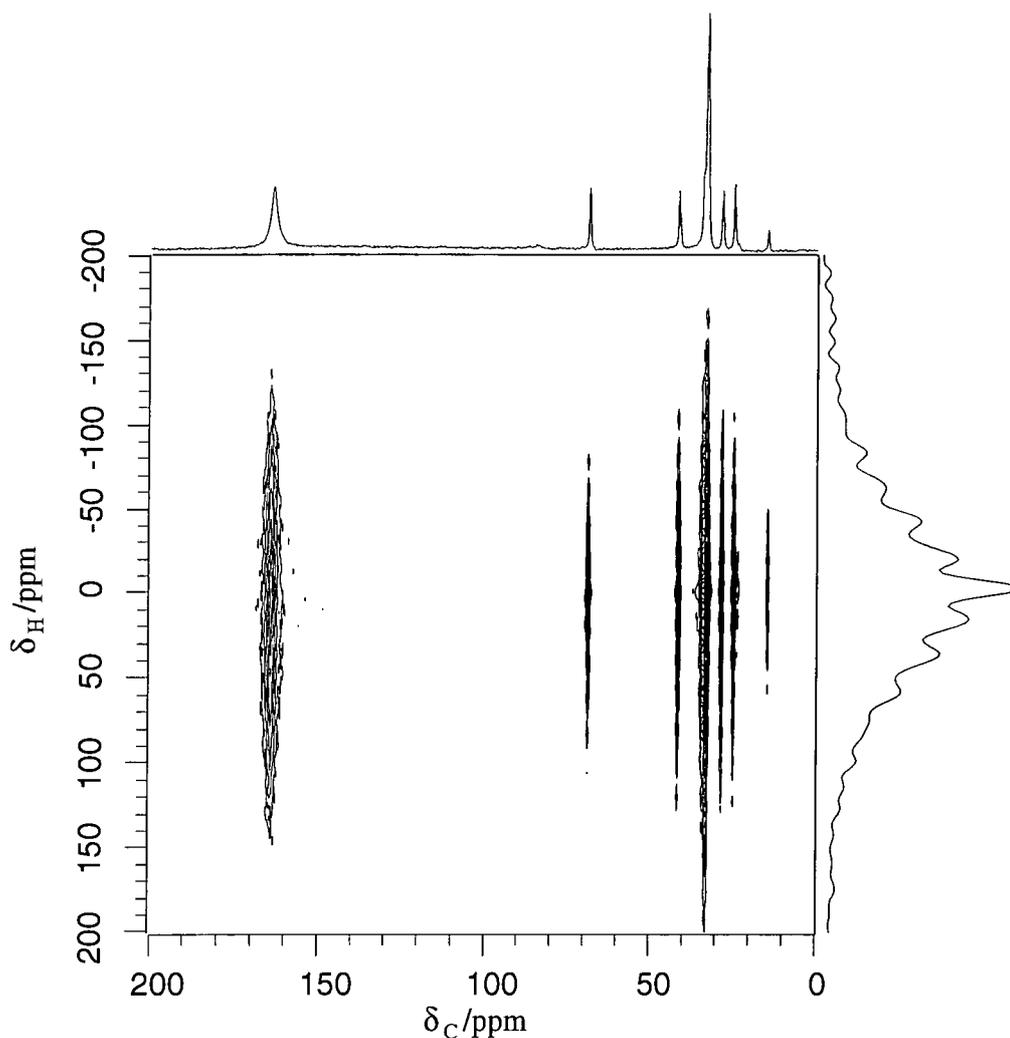
Figure 4.15. Contour plot of ^1H-^{13}C WISE spectrum of the 2-dodecanol/urea inclusion compound at 4 kHz. The spectra plotted along the F_1 (^1H chemical shift) and F_2 (^{13}C chemical shift) axes are summed projections.

The most noticeable feature of the spectra shown is that the urea ^1H spectrum has not broken up into sidebands, unlike the guest ^1H spectra, with a MAS rate of 4 kHz. This highlights the fact that the mobility of the host and guest molecules are very different. It is also evident that the very narrow peaks visible in the ^1H MAS

spectrum of 2-dodecanol/urea (Figure 4.13) are not present in the WISE spectrum. A ^{1}H MAS spectrum acquired using the same MAS rate as that used in the WISE experiment, 4 kHz, is shown in Figure 4.17b. If the narrow peaks arise from a small fraction of the sample in which the molecules are undergoing almost isotropic motion, then cross polarisation will be very inefficient due to averaging of ^{13}C-^{1}H dipolar interactions. Isotropic motion is impossible for guest molecules that are confined within the urea tunnels. However, if the guest molecules somehow manage to 'escape' from the tunnels, or they have simply adhered to the crystal surfaces during the formation of the inclusion compound, then some 'guest' molecules could be undergoing isotropic-type motion. Alternatively, if the peaks arise from water, then such peaks will have no correlation with ^{13}C given the short contact time used. Hence, the WISE experiment, which relies upon the existence of ^{1}H-^{13}C dipolar interactions to correlate the two nuclei, is not really an appropriate experiment for looking at such narrow ^{1}H peaks. The WISE experiment for 2-dodecanol/urea required approximately 40 hours of spectrometer time. If the ^{1}H wideline spectra could be correlated with a more sensitive nucleus than ^{13}C, such as ^{1}H (but under multiple-pulse decoupling to remove the homonuclear dipolar interactions), then this would provide a considerable saving in time. However, the major disadvantage of such an experiment is the substantially reduced chemical shift range of the ^{1}H in comparison to ^{13}C.

4.9.2 *Proton-proton (wideline/multiple pulse) correlation experiment*[73]

This experiment, like the ^{1}H-^{13}C WISE experiment, has been applied to the study of dynamics and phase separation in polymers. The two-dimensional ^{1}H wideline/multiple-pulse correlation experiment can be performed with the high-resolution ^{1}H spectrum in either the F_1 or F_2 dimension. If the ^{1}H wideline MAS spectrum contains both broad and narrow components, then from a time point of view, it is best to directly observe such a spectrum, i.e. in the F_2 dimension. It is also worth remembering that many people are deterred from the ^{1}H CRAMPS experiment because of its experimentally demanding requirements. Hence, aside from the extra

resolution afforded by correlating the ^{1}H chemical shift with that of ^{13}C, ^{1}H-^{13}C HETCOR experiments are frequently preferred to ^{1}H CRAMPS experiments. This is because of the less exacting conditions required for averaging the ^{1}H-^{1}H homonuclear dipolar interactions in the indirectly detected, i.e. F_1, dimension. Therefore, for both of the reasons mentioned, the ^{1}H wideline MAS spectrum was directly observed for the 2-dodecanol/urea inclusion compound. The pulse sequence used for the experiment is shown in Figure 4.16a.
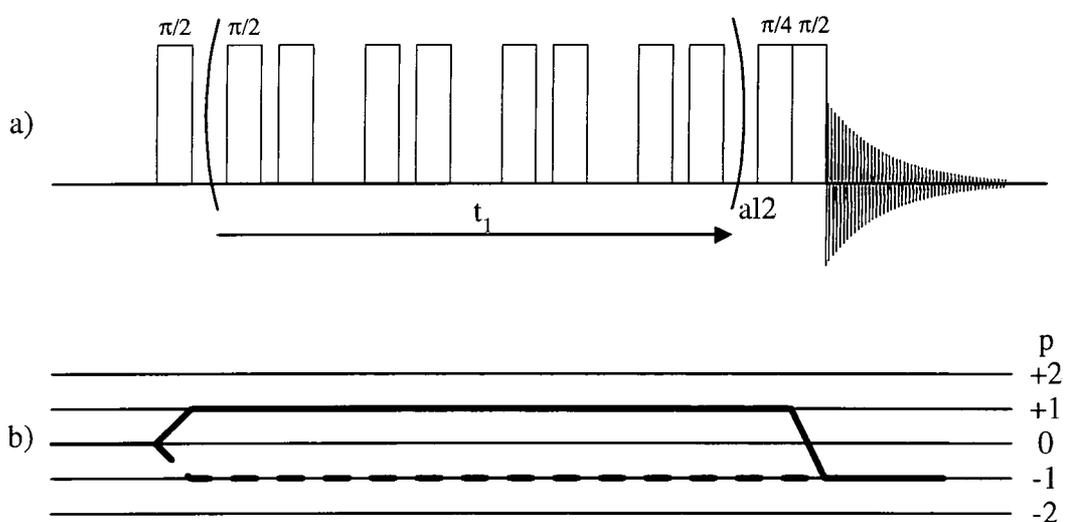
Figure 4.16. ^{1}H-^{1}H (wideline/multiple-pulse) correlation a) pulse sequence and b) coherence pathway diagram.

Transverse magnetisation was created using a $\pi/2$ pulse and averaging of the ^{1}H-^{1}H dipolar interactions was achieved during t_1 with the MREV-8 pulse sequence. Alternatively, a windowless or semi-windowless[64] multiple-pulse sequence could have been used to remove the homonuclear dipolar interactions. As points do not have to be acquired in between pulses using this method, the requirement for short pulse durations and probes with short ring-down times is removed. Hence, this experiment can be performed on a standard 7.5 mm two-channel MAS probe, although in this case the 'HF' probe was used. A $\pi/4$ pulse is required after t_1 to rotate the magnetisation back to the z axis, due to the fact that during the MREV-8 sequence the magnetisation precesses about (1, 0, 1). Then a $\pi/2$ pulse is applied to

create transverse magnetisation, which is allowed to evolve under chemical shift and homonuclear dipolar interactions.

For the purpose of phase cycling, the pulse sequence can be considered to be the same as the standard two-pulse COSY sequence. The corresponding coherence pathway diagram is shown in Figure 4.16b, with the desired pathways indicated by the dashed and solid lines. In order to achieve pure absorption lineshapes (see Chapter 6), it is necessary to retain both the $p=+1$ and $p=-1$ coherence pathways during t_1. As for the WISE experiment, two data sets are required, with the phase of the first pulse in the second experiment shifted by 90° with respect to that in the first experiment. For the first $\pi/2$ pulse, a phase cycle of 2 is required to select both the $p=+1$ and $p=-1$ coherence pathways. If the phase of the $\pi/4$ pulse is kept fixed, again a phase cycle of 2 is required to select $p=-1$ via $\Delta p=-2$ and $\Delta p=0$ for the final $\pi/2$ pulse. In order to have CYCLOPS on one of the pulses and on the receiver, the phase cycle to obtain the selection just described is repeated, except that the phase of the pulses is shifted by 90° (Table 4.3).

ϕ_1	ϕ_2	$\phi_{receiver}$
0	0	0
0	180	0
180	180	180
180	0	180
90	90	90
90	270	90
270	270	270
270	90	270

Table 4.3. Phase cycling for the ^1H wideline/multiple-pulse correlation experiment. ϕ_1, ϕ_2 and $\phi_{receiver}$ refer to the phases of the first and second $\pi/2$ pulses in Figure 4.16a and the receiver phase, respectively.

The spectral conditions used were: $\pi/2$ pulse duration, 1.8 µs; tau, 3.0 µs; recycle delay, 5.0 s; number of transients per slice, 8; number of slices in t_1, 400;

acquisition time, 10.24 ms; MAS rate, 4.0 kHz. One factor that must be considered when performing MAS multiple-pulse experiments is the relationship between the cycle time and a rotor period. In average Hamiltonian theory, it is assumed that the sample is effectively static during the individual periods over which the Hamiltonian is evaluated. This assumption is valid so long as the cycle time is much shorter than the rotor period. However, if this condition is not met, then interference of MAS with averaging of the multiple-pulse sequence can result in unwanted peaks at multiples of the MAS rate.[67] For the MAS rate used, 4.0 kHz, a rotor period is of the order of 7 times the multiple-pulse cycle time, which has been demonstrated to be sufficient for acceptable averaging.[67] A ^{1}H wideline and CRAMP spectrum, obtained at 4 kHz, are shown in Figure 4.17 for comparison with the two-dimensional ^{1}H wideline/multiple-pulse spectrum shown in Figure 4.18 and Figure 4.19.
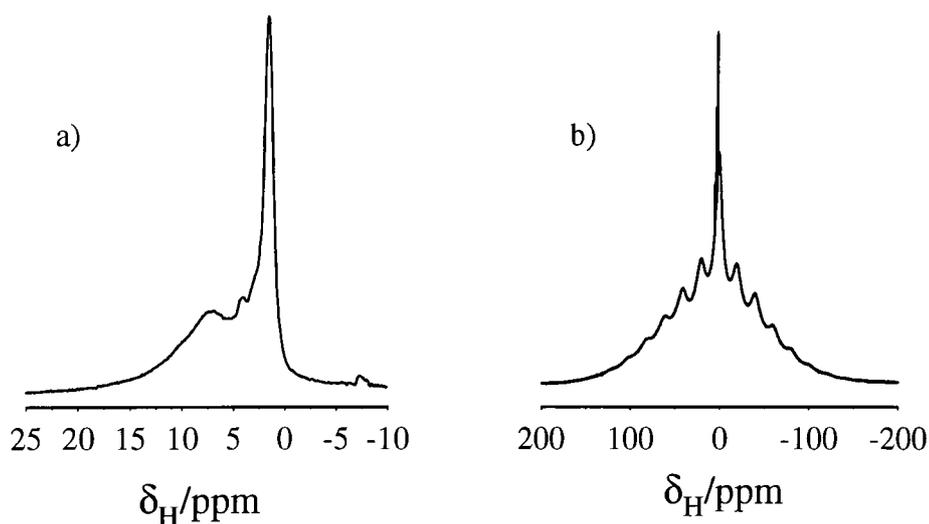
Figure 4.17. ^{1}H spectra of 2-dodecanol/urea at 4 kHz acquired using a) MREV-8 and b) single pulse sequences.

From the appearance of the narrow peaks at all the chemical shifts exhibited by 2-dodecanol/urea in the ^{1}H CRAMP spectrum, it appears that these peaks are from a small fraction of the 'guest' molecules undergoing virtually isotropic motion and/or from water. Although the broad urea peak does not show up very clearly in either the stacked or contour plot, in the summed projection parallel to F_1, it is clearly visible. In fact both the summed projections agree well with their respective 1-D spectra in Figure 4.17. Although not shown on the expansion plotted, there is also a peak at the

position of the transmitter in the F_1 dimension which is comparable in width to the other ^1H wideline cross-sections. This peak can be attributed to the interference of the multiple-pulse cycle time with a rotor period.[67] Although using a rotor period at least six times that of the cycle time has been previously deemed as acceptable, it has also been suggested that the rotor period should be ten times the cycle time. As mentioned earlier, this experiment lacks the resolution of the ^1H-^{13}C WISE experiment, but nevertheless in compounds with perhaps narrower resonances and a larger ^1H chemical shift range than in the 2-dodecanol/urea inclusion compound, it could have more potential. However, the experiment could perhaps be of greater application for fluorinated compounds in which the large chemical shift range of ^{19}F could be exploited.
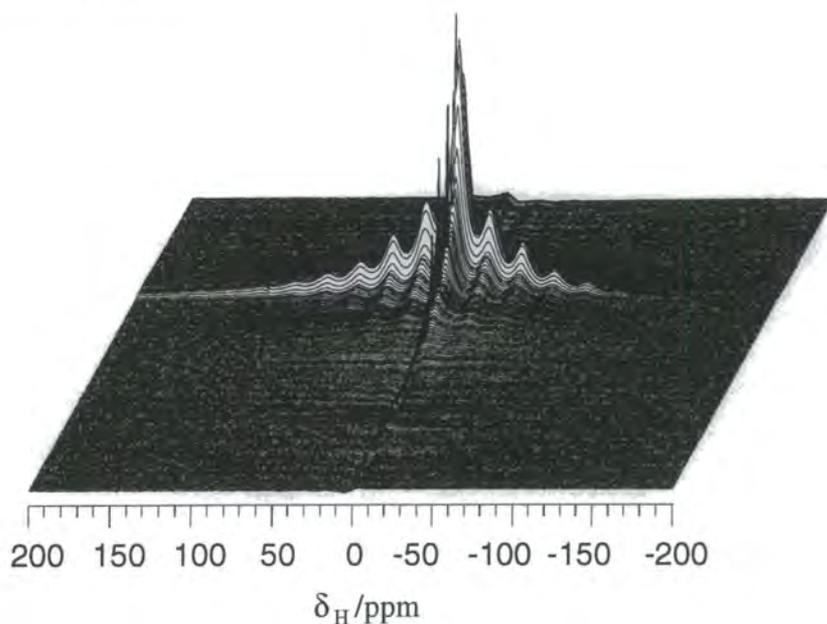
Figure 4.18. Stacked plot for the ^1H-^1H wideline/multiple-pulse spectrum of the 2-dodecanol/urea inclusion compound at 4 kHz.
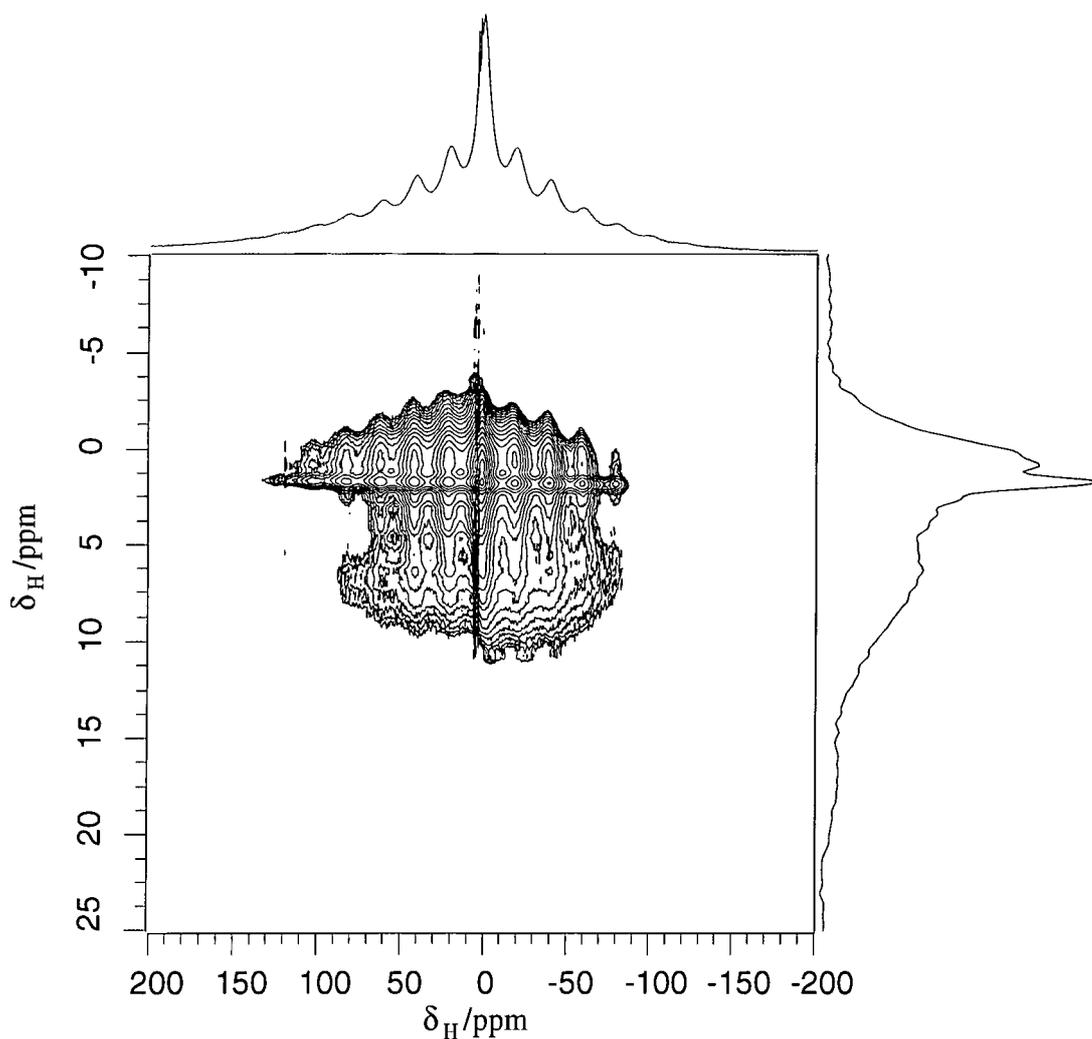
Figure 4.19. Contour plot of the ^1H-^1H wideline/multiple-pulse spectrum of the 2-dodecanol/urea inclusion compound at 4 kHz. The spectra plotted along the F_1 (^1H CRAMP) and F_2 (^1H wideline) axes are summed projections.

4.10 Conclusions

A combination of one- and two-dimensional ^1H and/or ^{13}C NMR experiments has been used to study the 2-hydroxyalkane/urea inclusion compounds. However, the ordering of the unsymmetric guest molecules in the urea tunnels was difficult to determine via ^{13}C NMR due to difficulties in preparing the mixed-guest inclusion compounds and the chiral nature of the guests. One way of simplifying the spectra, if

the latter is the complicating factor, would be to acquire ^{13}C spectra of inclusion compounds prepared from only one enantiomeric form of the guest. CRAMPS experiments have also been performed and the spectra obtained reveal an interference between the multiple-pulse averaging scheme and the motion of the urea. Corroboration of this was obtained by performing the same experiments on inclusion compounds prepared from d_4-urea, as opposed to h_4-urea.

Interpretation of ^{1}H wideline spectra is difficult, due to their typically broad, featureless nature. However, even for quite mobile systems, comparison of ^{1}H spectra obtained for the protonated and corresponding deuterated compound can help in their interpretation. An alternative approach used, was to correlate the ^{1}H wideline spectrum with, first, ^{13}C chemical shift and, second, ^{1}H chemical shift under homonuclear dipolar decoupling. Due to the fact that the WISE experiment relies on the existence of heteronuclear dipolar interactions, it is perhaps not the most suitable experiment for the study of mobile systems. However, the spectrum obtained does reveal the very different mobility of the host and guest molecules. The homonuclear wideline/multiple-pulse correlation experiment has been used to study the mobility of the 2-dodecanol/urea inclusion compound. However, limited information is available as a result of the narrow chemical shift range exhibited by ^{1}H and hence, the experiment should have more application in ^{19}F NMR, for example, in the study of polymers.

4.11 References

1. M.D. Hollingsworth, K.D.M. Harris, *Comprehensive Supramolecular Chemistry* (Editors: D.D. MacNicol, F. Toda, R. Bishop), 1996, Volume 6, Pergamon, pp. 177-237.

2. K.D.M. Harris, *J. Mol. Struct.*, 1996, **374**, 241.

3. K.D.M. Harris, *J. Solid State Chem.*, 1993, **106**, 83.

4. A.R. George and K.D.M. Harris, *J. Mol. Graphics*, 1995, **13**, 139.

5. K.D.M. Harris and J.M. Thomas, *J. Chem. Soc. Faraday Trans.*, 1990, **86**, 2985.

6. A.J.O. Rennie and K.D.M. Harris, *Proc. R. Soc. Lond. A*, 1990, **430**, 615.

7. K.D.M. Harris and M.D. Hollingsworth, *Proc. R. Soc. Lond. A*, 1990, **431**, 245.

8. J.D. Bell and R.E. Richards, *Trans. Faraday Soc.*, 1969, **65**, 2529.

9. R.K. Harris and A.C. Olivieri, *Prog. NMR Spectrosc.*, 1992, **24**, 435.

10. M. Okazaki, A. Naito and C.A. McDowell, *Chem. Phys. Lett.*, 1983, **100**, 15.

11. K.D.M. Harris and P. Jonsen, *Chem. Phys. Lett.*, 1989, **154**, 593.

12. G.M. Cannarozzi, G.H. Meresi, R.L. Vold and R.R. Vold, *J. Phys. Chem.*, 1991, **95**, 1525.

13. A. El Baghdadi, E.J. Dufourc and F. Guillaume, *J. Phys. Chem.*, 1996, **100**, 1746.

14. R.L. Vold, R.R. Vold and N.J. Heaton, *Adv. Magn. Reson.*, 1989, **13**, 17.

15. M. Okazaki and C.A. McDowell, *J. Mol. Struct.*, 1984, **118**, 149.

16. F. Imashiro, T. Maeda, T. Nakai, A. Saika and T. Terao, *J. Phys. Chem.*, 1986, **90**, 5498.

17. A. Kubo, F. Imashiro and T. Terao, *J. Phys. Chem.*, 1996, **100**, 10854.

18. F. Imashiro, D. Kuwahara, T. Nakai and T. Terao, *J. Chem. Phys.*, 1989, **90**, 3356.

19. S.P. Smart, A. El Baghdadi, F. Guillaume and K.D.M. Harris, *J. Chem. Soc., Faraday Trans.*, 1994, **90**, 1313.

20. M. Farina, *Inclusion Compounds*, (Editors: J.L. Atwood, J.E.D. Davies, D.D. MacNicol), Academic Press, New York, 1980, Volume 2, pp. 69-95.

21. M.D. Hollingsworth and A.R. Palmer, *J. Am. Chem. Soc.*, 1993, **115**, 5881.

22. K.D.M. Harris and P.E. Jupp, *Proc. R. Soc. Lond. A*, 1997, **453**, 333.

23. N.J. Heaton, R.L. Vold and R.R. Vold, *J. Am. Chem. Soc.*, 1989, **111**, 3211.

24. M.D. Hollingsworth and N. Cyr, *Mol. Cryst. Liq. Cryst.*, 1990, **187**, 135.

25. L. Yeo, personal communication.

26. D.M. Grant and E.G. Paul, *J. Am. Chem. Soc.*, 1964, **86**, 2984.

27. R.M. Silverstein, G.C. Bassler and T.C. Morrill, *Spectrometric Identification of Organic Compounds*, Wiley, 5th edition, 1991.

28. A. Nordon, R.K. Harris, L. Yeo and K.D.M. Harris, *Chem. Commun.*, 1997, 2045.

29. L. Yeo and K.D.M. Harris, *Tetrahedron: Asymmetry*, 1996, **7**, 1891.

30. W. Schlenk, *Justus Liebigs Ann. Chem.*, 1973, **7**, 1145.

31. W. Schlenk, *Justus Liebigs Ann. Chem.*, 1973, **7**, 1156.

32. W. Schlenk, *Justus Liebigs Ann. Chem.*, 1973, **7**, 1179.

33. W. Schlenk, *Justus Liebigs Ann. Chem.*, 1973, **7**, 1195.

34. R.K. Harris and P. Jackson, *J. Phys. Chem. Solids*, 1987, **48**, 813.

35. G. Scheler, U. Haubenreisser and H. Rosenberger, *J. Magn. Reson.*, 1981, **44**, 134.

36. R.K. Harris, P. Jackson, L. H. Merwin, B.J. Say and G. Hägele, *J. Chem. Soc., Faraday Trans. 1*, 1988, **84**, 3649.

37. C.F. Ridenour and A. McDermott, *Chemagnetics Applications Note*, October 1993.

38. K. Schmidt-Rohr and H.W. Spiess, *Multidimensional Solid-state NMR and Polymers*, Academic Press, London, 1994.

39. J.G. Powles and J.H. Strange, *Proc. Phys. Soc.*, 1963, **82**, 60.

40. A.E. Aliev, S.P. Smart, I.J. Shannon and K.D.M. Harris, *J. Chem. Soc., Faraday Trans.*, 1996, **92**, 2179.

41. A.E. Aliev, S.P. Smart and K.D.M. Harris, *J. Mater. Chem.*, 1994, **4**, 35.

42. P. Jackson and R.K. Harris, *J. Chem. Soc., Faraday Trans.*, 1995, **91**, 805.

43. A. Naito, A. Root and C.A. McDowell, *J. Phys. Chem.*, 1991, **95**, 3578.

44. M. Mehring, *Principles of High-resolution NMR in Solids*, (Editors: P. Diehl, E. Fluck and R. Kosfeld), Springer-Verlag, New York, 1976.

45. W.P. Rothwell and J.S. Waugh, *J. Chem. Phys.*, 1981, **74**, 2721.

46. D. Suwelack, W.P. Rothwell and J.S. Waugh, *J. Chem. Phys.*, 1980, **73**, 2559.

47. J.R. Long, B.Q. Sun, A. Bowen and R.G. Griffin, *J. Am. Chem. Soc.*, 1994, **116**, 11950.

48. R. Eckman, *J. Chem. Phys.*, 1982, **76**, 2767.

49. J.P. Yesinowski and H. Eckert, *J. Am. Chem. Soc.*, 1987, **109**, 6274.

50. S.F. Dec, C.E. Bronnimann, R.A. Wind and G.E. Maciel, *J. Magn. Reson.*, 1989, **82**, 454.

51. S. Ding and C.A. McDowell, *J. Magn. Reson., A*, 1994, **111**, 212.

52. S. Ding and C.A. McDowell, *J. Magn. Reson., A*, 1995, **117**, 171.

53. J.Z. Hu, J. Zhou, F. Deng, H. Feng, N. Yang, L. Li and C. Ye, *Solid State NMR*, 1996, **6**, 85.

54. B.C. Gerstein, J.Z. Hu, J. Zhou, C. Ye, M. Solum, R. Pugmire and D.M. Grant, *Solid State NMR*, 1996, **6**, 63.

55. B.M. Fung, T-H. Tong, T. Dollase and M.L. Magnuson, *J. Magn. Reson., A*, 1996, **123**, 56.

56. R.R. Ernst, G. Bodenhausen and A. Wokaun, *Principles of Nuclear Magnetic Resonance in One and Two Dimensions*, Oxford University Press, 1991.

57. K. Schmidt-Rohr, J. Clauss and H.W. Spiess, *Macromolecules*, 1992, **25**, 3273.

58. C.E. Bronnimann, C.F. Ridenour, D.R. Kinney and G.E. Maciel, *J. Magn. Reson.*, 1992, **97**, 522.

59. U. Scheler and R.K. Harris, *Solid State NMR*, 1996, **7**, 11.

60. J.C. Cherryman and R.K. Harris, *J. Magn. Reson.*, 1997, **128**, 21.

61. M. Baldus, D.G. Geurts, S. Hediger and B.H. Meier, *J. Magn. Reson., A*, 1996, **118**, 140.

62. K.K. Lau and K.K. Gleason, *ENC Poster*, Orlando, Florida, USA, March 1997.

63. W.K. Rhim, D.E. Elleman and R.W. Vaughan, *J. Chem. Phys.*, 1973, **59**, 3740.

64. D.P. Burum, M. Linder and R.R. Ernst, *J. Magn. Reson., A*, 1981, **44**, 173.

65. U. Haeberlen, *High Resolution NMR in Solids*, Academic Press, New York, 1976.

66. L. Braunschweiler and R.R. Ernst, *J. Magn. Reson.*, 1983, **53**, 521.

67. P. Caravatti, L. Braunschweiler and R.R. Ernst, *Chem. Phys. Lett.*, 1983, **100**, 305.

68. R. Tycko, G. Dabbagh and P.A. Mirau, *J. Magn. Reson.*, 1989, **85**, 265.

69. J.Z. Hu, W. Wang, F. Liu, M.S. Solum, D.W. Alderman, R.J. Pugmire and D.M. Grant, *J. Magn. Reson., A*, 1995, **113**, 210.

70. D. Massiot, B. Touzo, D. Trumeau, J.P. Coutures, J. Virlet, P. Florian and P.J. Grandinetti, *Solid State NMR*, 1996, **6**, 73.

71. M.G. Munowitz, R.G. Griffin, G. Bodenhausen and T.H. Huang, *J. Am. Chem. Soc.*, 1981, **103**, 2529.

72. B.Q. Sun, P.R. Costa, D. Kocisko, P.T. Lansbury and R.G. Griffin, *J. Chem. Phys.*, 1995, **102**, 702.

73. M. Wilhelm, S. Lehmann, C. Jäger, H.W. Spiess and R. Jerome, *Magn. Reson. Chem.*, 1994, **32**, 53.

74. S. Ding and C.A. McDowell, *J. Magn. Reson., A*, 1995, **115**, 141.

75. A.E. Derome, *Modern NMR Techniques for Chemistry Research*, Pergamon Press, Oxford, 1987.

76. J. Clauss, K. Schmidt-Rohr, A. Adam, C. Boeffel and H.W. Spiess, *Macromolecules*, 1992, **25**, 5208.

77. S.G. Breen, *M.Sc. Thesis*, University of Durham, 1996.

78. D.I. Hoult, *Prog. NMR Spectrosc.*, 1978, **12**, 41.

79. R.K. Harris, *Multinuclear Magnetic Resonance in Liquids and Solids - Chemical Applications*, (Editors: P. Granger and R.K. Harris), NATO ASI, Maratea, 1988.

Chapter 5

Solid-state NMR studies of fluoroalkane/urea inclusion compounds

5.1 Introduction

In the previous chapter, the use of solid-state NMR as a probe of guest ordering in urea tunnels was discussed and demonstrated. The compound of interest in this chapter is the 1-fluorotetradecane/urea inclusion compound. Powder X-ray diffraction studies of this compound have shown that it possesses the conventional urea tunnel structure. As 1-fluorotetradecane is an example of an unsymmetric guest, the ordering of the guest molecules will be examined. The fact that one of the end-groups contains both ^{1}H and ^{19}F, while the other contains only ^{1}H, increases the scope of experiments that can be performed. However, due to the fact that these molecules contain both ^{1}H and ^{19}F, equipment is required which has only recently become commercially available. To obtain high-resolution ^{13}C spectra in the solid state of organofluorine compounds, it is necessary to remove both ^{13}C-^{1}H and ^{13}C-^{19}F dipolar interactions. Therefore, both a triple-channel spectrometer and a triple-channel HFX probe are required. To be able to observe ^{19}F, while applying high-power decoupling to ^{1}H, a HF probe is required which has higher isolation between the two channels than a standard HX probe. Higher isolation is required as the frequencies of ^{1}H and ^{19}F are within 6% of each other.

The particular features of interest for fluoroalkane/urea inclusion compounds are the guest ordering preference in the case of unsymmetric guests, guest dynamics and the conformational preference of the guest end-groups. The last-mentioned feature is discussed in depth in Chapter 7 for the 1,10-difluorodecane/urea inclusion compound. The above-mentioned three features contribute to the disordered (both static and dynamic) nature of the inclusion compound: Hence the reason why X-ray diffraction studies are precluded from providing detailed structural information of the

guests. Being a typical incommensurate urea inclusion compound, the 1-fluorotetradecane molecules can be oriented head to head (HH), head to tail (HT) and tail to tail (TT).
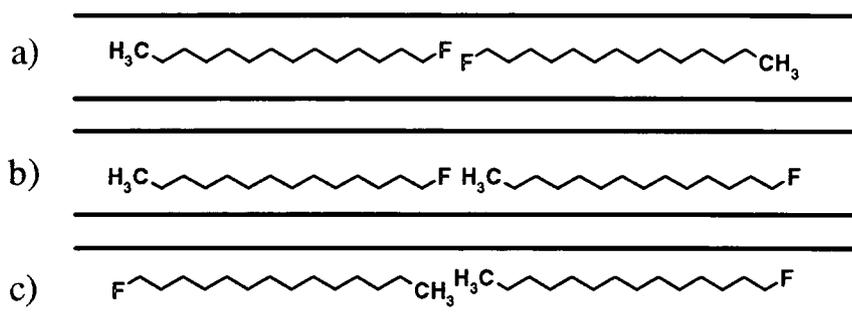
Figure 5.1. Possible ordering of 1-fluorotetradecane, a) head to head (HH), b) head to tail (HT) and c) tail to tail (TT).

As explained in the previous chapter, to assign particular end-group interactions to spectral features, one strategy that has been used involves comparing the spectra of unsymmetric X-Y molecules with that of the corresponding symmetric guest molecules (X-X and/or Y-Y) and/or comparing spectra of compounds containing mixtures of guest molecules (X-Y/X-X and/or X-Y/Y-Y).[1] Hence, inclusion compounds containing symmetric difluoroalkane guests (X-X) and a mixed guest fluoroalkane/alkane (X-Y/Y-Y) have also been studied. This method was used to assign the CH_2F resonances. However, a different approach, which utilises the presence of ^{19}F, has been devised in the work reported here to determine CH_3 end-group interactions.

Below is a list containing the guests in the four urea inclusion compounds studied and the description of their end-groups in terms of X (CH_2F) or Y (CH_3),

a) 1-fluorotetradecane (X-Y),

b) 1-fluorotetradecane/tetradecane (50/50) (X-Y/Y-Y),

c) 1,10-difluorodecane (X-X),

d) 1,12-difluorododecane (X-X).

Potentially, 1-fluorotetradecane contains three NMR active nuclei, ^{13}C, ^{19}F and ^{1}H, that can be used to examine the features of interest. Some are obviously more appropriate to the study of certain properties than others, but experiments have been undertaken involving all three nuclei.

5.2 Fluorine-19 solid-state NMR

For different end-group interactions to be discernible, the chemical shift range of the nucleus of choice should be large. It is also advantageous if the nucleus is particularly sensitive, since the spectrometer time required to obtain good signal to noise spectra is reduced. From these two criteria, ^{19}F NMR would appear to be the ideal choice for probing guest ordering.

5.2.1 Single-pulse ^{19}F experiments

Single-pulse ^{19}F spectra were acquired, both with and without ^{1}H decoupling, at room temperature. The results obtained for the 1-fluorotetradecane/urea inclusion compound are shown in Figure 5.2. Typical spectral conditions were: $\pi/2$ pulse duration, 3 μs; ^{1}H decoupling power, 100 kHz, number of transients, 4; recycle delay, 10 s; acquisition time, 30 ms; MAS rate, 10 kHz. A single peak at -216.7 ppm is obtained in both experiments, although it is particularly noticeable that when ^{1}H decoupling is applied, the ^{19}F peak becomes asymmetric in shape (inset in Figure 5.2b). The sidebands present in Figure 5.2a arise from [19]F-^{1}H dipolar interactions which mask the much less intense sidebands arising from SA. However, in the ^{1}H decoupled spectrum, Figure 5.2b, then only the very weak SA sidebands can be seen. Similar experiments were then carried out on 1,10-difluorodecane, 1,12-difluorododecane and 1-fluorotetradecane/tetradecane (50:50) urea inclusion compounds, with a summary of the results obtained shown in Table 5.1. Within experimental error, all four urea inclusion compounds have the same ^{19}F chemical shift. In a previous solid-state NMR study of urea inclusion compounds containing fluorine-substituted guest molecules, ^{19}F resonances of alkyl fluorides and

trifluoroacetyl groups showed chemical shift differences in the presence of different neighbouring groups.[2] However, in the present case it is not possible to distinguish chemical shifts arising from different end-group interactions, even with the extra resolution afforded from being able to apply ^1H decoupling. This is presumably because the ^{19}F chemical shift difference between end-group interactions in 1-fluorotetradecane is too small to be resolved. Commonly, ^{19}F linewidths are greater than those observed for ^{13}C. In this case, the ^{19}F linewidth is ~ 125 Hz which compares to ~ 12 Hz for the linewidths obtained in ^{13}C spectra. Hence, a combination of these factors prevents different end-group interactions from being observed in the ^{19}F spectrum.
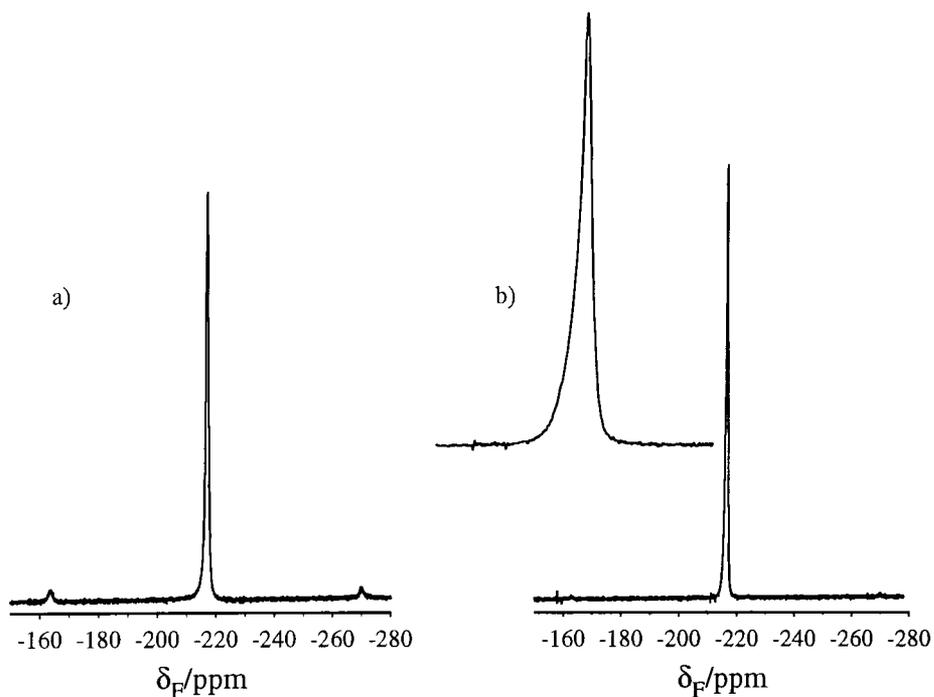
Figure 5.2. Fluorine-19 single-pulse spectra acquired a) without ^1H decoupling and b) with ^1H decoupling, of the 1-fluorotetradecane/urea inclusion compound at 10 kHz. The inset in b) shows the asymmetric shape of the ^1H decoupled spectrum.

guest	δ_F/ppm	$\Delta v_{1/2}$/Hz		$T_1(^{19}F)$/s
		without ^{1}H dec.	with ^{1}H dec.	± 0.1
1-fluorotetradecane	-216.7	180	125	2.0
1-fluorotetradecane/tetradecane (50/50)	-216.7	181	102	2.2
1,10-difluorodecane	-216.9	139	163	1.3
1,12-difluorododecane	-216.8	119	134	1.4

Table 5.1. Summary of solid-state ^{19}F NMR results.

For both the difluoroalkane/urea inclusion compounds, ^{1}H decoupling does not have a significant line narrowing effect. However, as for the 1-fluorotetradecane/urea inclusion compound, ^{1}H decoupling changes the shape of the ^{19}F peak and also removes the ^{19}F-^{1}H dipolar sidebands. For the two urea inclusion compounds containing 1-fluorotetradecane, ^{1}H decoupling does reduce the linewidth. The spin-lattice relaxation times (T_1) for ^{19}F were also obtained and again the difluoroalkane compounds behave differently to the inclusion compounds containing 1-fluorotetradecane. From variable-temperature $T_1(^{19}F)$ experiments (see below), the motion (or one of the motions) of the guest molecules is in the extreme narrowing limit. Hence, the fact that both the difluoroalkane guest molecules have shorter $T_1(^{19}F)$'s than 1-fluorotetradecane can be interpreted as the difluoroalkanes being less mobile. It is possible that different end-group interactions could affect the mobility of the guest molecules.

Variable-temperature NMR can be a very powerful technique for the study of dynamic processes. Hence, ^{19}F single-pulse experiments, both with and without ^{1}H decoupling, were performed at temperatures from 300 K to 137 K. As the temperature was decreased, the shape of the peak did not change in either the decoupled or coupled spectra. A summary of ^{19}F linewidth as a function of temperature for 1-fluorotetradecane, 1,10-difluorodecane and 1,12-difluorododecane urea inclusion compounds is shown in Figure 5.3. The ^{19}F spectra acquired with ^{1}H decoupling do not change dramatically with temperature for any of the three compounds studied. However, for those ^{19}F spectra acquired without ^{1}H decoupling,

at a temperature in the region of ~ 230 K, the linewidths start to show a marked increase. Another noticeable feature is that the linewidth is virtually the same for the difluoroalkane compounds both with and without ^1H decoupling from 300 K to 240 K. However, the linewidth is ~ 200 Hz narrower (in comparison to that observed without ^1H decoupling) on applying ^1H decoupling over the same temperature range for 1-fluorotetradecane/urea.
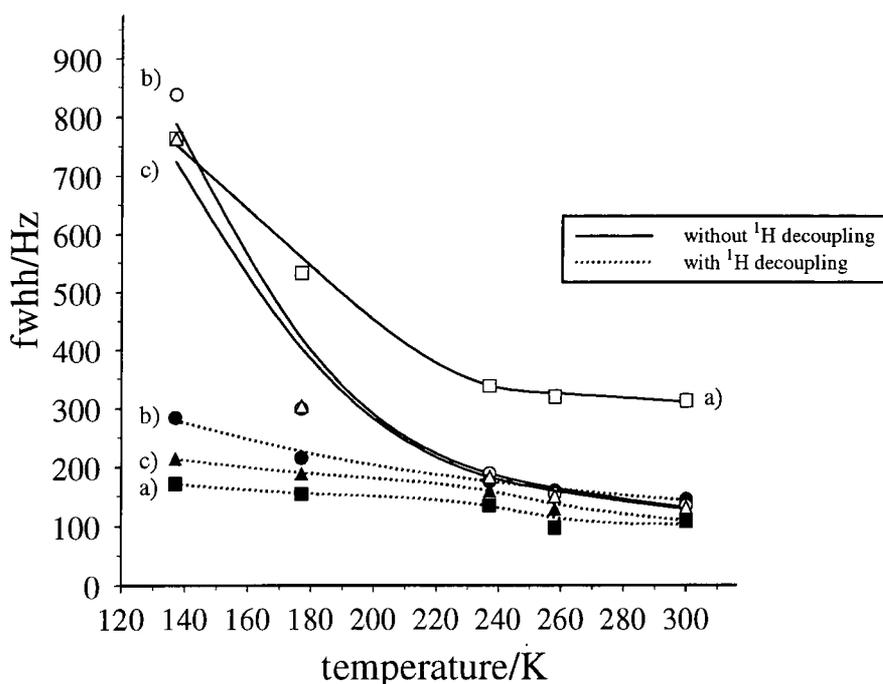
Figure 5.3. Variation of ^{19}F linewidth as a function of temperature for a) 1-fluorotetradecane, b) 1,10-difluorodecane and c) 1,12-difluorododecane urea inclusion compounds. The lines are merely to illustrate the trends.

5.2.2 $^1H \rightarrow {}^{19}F$ cross polarisation

In Chapter 3, the effect of motion upon cross-polarisation dynamics was demonstrated. However, on close inspection of these data it was noticed that not only does the signal intensity critically depend upon the ^1H and ^{19}F cross-polarisation powers, but the actual 'shape' of the peak is also affected. Figure 5.4 shows a stacked plot of the $^1H \rightarrow {}^{19}F$ matching profile of the 1-fluorotetradecane/urea inclusion compound obtained using a standard single-amplitude cross-polarisation sequence,

with selected slices taken from this plot shown on the right hand side of the page. It is clearly evident that the 'single' peak obtained via single-pulse operation is in fact made up of a number of peaks, i.e., it is inhomogeneous. Corroboration of this was provided by a $T_2(^{19}F)$ experiment, performed using a single-pulse spin-echo sequence,[3] with the results obtained suggesting that the 'single' peak is made up of a 'broad' (T_2 of 6 ms) and a 'narrow' (T_2 of 28 ms) peak with relative intensities of 9 and 1, respectively. At all matching conditions, it is always possible to fit the peak obtained via CP within the peak obtained via the single-pulse experiment. Reasons for the inhomogeneous nature of the peak include conformational disorder and different orientations of the guest. However, it is also worth remembering that there is an incommensurate relationship between host and guest. Hence, in principle, every guest molecule is in a different site. To determine the contribution of guest orientational disorder to the peak, the same experiment was repeated on the 1,10-difluorodecane/urea inclusion compound in which guest molecules can only be ordered head to head (CH_2F---FH_2C) in the urea tunnels (Figure 5.5). However, it can be seen that the 1,10-difluorodecane peak also is very dependent upon the cross-polarisation powers. Therefore, guest orientational disorder is not the main reason for the variation in lineshape.

Using the standard single-amplitude cross-polarisation pulse sequence, variable contact time experiments were performed on the 1,10-difluorodecane/urea inclusion compound. Experiments were performed at the Hartmann-Hahn matching condition and at the +1 matching sideband. At the Hartmann-Hahn matching condition, a small variation in the peak shape was observed at different contact times. However, at the +1 matching sideband, a wider range of peak shapes was observed at different contact times. When ramped cross-polarisation was used, the peak shape appears to become less dependent upon the precise matching condition as the ramp 'size' is increased. For comparison, variable contact experiments were performed using the ramp64 pulse sequence at both the Hartmann-Hahn match and the +1 matching sideband. At both matching conditions, the peak shape was invariant to changes in the contact time. A comparison of the spectra obtained at the +1 matching sideband with different contact times, using the single-amplitude cross-polarisation sequence and the ramp64 sequence is shown in Figure 5.6.
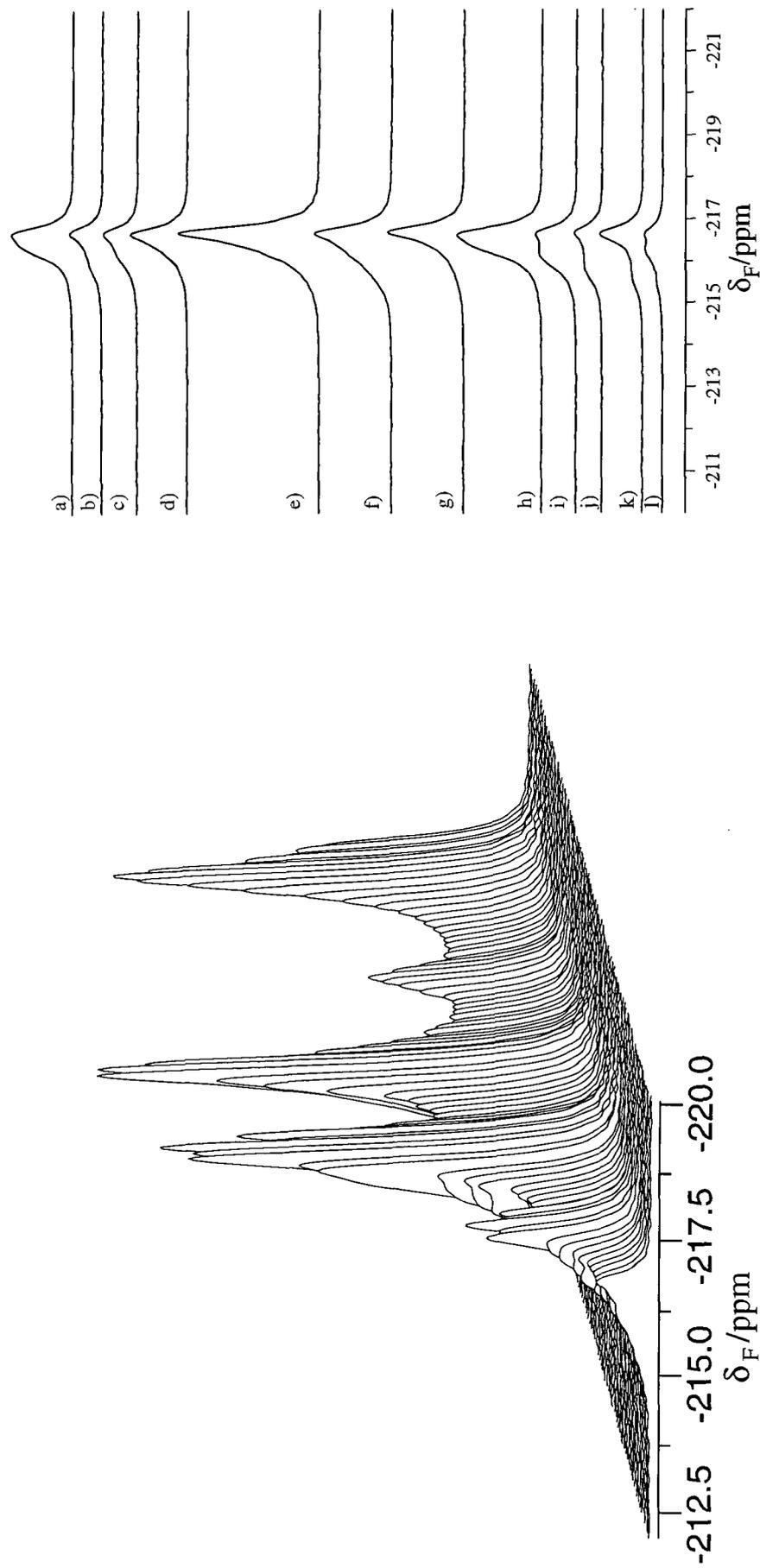
Figure 5.4. $^1H \rightarrow {}^{19}F$ *cross-polarisation matching profile for the 1-fluorotetradecane/urea inclusion compound at 10 kHz. The* ^1H *CP power used was 40 kHz and the* ^{19}F *CP power varies, from front to back in the stacked plot, from 78 kHz to27 kHz. Slices on the right hand side correspond to* ^{19}F *CP powers of a) 27 kHz, b) 35 kHz, c) 37 kHz, d) 39 kHz, e) 49 kHz, f) 52 kHz, g) 57 kHz, h) 62 kHz, i) 64 kHz, j) 66 kHz, k) 71 kHz and l) 74 kHz.*
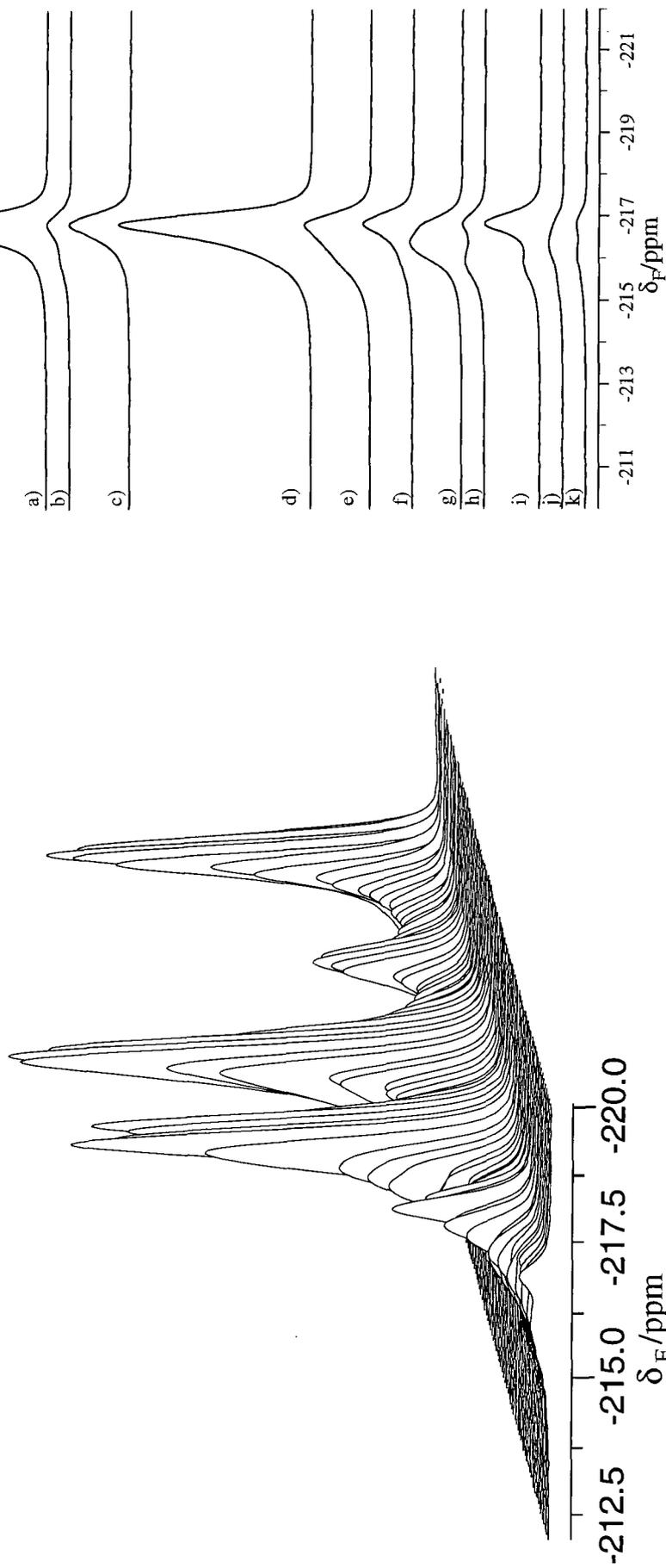
Figure 5.5. $^1H \rightarrow {}^{19}F$ cross-polarisation matching profile for the 1,10-difluorodecane/urea inclusion compound at 10 kHz. The ^1H CP power used was 40 kHz and the ^{19}F CP power varies, from front to back in the stacked plot, from 78 kHz to 27 kHz. Slices on the right hand side correspond to ^{19}F CP powers of a) 27 kHz, b) 32 kHz, c) 38 kHz (Hartmann-Hahn matching condition), d) 48 kHz, e) 50 kHz, f) 54 kHz, g) 62 kHz, h) 66 kHz, i) 68 kHz, j) 74 kHz and k) 77 kHz.
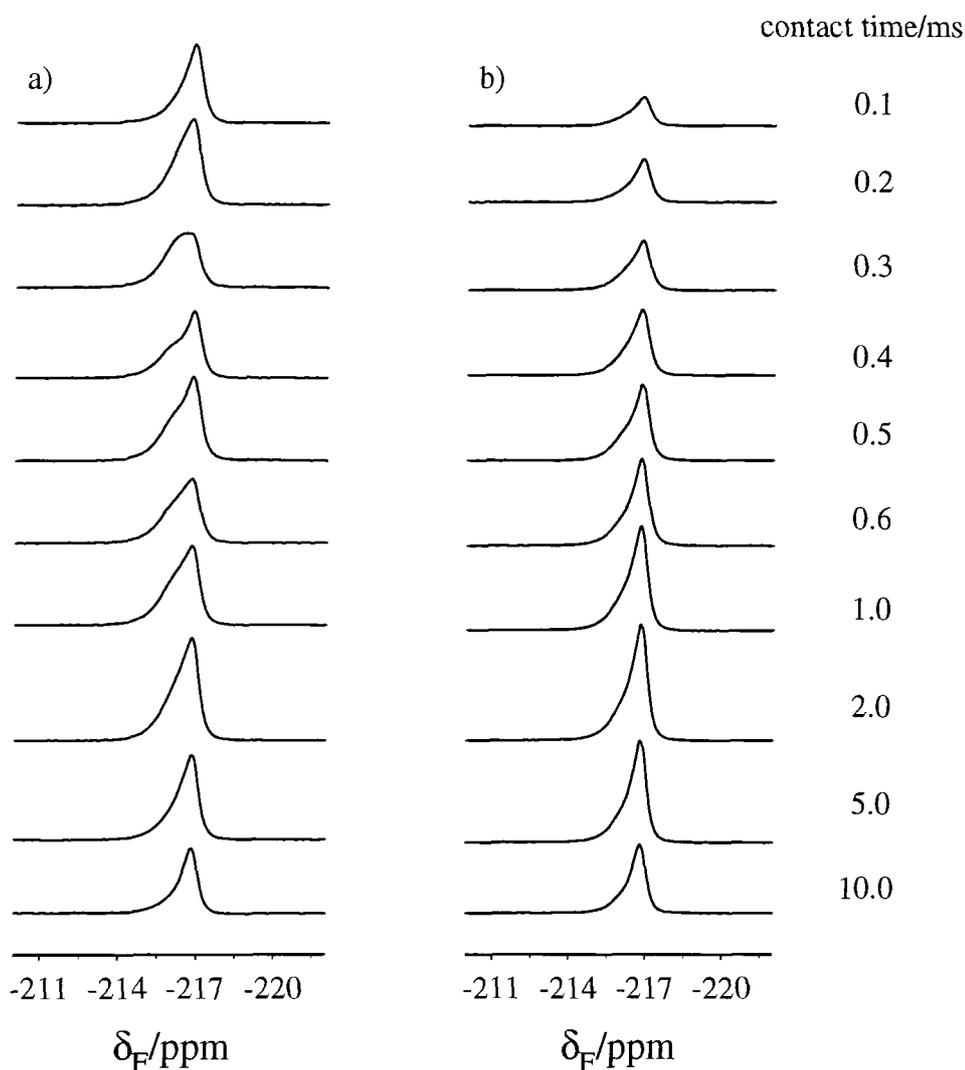
Figure 5.6. $^1H \rightarrow {}^{19}F$ cross-polarisation experiments obtained at the +1 matching sideband using a) single-amplitude cross polarisation and b) ramp64 cross polarisation. The contact time used is shown down the right-hand side. The vertical scale in b) is three times that in a).

The exact origin of the peak shape is not known, although from the cross-polarisation experiments, the signal is thought to be made up of several peaks. The variation in signal intensity as a function of the $^1H/^{13}C$ matching condition has been examined for mixtures of labelled amino acids.[4,5] It was shown that while the CH_2 cross polarises efficiently across a wide range of matching conditions, the cross-polarisation efficiency of the CH_3 and C=O groups is very dependent upon the matching condition. Therefore it is not unreasonable to assume that different parts of the peak cross polarise more efficiently at certain matching conditions than at others.

It is also known that the cross-polarisation dynamics are strongly dependent upon the matching condition and the type of spins involved. Therefore, if the peak is sensitive to the matching condition, then it might also be expected that the peak shape will be dependent upon the contact time.

5.2.3 Variable-temperature ^{19}F T_1 experiments

Variable-temperature $T_1(^2H)$ experiments have previously been used to investigate the dynamics of the 1,10-dibromodecane/urea inclusion compound.[6] Spin-lattice relaxation (T_1) measurements can be used to probe motions occurring on the MHz timescale. As it is the end-groups in the guest molecules that contain the ^{19}F, then, potentially, variable-temperature $T_1(^{19}F)$ experiments could provide a probe of the end-group dynamics. Therefore, $T_1(^{19}F)$ experiments were performed, at temperatures ranging from 300 K to 137 K, on the 1-fluorotetradecane, 1,10-difluorodecane and 1,12-difluorododecane urea inclusion compounds. The inversion-recovery pulse sequence was used, with the initial inversion pulse being a compensated π pulse to allow for tip angles other than 180°. Typical spectral conditions were: $\pi/2$ pulse duration, 3 µs; ^1H decoupling power, 100 kHz; number of transients, 4; MAS rate, 7 kHz; recycle delay, 15-30 s. Data for approximately ten different tau values (the time that the magnetisation is parallel to the z axis) were acquired at each temperature with values ranging from 0.001 s to 15-30 s. A summary of the results obtained is shown in Figure 5.7. It is clear that the system is on the high-temperature side of a T_1 minimum. According to BPP[7] theory, the variation of T_1 with the correlation time, τ_c, is given by,

$$\frac{1}{T_1} = K\left[\frac{\tau_c}{1+\omega^2\tau_c^2} + \frac{2\tau_c}{1+4\omega^2\tau_c^2}\right] \qquad \text{Equation 5.1}$$

where K is a constant and ω is the Larmor frequency. In the extreme narrowing region, $\omega^2\tau_c^2 < 1$, and so,

$$\frac{1}{T_1} = 3K\tau_c \qquad \text{Equation 5.2}$$

On the assumption of Arrhenius behaviour,

$$\tau_c = \tau_0 \exp\left(\frac{E_a}{RT}\right)$$
         Equation 5.3

where R is the gas constant and T is the temperature, the activation energy, E_a, can be determined by plotting $\ln(T_1)$ against $1/T$.
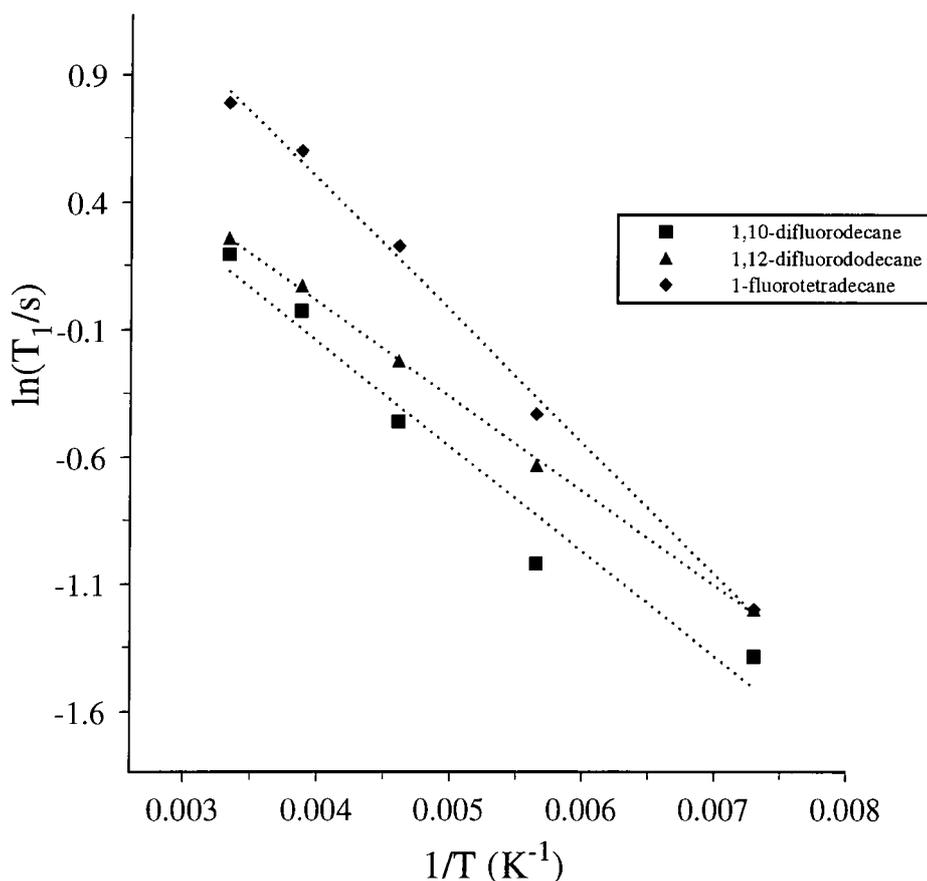
Figure 5.7. Graph plotting $\ln[T_1(^{19}F)]$ against $1/T$ for 1-fluorotetradecane, 1,10-difluorodecane and 1,12-difluorododecane/urea inclusion compounds. The dots represent the best fits to straight lines.

The activation energies, for presumably what is primarily CH_2F end-group rotation, obtained for the 1-fluorotetradecane, 1,10-difluorodecane and 1,12-difluorododecane urea inclusion compounds are 4.3 kJ mol^{-1}, 3.4 kJ mol^{-1} and 3.1 kJ mol^{-1} respectively. Given the limited number of data points, it can be assumed that the activation energy values obtained for all three compounds are approximately equal. In studies of

relaxation in n-alkanes ranging between C_6H_{14} and $C_{40}H_{82}$,[8,9] the activation energy for a methyl group rotation was found to be ~ 10 kJ mol^{-1}.

A particularly noticeable feature of many of the inversion-recovery plots, is that in the region of where the signal changes sign, the peak appears to have different T_1 values across it. An example of this behaviour can be clearly seen in Figure 5.8.
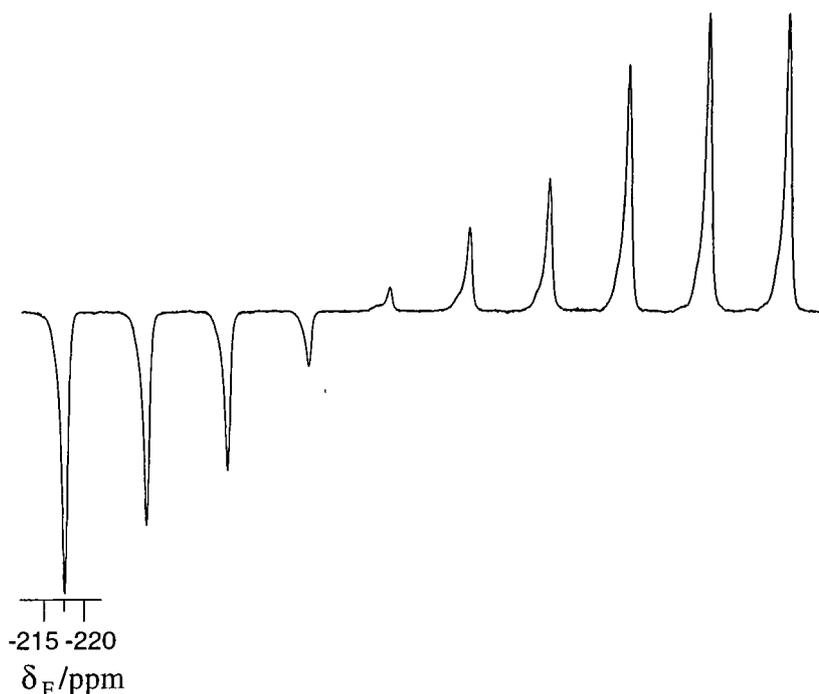
Figure 5.8. Stacked plot of $T_1(^{19}F)$ data obtained for the 1,12-difluorododecane/urea inclusion compound at 217 K.

Therefore, the $T_1(^{19}F)$ results lend weight to the notion that the 'single' peak obtained in ^{19}F spectra is in fact made up of a number of peaks. In many of the spectra which reveal the inhomogeneous nature of the peak, it appears that there is a broad peak underlying a narrower peak, thus corroborating the results obtained from the $T_2(^{19}F)$ experiment. However, the exact reason as to why this should be the case is not clear.

5.2.4 The nuclear Overhauser effect (NOE) in solid-state ^{19}F NMR

The use of the NOE as a tool for structural elucidation has been extensively demonstrated in solution-state NMR. Intramolecular NOE enhancements have been used to determine, for example, whether a functionality is cis or trans, or whether a cyclohexane derivative adopts the chair or boat conformation. On the other hand, intermolecular NOE enhancements[10] have been used to study hydrogen bonding, covalent complexes and closed-shell ion pairs. Of particular relevance to this work is the use of NOE enhancements to study host-guest systems. For example, using NOE experiments it was possible to deduce the orientational preference of p-nitrophenol in α-cyclodextrin.[11] In the p-allylcalix[4]arene/t-butyl amine complex, it was possible to determine, via the observation of an intermolecular NOE, that proton transfer can take place between the amino group and the phenol hydroxy groups.[10]

In the solid state, the observation of NOE enhancements has been applied to the study of miscibility and intermolecular interactions in polymers. In one such study, the rapid rotation of a methyl group in poly(vinyl methyl ether) was used to probe the miscibility of polystyrene-poly(vinyl methyl ether) blends.[23] For an immiscible blend, NOE enhancements were observed for only the poly(vinyl methyl ether) carbons. In comparison, for a miscible blend NOE enhancements were observed for carbons in both components. In PVF_2 and PMMA blends, the ^{19}F transient NOE effect has been used to determine the fact that a substantial number of amorphous PVF_2 molecules are mixed with the PMMA molecules.[12]

5.2.4.1 Theory of NOE

The nuclear Overhauser effect is defined as the change in overall intensity of one resonance (I) that occurs when another resonance (S) is saturated. The origin of the NOE can be seen by looking at the effect of perturbing the populations of the energy levels for a heteronuclear two-spin (IS) system as illustrated in Figure 5.9.
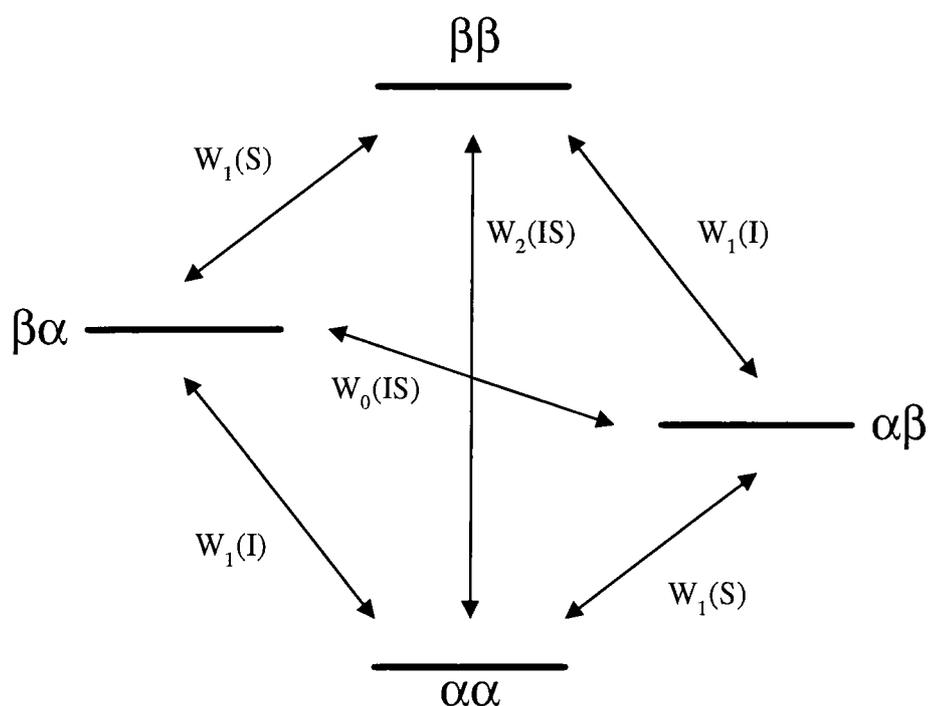
Figure 5.9. Energy level diagram for a heteronuclear two-spin (IS) system.

The intensity of the observed signal depends upon the population difference between the two energy levels of the transition. Using the nomenclature in Figure 5.9, the intensity of the I signal will be proportional to $N_{\beta\alpha}-N_{\alpha\alpha}$ and $N_{\beta\beta}-N_{\alpha\beta}$ while the S signal will be proportional to $N_{\alpha\beta}-N_{\alpha\alpha}$ and $N_{\beta\beta}-N_{\beta\alpha}$. Upon saturation of S, the populations of the $\alpha\alpha$ and $\alpha\beta$ levels will become the same, as will those of the $\beta\alpha$ and $\beta\beta$ levels. The net result will be a decrease in the populations of the $\alpha\alpha$ and $\beta\alpha$ levels while the $\alpha\beta$ and $\beta\beta$ populations will increase. At this stage it is important to note that the I signal intensity is unaffected by saturation of S as there is no change in the population difference across the relevant energy levels. In Figure 5.9 the parameters

W_0, W_1 and W_2 denote the zero, single and double quantum transition probabilities, respectively. With saturation of S and the resultant changes in populations, the transitions given by W_2 and W_0 tend to restore the populations of the energy levels to their equilibrium values. If the transition probability of W_2 is greater than that of W_0, then W_2 relaxation will restore the relative populations of $\alpha\alpha$ and $\beta\beta$. Therefore, the population of $\alpha\alpha$ increases while the population of $\beta\beta$ decreases, resulting in an increase in population difference across the energy levels of the I transition. Hence, a positive NOE will be observed, as the I signal intensity increases upon saturation of S. However, if the transition probability of W_0 is greater than that of W_2, then W_0 relaxation will restore the populations of $\alpha\beta$ and $\beta\alpha$. Therefore, the population of $\alpha\beta$ decreases while the population of $\beta\alpha$ increases, resulting in a decrease in population difference across the energy levels of the I transition. Hence, a negative NOE will be observed, as the I signal intensity decreases upon saturation of S.

The fundamentals of cross relaxation between two heteronuclear spins can be described by the Solomon[13] equations,

$$\frac{dI_z}{dt} = -\left(W_0(IS) + 2W_1(I) + W_2(IS)\right)\left(I_z - I_z^0\right) - \left(W_2(IS) - W_0(IS)\right)\left(S_z - S_z^0\right)$$

$$\frac{dS_z}{dt} = -\left(W_0(IS) + 2W_1(S) + W_2(IS)\right)\left(S_z - S_z^0\right) - \left(W_2(IS) - W_0(IS)\right)\left(I_z - I_z^0\right)$$

Equation 5.4

where I_z and S_z are proportional to the signal intensities of I and S, I_z^0 and S_z^0 are proportional to the equilibrium intensities of I and S, $(W_0 + 2W_1 + W_2)$ defines the longitudinal relaxation rate of spins I and S, and $(W_2 - W_0)$ defines the rate of dipole-dipole transitions (in the absence of scalar relaxation) which give rise to the NOE. Instead of writing Equation 5.4 in terms of transition probabilities, $(W_0 + 2W_1 + W_2)$ and $(W_2 - W_0)$ can be replaced with the symbols ρ and σ (σ is often termed the cross-relaxation rate), respectively. A full derivation of Equation 5.4 can be found in standard texts covering the NOE.[14,15]

5.2.4.2 Steady-state NOE

If a steady state is reached in which the S spin is completely saturated, the populations of the $\alpha\alpha$ and $\alpha\beta$ levels are the same, as are those of the $\beta\alpha$ and $\beta\beta$ levels, and so $S_z=0$. At such a time, $\dfrac{dI_z}{dt} = 0$ and given that $S_z^0 = \dfrac{\gamma_S}{\gamma_I} I_z^0$, rearranging the Solomon equation for the I spin gives,

$$\frac{I_z - I_z^0}{I_z^0} = \frac{\gamma_S}{\gamma_I} \frac{W_2(IS) - W_0(IS)}{W_0(IS) + 2W_1(I) + W_2(IS)} = \frac{\gamma_S}{\gamma_I} \frac{\sigma}{\rho} \qquad \textit{Equation 5.5}$$

where $\dfrac{I_z - I_z^0}{I_z^0}$ defines the NOE in terms of a fractional change in the intensity of I on saturation of S, $f_I\{S\}$. A steady-state NOE experiment typically involves a comparison of single-pulse spectra obtained with and without irradiation of the S spins during the recycle delay.

In order to consider what the maximum theoretical NOE will be, it is necessary to express the transition probabilities, W, in terms of spectral density functions, J(ω),

$$f_I\{S\} = \frac{\gamma_S}{\gamma_I} \frac{6J(\omega_I + \omega_S) - J(\omega_I - \omega_S)}{6J(\omega_I + \omega_S) + 3J(\omega_I) + J(\omega_I - \omega_S)} \qquad \textit{Equation 5.6}$$

where $J(\omega) = \dfrac{2\tau_c}{\left(1 + \omega^2 \tau_c^2\right)}$ (assuming the BPP motional model),[16] and τ_c is the unique relevant motional correlation time. It can be seen immediately that the NOE is dependent on the mobility of the molecules.

$$f_I\{S\} = \frac{\gamma_S}{\gamma_I} \frac{\left[\dfrac{6}{1 + (\omega_I + \omega_S)^2 \tau_c^2} - \dfrac{1}{1 + (\omega_I - \omega_S)^2 \tau_c^2}\right]}{\left[\dfrac{1}{1 + (\omega_I - \omega_S)^2 \tau_c^2} + \dfrac{3}{1 + \omega_I^2 \tau_c^2} + \dfrac{6}{1 + (\omega_I + \omega_S)^2 \tau_c^2}\right]} \qquad \textit{Equation 5.7}$$

The variation in the theoretical NOE enhancement as a function of mobility when ω_I and ω_S are the angular frequencies of fluorine and proton respectively, is shown in

Figure 5.10. Obviously this is for the ideal heteronuclear (dipolar) two-spin case and assumes that there are no other competing relaxation mechanisms,[14,17] and that the molecular tumbling is isotropic. To stand any chance of observing the theoretical NOE, the recycle delay, i.e., the time allowed for the steady-state condition to be achieved, must be of the order of $10 \times T_1$. In solution-state NMR, the presence of dissolved oxygen can severely reduce the NOE enhancement. Frequently, for ^{13}C NMR other paramagnetic species such as $Cr(acac)_3$ are added to solutions to reduce the T_1 for quaternary carbons and hence their NOE enhancements.
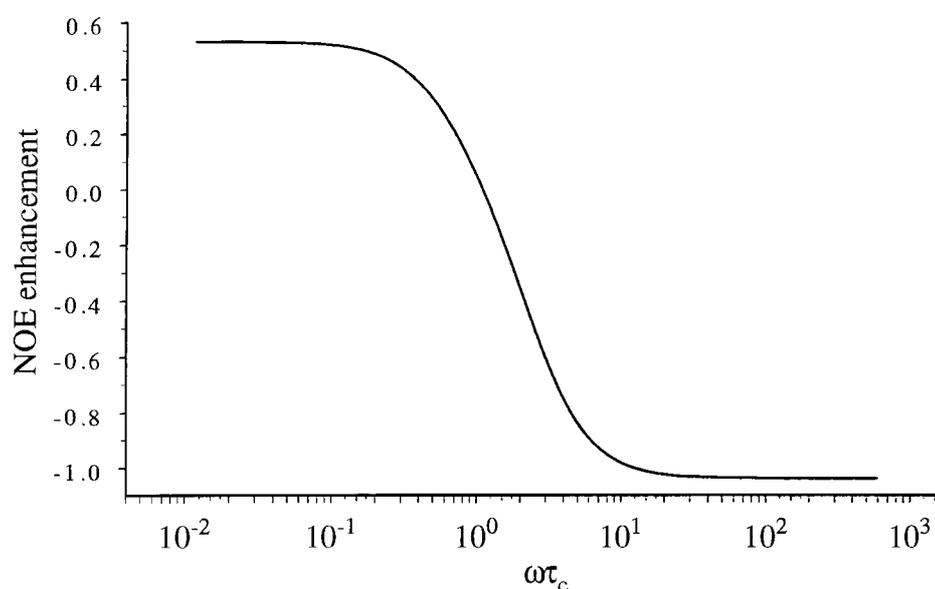
Figure 5.10. Dependence of maximum theoretical NOE enhancement on mobility for $^{19}F\{^1H\}$.

In Figure 5.10, it can be seen that at a certain point, the NOE enhancement will be zero. The value of τ_c at the 'zero crossing point' can be found by setting the numerator in Equation 5.7 to be equal to zero which gives,

$$\tau_c = \sqrt{\left(\frac{5}{\left(\omega_I + \omega_S\right)^2 - 6\left(\omega_I - \omega_S\right)^2} \right)}$$ *Equation 5.8*

Therefore, when $\omega_I \tau_c$ has a value of 1.087 the NOE enhancement is zero. When $\omega_I \tau_c > 1.087$, the NOE enhancement will be negative whereas when $\omega_I \tau_c < 1.087$ the NOE enhancement will be positive. The limiting values for the NOE enhancement

are given in the extreme narrowing condition and the spin-diffusion limit. For relatively small molecules undergoing rapid molecular motion, i.e., in the extreme narrowing region, $\omega\tau_c \ll 1$ and so Equation 5.7 can be simplified to give,

$$f_I\{S\} = \frac{1}{2}\frac{\gamma_S}{\gamma_I} \qquad\qquad \textit{Equation 5.9}$$

which represents the theoretical maximum NOE that can be observed. Hence, the maximum theoretical NOE enhancement is dependent upon the ratio of γ for the two nuclei and is 0.53 for $^{19}F\{^{1}H\}$ experiments. However, for anhydrous hydrogen fluoride at room temperature, the experimentally observed NOE enhancement was found to be ~ 0.3 implying that the two spin model assuming dipole-dipole cross relaxation only in the extreme narrowing region is inadequate.[13] For larger molecules, such as 4-trifluoromethylbenzenesulphonyl-α-chymotrypsin, a $^{19}F\{^{1}H\}$ NOE enhancement of -0.8 was observed,[18,19] which is close to the NOE enhancement of -1.04 when $\omega_I\tau_c \gg 1$. As the NOE enhancement is dependent upon $\omega\tau_c$, in principle for ^{19}F NOE experiments, as for homonuclear ^{1}H NOE experiments, it is possible to change the sign of the NOE by altering ω, i.e., moving to a different field strength, or by altering τ_c, for example by varying the temperature.

5.2.4.3 Transient NOE

After perturbing the population levels of the S spin, the population redistribution as a function of time can be measured via the signal intensity of I. This experiment measures what is termed a transient NOE. In the transient NOE experiment, the S spin is inverted using a 180° pulse and then after a time t, a 90° pulse is applied to the I spin after which the signal is detected.[13] By solving Equation 5.4 it is then possible to measure the kinetics of the NOE experiment. A more involved discussion of this point can be found in the analysis of the appropriate experimental results.

5.2.4.4 The nuclear Overhauser effect in solids

In the solid state, the NOE experiment has been used far less than in solution. Most solid-state NMR experiments use cross polarisation rather than single pulse and so the NOE in not observed. Even if the single-pulse experiment is used, more often than not the possibility of NOE enhancements is not even considered. If a quantitative analysis of single-pulse spectra is required and insufficient recycle delays are used then NOE effects could be important.[27] As the rate of motion slows, then the dipolar fluctuations may no longer be of high enough frequency to stimulate W_0, W_1 and W_2 relaxation, i.e., $J(\omega_I-\omega_S)$, $J(\omega_I)$ and $J(\omega_I+\omega_S)$ will have a negligible contribution to the NOE. This fact wrongly leads to the conclusion that in solids there are no motions fast enough to stimulate relaxation such that a significant NOE enhancement would result. However, some solids are mobile, such as adamantane,[20] hexamethylbenzene,[21] molecules adsorbed on zeolites[22] and various polymers[23,27,28] and so significant NOE enhancements have been observed in such cases. It is also possible to observe NOE enhancements in solids where there exists local motions, such as in methyl groups,[24] of a frequency such that cross relaxation can occur. It is also important to note that the transition probabilities are orientation dependent in solids.[25] Therefore, it may be necessary to use spectral density functions which take into account anisotropic motions to calculate NOE enhancements.[24,26]

In experimental terms, the NOE pulse sequence for solids is different to that for solutions. In solution-state steady-state NOE experiments, saturation of the S spins is simply achieved by leaving the decoupler on during the recycle delay. However, this obviously is not possible in the solid state as the decoupler powers used would very rapidly (after about 200 ms) degrade the probe. An alternative method that has been used to saturate the S spins in the solid state involves applying 90° pulses during the recycle delay at intervals of the order of $T_1(S)$.[27,28]

5.2.4.5 Experimental results

5.2.4.5.1 Variable-temperature $^{19}F\{^1H\}$ steady-state NOE

As previously stated, in solid-state NMR it is not possible to simply leave the decoupler on during the recycle delay to saturate the S spins. Therefore, saturation was achieved with a series of 90° pulses, as reported in previous studies,[27,28] and the spectra obtained using this pulse sequence (Figure 5.11b) were then compared with those obtained using the conventional single-pulse sequence (Figure 5.11a).
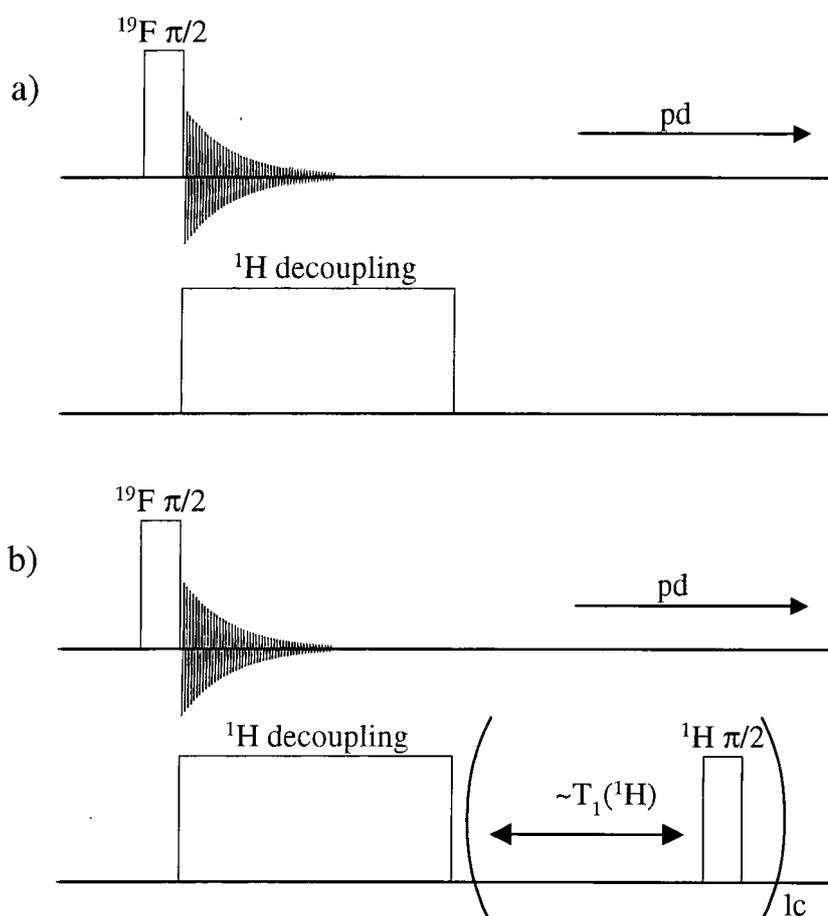
Figure 5.11. Pulse sequences (not interleaved) used to obtain the steady-state NOE enhancement, a) single pulse with ^1H decoupling during the acquisition time and b) single pulse with ^1H decoupling during the acquisition time and recycle delay (denoted pd in figure). In b), lc denotes a loop counter parameter in the pulse program, which is used to apply pulses at regular intervals during the recycle delay.

The experimentally observed NOE values are expressed in terms of a fractional enhancement, $f_I\{S\}$ which is calculated from $\dfrac{I_z - I_z^0}{I_z^0}$ where I_z and I_z^0 are proportional to the ^{19}F signal intensities in the NOE and single-pulse spectra respectively. Typical spectral conditions were: $\pi/2$ pulse duration, 3 µs; ^1H decoupling power, 100 kHz; MAS rate, 7 kHz; number of transients, 32; number of dummy pulses, 4; interval between ^1H 90° pulses in recycle delay, 10 ms; recycle delay, 30 s. At room temperature, a fractional NOE enhancement of -0.16 was obtained for the 1-fluorotetradecane/urea inclusion compound. Variable-temperature NOE experiments were then performed at temperatures ranging from 314 K to 141 K, with the results obtained shown in Figure 5.12. Unfortunately, due to probe and sample limitations, it was not possible to go any lower or higher in temperature. However, it can be seen that at the two limiting temperatures of 314 K and 141 K (Figure 5.13), the NOE is negative whereas in the intervening temperature region the NOE goes through a maximum. The variation of the NOE with temperature (assuming Arrhenius behaviour) is clearly not as predicted for the two-spin case undergoing isotropic motion (Figure 5.10). For 1-fluorotetradecane in its free state (liquid), a value of ~ 0.5 for $f_I\{S\}$ was obtained, which is the value predicted by theory in the extreme narrowing limit.
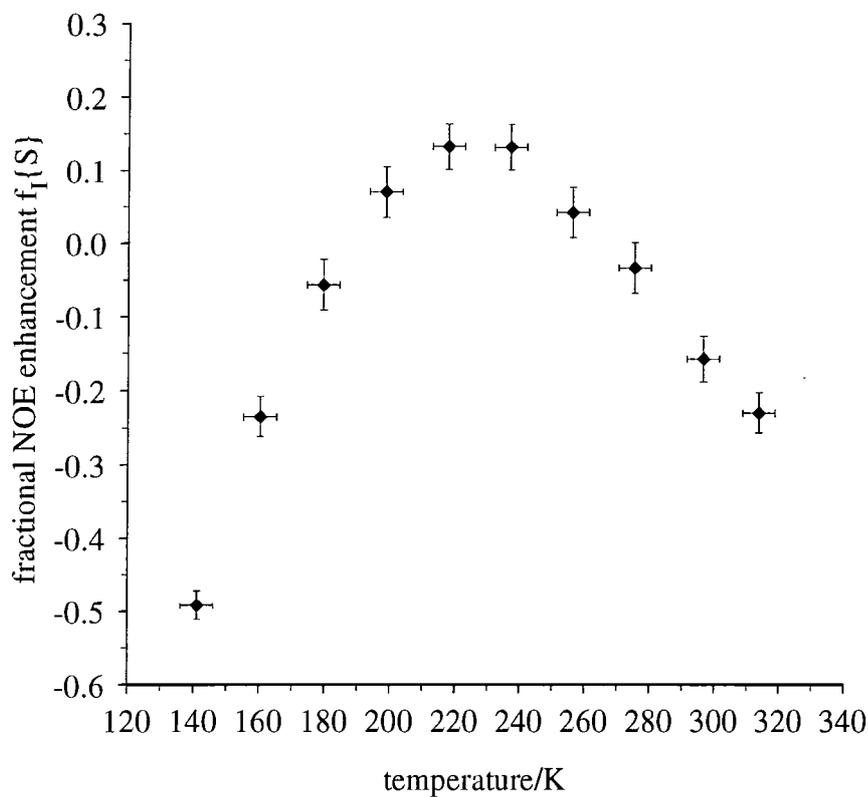
Figure 5.12. Graph plotting fractional NOE enhancement for the ^{19}F peak of 1-fluorotetradecane/urea as a function of temperature. The fractional NOE enhancement values were obtained from peak integrals.
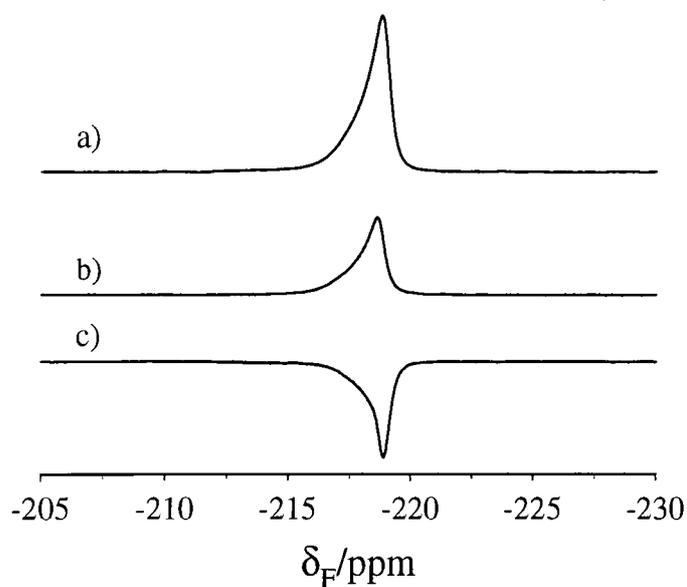
Figure 5.13. $^{19}F\{^1H\}$ spectra of 1-fluorotetradecane/urea at 141 K obtained a) without NOE, b) with NOE and c) is the difference spectrum.

Frequently, the reason for not observing the theoretically predicted NOE enhancement is the existence of other sources of relaxation such as SA, scalar, spin-rotation and quadrupolar. This is accommodated by adding a so-called 'leakage' term, ρ^*, to the denominator of Equation 5.5, which has the effect of increasing the NOE at the spin-diffusion limit if one assumes that ρ^* is invariant with $\omega\tau_c$. A minimum can then be predicted in a plot of NOE enhancement against $\omega\tau_c$ as shown in Figure 5.14. Therefore, this reason cannot explain why as the temperature is increased the NOE becomes negative again. Another complicating factor is the number of spins involved in the NOE, which has so far assumed to be two. In solid-state NMR it is not possible to selectively saturate only one proton frequency and this is the very reason why it is not possible to observe ^1H homonuclear NOE enhancements in solids. The Solomon equations have been derived to describe NOE enhancements in multiple-spin systems.[14] However, for the particular case in which all S spins are saturated it can be shown that,[14] irrespective of the geometry and the number of S spins, the same theoretical $f_I\{S\}$ is obtained as for the two-spin case.
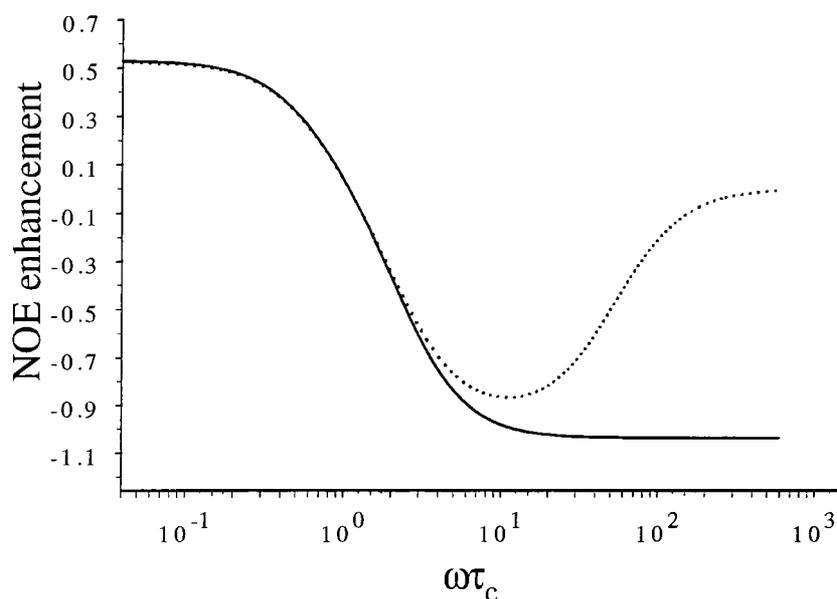
Figure 5.14. Comparison of NOE enhancement with $\rho^*=0\ s^{-1}$, i.e., no other competing relaxation mechanisms, (solid line) and with $\rho^*=0.1\ s^{-1}$ (dotted line).

Anisotropic motion can also affect the NOE enhancement observed. In this case, the motion of the 1-fluorotetradecane is clearly anisotropic due to its confinement within the urea tunnels. Spectral density functions have been derived for methyl group rotation in an MAS experiment.[24] The equations are dependent upon the angle between the C_3 axis of rotation and the internuclear vector of the relevant spin pair, Δ, and the angle between the C_3 axis and the MAS axis, β (Figure 5.15). Assuming that cross relaxation occurs between ^1H and ^{19}F in the same CH_2F end-group, then the H---F internuclear vector is approximately at 90° to the C_3 axis.
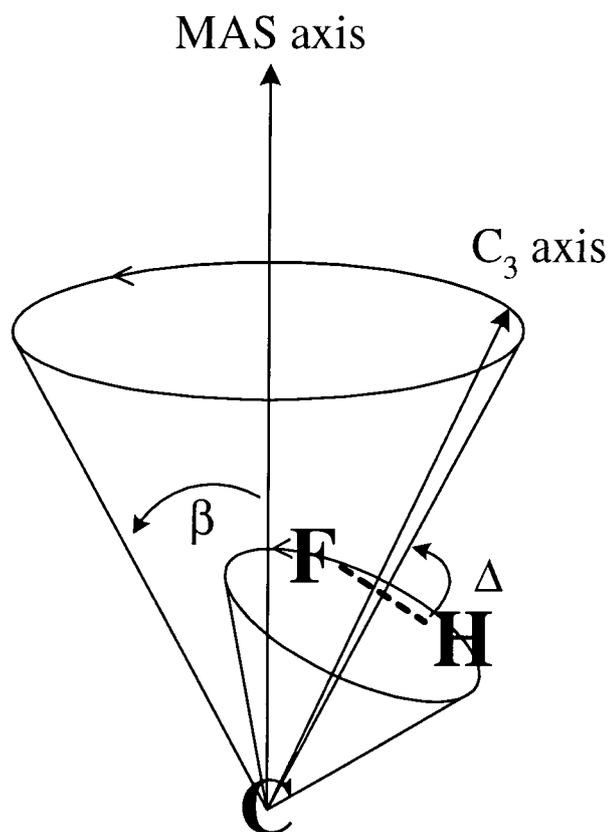
Figure 5.15. Motion of the H---F internuclear vector in a MAS experiment.

Allowing for all possible orientations of the C_3 axis with respect to the MAS axis, i.e., taking a powder average, it is then possible to calculate the effect of anisotropic motion on the NOE enhancement (Figure 5.16). Although anisotropic motion does affect the NOE enhancement, clearly such effects cannot explain the variation of NOE with temperature observed. It has also been suggested by $^1H \rightarrow ^{19}F$ cross polarisation and $T_1(^{19}F)$ experiments that the ^{19}F resonance is in fact made up

of more than one peak. The reason why it has been possible to detect this is assumed to be because there are different rates of motions occurring across the peak. The implication of this is that there is a distribution of correlation times and this can also reduce the NOE enhancement observed.
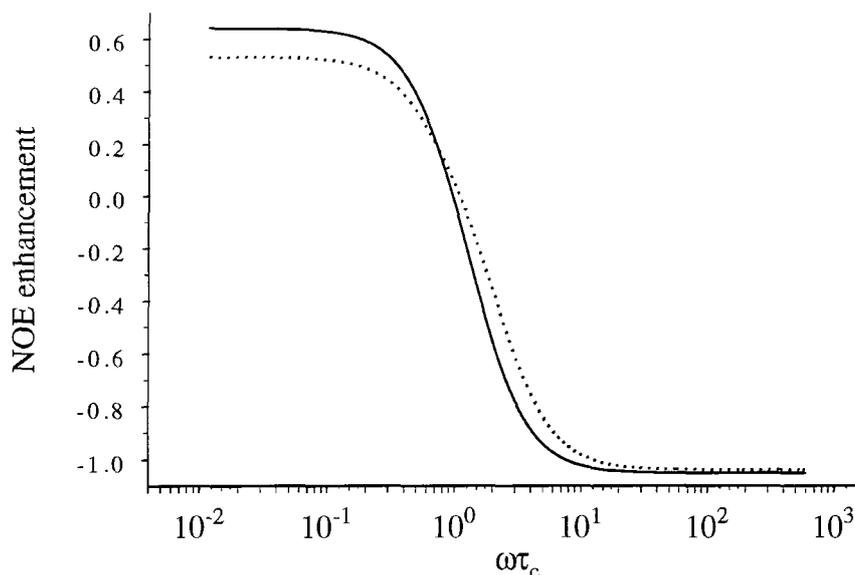
Figure 5.16. Comparison of NOE enhancement calculated assuming isotropic (dotted line) and anisotropic (solid line) motion.

5.2.4.5.2 Transient NOE experiments

The pulse sequence used was that first suggested by Solomon.[13] A 180° pulse is applied to the S spins, ^{1}H, and then a 90° pulse is applied to the I spins, ^{19}F, after a time denoted t in Figure 5.17. Hence by varying t, it is possible to monitor cross relaxation between ^{1}H and ^{19}F. Typically, spectra were acquired with 12 different values of t per experiment, ranging from 10 μs to 30 s. Other spectral conditions were: ^{19}F π/2 pulse duration, 3 μs; ^{1}H π pulse duration, 6 μs; ^{1}H decoupling power, 100 kHz; MAS rate, 7 kHz; number of transients, 4; recycle delay, 30 s. Experiments were performed at temperatures ranging from 314 K to 141 K, with the results of the experiment performed at 141 K shown in Figure 5.18.
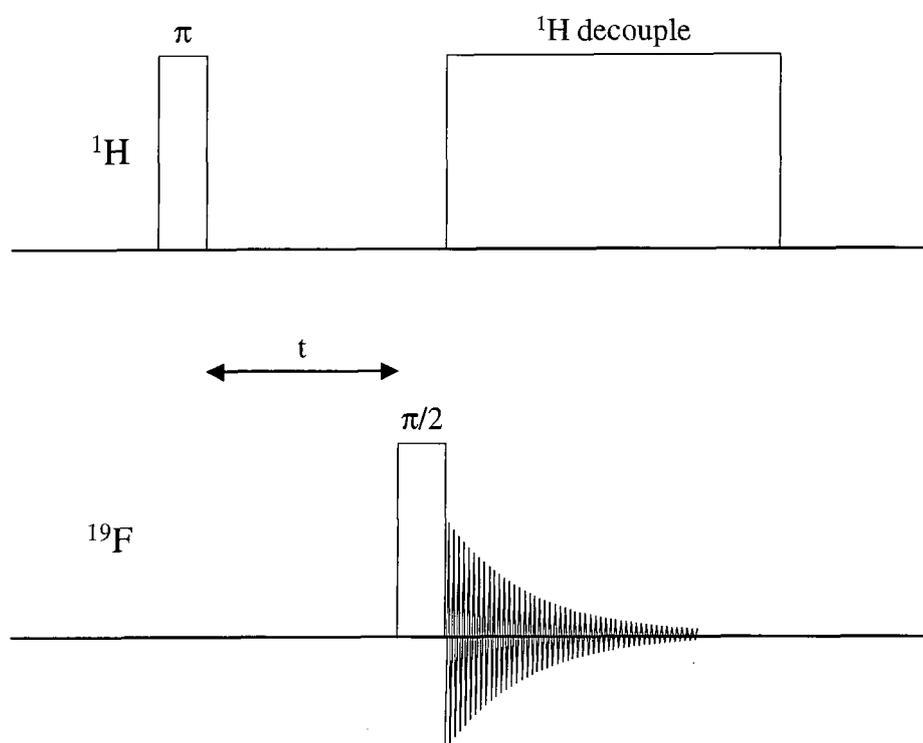
Figure 5.17. Pulse sequence used to observe transient NOE effects.
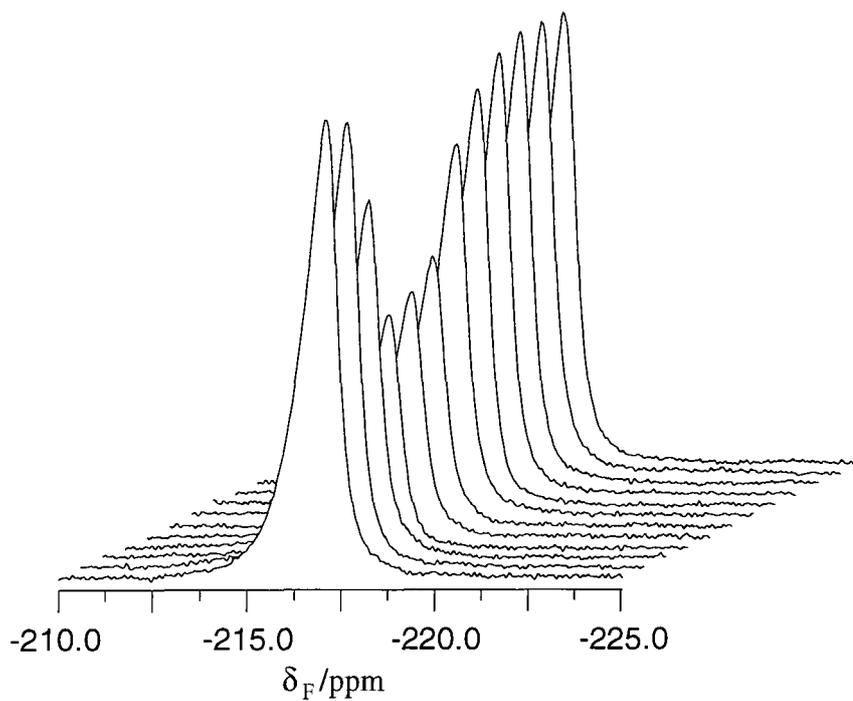
Figure 5.18. Fluorine-19 transient NOE experiment ran at 141 K.

Before showing the results of the experiments performed at the other temperatures, it is necessary to discuss the equations to which such data are fitted. In the transient NOE experiment performed on HF, the number of I spins was equal to the number of S spins. Although Solomon equations for an unequal number of I and S spins have been derived and solved, for simplicity the equations to which the data have been fitted are those for equal numbers of I and S spins. The cross relaxation between two spins can be described by,

$$\frac{dI_z}{dt} = -\rho(I_z - I_0) - \sigma(S_z - S_0)$$

$$\frac{dS_z}{dt} = -\rho'(S_z - S_0) - \sigma(I_z - I_0)$$

Equation 5.10

It will be assumed that, $\rho = \rho'$, which is perfectly valid in the extreme narrowing limit. However, even when outside this region, this equality will hold approximately for ^{1}H and ^{19}F as their Larmor frequencies are so close (within 6 %).[13,30] The solution to these equations with initial conditions of $S_z = -S_z^{\,0}$ and $I_z = I_z^{\,0}$ is,

$$\frac{I_z - I_0}{I_0} = \left[-e^{-t(\rho+\sigma)} + e^{-t(\rho-\sigma)} \right]$$

Equation 5.11

$$\frac{S_z - S_0}{S_0} = \left[-e^{-t(\rho+\sigma)} - e^{-t(\rho-\sigma)} \right]$$

Therefore, if the S spins are inverted at time t=0, then the return of S_z and I_z to equilibrium is biexponential. In this case, the relaxation of S_z is given by two rising exponentials, whereas the relaxation of I_z can be described by a 'fast' rising exponential and a 'slow' decaying exponential. The equation describing the I spins in Equation 5.11 is for when the NOE enhancement is positive, i.e., σ is positive. When σ is negative, the signs of the exponentials are simply reversed. From the values of σ and ρ, it is then possible to resolve two spin-lattice relaxation times, denoted T_1 and D_1,

$$T_1 = \frac{1}{(\rho+\sigma)} \quad \text{and} \quad D_1 = \frac{1}{(\rho-\sigma)} \qquad \textit{Equation 5.12}$$

Typically, spin-lattice relaxation times (T_1) are obtained using the inversion-recovery experiment by 'fitting' the data to a single exponential. However, in

two-spin and multi-spin systems where cross relaxation can occur, relaxation in such systems is biexponential (Equation 5.11). Therefore, 'T_1' obtained from fitting data to a single exponential is no longer formally defined. The reason for this can be seen, if one considers an inversion-recovery experiment performed on a two-spin, ^1H and ^{19}F, system. If the ^{19}F spin is initially inverted, as it relaxes back to equilibrium, a transient NOE appears at the ^1H. However, as magnetisation builds up at the ^1H, the ^1H itself will return to equilibrium. One mechanism available to the ^1H for the restoration of its equilibrium state is cross relaxation with ^{19}F, which hinders the relaxation of ^{19}F back to an equilibrium state.

The results of the transient NOE experiments are shown in Figure 5.19. In the steady-state NOE experiment, with increasing temperature, the NOE enhancement starts off negative then becomes positive before becoming negative again. Hence, the sign of the initial build up of the ^{19}F signal in the transient NOE experiment follows the sign of the steady-state NOE enhancement. When the steady-state NOE enhancement is zero, it therefore follows that the transient NOE results at the corresponding temperatures will be difficult to fit. Hence, at 179 K and 275 K, where the NOE enhancement is virtually zero, the results have not been fitted. The values obtained for σ, ρ, T_1 and D_1 are summarised in Table 5.2.

Temp/K	σ/s^{-1}	ρ/s^{-1}	T_1/s	D_1/s	R^2
141	-1.51	2.30	0.26	1.27	0.99
160	-0.50	1.54	0.49	0.96	1.00
199	0.08	0.78	1.16	1.43	0.97
218	0.28	0.67	1.05	2.56	0.96
237	0.23	0.57	1.25	2.94	0.99
256	0.17	0.44	1.64	3.70	0.86
296	-0.24	0.54	1.28	3.33	0.97
314	-0.74	0.98	0.58	4.17	0.92

Table 5.2. Values obtained for σ, ρ, T_1 and D_1 (R^2 denotes the sum of differences squared).
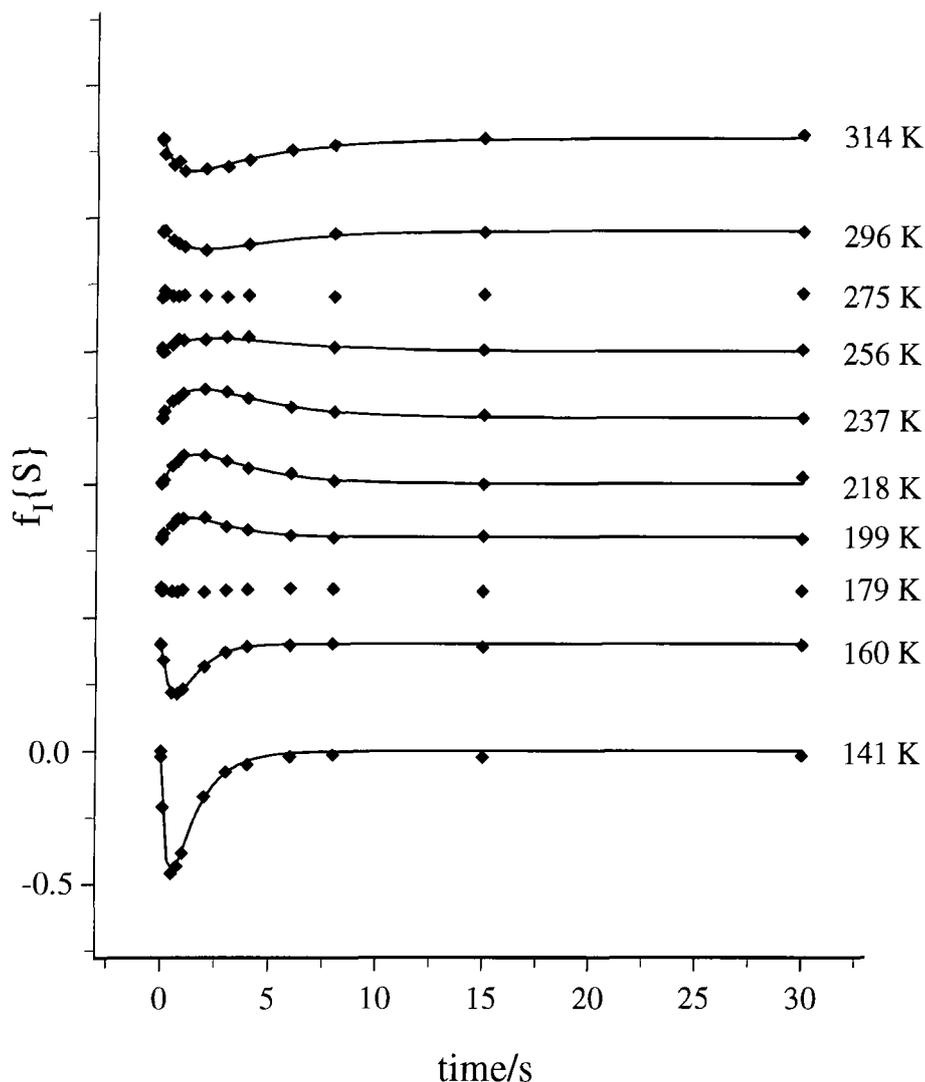
Figure 5.19. Variable-temperature transient NOE experiments. The solid lines indicate the best fit through the experimental data.

The temperature dependence of σ and σ/ρ is shown in Figure 5.20 while that of T_1 and D_1 is shown in Figure 5.21. Variable temperature $T_1(^{19}F)$ data obtained via the inversion-recovery experiment are also shown for comparison. The variation of σ/ρ from the transient NOE experiment (Figure 5.20) parallels that of the steady-state NOE (Figure 5.12), as expected. In studies of PVF_2,[12,29,30] where there was a minimum in σ/ρ, there was also a minimum in the $T_1(^1H)$ plot. Hence, it was possible to ascribe the occurrence of certain relaxation processes to the features in the NOE plots. However, in this case the T_1 plot does not show any well-defined features, except perhaps a maximum centred at about 260 K.
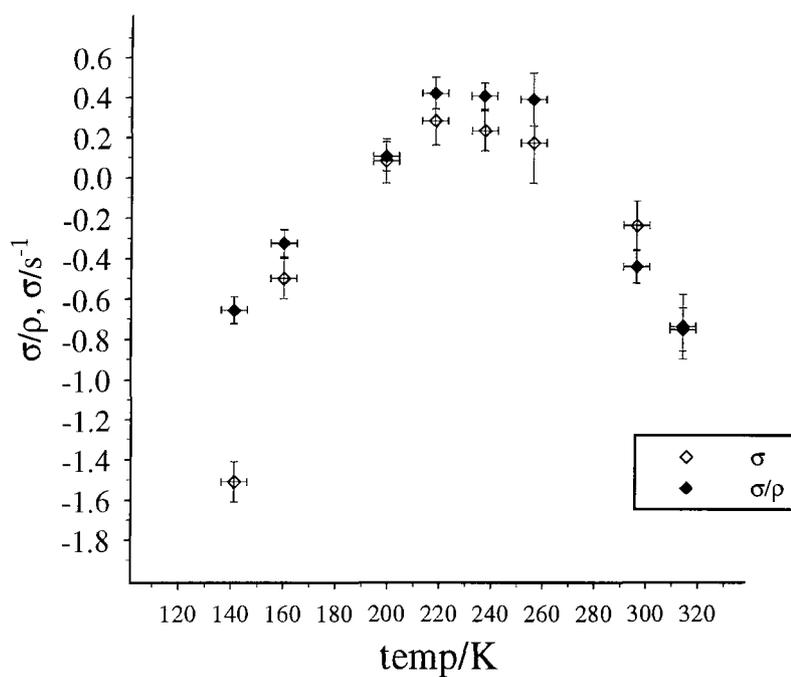
Figure 5.20. Temperature dependence of σ and σ/ρ.
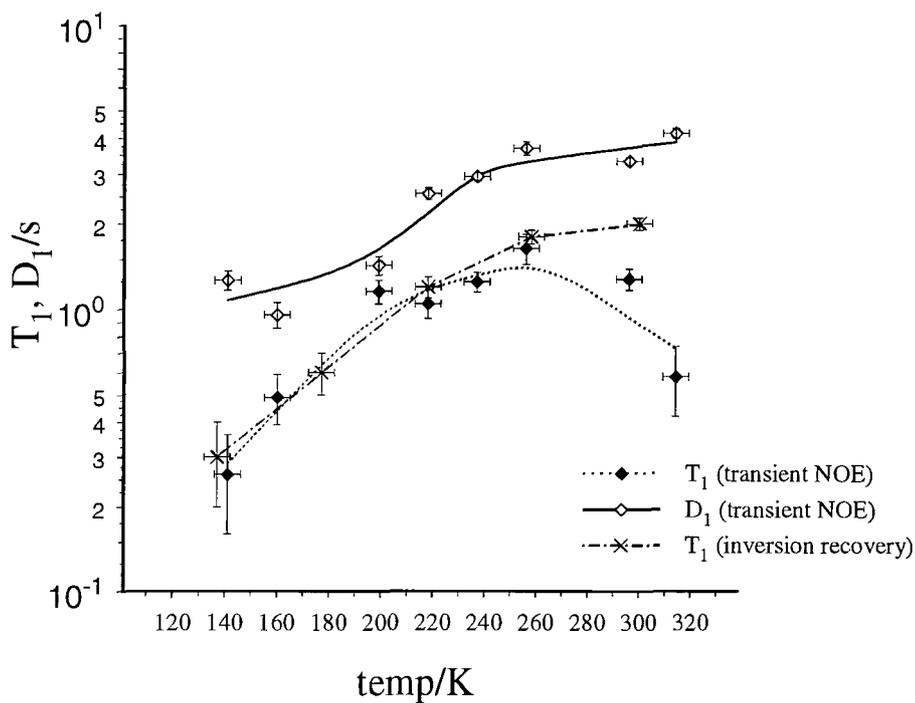
Figure 5.21. Temperature dependence of T_1 and D_1. The lines are merely to illustrate the trends.

From the variation of NOE with temperature for the 1-fluorotetradecane/urea inclusion compound, it appears that there is more than one motional process occurring. A $^{19}F\{^1H\}$ steady-state NOE experiment was performed at room temperature on a trifluorinated steroid,[31] in which the motion is thought to be much simpler. In such a compound, there are three different F environments, CF, CHF and CH_2F. For all three sites the observed NOE enhancement was 0.23. This is at first sight surprising for such a rigid molecule in comparison to the mobile 1-fluorotetradecane guest molecules, which gave rise to an NOE enhancement of -0.16. If it is assumed that the only motion that is rapid enough for NOE enhancements to occur in the trifluorinated steroid is rotation of the CH_2F group then the observation of a positive NOE enhancement is not unexpected. The reason why the NOE enhancement is the same for all three fluorines probably arises from the fact that all S spins are saturated. In $^{13}C\{^1H\}$ NOE experiments, irradiation of all ^1H results in the same NOE enhancement factor for CH, CH_2 and CH_3. However, it is known that there is spin diffusion among the fluorines which could also account for this observation.[31]

Returning to the 1-fluorotetradecane/urea inclusion compound, which also has a rapidly rotating CH_2F group, there must be additional motions which are causing the NOE enhancement to be negative. From previous ^2H NMR studies, the guest motions in alkane/urea inclusion compounds have been identified as rapid ($> 10^7$ Hz) reorientation of the whole molecule, rapid torsional libration about the penultimate C-C bond and rapid CH_3 rotation.[32] However, in a ^2H NMR study of 1,10-dibromodecane/urea,[6] all the CD_2 groups behaved the same on the ^2H NMR timescale, thus implying that torsional libration about the penultimate C-C bond is restricted. As the temperature is increased, the guest motions just described will tend to increase and so it seems unlikely that such guest motions are responsible for the observation of negative NOE enhancements at higher temperatures. It is also noticeable that $T_1(^{19}F)$ increases with increasing temperature, implying that the motion of the CH_2F, in the 137-300 K temperature range, is in the extreme narrowing limit, i.e., $\omega\tau_c < 1$, of the T_1 curve. For the NOE enhancement to be negative, the transition probability of W_0 must be greater than that of W_2. For an increase in zero quantum transitions, there must be an increase in molecular motions at a frequency of

~$(\omega_I - \omega_S)$. However, as already explained, the guest motions are too rapid ($> 10^7$ Hz) to increase W_0 relative to W_2. In all the discussions so far, the urea (host) molecules have been neglected when considering the NOE. It is known, from ^{2}H NMR studies,[6] that at room temperature the urea molecules undergo 180° flips at a rate of 5×10^6 MHz. Therefore, it is possible that the reason for the NOE becoming negative at higher temperatures could be the motion of the urea molecules, which is of the correct order of magnitude to cause an increase in W_0 transitions. It could equally be possible that additional guest motions, other than those described above, are responsible for the negative NOE enhancement if they are of the appropriate order of magnitude.

Therefore, the initial increase in the NOE enhancement as the temperature is increased is consistent with an increase in molecular motion. However, as the temperature is increased above 200 K, it is possible that the onset of additional motions on the MHz timescale, serve to reduce the NOE enhancement.

5.3 Solid-state ^1H NMR

The use of ^1H NMR in the solid state is limited by the narrow ^1H chemical shift range and the strong ^1H-^1H homonuclear dipolar interactions. Frequently, in the solid state, even at MAS rates of the order of 10 kHz, broad, relatively featureless spectra result. However, in cases where there are particularly mobile species present, it can be possible to resolve a mobile component from a broad background. The fact that the $^1H \rightarrow \,^{19}F$ CP matching profile has broken up into sidebands with a MAS rate of 10 kHz suggests that the ^1H spectrum at this speed would be relatively narrow (Figure 5.22a). The broader peaks underlying the narrower ones can be attributed to the urea ^1H, as in the $^{19}F \rightarrow \,^1H$ CP spectrum (Figure 5.22b) acquired with a contact time of 1 ms, only two narrow peaks are observable. The narrow peaks can be assigned as arising from ^1H in the CH_2F (4.0 ppm) and in the alkyl chain (1.0 ppm). An expansion of the two spectra in this region is shown in Figure 5.23 along with ^1H CRAMP spectra acquired both with and without ^{19}F decoupling. It is worth pointing out that ^{19}F decoupling was not used in the ^1H single-pulse and $^{19}F \rightarrow \,^1H$ CP spectra. This is because at the MAS rate used, 10 kHz, the effect of ^1H-^{19}F dipolar interactions are removed. However, in the ^1H CRAMP spectra, it can be seen that ^{19}F decoupling does improve the resolution of the CH_2F peak because a much slower MAS rate was used (800 Hz).
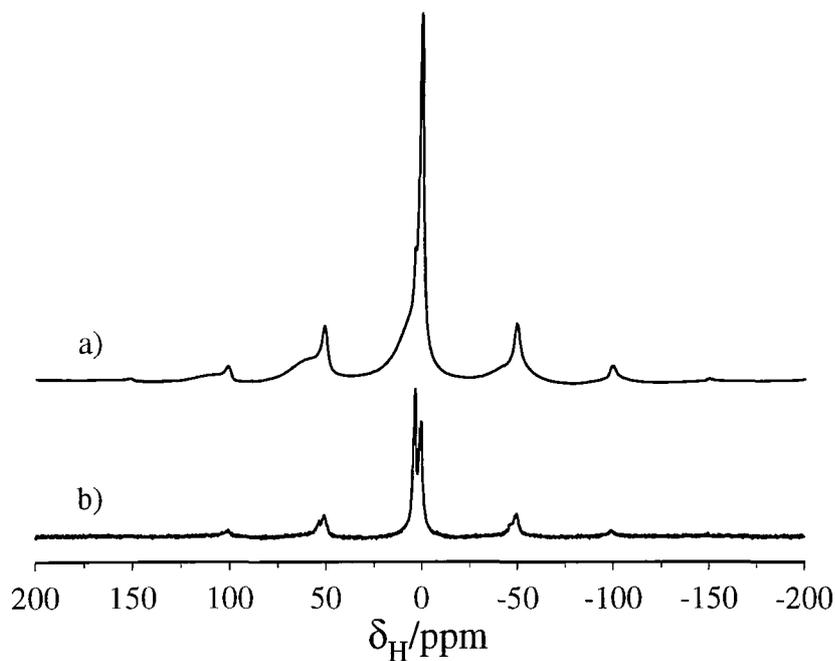
Figure 5.22. Solid-state ^1H NMR spectra of the 1-fluorotetradecane/urea inclusion compound at 10 kHz obtained using a) single pulse and b) $^{19}F \rightarrow {^1H}$ cross polarisation with a contact time of 1 ms.
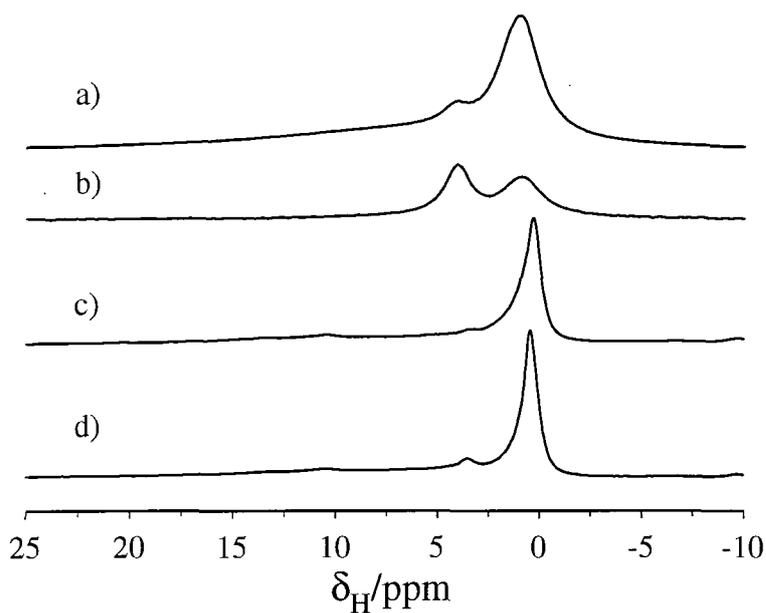
Figure 5.23. Solid-state ^1H NMR spectra of the 1-fluorotetradecane/urea acquired using a) single pulse at 10 kHz, b) $^{19}F \rightarrow {^1H}$ CP with a contact time of 1.0 ms at 10 kHz, c) BR-24 at 800 Hz and d) BR-24 with ^{19}F decoupling at 800 Hz.

In principle, the $^{19}F \rightarrow {}^1H$ cross-polarisation experiment can be used to selectively detect the end-group ^1H and those adjacent, but only if relatively short contact times are used. Therefore, $^{19}F \rightarrow {}^1H$ cross-polarisation spectra were obtained for 1-fluorotetradecane/urea and 1,10-difluorodecane/urea inclusion compounds at contact times ranging from 0.1 ms to 9.0 ms. However, because of the combination of the narrow chemical shift range exhibited by ^1H and the relatively broad signals (fwhh ~ 200 Hz), it was not possible to distinguish different end-group interactions between 1-fluorotetradecane molecules. At all the contact times, only two peaks were obtained at ~ 1 ppm and 4.1 ppm for both compounds which can be assigned as CH_2 (and CH_3 for 1-fluorotetradecane) and CH_2F respectively. The spectra obtained using a contact time of 1.0 ms are shown in Figure 5.24.
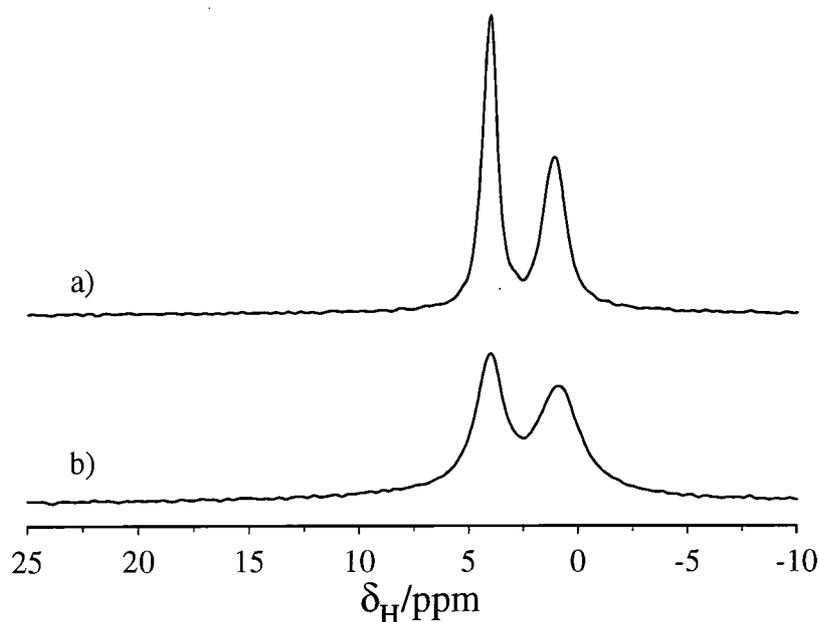
Figure 5.24. Solid-state $^{19}F \rightarrow {}^1H$ CP spectra of a) 1,10-difluorodecane/urea and b) 1-fluorotetradecane/urea inclusion compounds at 10 kHz with a contact time of 1.0 ms.

5.4 Solid-state ^{13}C NMR studies

As it was not possible to use either ^{1}H or ^{19}F NMR to distinguish different end-group interactions, ^{13}C NMR experiments were undertaken. Carbon-13 NMR has been used successfully to distinguish end-group interactions in 1-cyanododecane[2] and methyl undecanoate/urea[1] inclusion compounds. Typically, in ^{13}C NMR spectra of such compounds, due to the mobility of the guests, narrow lines (~ 10-20 Hz) are observed. Hence, the combination of this factor with the relatively wide chemical shift range of ^{13}C lends itself well to the study of end-group interactions. In the 1-fluorotetradecane/urea inclusion compound, the guest molecules contain both ^{1}H and ^{19}F. Therefore, in order to obtain narrow lines for end-group carbons and those adjacent, removal of both the ^{1}H-^{13}C and ^{19}F-^{13}C dipolar interactions is crucial. This requirement can be met with a triple-channel 'HFX' probe. The ^{1}H $\rightarrow$ ^{13}C CP spectrum of the 1-fluorotetradecane/urea inclusion compound, acquired with both ^{1}H and ^{19}F decoupling, is shown in Figure 5.25. Typical spectral conditions for ^{1}H $\rightarrow$ ^{13}C CP experiments were: $\pi/2$ pulse duration, 4.5 μs; contact time, 1.0 ms; spectral width, 20 kHz; recycle delay, 5-10 s; acquisition time, 102.4-153.6 ms; ^{1}H and ^{19}F decoupling powers, 56 kHz; MAS rate, 3.0 kHz. Similar conditions were employed for ^{19}F$\rightarrow$^{13}C CP experiments except that a contact time of 12.0 ms and a MAS rate of 1 kHz were used to acquire the spectrum in Figure 5.27b. It is worth pointing out that the ^{19}F$\rightarrow$^{13}C CP matching profile easily breaks up into sidebands for the 1-fluorotetradecane/urea inclusion compound. Therefore, if the standard single-amplitude cross-polarisation sequence is used, then the most efficient matching condition is the +1 sideband.
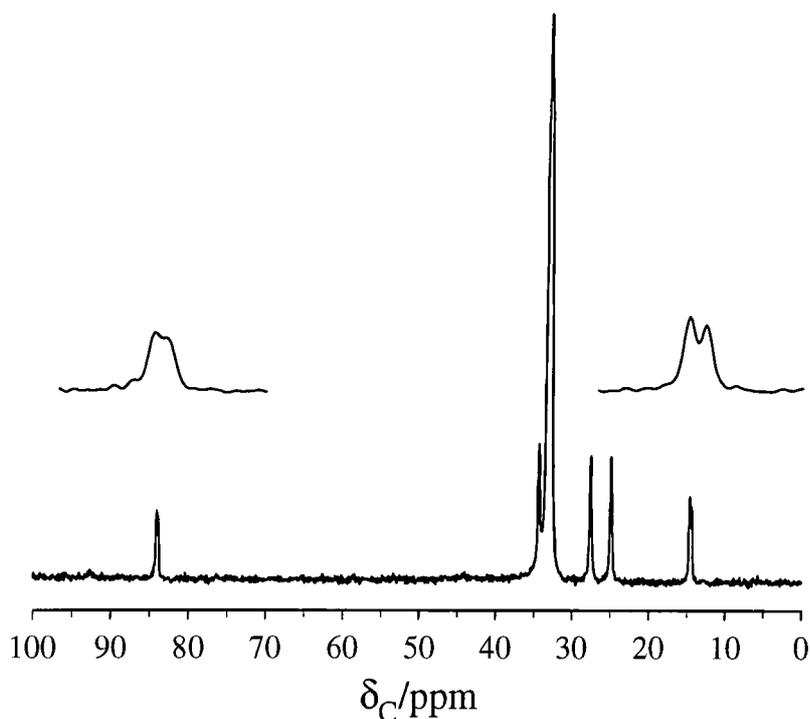
Figure 5.25. $^1H \rightarrow \, ^{13}C$ CP spectrum (guest region only), acquired with both ^1H and ^{19}F decoupling, of the 1-fluorotetradecane/urea inclusion compound at 3 kHz. The expansions show the end-group carbons.

As can be seen above, all the guest resonances are very narrow, with typical linewidths of ~ 12 Hz. For assignment purposes, Figure 5.26, shows the nomenclature used to distinguish individual carbons.
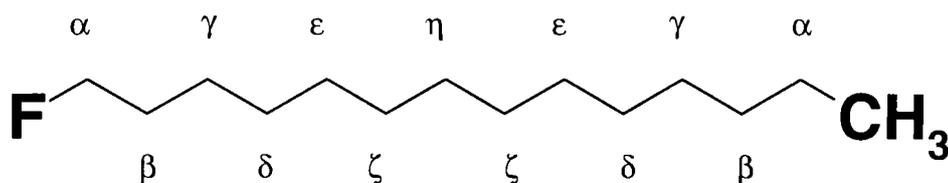
Figure 5.26. Nomenclature used to assign carbon resonances in 1-fluorotetradecane.

The CH_3 end of the molecule was assigned using a previous study of ^{13}C chemical shifts of alkane/urea inclusion compounds,[33] which was based on solution-state ^{13}C NMR[34] data. The CH_2F end of the molecule was assigned from solution-state ^{13}C chemical shifts of ω-fluorinated lipids[35] which were assigned using $J_{C\text{-}F}$. The

assignment was also confirmed by data for ^{19}F substituent effects.[36] A summary of the general assignments is shown in Table 5.3.

δ_C/ppm	Assignment
14.4	**CH$_3$**
14.7	**CH$_3$**
25.0	α-**CH$_2$CH$_3$**
27.6	γ-**CH$_2$CH$_2$CH$_2$F**
32.8	β-**CH$_2$CH$_2$F**
33.0	'inner' **CH$_2$**
34.3	β-**CH$_2$CH$_2$CH$_3$**
83.9	**CH$_2$F**
84.1	**CH$_2$F**

Table 5.3. Assignment of ^{13}C chemical shifts of 1-fluorotetradecane.

It can immediately be seen that there are double the number of resonances observed for the end-group carbons (shown by expansions in Figure 5.25) compared to those for all other carbons. In previous studies,[1,2] this feature was attributed to different orientations of the guest molecules in the urea tunnels. Of course, there are other possible sources for this observation, such as conformational disorder, but from spectra of the analogous inclusion compound made from symmetrical guest molecules, it is valid to assume that guest ordering is the source of the two peaks. The different end-group interactions that are possible between the 1-fluorotetradecane guest molecules inside the urea tunnels are shown in Figure 5.1.

5.4.1 Assignment of end-group interactions[37]

5.4.1.1 Assignment of CH₃ peaks

To assign the two CH_3 end-group resonances, two complementary experiments can be performed which exploit the ^{13}C - ^{19}F dipolar interaction.
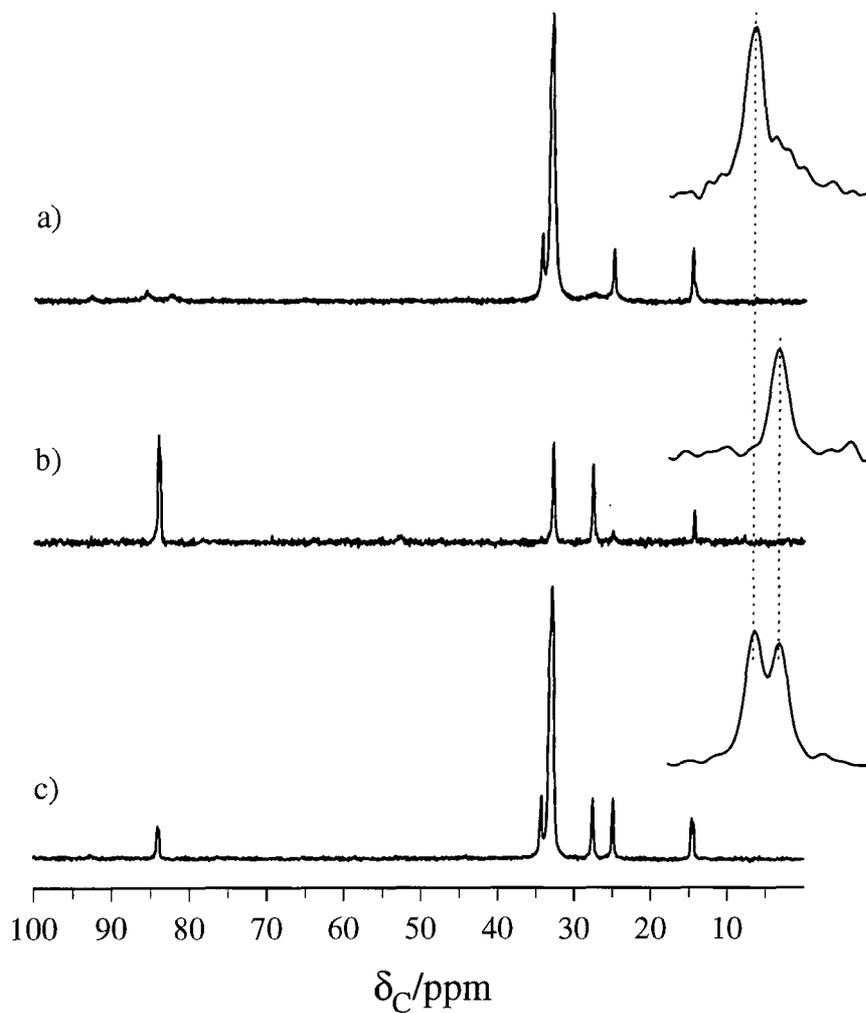
Figure 5.27. Carbon-13 spectra of the 1-fluorotetradecane/urea inclusion compound obtained via a) $^1H \rightarrow ^{13}C$ *CP with* ^1H *decoupling, b)* $^{19}F \rightarrow ^{13}C$ *CP with both* ^1H *and* ^{19}F *decoupling and c)* $^1H \rightarrow ^{13}C$ *CP with both* ^1H *and* ^{19}F *decoupling. The expansions show the CH₃ resonances.*

In a ^{19}F $\rightarrow$ ^{13}C CP spectrum, acquired with both ^{1}H and ^{19}F decoupling, only those ^{13}C nuclei which have a dipolar interaction with, and hence are in close proximity to, ^{19}F, will be present. In a ^{1}H $\rightarrow$ ^{13}C CP spectrum acquired with only ^{1}H decoupling, although all ^{13}C nuclei cross polarise from ^{1}H, those ^{13}C nuclei which are close to ^{19}F will be significantly broadened due to the ^{13}C-^{19}F dipolar interaction. In Figure 5.27b, it is possible to see a resonance at 14.4 ppm, whereas the resonance at 14.7 ppm seen in Figure 5.27c is not present. In comparison, the resonance at 14.4 ppm is severely broadened in Figure 5.27a, whereas the resonance at 14.7 ppm is a narrow peak. These observations imply that the resonance at 14.4 ppm arises from **CH$_3$---FH$_2$C** end-group interactions, whereas that at 14.7 ppm arises from **CH$_3$---H$_3$C** end-groups.

5.4.1.2 *Assignment of CH$_2$F peaks*

Clearly, the resonances due to CH$_2$F cannot be assigned using this approach, as the ^{13}C nucleus of interest is directly bonded to ^{19}F in both environments. Hence, when only ^{1}H decoupling is applied the CH$_2$F peak appears as a broadened doublet. This can be attributed to $^1J_{C-F}$, ~ -160 Hz, which is in agreement with the value of -165 Hz expected for RCH$_2$CH$_2$CH$_2$F groups.[38] Therefore, it is necessary to use the conventional approach in which spectra of symmetric guests and/or mixed guests are compared with that obtained of the unsymmetric guest.[1,39] ^{1}H $\rightarrow$ ^{13}C CP spectra were acquired, using both ^{1}H and ^{19}F decoupling, for the 1,10-difluorodecane/urea and 1,12-difluorododecane/urea inclusion compounds. Only one CH$_2$F resonance is observable, at 84.1 ppm for 1,12-difluorododecane/urea and at 84.2 ppm for 1,10-difluorodecane/urea, as in these two compounds all end-group interactions are of the **CH$_2$F---FH$_2$C** type. This suggests that the resonance at 84.1 ppm for 1-fluorotetradecane/urea arises from **CH$_2$F---CH$_2$F** end-groups. This assignment can also be corroborated from the ^{1}H $\rightarrow$ ^{13}C CP spectrum, acquired using both ^{1}H and ^{19}F decoupling, of a urea inclusion compound made from a 50:50 mixture of 1-fluorotetradecane and tetradecane. The resulting spectrum contains two peaks in the CH$_2$F region, with the higher frequency peak, 84.1 ppm, being of greater intensity. In the mixed guest compound, the number of **CH$_2$F---CH$_3$** interactions will be greater

than the number of **CH₂F---CH₂F** interactions. Hence, the more intense peak at 84.1 ppm is confirmed as arising from **CH₂F---CH₂F** end-groups. It is also worth mentioning that the number of **CH₃---CH₃** interactions is greater than the number of **CH₃---CH₂F** interactions and hence in the CH_3 region of the spectrum, the peak at 14.7 ppm is more intense than that at 14.4 ppm. Again, this confirms the assignment made using the ^{13}C-^{19}F to distinguish the two types of CH_3 end-groups. Figure 5.28 shows the spectra of the inclusion compounds used to assign the CH_2F end-group interactions.
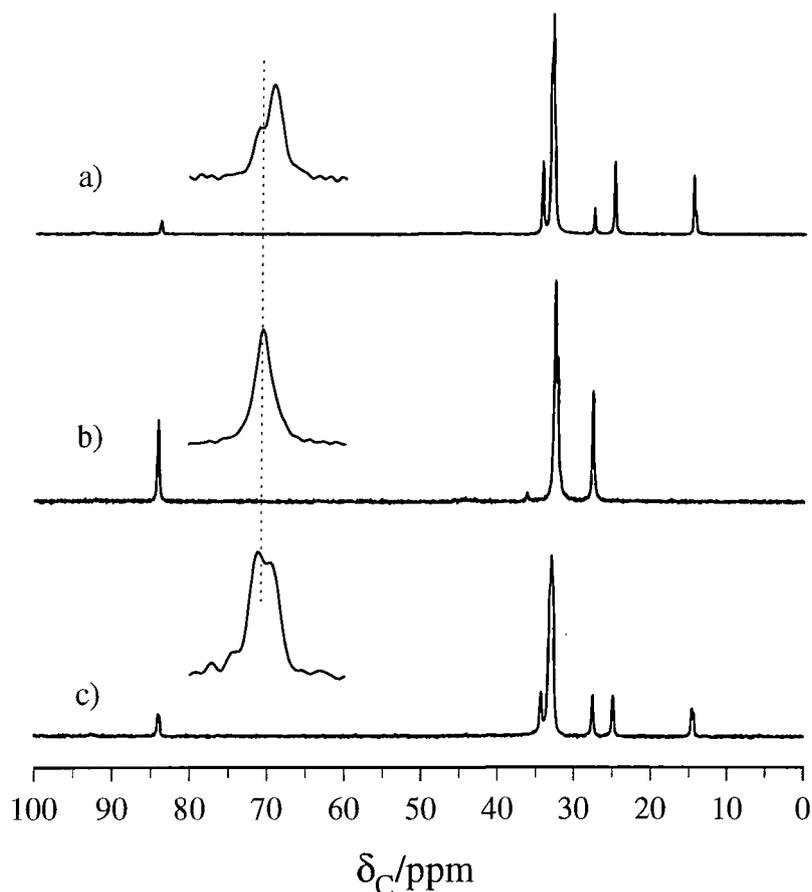
Figure 5.28. Guest regions of $^1H \rightarrow {}^{13}C$ CP spectra, acquired with both ^1H and ^{19}F decoupling of a) 1-fluorotetradecane/tetradecane (50:50), b) 1,10-difluorodecane and c) 1-fluorotetradecane urea inclusion compounds. The expansions show the CH_2F resonances.

5.4.2 Assignment of other carbons

From the spectra in Figure 5.27 and Figure 5.28, it is also possible to confirm the assignment of other carbons in 1-fluorotetradecane. For example, the α-**CH₂CH₃**, 25.0 ppm, is not present in the ^{13}C spectrum of 1,10-difluorodecane/urea, is more intense in the mixed guest compound and is also evident in the ^{1}H→^{13}C CP spectrum, acquired with only ^{1}H decoupling, of 1-fluorotetradecane/urea. Other assignments are also possible from variable contact ^{19}F→^{13}C CP experiments, using contact times from 0.5 ms to 12.0 ms (Figure 5.29). The rate of cross polarisation for the CH₂F group is, not surprisingly, much faster than for any of the other carbons. In fact, with a contact time of 0.5 ms the signal has already passed through its maximum value. However, for the other carbons the signal is still increasing at the longest contact time used.

The peak at 27.6 ppm obviously arises from a carbon which has a dipolar interaction with ^{19}F. This resonance and the one at 32.8 ppm are evident in ^{19}F→^{13}C CP spectra acquired with a relatively short contact time of 0.5 ms. Without the ^{19}F→^{13}C CP experiment, it would have been impossible to see the β-**CH₂CH₂F** peak, which is masked in ^{1}H→^{13}C CP spectra by the large resonance attributed to 'inner' CH₂. Although it is not possible to distinguish the β-**CH₂CH₂F** or the α-**CH₂CH₃** in their two different orientations, it is possible to see the resonance (25.0 ppm) which arises from α-**CH₂CH₃**---FH₂C end-group interactions in ^{19}F→^{13}C CP spectra at longer contact times (> 4.0 ms). This interaction would have been indistinguishable from the α-**CH₂CH₃**---H₃C interaction without ^{19}F→^{13}C CP experiments as the chemical shift for the two orientations is the same. Therefore, the ^{13}C-^{19}F dipolar interaction is a particularly valuable tool for the interpretation of the ^{13}C NMR spectra obtained.[40-42]
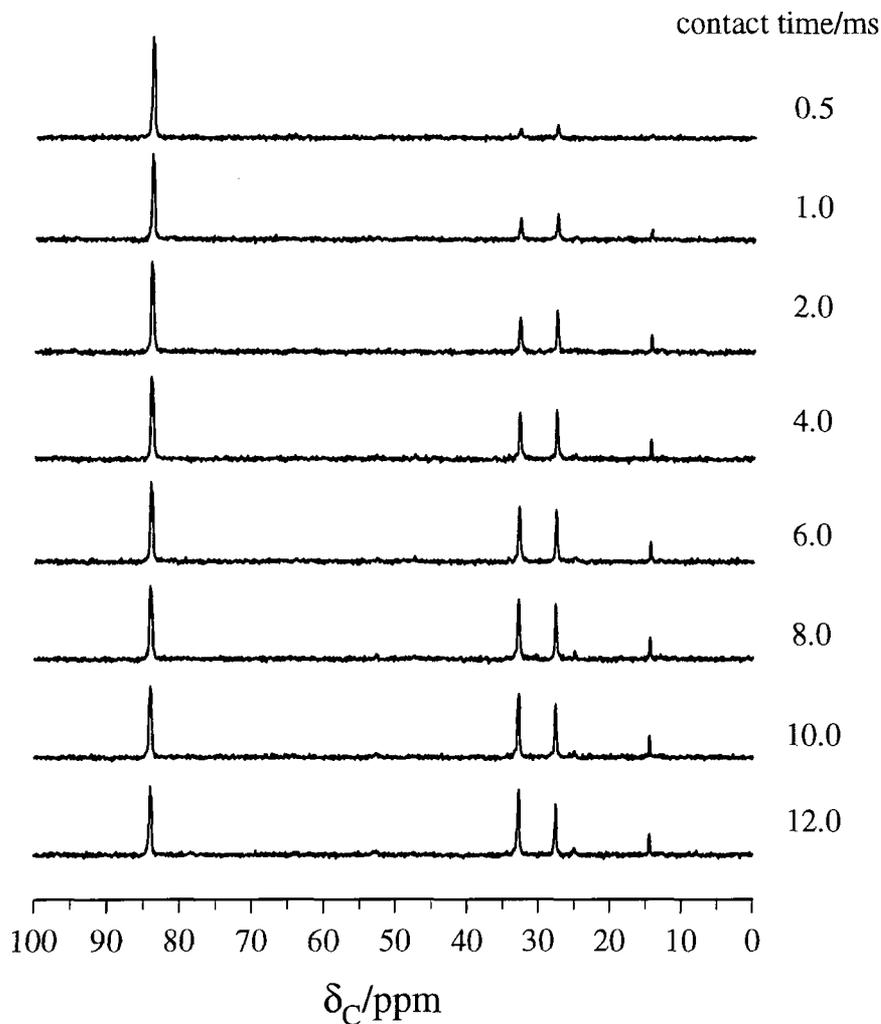
Figure 5.29. Variable contact time $^{19}F{\rightarrow}^{13}C$ CP spectra, acquired with ^{1}H and ^{19}F decoupling, of the 1-fluorotetradecane/urea inclusion compound.

In Figure 5.27a, the γ-$CH_2CH_2CH_2F$ resonance is broadened due to the ^{13}C-^{19}F dipolar interaction. Therefore, it would be interesting to calculate the distance over which the ^{13}C-^{19}F dipolar interaction is effective. The internuclear distance between ^{19}F and a ^{13}C can be determined from standard bond length data.[43]
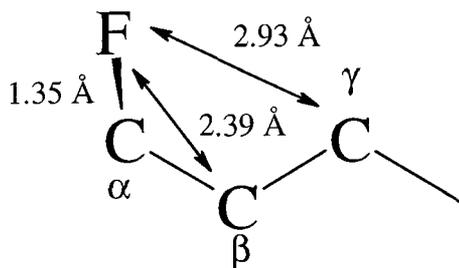
Figure 5.30. Internuclear ^{13}C-^{19}F distances in 1-fluorotetradecane.

The dipolar coupling constant, D (in Hz), for a heteronuclear spin pair can be calculated using,

$$D = \frac{\mu_0}{8\pi^2} \hbar \frac{\gamma_1 \gamma_2}{r_{12}^3}$$ *Equation 5.13*

where μ_0 is the vacuum permeability, $2\pi\hbar$ is the Planck constant, γ is the magnetogyric ratio and r is the distance between the two spins. Substitution of the appropriate values into Equation 5.13, assuming that the fluorine is gauche with respect to the alkyl chain (see Chapter 7), gives a ^{13}C-^{19}F dipolar coupling constant of 1.1 kHz for γ-^{13}C, 2.1 kHz for β-^{13}C and 11.6 kHz for α-^{13}C. Motion may reduce these dipolar coupling constants, and so the values quoted are the maximum possible. With the knowledge of these ^{13}C-^{19}F dipolar constants, the appearance or non-appearance of certain peaks in Figure 5.27 is perhaps a little surprising. In the $^1H \rightarrow ^{13}C$ CP spectrum, acquired with only ^1H decoupling and a MAS rate of 3 kHz, the γ-^{13}C which has a ^{13}C-^{19}F dipolar coupling constant of only 1.1 kHz is severely broadened. In $^{19}F \rightarrow ^{13}C$ CP spectra, acquired with both ^1H and ^{19}F decoupling and a MAS rate of 1 kHz, the γ-^{13}C peak appears with a contact time of only 0.5 ms.

As the Hamiltonian describing the ^{13}C-^{19}F dipolar interaction is inhomogeneous,[44] then with the MAS rates used, the γ-^{13}C-^{19}F dipolar interaction should be averaged to zero. In contrast, the Hamiltonian describing ^1H-^1H dipolar interactions is termed homogeneous. However, if the Hamiltonian describing the total spin system contains both inhomogeneous and homogeneous terms, then it can be described as homogeneous.[45] This means that MAS cannot average the interaction described by the inhomogeneous Hamiltonian. An example where this occurs is in ^{13}C spin-diffusion experiments, which rely on ^{13}C-^1H and ^1H-^1H dipolar interactions to prevent the ^{13}C-^{13}C dipolar interaction from being removed by MAS.[46] In this particular case, if the ^{19}F-^1H and ^1H-^1H dipolar interactions are not completely removed via ^1H decoupling, then the spin system would be homogeneous and hence quite weak ^{13}C-^{19}F dipolar interactions cannot be spun out. Hence, the broad appearance of the γ-^{13}C resonance in Figure 5.27a and the fact that it is possible to cross polarise from ^{19}F to the γ-^{13}C (Figure 5.27b), which may actually involve the protons. In a triple-channel study of fluorinated steroids,[31] the severe broadening of

the CHF and CH_2F ^{13}C resonances when only ^{1}H decoupling was applied was attributed to residual [1]H-^{1}H homonuclear dipolar interactions. In comparison, the CF (quaternary) ^{13}C is further away from protons and hence MAS can average the [13]C-^{19}F dipolar interaction. However, the resonance appeared as a doublet due to [1]J_{CF}.

5.4.3 Determination of guest ordering preference

To obtain quantitative information regarding the ordering preference of 1-fluorotetradecane, ^{13}C single-pulse spectra were acquired with both ^{1}H and ^{19}F decoupling. Cross-polarisation experiments cannot be used to provide quantitative data unless a detailed analysis of the cross-polarisation dynamics has been performed. However, in order for the single-pulse spectra to be quantitative, a recycle delay of the order of $10 \times T_1$(^{13}C) is required to ensure that the system has returned to equilibrium and also to avoid the possibility of anomalous intensities arising from NOE effects.[27] Using the method of Torchia,[47] the longest T_1(^{13}C) in 1-fluorotetradecane/urea was found to be ~ 18 s, and so a recycle delay of 180 s was used. Other spectral conditions were as for the [1]$H \rightarrow$ [13]C CP experiments. Spectra of both the 1-fluorotetradecane and the 1-fluorotetradecane/tetradecane (50:50) urea inclusion compounds are shown in Figure 5.31. In the compound made from a mixture of 1-fluorotetradecane and tetradecane, there should be an increase in the number of CH_2F---CH_3 end-group interactions. The manifestation of this can be seen in Figure 5.31, where the peaks at 14.7 ppm and 84.3 ppm which arise from such interactions are more intense for the mixed guest compound than for the 1-fluorotetradecane compound. As the number of CH_2F groups was diluted due to the addition of tetradecane in the mixed guest compound and the chemical shift difference between the **CH_2F---CH_2F** and **CH_2F---CH_3** resonances is smaller than that between the **CH_3---CH_3** and **CH_3---CH_2F**, the latter was used to quantify the ordering of the 1-fluorotetradecane molecules.
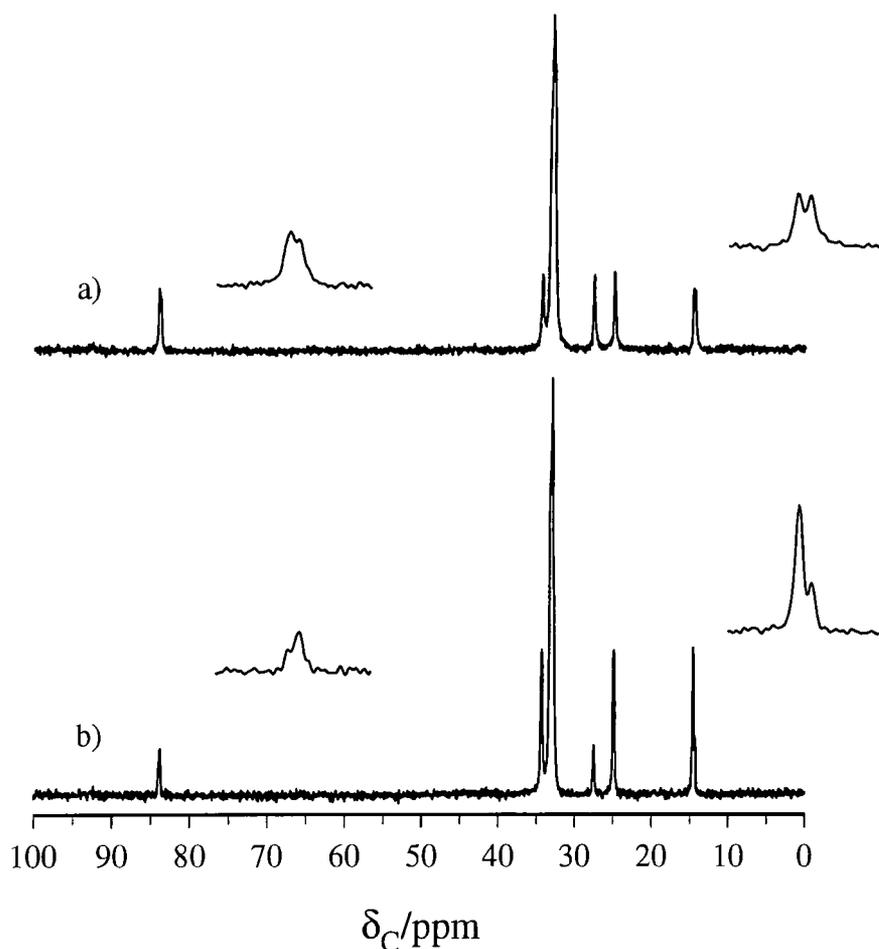
Figure 5.31. Carbon-13 single-pulse spectra (guest region only shown), acquired with both ^1H and ^{19}F decoupling, of a) 1-fluorotetradecane and b) 1-fluorotetradecane/tetradecane (50/50) urea inclusion compounds.

Deconvolution results of the CH_3 peaks in Figure 5.31a and b indicate that for 1-fluorotetradecane/urea there is an approximately equal number of **CH_3---H_3C** and **CH_3---FH_2C** end-group interactions, whereas for the mixed guest compounds there are approximately three times as many **CH_3---H_3C** end-group interactions as there are **CH_3---FH_2C** end-group interactions. Therefore it can be concluded that there is a purely random distribution of guest orientations in the 1-fluorotetradecane/urea inclusion compounds.

5.5 Conclusions

Both steady-state and transient ^{19}F MAS heteronuclear NOE experiments have been performed on the 1-fluorotetradecane/urea inclusion compound. In the steady-state NOE experiment, an interesting variation in the NOE enhancement as a function of temperature was observed. At low temperatures, a negative enhancement was observed, which eventually decreased in magnitude until it became positive and at the maximum temperature studied, the enhancement became negative again. This was ascribed to the onset of motion on the MHz timescale, and as the main guest motions were judged to be too rapid, the particular motion was attributed to urea. Transient NOE experiments have also been performed and longitudinal relaxation times (^{19}F) were obtained which incorporated the effects of cross relaxation between the ^{1}H and ^{19}F spins.

From a combination of ^{1}H→^{19}F CP, T_1(^{19}F) and T_2(^{19}F) experiments, it can be concluded that the 'peak' obtained in ^{19}F spectra of the fluoroalkane/urea inclusion compounds is inhomogeneous. As a consequence of the number of factors which might contribute to the inhomogeneity of the resonance, it was not possible to use ^{19}F NMR to obtain information regarding guest ordering. It was not possible to use ^{1}H NMR to obtain structural information, although in systems containing both ^{1}H and ^{19}F, ^{19}F→^{1}H cross-polarisation experiments can be used to give high-resolution ^{1}H spectra. It was deduced using triple-channel ^{13}C NMR experiments, that the 1-fluorotetradecane molecules are randomly oriented within the urea tunnels. The CH$_3$ resonances were assigned using two complementary experiments which exploit the ^{13}C-^{19}F dipolar interaction. The presence of three NMR active nuclei, such as ^{1}H, ^{19}F and ^{13}C, can increase the scope of experiments that can be performed and hence, enable more structural information to be attained.

5.6 References

1. M.D. Hollingsworth and N. Cyr, *Mol. Cryst. Liq. Cryst.*, 1990, **187**, 135.

2. M.D. Hollingsworth and K.D.M. Harris, *Comprehensive Supramolecular Chemistry* (Editors: D.D. MacNicol, F. Toda, R. Bishop), 1996, Volume 6, Pergamon, pp. 177-237.

3. E.L. Hahn, *Phys. Rev.*, 1950, **80**, 580.

4. G. Metz, X. Wu and S.O. Smith, *J. Magn. Reson. A*, 1994, **110**, 219.

5. A.C. Kolbert and A. Bielecki, *J. Magn. Reson. A*, 1995, **116**, 29.

6. A.E. Aliev, S.P. Smart, I.J. Shannon and K.D.M. Harris, *J. Chem. Soc., Faraday Trans.*, 1996, **92**, 2179.

7. N. Bloembergen, E.M. Purcell and R.V. Pound, *Phys. Rev.*, 1948, **73**, 679.

8. J.E. Anderson ans W.P. Slichter, *J. Phys. Chem.*, 1965, **69**, 3099.

9. D.C. Douglass and G.P Jones, *J. Chem. Phys.*, 1966, **45**, 956.

10. H. Mo and T.C. Pochapsky, *Prog. NMR Spectrosc.*, 1997, **30**, 1.

11. Y. Yamamoto and Y. Inoue, *J. Carbohydrate Chem.*, 1989, **8**, 29.

12. D.C. Douglass and V.J. McBrierty, *Macromolecules*, 1978, **11**, 766.

13. I. Solomon, *Phys. Rev.*, 1955, **99**, 559.

14. D. Neuhaus and M. Williamson, *The Nuclear Overhauser Effect in Structural and Conformational Analysis*, VCH, New York, 1989.

15. J.H. Noggle and R.E. Schirmer, *The Nuclear Overhauser Effect*, Academic Press, New York, 1971.

16. P.A. Beckmann, *Phys. Reports*, 1988, **171**, 85.

17. D. Neuhaus, 'Nuclear Overhauser Effect', *Encyclopedia of NMR*, (Editors: D.M. Grant and R.K. Harris), Wiley, London, 1996, **5**, 3290.

18. J.T. Gerig, D.T. Loehr, K.F.S. Luk and D.C. Roe, *J. Am. Chem. Soc.*, 1979, **101**, 7482.

19. J.T. Gerig, K.F.S. Luk and D.C. Roe, *J. Am. Chem. Soc.*, 1979, **101**, 7698.

20. A. Findlay, *Ph.D. Thesis*, University of Durham, 1991.

21. J.L. White and J.F. Haw, *J. Am. Chem. Soc.*, 1990, **112**, 5896.

22. U. Schwerk and D. Michel, *J. Phys. Chem.*, 1996, **100**, 352.

23. P.A. Mirau and J.L. White, *Magn. Reson. Chem.*, 1994, **32**, S23.

24. A. Naito, S. Ganapathy, K. Akasaka and C.A. McDowell, *J. Magn. Reson.*, 1983, **54**, 226.

25. M.G. Gibby, A. Pines and J.S. Waugh, *Chem. Phys. Lett.*, 1972, **16**, 296.

26. D.E. Woessner, *J. Chem. Phys.*, 1962, **36**, 1.

27. A. Findlay and R.K. Harris, *J. Magn. Reson.*, 1990, **87**, 605.

28. J.L. White and P. Mirau, *Macromolecules*, 1993, **26**, 3049.

29. V.J. McBrierty and D.C. Douglass, *Macromolecules*, 1977, **10**, 855.

30. V.J. McBrierty and D.C. Douglass, *J. Polymer Sci.: Macromolecular Rev.*, 1981, **16**, 295.

31. S.A. Carss, *Ph.D. Thesis*, University of Durham, 1995.

32. K.D.M. Harris and P. Jonsen, *Chem. Phys. Lett.*, 1989, **154**, 593.

33. F. Imashiro, T. Maeda, T. Nakai, A. Saika and T. Terao, *J. Phys. Chem.*, 1986, **90**, 5498.

34. D.M. Grant and E.G. Paul, *J. Am. Chem. Soc.*, 1964, **86**, 2984.

35. S. Moss and D. O'Hagan, personal communication.

36. F.W. Wehrli, A.P. Marchand and S. Wehrli, *Interpretation of Carbon-13 NMR Spectra*, Wiley, 2nd edition, 1988.

37. A. Nordon, R.K. Harris, L. Yeo and K.D.M. Harris, *Chem. Commun.*, 1997, 2045.

38. D.H. Williams and I. Flemming, *Spectroscopic Methods in Organic Chemistry*, McGraw-Hill, UK, 4th edition, 1989.

39. M.D. Hollingsworth and A.R. Palmer, *J. Am. Chem. Soc.*, 1993, **115**, 5881.

40. W.E.J.R. Maas, W.A.C. van der Heijden, W.S. Veeman, J.M.J. Vankan and G.H. Werumeus Buning, *J. Chem. Phys.*, 1991, **95**, 4698.

41. A.P.A.M. Eijkelenboom, W.E.J.R. Maas, W.S. Veeman G.H. Werumeus Buning and J.M.J. Vankan, *Macromolecules*, 1992, **25**, 4511.

42. E.W. Hagaman, *J. Magn. Reson., A*, 1993, **104**, 125.

43. J.E. Huheey, *Inorganic Chemistry, Principles of Structure and Reactivity*, Harper Collins, 3rd edition, 1983.

44. M.M. Maricq and J.S. Waugh, *J. Chem. Phys.*, 1979, **70**, 3300.

45. C.A. Fyfe, *Multinuclear Magnetic Resonance in Liquids and Solids - Chemical Applications*, (Editors: P. Granger and R.K. Harris), NATO ASI, Maratea, 1988.

46. K. Schmidt-Rohr and H.W. Spiess, *Multidimensional Solid-state NMR and Polymers*, Academic Press, London, 1994.

47. D.A. Torchia, *J. Magn. Reson.*, 1978, **30**, 613.

Chapter 6

Solid-state NMR studies of the fluorocyclohexane/thiourea inclusion compound

6.1 Introduction

When molecules are constrained within suitable host structures to form a solid inclusion compound, their behaviour can differ compared to that in their pure crystalline phase or in dispersed phases. One example of a class of molecules that can exhibit such behaviour when included within thiourea is substituted cyclohexanes. In substituted cyclohexanes, for the favoured chair conformation, the substituent (X) can either be axial or equatorial. In the pure phase, there is a dynamic equilibrium between the two possible conformations proceeding via a 'chair-chair' ring inversion process (Figure 6.1), with the equatorial conformation generally predominating. This is because of the destabilising interactions between 1,3-diaxial substituents that exist when the molecule adopts the axial conformation. However, for certain monosubstituted cyclohexanes when confined within thiourea, the axial conformer predominates.[1] Therefore, the conformational properties of these molecules can provide a sensitive probe of the structural constraints imposed by a solid host structure.
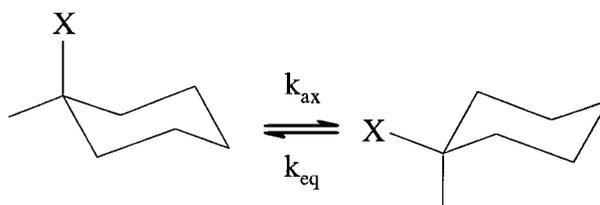
Figure 6.1. 'Chair-chair' ring inversion process

In thiourea inclusion compounds, the thiourea molecules form an extensively hydrogen-bonded structure which contains uni-directional, non-intersecting tunnels within which guest molecules can reside.[2,3] The thiourea host structure is rhombohedral for cyclohexane and other 'isotropic' guest molecules, though for more planar guests the thiourea adopts a monoclinic structure. However, at low temperatures the rhombohedral structure reverts to a monoclinic structure. The tunnel diameter varies between 5.8 Å (at a constriction) and 7.1 Å (at a bulge) along the tunnel axis. Over one lattice period of the host structure, the constrictions occur at 0 and 0.5 and the bulges occur at 0.25 and 0.75. In the cyclohexane/thiourea inclusion compound,[25] the guest molecules undergo rapid reorientation ($\sim 10^5$-10^9 Hz) about their triad axes at temperatures between -200 °C and -144 °C. At temperatures above -117 °C, it is known that the guest molecules undergo ring inversion (~ 0-10^6 Hz). The guest molecules exhibit considerable disorder within the thiourea tunnels, though single-crystal X-ray studies of the chlorocyclohexane/thiourea inclusion compound have shown[4] that, at ambient temperature, the guest molecules occupy preferred sites which are centred on the bulges in the thiourea tunnels. Hence, thiourea inclusion compounds are usually commensurate, with two guest molecules per unit repeat distance of the thiourea structure. Therefore, in some respects it is more accurate to refer to the thiourea structure as being of the 'cage' type as opposed to the 'tunnel' type exhibited by urea.

Conventional diffraction techniques depend on long-range crystalline order to yield structural information. Hence, in the study of inclusion compounds, such techniques can provide detailed structural information on the host, but can only show that the guest structure is disordered. Therefore, in order to obtain information regarding guest conformation and dynamics, it is necessary to use techniques which probe local environments and/or the dynamics of the system in question. Both IR and Raman spectroscopies have been used to examine the conformation of halogenated cyclohexanes in thiourea.[5] These investigations indicated a tendency for the guest to adopt an axial conformation. However, accurate quantitative results may not result from IR, due to the assumption of identical absorption coefficients for both conformers, which is not necessarily the case.[10] Bromine K-edge EXAFS spectroscopy has also been used to investigate local structural properties of

bromocyclohexane and trans-1-bromo-2-chlorocyclohexane in thiourea.[6] In both compounds, from Br---C(3,5) distance measurements and the detection of an intermolecular Br---Br distance (3.82 Å), it was concluded that the substituents preferred to be axial and the guest molecules were ordered head-to-head.

In solution, high-resolution ^{13}C NMR[7] has proven to be one of the most powerful techniques for studying the conformational equilibrium of substituted cyclohexanes, primarily because of the extreme sensitivity of ^{13}C chemical shifts to the conformation of X. Similarly, solid-state ^{13}C NMR can be used to study the conformation of these molecules included within thiourea.[1,8-10] For monosubstituted cyclohexanes with X = Me, NH_2 and OH, the equatorial conformer predominates as found in solution and in their pure phases. In comparison, when X = Cl, Br and I, the axial conformer predominates. The preferred conformation of the halogen-monosubstituted cyclohexane in thiourea differs from that of the halogen-monosubstituted cyclohexane when in its pure phase, in solution or when confined within zeolitic host[11] materials, where the equatorial conformer predominates. Reasons for the preference of chlorocyclohexane to adopt the axial conformation when included within thiourea have been examined using a mathematical model developed to enable the structural properties of one-dimensional inclusion compounds to be predicted and rationalised.[12,13] Such studies reveal that when the guest structure is commensurate, the axial conformation is energetically far more favourable than the equatorial conformation. The adoption of the axial conformation also permits more efficient packing of the guest molecules within the thiourea tunnels in comparison to the equatorial conformation. In a study by Müller,[10] it was concluded that the polar host-guest interactions provide a major contribution to the stabilisation of the axial conformation.

6.2 Fluorocyclohexane/thiourea inclusion compound

From the discussion above, it can be seen that most halogen-monosubstituted cyclohexane/thiourea inclusion compounds have been studied extensively. However, less attention appears to have been paid to the fluorocyclohexane/thiourea inclusion

compound. The conformation of fluorocyclohexane in the gas, liquid and solid phases has been studied using IR, Raman and UV spectroscopies.[14] It was found, as for other substituted cyclohexanes, that the equatorial conformation predominates. Solution-state ^{13}C NMR has also been used to study the conformation of fluorocyclohexane.[7] However, in fluorocyclohexane there exists another NMR active nucleus, namely ^{19}F, which has a large chemical shift range,[15] and so ^{19}F NMR has also been used to study the 'chair-chair' ring inversion process both in the gas phase[16] and in solution.[17] Both ^{13}C and ^{19}F NMR results indicate a predominance of the equatorial conformation. As with other halogen-substituted cyclohexane/thiourea inclusion compounds, the host affects the conformational behaviour of the guest molecules. The fluorocyclohexane/thiourea inclusion compound has previously been studied using ^{13}C solid-state NMR[8,10] and UV spectroscopy.[14] Using both techniques, the axial and equatorial conformations were found to be present in equal proportions, again illustrating the stabilisation of the axial conformation by the host. However, it is particularly noticeable that the axial conformation for fluorocyclohexane is not as favourable as for other halogen-substituted cyclohexane molecules included within thiourea.

In previous solid-state ^{13}C NMR studies of the fluorocyclohexane/thiourea inclusion compound,[8,10] it was not possible to remove simultaneously the [13]C-^{19}F and [13]C-^{1}H dipolar interactions. When only ^{1}H decoupling is applied during acquisition, as was the case in these previous studies, ^{13}C spectra could exhibit both J_{CF} and [13]C-^{19}F dipolar couplings. However, if the motion of the molecule and/or MAS is not sufficient to remove the [13]C-^{19}F dipolar interaction, broadening of resonances will occur. This broadening will be accentuated at low temperatures and so simulation of spectra, from which exchange rates are to be obtained, may be difficult. Therefore, in this study a triple-channel 'HFX' probe was used to obtain ^{13}C spectra, which enables ^{1}H and ^{19}F decoupling to be applied simultaneously. Due to recent advances in probe technology, it is possible to observe ^{19}F, while applying ^{1}H decoupling, in the solid state using a 'HF' probe.[18] Therefore, the dynamics and conformation of fluorocyclohexane included within the thiourea tunnels have been investigated using both ^{13}C and ^{19}F NMR. This chapter will also demonstrate the considerable advantages of being able to study such processes via solid-state ^{19}F NMR. In terms of

sensitivity, ^{1}H NMR is far superior to ^{13}C NMR, but in solution, the axial and equatorial α protons differ in chemical shift by only 0.46 ppm.[17] Even with multiple-pulse techniques, due to the narrow chemical shift range exhibited by ^{1}H nuclei, it is not possible to study in detail the 'chair-chair' ring inversion process exhibited by fluorocyclohexane guest molecules in the solid inclusion compound. Nevertheless, variable-temperature ^{1}H CRAMP spectra have been obtained both with and without ^{19}F multiple-pulse decoupling to yield additional structural information of the fluorocyclohexane/thiourea inclusion compound.

6.3 Fluorine-19 solid-state NMR studies of the fluorocyclohexane/thiourea inclusion compound[19]

At room temperature, 300 K, a single resonance was observed at -174.7 ppm in the ^{19}F MAS NMR spectrum, acquired with ^{1}H decoupling, of the fluorocyclohexane/thiourea inclusion compound. A series of low-temperature spectra was then acquired. Typical spectral conditions were: $\pi/2$ pulse duration, 3 μs; recycle delay, 60 s; ^{1}H decoupling power, 105 kHz; number of transients, 4; spin rate, 7.0 kHz. On lowering the temperature, this resonance broadened, coalesced and then sharpened to give two peaks of approximately equal intensity at 177 K, as can be seen in Figure 6.2. This observation can be attributed to the well-documented 'chair-chair' ring-inversion process in cyclohexane-type molecules. The resonances at -163.9 ppm and -187.0 ppm at 177 K can be assigned to the equatorial and axial conformers respectively using solution-state NMR data.[17]
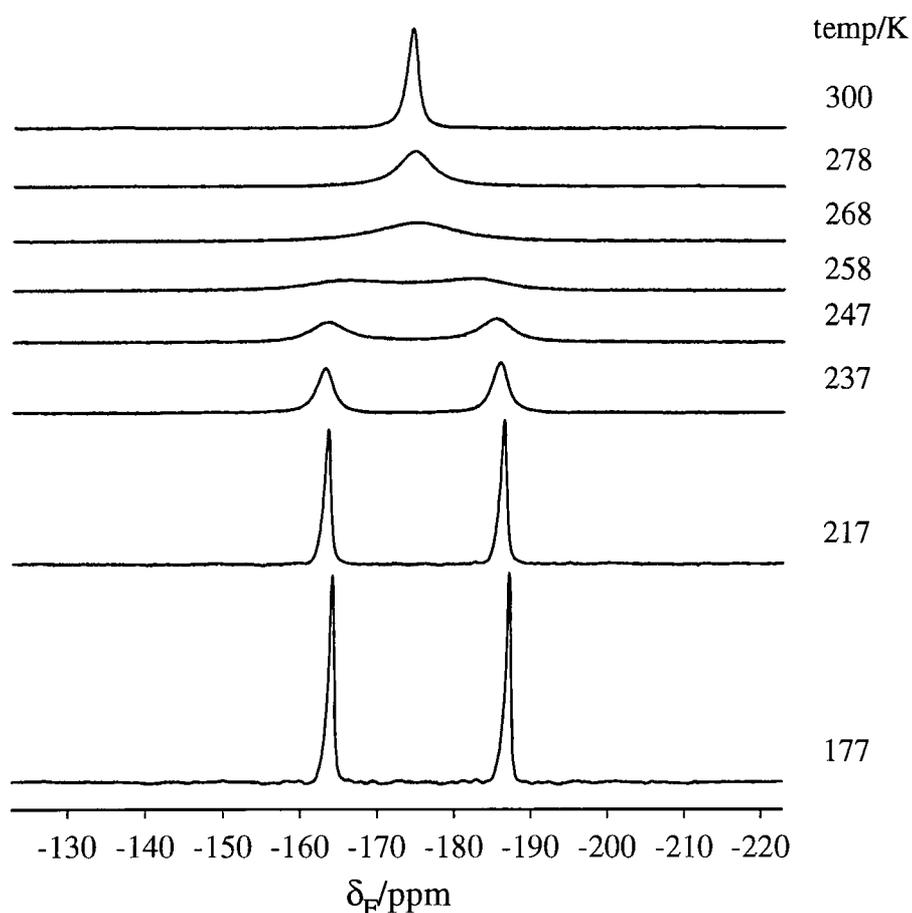
Figure 6.2. Variable-temperature ^{19}F MAS NMR spectra, acquired with ^{1}H decoupling, of the fluorocyclohexane/thiourea inclusion compound.

6.3.1 Analysis of the 'chair-chair' ring inversion process

The choice of method for the analysis of dynamic processes depends upon the magnitude of the motional rate. At the top end of motional processes able to be characterised using NMR are those occurring at rates of the order of tens to hundreds of MHz. This motional regime is accessible via spin-lattice (T_1) relaxation measurements.[20-22] For motions occurring at frequencies of the order of 10^7 to 10^3 Hz, ^2H lineshape analysis may be used to determine not only the rate of motion but also its mechanism.[22-25] Spin-lattice relaxation in the rotating frame ($T_{1\rho}$) measurements[26,27] may be used to study motions occurring at rates of the order of tens of kHz. It is also possible to characterise motions in the 'kHz' region if the rate

is of the order of the decoupler power,[28-30] the inverse of the multiple-pulse cycle time[28,31] or the MAS rate.[32] The 2D exchange experiment[33] or its 1D analogue, the selective polarisation inversion experiment,[34,35] may also be used to obtain rate constants, particularly when the exchange rate is fast compared to T_1 but slow compared to the chemical shift separation between the sites involved. The motional region defined by the latter delineates an area in which the bandshapes are very sensitive to the rate of motion. Therefore, by looking at the variation of bandshape as a function of motion (bandshape analysis[36]), motional rates of the order of 10^1 to 10^5 Hz can be determined. The lower limit of motional rates, typically of the order of Hz, accessible via NMR can be probed by saturation transfer methods.[37]

Clearly, to obtain exchange rates over a broad range of temperatures, it is best if more than one method can be used. Methods considered in the present study are bandshape analysis, 2D exchange, selective polarisation inversion and $T_{1\rho}$ measurements.

6.3.1.1 Bandshape analysis

6.3.1.1.1 Introduction

Bandshape analysis requires the simulation of spectra in which exchange between the desired number of sites is occurring. For the 'chair-chair' ring inversion process exhibited by fluorocyclohexane, it is reasonable to assume a two-site exchange model. In this case, the modified Bloch equations describing exchange between two sites, first derived by McConnell[38] and expressed in their final form by Rogers and Woodbrey,[39] were used to simulate spectra. For exchange between nuclei which are coupled, a density matrix based method is required to simulate bandshapes. However, in this case, due to the assumption that the two exchanging spins are uncoupled, the former approach was deemed to be adequate. The equations were incorporated into a Mathcad[40] program to create the simulated spectra.[41] The exchange process in substituted cyclohexanes can be defined by two rate constants, k_{ax} and k_{eq} (Figure 6.1). The input data required for simulation of spectra are k_{ax}, the

rate constant defining axial to equatorial conformational exchange, p_{ax}, the population of the axial conformation, v_{ax} and v_{eq}, the ^{19}F isotropic chemical shifts of the axial and equatorial conformations, and $T_2(^{19}F)$, the spin-spin relaxation time (assumed to be equal for the axial and equatorial spins). Using the Mathcad program, exchange rates are obtained by comparing 'by eye' the simulated and experimental data, which can readily be imported into Mathcad as an 'xy' data set.

In the simulation of spectra, the effect of temperature upon chemical shift should be considered by examining the shifts of the two exchanging sites in the slow-exchange region. Similarly, the relative populations of the two exchanging sites can be determined from spectra acquired in this region via integration. Hence, an idea of the change of relative populations as a function of temperature can be obtained. An estimate of $T_2(^{19}F)$ can be obtained from linewidths in the slow and fast exchange regions. It is important to realise that exchange between two isotropic chemical shifts only has been considered. This is valid in this particular case, as there are no spinning sidebands in the spectra obtained. Clearly in cases where spinning sidebands are present, the 'intensities' of the isotropic peaks will not yield the true populations of the two exchanging sites. Hence, a simulation program would have to be written in which the effects of spinning on shielding anisotropy (SA) could be taken into account. An alternative approach would be to sum the intensities of the spinning sideband manifold including the corresponding isotropic peak for each of the exchanging sites.

6.3.1.1.2 Experimental results

From the variable-temperature spectra it can be seen that the exchange rate has a profound effect on the bandshape. At the slow and fast exchange limits, where slow and fast are defined in relation to the chemical shift separation, the bandshapes are insensitive to the exchange rate. However, in the region of the coalescence temperature (263 K), the bandshapes provide a very sensitive probe of the exchange rate. At 177 K, the populations of the axial and equatorial conformations are equal. Bandshape analysis shows that upon increasing the temperature there is only a very

slight shift in the equilibrium position towards the axial conformer. Hence, the calculated exchange rates shown in Figure 6.3 are the average of k_{ax} and k_{eq}. Bandshape analysis is, as already mentioned, less sensitive to the exchange rate at the slow exchange limit, which can be considered to be below 217 K in this case. However, at these temperatures the bandshapes also become asymmetric in shape (thought to be disorder-related) and so bandshape analysis becomes increasingly less accurate for this reason as well. Therefore, it is clear that bandshape analysis can only be used in this case to determine, with a high degree of certainty, exchange rates between 237 K and 300 K. This temperature range nevertheless is still considerable in comparison to that over which bandshape analysis would be possible had ^{13}C NMR been used. This is due to the large chemical shift difference, 4.3 kHz, that exists between the axial and equatorial conformations in the ^{19}F spectrum. In comparison, in a ^{13}C NMR study of the conformational exchange process exhibited by fluorocyclohexane,[10] differences in the chemical shifts of axial and equatorial carbons ranged only from 30 to 200 Hz depending upon which 'pair' of exchanging carbons was chosen.
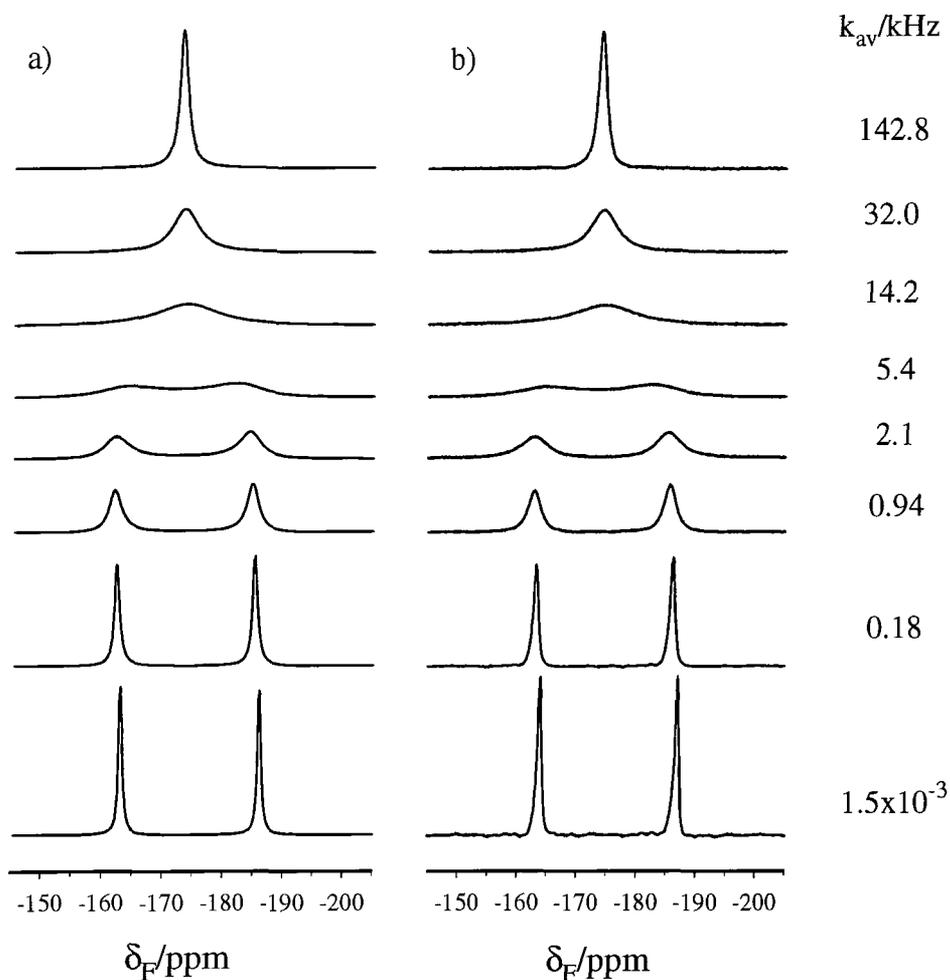
Figure 6.3. a) Simulated and b) experimental ^{19}F spectra at (from bottom to top) 177 K, 217 K, 237 K, 247 K, 258 K, 268 K, 278 K and 300 K, with the average exchange rates given down the right hand side. The rate constants given at 177 K and 217 K were obtained using the ^{19}F selective polarisation inversion (SPI) experiment.

6.3.1.2 The two-dimensional exchange experiment (2D EXSY)

The two-dimensional exchange experiment can be used to determine exchange rates, particularly in the slow-exchange region. The pulse sequence used is shown in Figure 6.4.
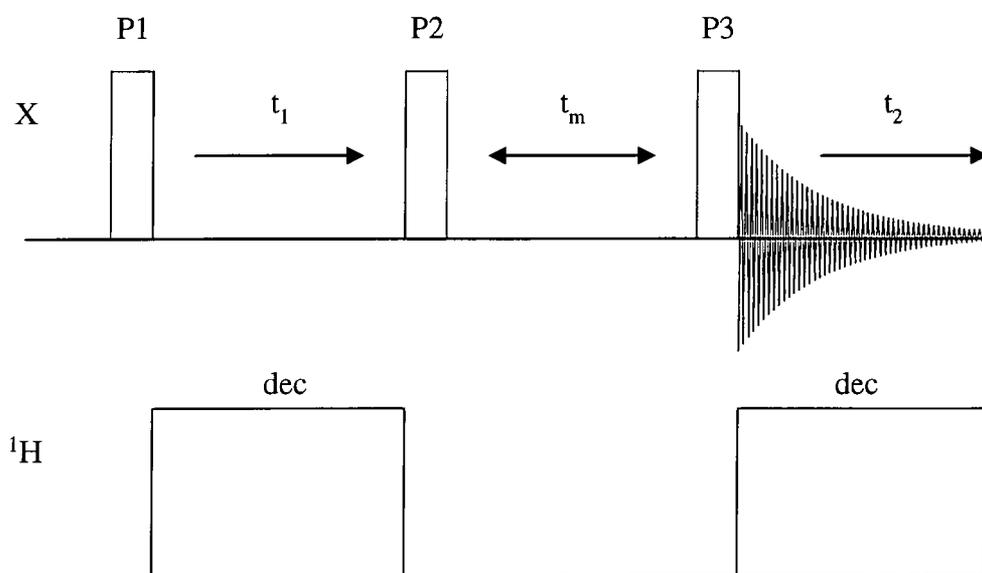
Figure 6.4. Pulse sequence (single pulse) for the two-dimensional exchange experiment. P1, P2 and P3 are all π/2 pulses, with their respective phases given in Table 6.1.

First, transverse magnetisation is created by a π/2 pulse and then the spins are allowed to evolve during t_1 under their chemical shifts. During the mixing time (t_m), the magnetisation labels are able to redistribute, and during t_2 the spins are again allowed to evolve, but this time under their new chemical shifts. Hence, if there is no exchange, then peaks are observed only along the diagonal. The presence of cross-peak intensity indicates that during the mixing period exchange has occurred involving the sites with chemical shifts connected by the cross peaks. The intensity of the cross peaks is determined by the exchange rate and the duration of the mixing period. Therefore, in principle it is possible to calculate the exchange rate at a given temperature by performing several experiments with different mixing times.[35,42] One can immediately see that if the exchange rate is to be determined across a range of temperatures, then this is an extremely time-consuming method for obtaining exchange rates, particularly as pure absorption lineshapes[43] are necessary for quantitative results. Nevertheless, the 2D exchange experiment can be a powerful tool for determining exchange mechanisms.[33,44]

To obtain pure absorption lineshapes, the phase cycling must be such that both the p=±1 coherence pathways[45,46] (Figure 6.5) are retained during t_1.
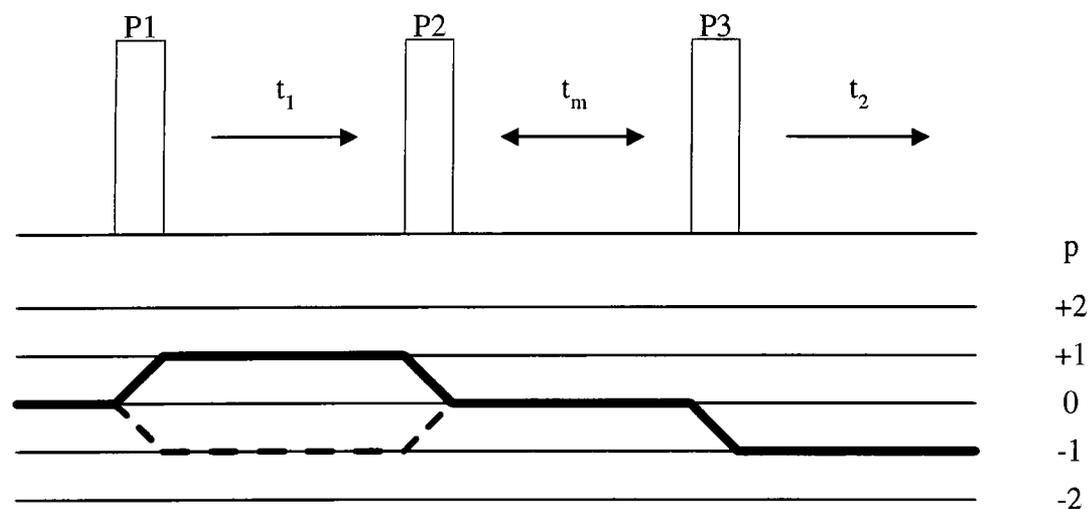
Figure 6.5. Coherence pathway diagram for two-dimensional exchange experiment (p denotes the coherence order).

When a pulse is applied to a spin system, a change in coherence order, Δp, occurs. If the pulse is repeated N times, a number of Δp values are generated with the individual values given by $\Delta p \pm nN$ where n=0, 1, 2, ... If the total number of Δp values is given by r, to select a unique Δp from all the possibilities, then N, the number of pulses in a phase cycle, must be at least equal to r. In Figure 6.5, the first pulse denoted P1 must select the $\Delta p = \pm 1$ coherence pathways. However, from the preceding discussion, if the pulse is applied only once the following changes in coherence order will result; Δp ..., -2, -1, 0, 1, 2, ... As coherence levels higher than 1 can be neglected, only $\Delta p = -1$, 0, 1 need to be considered. Therefore, in order to select only $\Delta p = \pm 1$ during t_1, N must be equal to 2 and so P1 must have a phase cycle of 2. The required rf phase, ϕ, of a pulse in order to select the desired coherence pathways is given by $\phi = k2\pi/N$ where k=0, 1, ..., N-1. Therefore to select the $\Delta p = \pm 1$ coherence pathways, the rf phase of P1 must be 0 for the first transient and 180 for the second transient. It is not necessary to phase cycle all the pulses in a pulse sequence as all coherence pathways must start at p=0 and end with p=-1. The latter condition

assumes that pathways ending with values other than p=-1 can be disregarded. In practice, due to a gain imbalance of the two receiver channels, it may be possible to observe p=1. However, by applying a cyclically ordered phase sequence[47] (CYCLOPS) to one of the pulses and the receiver, then the assumption that only pathways ending with p=-1 can be observed is perfectly valid. Therefore, if there are n pulses in a pulse sequence, then only (n-1) pulses need to be phase cycled, with the remaining pulse having a fixed rf phase.

In the 2D exchange pulse sequence, P3 has a phase cycle of 4 to select Δp=-1 and hence the sequence meets the requirement for CYCLOPS to be applied to one of the pulses. The phase of P2 can then be fixed, with its absolute value being unimportant. Finally, the receiver phase, ϕ_{rec}, is given by the sum of -Δpϕ for each pulse. The overall phase cycle required for the 2D exchange experiment is given in Table 6.1.

P1	P2	P3	receiver
0	0	0	0
180	0	0	180
0	0	90	90
180	0	90	270
0	0	180	180
180	0	180	0
0	0	270	270
180	0	270	90

Table 6.1. Phase cycling for the two-dimensional exchange experiment.

To obtain phase-sensitive detection in the second dimension and pure absorption lineshapes, two separate experiments are necessary in which the phase of the first pulse, denoted P1 in Table 6.1, is shifted by π/2 in the second experiment, in relation to its phase in the first experiment.[48] This phase shift of the first pulse enables frequency discrimination in the second dimension to be achieved. Pure absorption lineshapes are obtained by combining the two data sets in the appropriate

manner. How this is actually achieved will now be discussed in the context of data processing using Spinsight. The first experiment, sine-modulated in t_1, and the second experiment, cosine-modulated in t_1, are acquired using an acquisition macro which permits interleaved acquisition of the two experiments, but importantly also allows the data to be written to two separate files. Using the nomenclature of Keeler and Neuhaus,[43] the time-domain signal, $S(t_1, t_2)$, for the two experiments can be described by,

$$S_{cos}(t_1,t_2) = cos(\Omega_1 t_1) exp(i\Omega_2 t_2)$$

Equation 6.1

$$S_{sin}(t_1,t_2) = sin(\Omega_1 t_1) exp(i\Omega_2 t_2)$$

where Ω_1 and Ω_2 are the ω_1 and ω_2 frequencies of a given signal in angular units. The Fourier transform of a time domain signal can be given by,

$$exp(\pm i\Omega_j t) \xrightarrow{\text{FT}} A_j^{\pm} + iD_j^{\pm}$$

Equation 6.2

where A and D are the absorptive and dispersive components of a Lorentzian, j denotes the dimension and $\pm$ refers to the sign of Ω. Hence, Fourier transformation with respect to t_2 of $S(t_1, t_2)$ gives,

$$S_{cos}(t_1,\omega_2) = cos(\Omega_1 t_1)[A_2 + iD_2]$$
$$S_{sin}(t_1,\omega_2) = sin(\Omega_1 t_1)[A_2 + iD_2]$$

Equation 6.3

To get to this stage using Spinsight, the two data sets are zero filled to twice their original acquisition length in t_2. The $S_{sin}(t_1, t_2)$ data set is then data shifted to the right, by the original acquisition length in t_2 before adding to the $S_{cos}(t_1, t_2)$ data set. The acquisition length is then set back to its original value, using the setsize command, which results in the interleaving of the data sets. Visually, this means that the real parts of $S_{cos}(t_1, t_2)$ and $S_{sin}(t_1, t_2)$ appear on even and odd rows respectively, with row numbering starting with 0. The data set is then Fourier transformed with respect to t_2, and ω_2 is then phased with the values required to phase the first row. It is important to stress that at this stage, despite appearances the two data sets are still separate.

If only the real parts of $S_{cos}(t_1, \omega_2)$ and $S_{sin}(t_1, \omega_2)$ are combined to give a data set, $S_r(t_1, \omega_2)$, such that the real part of $S_{cos}(t_1, \omega_2)$ becomes the real part of $S_r(t_1, \omega_2)$ and the real part of $S_{sin}(t_1, \omega_2)$ becomes the imaginary part of $S_r(t_1, \omega_2)$, then

$$S_r(t_1, \omega_2) = A_2 \exp(i\Omega_1 t_1) \qquad \textit{Equation 6.4}$$

This is achieved in practice by using the psort command, which substitutes the imaginary parts of even rows, i.e., $S_{cos}(t_1, \omega_2)$ with the real parts of odd rows, i.e., $S_{sin}(t_1, \omega_2)$. Fourier transformation of $S_r(t_1, \omega_2)$ with respect to t_1 gives,

$$S_r(\omega_1, \omega_2) = A_1^+ A_2 \qquad \textit{Equation 6.5}$$

in the real part of the resulting spectrum. Hence, by this approach the sign of Ω_1 can be discriminated and pure absorption lineshapes result. To avoid having to perform this quite lengthy process every time, a macro has been written (see Appendix) to 'automate' the processing of two-dimensional data sets acquired according to States' method.[48]

6.3.1.2.1 Experimental results

A ^{19}F two-dimensional exchange spectrum was recorded at 227 K (Figure 6.6). Spectral conditions were: $\pi/2$ pulse duration, 3 μs; recycle delay, 20 s; ^{1}H decoupling power, 105 kHz; spin rate, 7.0 kHz; number of transients, 8; number of slices in t_1, 30; dwell in t_1, 125 μs. With a mixing time of 50 ms, all four peaks are of equal intensity, indicating that exchange is 'fast' on this timescale. For the reasons explained in the previous section, this method was not chosen to determine exchange rates in the slow-exchange limit. However, the duration of this experiment, approximately 2.7 hours, shows the clear advantage of being able to observe ^{19}F as opposed to ^{13}C, for which of the order of 4 days of spectrometer time would have been required. This would have been impossible with the current variable temperature facilities available, where it is only feasible to run continuously for approximately 36 hours.
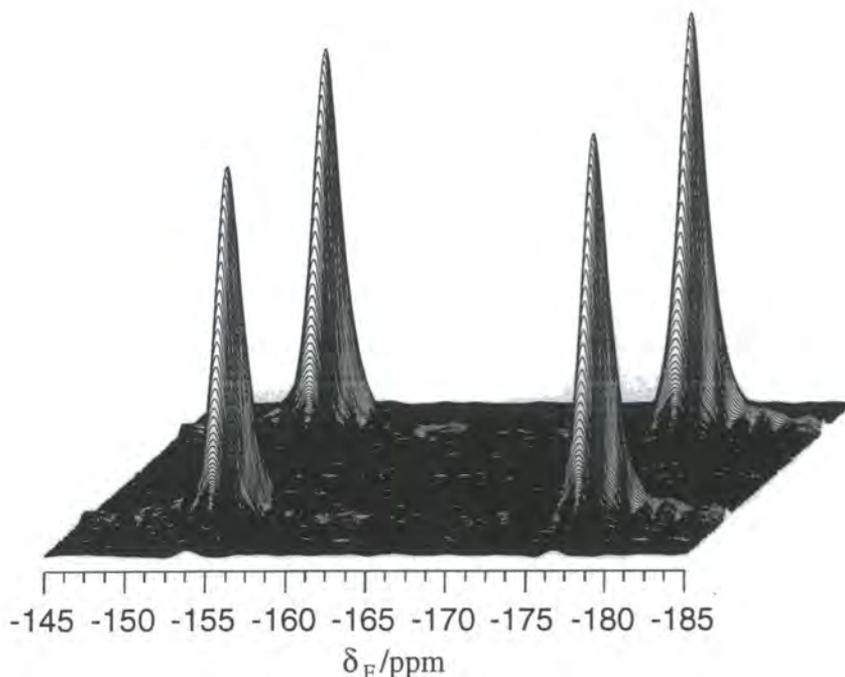
Figure 6.6. Two-dimensional ^{19}F exchange spectrum of the fluorocyclohexane/thiourea inclusion compound at 227 K.

In this particular experiment, ^1H decoupling was applied during t_1 and t_2, but not during the mixing time. In this case the nature of the exchange is clearly understood (conformational exchange), and the same spectrum would arise for experiments performed with and without ^1H decoupling during the mixing time. However, if for example the exchange is spin diffusion and involves the ^1H spins, then the application of ^1H decoupling could affect the resulting spectrum.[49,50]

6.3.1.3 Selective polarisation inversion experiments[34,35]

The selective polarisation inversion (SPI) experiment is the one-dimensional analogue of the two-dimensional exchange experiment. In the SPI experiment, a $\pi/2$ pulse is first applied to create transverse magnetisation. Then one of the spins is selectively inverted during the time denoted t_1 in the 2D exchange pulse sequence

(Figure 6.4). Exchange of magnetisation between spins is then allowed to occur during the mixing time, t_m. Another $\pi/2$ pulse is then applied so that any exchange of magnetisation that occurred during the mixing time can be detected. Rates of spin exchange are measured by varying t_m, while t_1 is kept constant (its only function being to secure antiphase magnetisation between the two spin types). Selective inversion can be achieved via selective[51] means, for example using soft[52,53] pulses or DANTE,[54] or via a non-selective pulse, which is the method of choice in this case. The pulse sequence used for the SPI experiment is essentially the same as that used in the 2D exchange experiment (Figure 6.4). One of the spins is selectively inverted by selecting the transmitter frequency and the evolution time t_1, such that the two magnetisation vectors for the two exchanging species, denoted M(A) and M(B), are separated by 180° at the end of t_1. How this is actually achieved can be explained pictorially using vectors to describe the progression of the experiment (Figure 6.7).
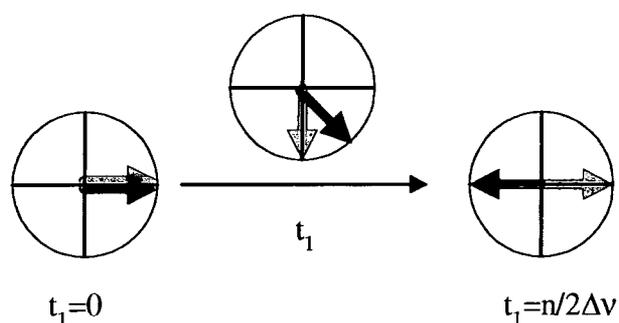
Figure 6.7. Vector representation of how selective inversion is achieved via a non-selective pulse. The red and blue vectors denote the two exchanging species, M(A) and M(B) respectively.

If two peaks, A and B, are separated by a frequency Δv, then the transmitter is offset from A by a frequency of $2\Delta v$ and from B by a frequency of Δv. Therefore during t_1, pictured in the rotating frame, A will precess at twice the rate of B. It is clear therefore that if t_1 is set to be equal to $n/2\Delta v$ where n is an integer, then the phase difference between the two magnetisation vectors will be 180°. However, it is also important to note that during t_1, evolution occurs not only under the isotropic chemical shifts but also under SA which renders the chemical shift under MAS

time-dependent. However, it is possible to refocus dephasing of the spins due to SA by ensuring that the MAS rate is set to be equal to a multiple of $2\Delta v$. For spins with small SA, the necessity for rotor synchronisation of t_1 is not critical. This particular feature of the SPI experiment has previously been examined for ^{15}N spins with a large SA.[41] Other variations for achieving selective inversion using a non-selective pulse have included placing the transmitter in between the two peaks to create a 180° phase difference during t_1,[34,55] placing the transmitter on resonance for one of the peaks to create a 180° phase difference during t_1[50,56] and offsetting the transmitter from one peak by the frequency separation between the two peaks to create a 90° phase difference during t_1.[35]

At the end of t_1, another $\pi/2$ pulse is applied which places one vector along the +z axis and the other along the –z axis. During the mixing time, magnetisation exchange occurs, thus resulting in a net decrease in the magnitude of z magnetisation at both sites. A final $\pi/2$ pulse converts the magnetisation to detectable transverse magnetisation. Therefore, by monitoring the intensity of the magnetisation as a function of mixing time, it is possible to obtain rates of exchange. In this discussion, the effect of T_2 during t_1 and the effect of T_1[35] during the mixing time has so far been neglected. In the present study, due to the fact that $T_2 \gg t_1$, the effect of T_2 will not be considered. In studies involving exchange between broad peaks,[57] T_2 effects during t_1 need to be included. To examine the possible effects of T_1 relaxation during the mixing time, it is necessary to consider the modified (to incorporate exchange) Bloch equations for two exchanging species, A and B,

$$\frac{dM(A)_z}{dt} = \frac{M(A)_\infty - M(A)_z}{T_1} - k_A M(A)_z + k_B M(B)_z$$

Equation 6.6

$$\frac{dM(B)_z}{dt} = \frac{M(B)_\infty - M(B)_z}{T_1} - k_B M(B)_z + k_A M(A)_z$$

where $M(A)_\infty$ and $M(B)_\infty$ represent the A and B magnetisations at thermal equilibrium, $M(A)_z$ and $M(B)_z$ represent the A and B magnetisations at time t and k_A and k_B are the rate constants for the conversion of A to B and B to A, respectively. When T_1 is long relative to the lifetime of the species undergoing exchange, then a simplified form of these equations can be used,

$$\frac{dM(A)_z}{dt} = -k_A M(A)_z + k_B M(B)_z$$

Equation 6.7

$$\frac{dM(B)_z}{dt} = -k_B M(B)_z + k_A M(A)_z$$

Solving for $M(A)_z$ and $M(B)_z$ using the standard solution for a pair of first order differential equations[58] gives,[50]

$$M(A)_z = M(A)_i \exp(-kt) + M(A)_f$$

Equation 6.8

$$M(B)_z = M(B)_i \exp(-kt) + M(B)_f$$

where B is the spin that is inverted and k is the sum of k_A and k_B.

The M_i term in each equation defines the initial A and B magnetisations and the M_f term defines the final A and B magnetisations after exchange, in the absence of any spin-lattice relaxation. The exact form of the M_f term can be derived by considering a general case where the initial z magnetisation of B is -n times that of A, i.e., $-M(B)_i = nM(A)_i$. When exchange is complete, the sum of the final A and B magnetisations must be equal to the sum of their initial magnetisations, i.e., $M(A)_i + M(B)_i$, but $M(B)_f$ must still be equal to $nM_f(A)$. Therefore, after complete exchange, the z magnetisations of A and B are,

$$M(A)_f = \frac{M(A)_i + M(B)_i}{M(A)_i - M(B)_i} M(A)_i$$

Equation 6.9

$$M(B)_f = -\frac{M(A)_i + M(B)_i}{M(A)_i - M(B)_i} M(B)_i$$

Therefore, for the general case where the z magnetisations of A and B are opposite in sign, but not equal, $M(A)_z$ and $M(B)_z$ will decay exponentially to their respective final magnetisations, $M(A)_f$ and $M(B)_f$. However, if the initial A and B magnetisations are equal, but opposite in sign then, $M(A)_f$ and $M(B)_f$ will be equal to zero and so $M(A)_z$ and $M(B)_z$ will decay exponentially towards zero. Figure 6.8 shows the magnetisation exchange curves (SPI plots) where a) the initial A and B magnetisations are equal (n=1), but opposite in sign, and b) the initial magnetisation of B is twice that of A (n=2), but again is opposite in sign.
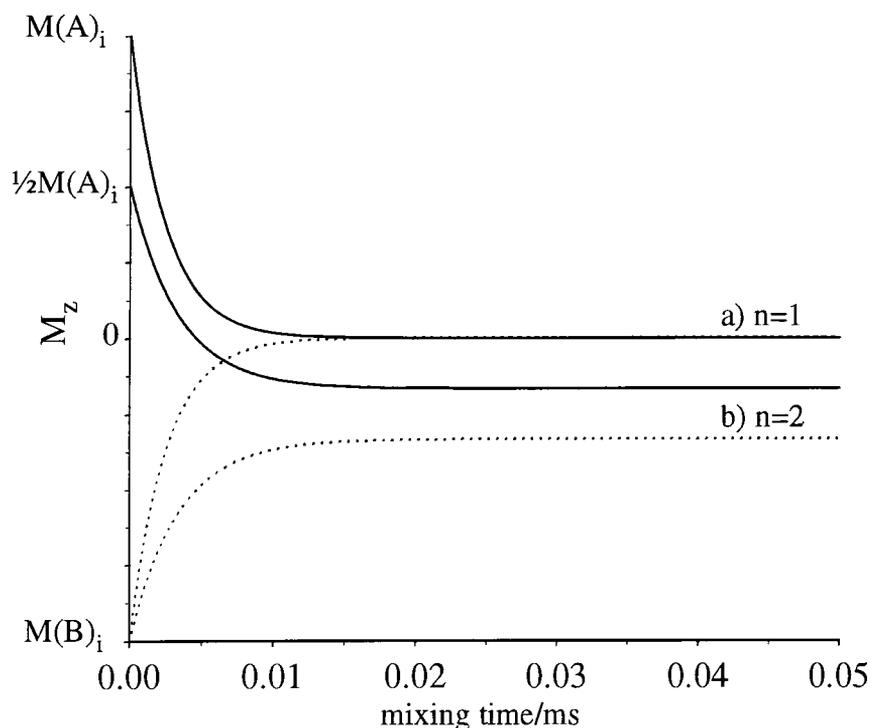
Figure 6.8. Graph plotting magnetisation exchange curves for a) M(A)$_i$ = -M(B)$_i$ and b) 2M(A)$_i$ = -M(B)$_i$. The A and B magnetisations as a function of time are represented by the solid and dotted lines respectively.

In the absence of T$_1$ relaxation during the mixing time and T$_2$ relaxation during t$_1$, the sum of the exchange rates can simply be obtained from the decay constant of the two exponentials. Experimental data can readily be fitted using a nonlinear least squares (nonlinear regression) analysis in Axum[59] which uses the Marquardt-Levenberg algorithm.[60] It is then possible to obtain each rate constant individually using the A and B magnetisations at thermal equilibrium,

$$k = k_A + k_A \frac{M(A)_\infty}{M(B)_\infty} \qquad Equation\ 6.10$$

When T$_1$ is short or of the order of the timescale of the exchange process, then T$_1$ effects needed to be included in the analysis. How these effects will manifest themselves depends upon the phase cycling employed, and this particular aspect of the experiment will be examined in the following section.

6.3.1.3.1 Phase cycling

If the same phase cycling is used as was used for the two-dimensional exchange experiment, then it is not possible to separate exchange from T_1 relaxation effects. The reason as to why it is not possible to separate these effects using the phase cycle in Table 6.1, can be understood by examining the evolution of the spins using the phase cycling for the first two transients (Figure 6.9). On the first transient, at the start of the mixing time A and B are labelled with positive and negative z magnetisation respectively, i.e., $M(A)_z$ and $-M(B)_z$. However on the second transient the labelling of A and B is reversed at the start of the mixing time. Considering T_1 effects only during the mixing time, then on the first transient species B undergoes T_1 relaxation whereas on the second transient it is species A that undergoes T_1 relaxation. Hence, if there is only T_1 relaxation during the mixing time, then over a complete phase cycle the signals of both A and B will decay.
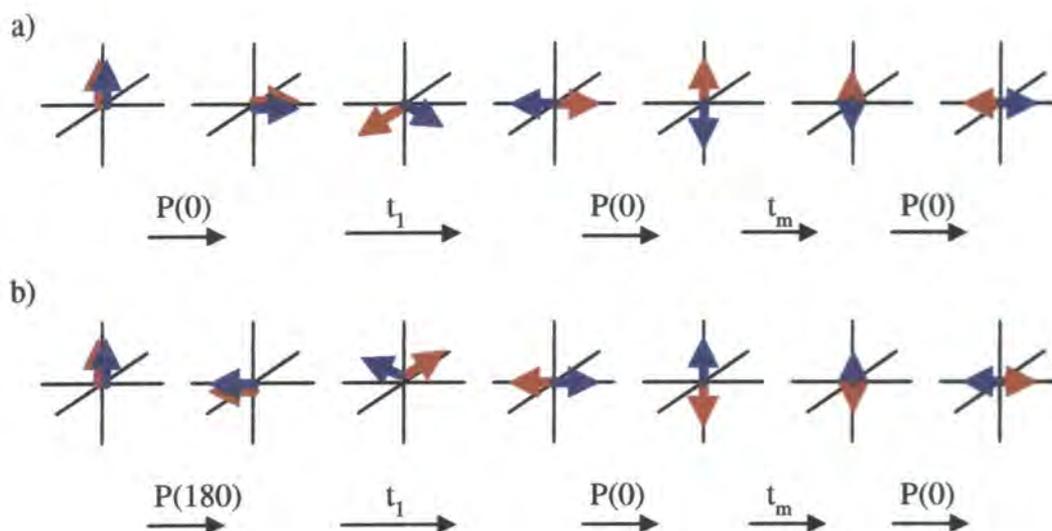
Figure 6.9. Vector representation of SPI experiment using the phase cycling given in Table 6.1 on a) first transient and b) second transient. The red and blue vectors denote M(A) and M(B) respectively.

However, if exchange and T_1 relaxation both occur during the mixing time, then a pair of magnetisation exchange curves will result which can be described by the product of two exponentials with decay constants of k and $1/T_1$,

$$M(A)_z = M(A)_i \exp(-kt) \exp\left(\frac{-t}{T_1}\right)$$

$$M(B)_z = M(B)_i \exp(-kt) \exp\left(\frac{-t}{T_1}\right)$$

Equation 6.11

It is assumed in the above equations that both spins have the same T_1 value and that T_1 can be described using a single exponential function. Clearly, in this situation an independent evaluation of T_1 must be made in order to determine k.

However, if every alternate line in the Table 6.1 is removed, thus reducing the phase cycle to 4, the same magnetisation labelling is applied to the two spins at the start of the mixing time on every acquisition. If there is no exchange, then the inverted spin will simply return to equilibrium and the intensity of the non-inverted spin will remain constant. However, if exchange effects are superimposed, assuming that the timescale for T_1 is long relative to that for exchange, then the two magnetisation exchange curves will first decay exponentially (in a manner as described previously) and then as the timescale for T_1 is encountered both magnetisation vectors return to thermal equilibrium. However, it has also been shown that T_1 effects and exchange can be separated by performing two experiments, one with $t_1=0$ and the other with t_1 set to a value such that one of the two spins is selectively inverted.[50] The equations describing the evolution of magnetisation undergoing both exchange and T_1 relaxation can be solved using the *rkfixed* function in Mathcad which is based on the Fourth order Runge-Kutta method[61] for solving two differential equations. The solutions can then be compared to experimental data to find k, and subsequently k_A and k_B, and T_1.

6.3.1.3.2 Experimental results

SPI experiments were performed at 217, 197 and 177 K. Figure 6.10 shows a typical SPI spectrum which is actually the result of the experiment performed at

197 K. The frequency separation between the axial and equatorial peaks is 4.3 kHz and so the transmitter was positioned 4.3 kHz, to the high frequency side of the equatorial peak. Therefore a time of 116 μs was used to create a phase difference of 180° between the magnetisation vectors for the axial and equatorial spins. To refocus the effects of SA during this time, a spin rate of 8.6 kHz was used. Experiments were performed with approximately 10 - 11 different mixing times in order to generate enough data so that k could be accurately determined. Other spectral conditions were: $\pi/2$ pulse duration, 3 μs; recycle delay, 20 s; ^{1}H decoupling power, 105 kHz; number of transients per mixing time, 8.

-150 -200
δ_F/ppm
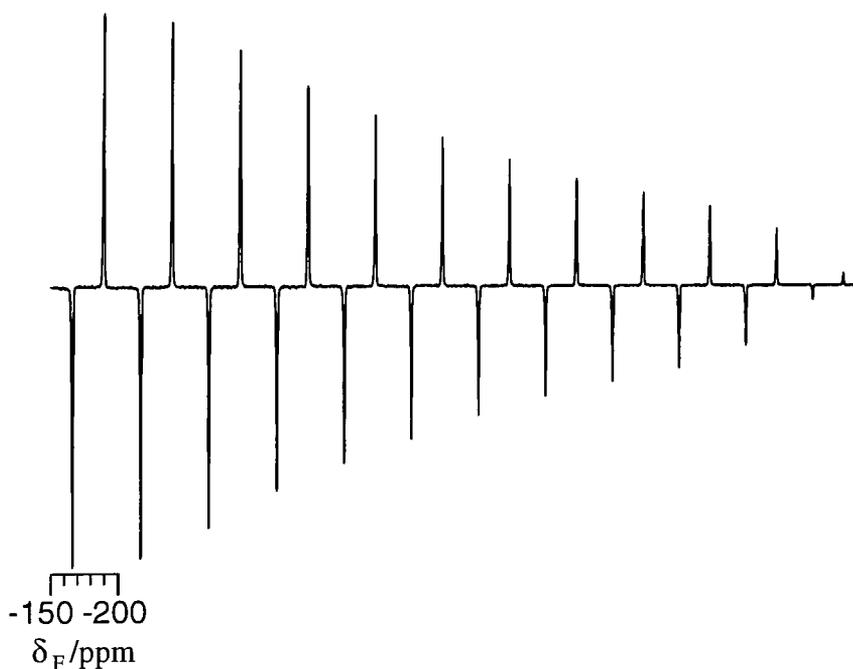
Figure 6.10. Fluorine-19 SPI experiment performed at 197 K.

At 217 and 197 K, the magnitude of T_1 was deemed to be long relative to the maximum mixing times needed, 30 ms and 200 ms respectively, to achieve complete exchange. Therefore, for these two temperatures the phase cycle given in Table 6.1 was used and T_1 effects were not included in the fitting of the magnetisation curves. However, at 177 K, T_1 was estimated to be of the same order of magnitude as the maximum mixing time required, 2 s, to achieve complete exchange. An independent

measurement of $T_1(^{19}F)$ was made using the inversion-recovery pulse sequence and was determined to be 3.8 s. However, upon fitting the experimental data to the equations which do and do not allow for T_1 effects, the same average rate constant of 1.5 Hz was obtained. Therefore, it can be concluded that T_1 relaxation contributes a negligible amount to the decay of the magnetisation exchange curves obtained using the 8 phase cycle pulse sequence. However, a second experiment was performed at 177 K using the phase cycle of four sequence to see how the two methods compared for the determination of the average rate constant. Figure 6.11 shows the results obtained using the two phase cycling schemes.
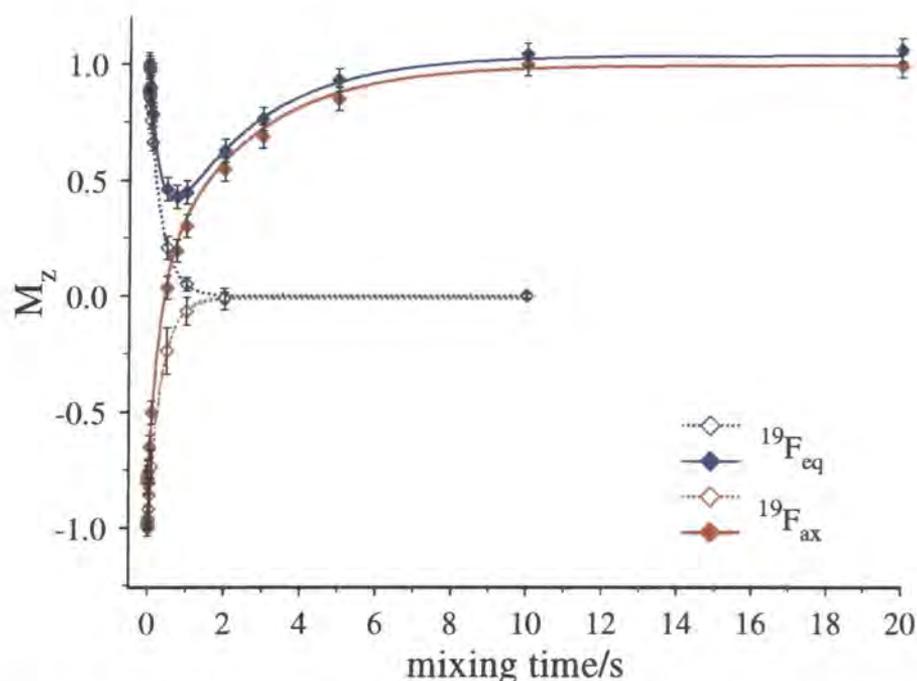
Figure 6.11. Graph plotting ^{19}F signal intensity as a function of mixing time for the SPI experiments ran at 177 K using a phase cycle of eight (empty boxes) and four (filled boxes). The best fit to the experimental data is indicated by the dotted and solid lines.

The rate constant, $k_{average}$, obtained via these two experiments along with the experiments performed at 217 and 197 K is shown in Table 6.2. It can be seen that within experimental error, the rate constants obtained at 177 K using the two different methods are identical. As ^{19}F NMR is particularly sensitive, the SPI experiments can be acquired in a relatively short period of time and with excellent signal-to-noise (see Figure 6.10), thus improving the accuracy of the data obtained.

Temperature/K	$k_{average}$/Hz
217	179 ± 5
197	16 ± 1
177	1.5 ± 0.2
$177^{\dagger}$	1.4 ± 0.2

Table 6.2. Rate constants obtained at 217, 197 and 177 K using the ^{19}F SPI experiment. All experiments were performed using the eight-pulse phase cycle sequence except that indicated by †, which used the four-pulse phase cycle sequence.

6.3.1.4 Spin-lattice relaxation in the rotating frame.

Relaxation measurements can be used to investigate molecular motions, with the rate that can be probed dictated by the relaxation time examined. The three relaxation times, T_1 (spin-lattice relaxation time), $T_{1\rho}$ (spin-lattice relaxation time in the rotating frame) and T_2 (spin-spin relaxation time) are affected by motions occurring at rates of the order of MHz, kHz and Hz, respectively. For example, T_1 measurements have been used to investigate CH_3 rotations,[62] $T_{1\rho}$ measurements have been used to measure rotations in porphine macrocycles,[27] phenyl[63] and tert-butyl[26,64] rotations and T_2 measurements have been used to study the nature of the rotation process in benzene.[65] Hence, a wide range of molecular motions can be studied via relaxation time measurements. Relaxation studies involving T_1 and $T_{1\rho}$ utilise, in a plot of relaxation time against temperature, the 'minimum' and the gradient of the slopes in the slow and fast motional regimes to obtain rate constants and activation energies of a particular motion. However, the theory used to calculate such parameters from relaxation data depends upon the relative magnitudes of the relevant correlation time, τ_c, and T_2. When $\tau_c \ll T_{2RL}$ as in the case of rapid motion or 'weak collisions', where T_{2RL} is the rigid lattice T_2, the theory developed by Bloembergen, Purcell and Pound[66] (BPP) is applicable. However, in the case of slow motions or

'strong collisions' (and so $\tau_c > T_{2RL}$), then the theory of Slichter and Ailion[67,68] is valid.

Bandshape analysis has already been used to determine that the rate of exchange of interest in this chapter is of the order of 100 kHz at 300 K, and so the study of exchange in this region should be amenable to $T_{1\rho}$ measurements. The interpretation of $T_{1\rho}$ in terms of τ_c depends upon whether the motion is rapid, slow or intermediate in the context of the above discussion.[69] In this particular case, BPP theory is applicable and the corresponding expression for $T_{1\rho}$ based on that derived by Jones[70] will be used. Assuming that $T_{1\rho}$ is determined on resonance and $\omega_1 \ll \omega_0$, then the expression relating $T_{1\rho}$ to the motional correlation time is given by,

$$\frac{1}{T_{1\rho}} = K\left[\frac{3}{2}\frac{\tau_c}{1+\omega_e^2\tau_c^2} + \frac{5}{2}\frac{\tau_c}{1+\omega_0^2\tau_c^2} + \frac{\tau_c}{1+4\omega_0^2\tau_c^2}\right] \qquad \textit{Equation 6.12}$$

where K is equal to,

$$K = \frac{2}{5}\frac{\gamma^4\hbar^2}{r^6}I(I+1) \qquad \textit{Equation 6.13}$$

γ is the magnetogyric ratio, r is the internuclear distance, I is the nuclear spin quantum number, $2\pi\hbar$ is the Planck constant, τ_c is the correlation time, ω_e is the effective precession frequency in the rotating frame ($\omega_e = \gamma B_1$) and ω_0 is the resonance frequency. For motions occurring at rates of the order of kHz, the system can be considered 'rigid' as far as T_1 is concerned, i.e., $\omega_0^2\tau_c^2 \gg 1$. Therefore, the final two terms in the above expression can be neglected as they approximate to zero and so do not influence $T_{1\rho}$. In the extreme narrowing situation for $T_{1\rho}$, $\omega_e^2\tau_c^2 \ll 1$,

$$\frac{1}{T_{1\rho}} = K\frac{3}{2}\tau_c \qquad \textit{Equation 6.14}$$

and so as τ_c increases, $T_{1\rho}$ decreases. When $\omega_e^2\tau_c^2 \gg 1$, as in the rigid lattice limit for both T_1 and $T_{1\rho}$,

$$\frac{1}{T_{1\rho}} = K\frac{3}{2}\frac{1}{\omega_e^2\tau_c} \qquad \textit{Equation 6.15}$$

and so as τ_c increases, $T_{1\rho}$ increases. Therefore, in the intermediate region, $T_{1\rho}$ will pass through a minimum at which $\omega_e^2\tau_c^2 \sim 1$. Hence, in a plot of $T_{1\rho}$ against τ_c, a

minimum will be observed when the inverse of the correlation time is approximately equal to B_1.
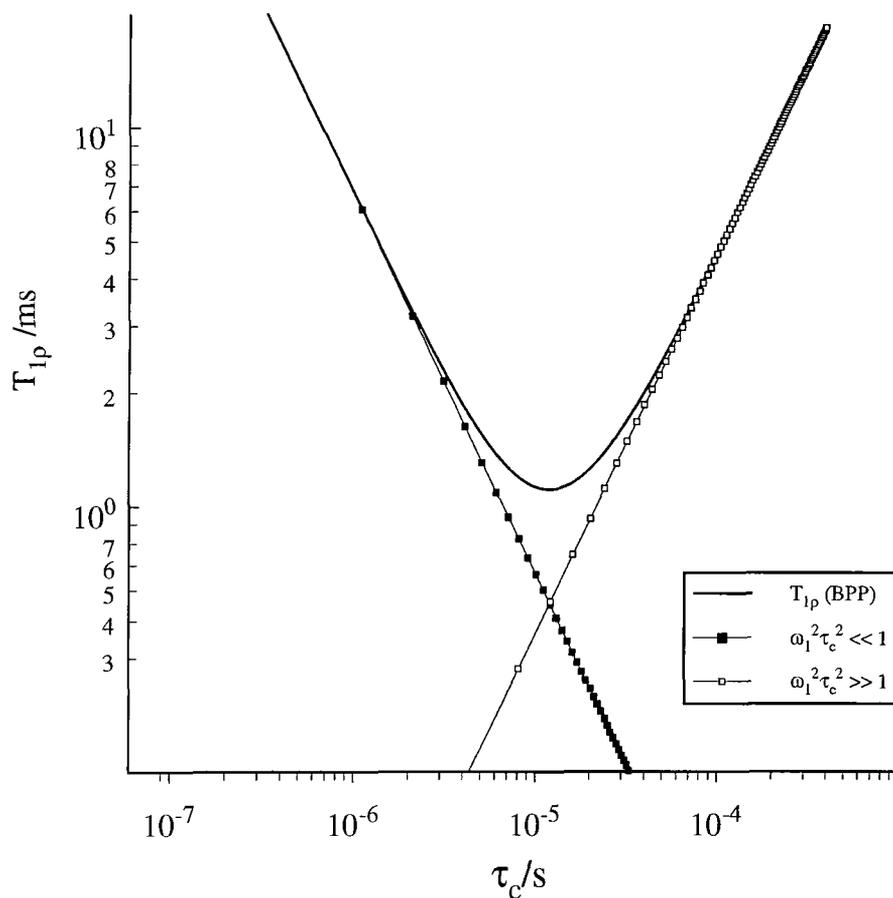
Figure 6.12. Variation of $T_{1\rho}$ with motional correlation time (plotted on a log scale) calculated using BPP theory. The variation of $T_{1\rho}$ at the slow and fast limits is shown via the empty and filled boxes respectively.

An important point to note is that the behaviour of $T_{1\rho}$ in the rigid-lattice region is no longer adequately described using BPP theory and is better described using the 'strong collision' theory. However, the purpose of this discussion was to illustrate that a minimum value of $T_{1\rho}$ can be observed in a plot against τ_c. To vary τ_c, variable-temperature experiments are necessary and so $T_{1\rho}$ values are obtained as a

function of temperature. However, assuming that T and τ_c are related via the Arrhenius equation,

$$\tau_c = \tau_0 \exp\left(\frac{E_a}{kT}\right) \qquad \textit{Equation 6.16}$$

then plots of $\ln T_{1\rho}$ against $\ln(\tau_c)$ and $1/T$ are analogous. Therefore, the observation of a minimum in a plot of $\ln T_{1\rho}$ against $1/T$ will yield the motional correlation time and also an activation energy may be determined.

6.3.1.4.1 Experimental results

Variable-temperature $T_{1\rho}(^{19}F)$ times were measured using a variable spin-lock time experiment. This involved the creation of ^{19}F transverse magnetisation via a $\pi/2$ pulse and then applying a spin-locking pulse of varying duration, before directly observing the ^{19}F signal while simultaneously applying ^1H decoupling. Typically ten spin-lock times, up to a maximum of 19 ms, were used to determine $T_{1\rho}$ at each temperature. Values of $T_{1\rho}$ were obtained by integrating the peak(s) at each spin-lock time and then fitting the data with the 't1rho' function in the XY panel in Spinsight. Measurements were performed at temperatures between 217 and 328 K in order to characterise sufficiently the $T_{1\rho}$ minimum. Typical spectral conditions were: ^{19}F $\pi/2$ pulse duration, 3 μs; recycle delay, 40 s; ^1H decoupling power, 105 kHz; number of transients per spin-lock time, 8; MAS rate, 7.0 kHz.

At the temperature at which the minimum $T_{1\rho}$ value is observed, then the inverse of the correlation time for the 'chair-chair' ring inversion process is approximately equal to the spin-locking field expressed in frequency units. Therefore, at 1000K/T = 3.3 which corresponds to a temperature of ~300 K, the ring inversion rate is equal to 83 kHz. It is noticeable that the behaviour of $T_{1\rho}$ where $\omega_e^2\tau_c^2 \ll 1$, is not as well defined as in the region where $\omega_e^2\tau_c^2 \gg 1$. The reason is that it was not possible to go to higher temperatures, as the fluorocyclohexane/thiourea inclusion compound becomes unstable and decomposes to give the host and guest.
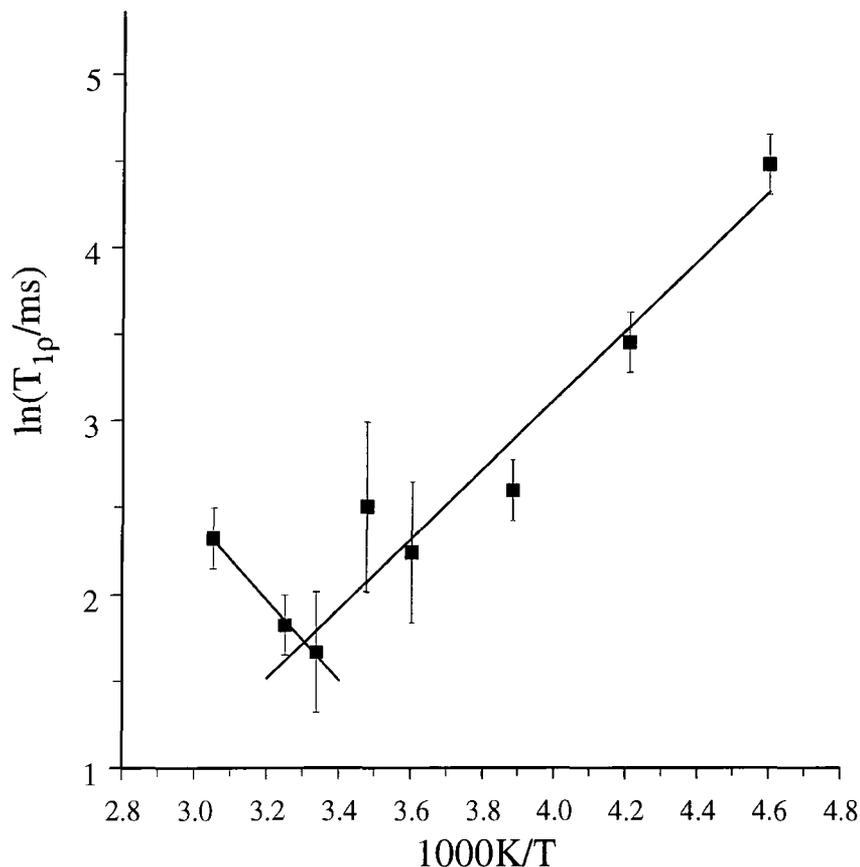
Figure 6.13. Graph plotting the variation in ln[$T_{1\rho}(^{19}F)$] against the inverse of temperature. The solid line is the best fit to the experimental data (filled squares). The minimum $T_{1\rho}(^{19}F)$ value is observed at $1000K/T \sim 3.3$.

6.3.2 Thermodynamics of the 'chair-chair' ring inversion process.

The rate constants obtained via the three methods described in the previous section, can be used to determine the thermodynamics of the 'chair-chair' ring inversion process. As the populations of the axial and equatorial conformations are virtually invariant with temperature, and so the forward and reverse exchange rates are almost identical, only the average activation parameters have been determined. These can be determined using the Eyring[71] equation,

$$k = \kappa \frac{k_B T}{h} K^{\ddagger}$$ *Equation 6.17*

where $K^{\ddagger}$ is a pseudo-equilibrium constant (and in this case is equal to 1), κ is the transmission coefficient (assumed to be 0.5), k_B is the Boltzmann constant, h is the

Planck constant, T is temperature and k is the average rate constant. Rewriting $K^{\ddagger}$ in terms of the Gibbs[71] free energy of activation parameter and expanding the resultant in terms of the enthalpy and entropy of activation parameters, $\Delta H^{\ddagger}$ and $\Delta S^{\ddagger}$ gives,

$$k = \kappa \frac{k_B T}{h} \exp\left(\frac{-\Delta H^{\ddagger}}{RT}\right) \exp\left(\frac{\Delta S^{\ddagger}}{R}\right) \qquad \textit{Equation 6.18}$$

Therefore, in a plot of $\ln(k/T)$ against $1/T$, the slope and intercept will give $-\Delta H^{\ddagger}/R$

and $\left(\dfrac{\Delta S^{\ddagger}}{R} + \ln\dfrac{\kappa k_B}{T}\right)$ respectively. Clearly, to increase the accuracy to which the

thermodynamic parameters can be determined, it is desirable to obtain rate constants over a wide temperature range. As already mentioned, bandshape analysis can only be used to determine rate constants accurately within the vicinity of the coalescence temperature, 237 - 290 K. However, with the addition of the SPI and $T_{1\rho}$ experiments, it is possible to obtain rate constants at temperatures above (300 K) and below (177 - 217 K) the region where bandshape analysis is applicable. Notice that the temperature ranges over which the rate constants were obtained overlap to some extent. Therefore, it is possible to increase the precision to which the thermodynamic parameters can be determined by using more than one method to determine the rate constants.

Figure 6.14 shows the rate constants obtained using the three methods previously outlined, in the form of an Eyring plot. The solid line is the best-fit line of the experimental data. The average activation parameters for the forward and backward processes obtained from the Eyring plot are: $\Delta H^{\ddagger} = 39.4 \pm 2.6$ kJ mol^{-1}, $\Delta S^{\ddagger} = -11.9 \pm 11.0$ J mol^{-1} K^{-1} and $\Delta G^{\ddagger}$ (263 K) $= 42.5 \pm 5.5$ kJ mol^{-1}. The values obtained for $\Delta H^{\ddagger}$ and $\Delta S^{\ddagger}$ via ^{19}F NMR differ from those reported using ^{13}C NMR in a previous study,[10] although data for $\Delta G^{\ddagger}$ (263 K) are comparable. However, in this work the ring-inversion process has been studied over a wider temperature range (120 K) exploiting the sensitivity advantage of ^{19}F NMR. Moreover, rate constants have also been obtained in the slow and fast exchange regimes where bandshape analysis lacks precision using selective polarisation inversion experiments and $T_{1\rho}$ measurements, respectively. The temperature range over which bandshape analysis can be used to accurately determine rate constants is also greater for ^{19}F compared to

^{13}C because the chemical shift difference being averaged is larger. Therefore, the values obtained for the activation parameters using ^{19}F NMR are significantly better than those obtained via ^{13}C NMR.
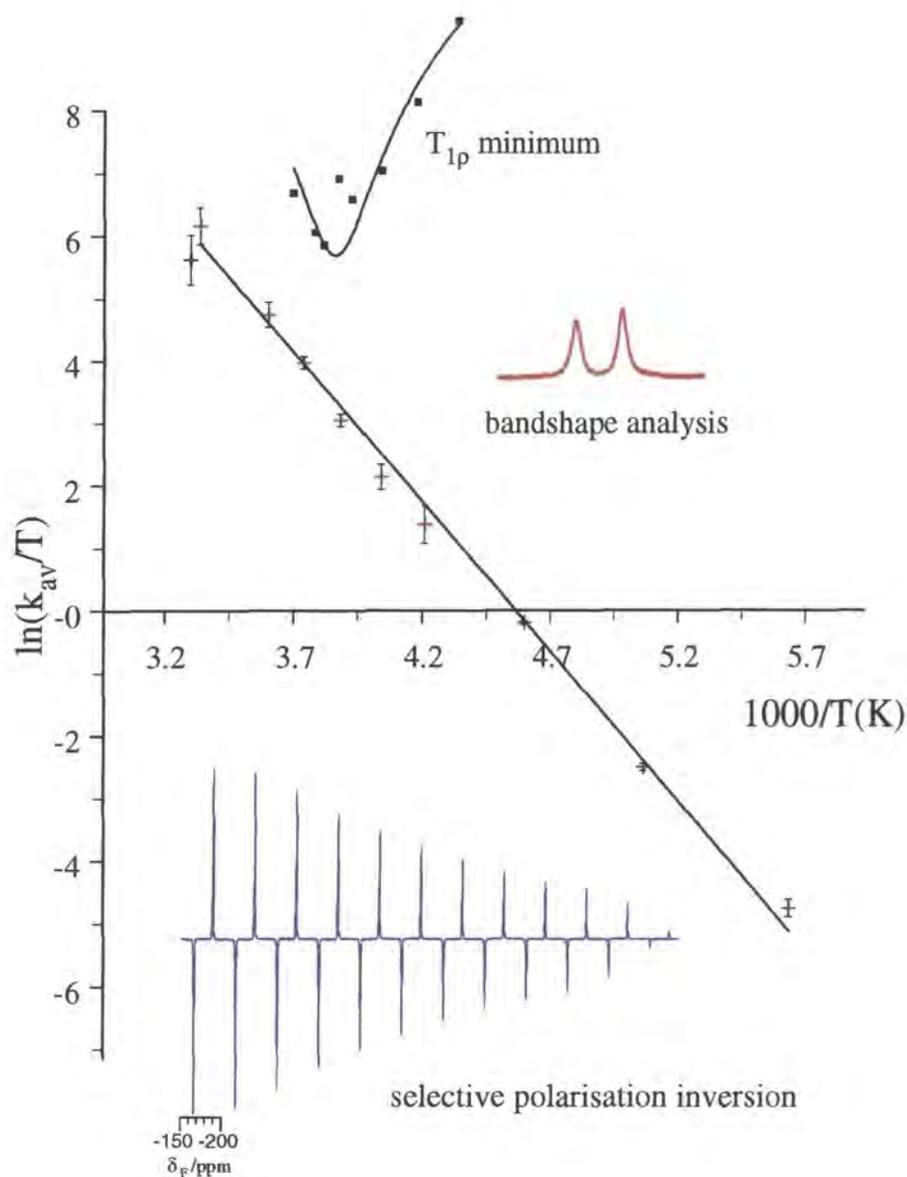
Figure 6.14. Graph plotting ln(k/T) against 1/T, with $k_{average}$ obtained using selective polarisation inversion experiments (blue), bandshape analysis (red) and $T_{1\rho}$ measurements (black).

A summary of activation parameters obtained for the ring inversion process in fluorocyclohexane in a variety of phases is shown in Table 6.3. As expected when fluorocyclohexane is in the pure phase or solution, the equatorial conformer predominates. However, the axial conformer is still slightly more stable relative to the equatorial form than in other halogen-monosubstituted cyclohexanes. In fluorocyclohexane, the energy difference between the preferred equatorial conformation, and the axial conformer, ΔG° (180 K) = 1.0 kJ mol^{-1}, is smaller than, for example, between the equatorial and axial conformations in bromocyclohexane, ΔG° (169 - 187 K) = 2.4 kJ mol^{-1}. The relative stability of the axial conformer in fluorocyclohexane has been interpreted as arising from a shorter carbon-halogen bond and a less polarisable electron cloud about the fluorine, hence decreasing the destabilising effect of 1,3-diaxial substituent interactions.[73]

Phase	Technique used	Average activation parameters			Equilibrium data $K = \dfrac{ax}{eq}$	Comments	Reference
		$\Delta H^{\ddagger}/\text{kJ mol}^{-1}$	$\Delta S^{\ddagger}/\text{J mol}^{-1}\,\text{K}^{-1}$	$\Delta G^{\ddagger}/\text{kJ mol}^{-1}$			
inclusion compound (host - thiourea)	solid-state ^{13}C NMR	57.3 ± 2.1	61.9 ± 8.5 ($\kappa = 0.5$)	41.0	1.0	$\Delta G^{\ddagger}$ calculated at 263 K from the literature	10
inclusion compound (host - thiourea)	solid-state ^{19}F NMR	39.4 ± 2.6	-11.9 ± 11.0 ($\kappa = 0.5$)	42.5 ± 5.5	1.0 (177 K)	$\Delta G^{\ddagger}$ calculated at 263 K	19
solution	^{13}C NMR	43.13 ± 0.84	-0.33 ± 4.05	43.2		$\Delta G^{\ddagger}$ calculated at 263 K from the literature	72
solution (CS$_2$/(CH$_3$)$_2$CO/CD$_3$OD)	^{13}C NMR				0.35 (183 K)		7
solution (CFCl$_3$)	^{19}F NMR	40.06 ± 0.42	-3.47 ± 2.09 ($\kappa = 1.0$)	40.85	0.78 (300 K) 0.51 (185 K)	$\Delta G^{\ddagger}$ given for 217 - 269 K	17
solution(CS$_2$)	^{1}H NMR				0.48 (187 K)		73
gas (3.98 Torr in 2439 Torr CO$_2$)	^{19}F NMR	48.6	3.3	44.8	1.65 (250 K)		16
gas, liquid and solid	IR/Raman				ax and eq present. Phase transition at 180 K , K < 1. Increase p, liquid → solid, K < 1.		14
solution (CS$_2$)					Increase p, K > 1.		
inclusion compound (host - thiourea)					1.0		

Table 6.3. Average activation parameters obtained for the ring inversion process in fluorocyclohexane.

Although average values for the activation parameters are given in Table 6.3, some studies give the activation parameters for the exchange process in both the forward and reverse directions, with the forward reaction being defined as conversion of the axial conformer to the equatorial conformer. Obviously, if the equatorial conformation is more stable than the axial conformation as for fluorocyclohexane in $CFCl_3$,[17] then $\Delta G^{\ddagger}(eq \rightarrow ax) > \Delta G^{\ddagger}(ax \rightarrow eq)$. However, in the thiourea inclusion compound, fluorocyclohexane has no preferred conformation and hence $\Delta G^{\ddagger}(eq \rightarrow ax) = \Delta G^{\ddagger}(ax \rightarrow eq)$. The relative stability of the two fluorocyclohexane conformations in $CFCl_3$ (solution) and thiourea (inclusion compound) is shown in Figure 6.15.

transition state

$\Delta G^{\ddagger} = 40.6$ kJ mol⁻¹

$\Delta G^{\ddagger} = 41.4$ kJ mol⁻¹

$\Delta G^{\ddagger} = 42.5$ kJ mol⁻¹

solution

solution

thiourea

thiourea

F
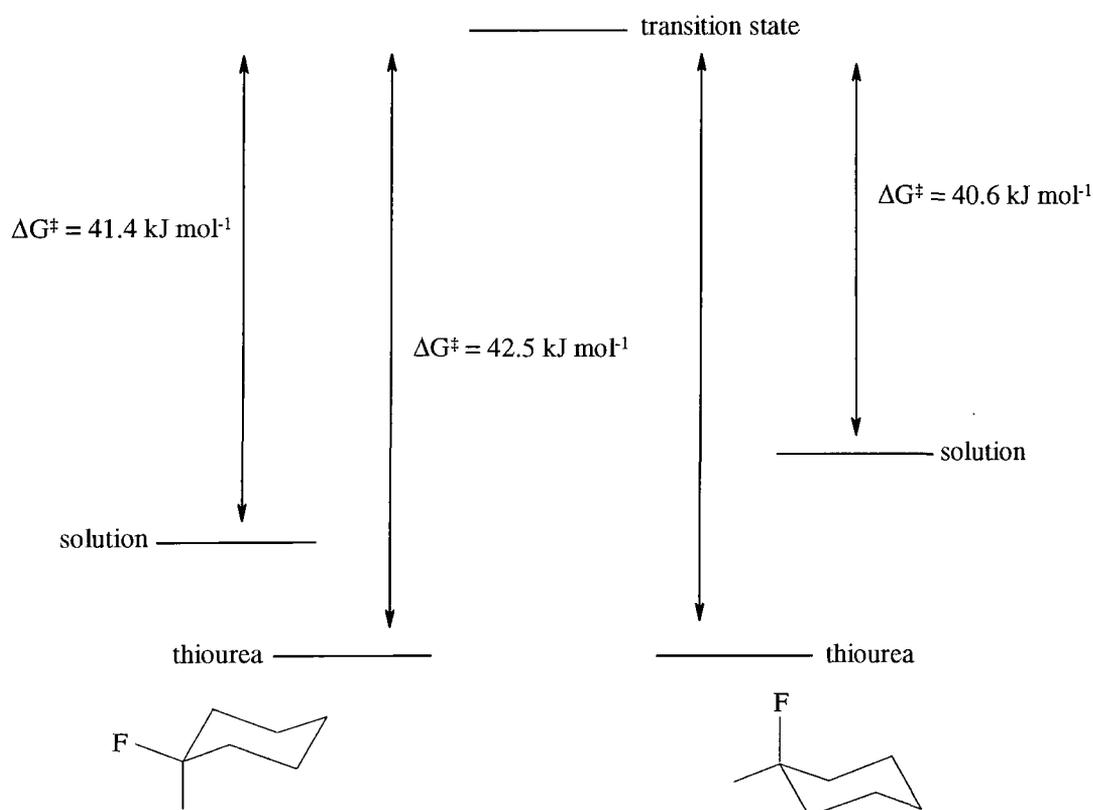
Figure 6.15. Schematic representation of the relative activation energies (at 263 K) for the 'chair-chair' ring inversion of fluorocyclohexane in solution[17] (CFCl₃) and in thiourea.[19] The activation energy values calculated from data within reference 17 have assumed that κ = 0.5 to be comparable with the present study.

It is worth noting at this point, that in assuming $\kappa = 0.5$, then every molecule that reaches the transition state has an equal probability of ring inverting or returning to its original conformation. However, in some studies,[17] it has been assumed that

$\kappa = 1.0$, and so every molecule which proceeds to the transition state will undergo ring inversion. Obviously neither of these assumptions provide a true representation of the reaction pathway for the ring inversion process, which is actually thought to involve cyclohexene-like, boat and twist-boat forms.[17,36]

It can be concluded from the close similarity between $\Delta G^{\ddagger}(\text{eq} \rightarrow \text{ax})$ and $\Delta G^{\ddagger}(\text{ax} \rightarrow \text{eq})$ for fluorocyclohexane in solution and in the thiourea inclusion compound, that the host does not have a significant effect upon the relative energies of the transition state, and the axial and equatorial conformations. It could be said that in the thiourea inclusion compound the axial conformer is marginally more favourable than in solution, although the differences in activation energies are not significant enough to be conclusive.[11] However, the axial conformation is significantly stabilised by the host in other halogen-monosubstituted cyclohexane/thiourea inclusion compounds,[10-12] where differences of at least 5 kJ mol^{-1} were observed in the activation energies.[11] One possible suggestion for the deviant behaviour of fluorocyclohexane, compared to other halogen-monosubstituted cyclohexanes, is that the relative packing efficiencies of the axial and equatorial conformations of fluorocyclohexane in thiourea do not differ to the extent that, for example, the two conformations in chlorocyclohexane do.[12] However, such steric factors cannot be the sole reason, since more bulky substituted cyclohexanes, such as methylcyclohexane, adopt the equatorial conformation in thiourea.[10,11] From previous theoretical studies, it is known that the factors which contribute to the conformational preference of guest molecules in thiourea are guest-guest interactions, host-guest interactions and the potential energy of the guest molecule itself.[12] From the above discussion, it would appear that the host-guest energy term that was deemed to be a major contributory factor to the stabilisation of the axial conformation of chlorocyclohexane in thiourea[12] is not as favourable for fluorocyclohexane. However, in order to assess the factors which contribute to the rather different conformational behaviour of fluorocyclohexane in thiourea, in comparison to other halogen-monsubstituted cyclohexanes, theoretical calculations are needed.

6.4 Solid-state ^{13}C NMR studies

Several ^{13}C studies[8,10] of the ring inversion process have already been published and in one study[10] variable-temperature experiments were performed. At room temperature, a single set of ^{13}C resonances was observed which were assigned using ^{13}C solution-state data.[7] However, in both of these studies only ^{1}H decoupling was applied during acquisition of the ^{13}C FID. In the study by McKinnon et al.,[8] the ^{13}C resonance bonded to the ^{19}F was not observed due to 'a ^{19}F-^{13}C dipolar interaction in excess of 3 kHz'. Clearly, then, the ability to simultaneously decouple both ^{1}H and ^{19}F during acquisition of the ^{13}C FID would be particularly advantageous. Therefore, in this study a 'HFX' triple-channel probe was used to enable ^{13}C spectra to be obtained, particularly at low temperatures, without broadening effects from ^{13}C-^{19}F dipolar interactions. For the purpose of the ensuing discussions, Figure 6.16 gives the numbering system of the carbons in a fluorocyclohexane molecule.
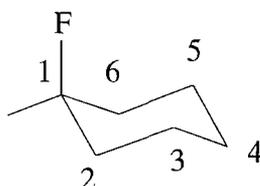
Figure 6.16. Numbering of carbons in fluorocyclohexane.

6.4.1 Variable-temperature ^{13}C experiments

Variable-temperature ^{13}C experiments were performed on the fluorocyclohexane/thiourea inclusion compound. At room temperature, single-pulse experiments were far more efficient than cross polarisation, presumably due to the significant motion of the fluorocyclohexane. However, as the temperature was decreased, $^{1}H \rightarrow {}^{13}C$ cross-polarisation experiments were possible. For the ^{13}C single-pulse experiments typical spectra conditions were: $\pi/2$ pulse duration, 4.5 μs;

recycle delay, 60 s; ^{1}H and ^{19}F decoupling power, 56 kHz; spin rate, 3.0 kHz; number of transients, 480; acquisition time, 102.4 ms. For the low temperature ^{1}H → ^{13}C cross-polarisation experiments, typical spectral conditions were: ^{1}H π/2 pulse duration, 4.5 μs; contact time, 1.0 ms; recycle delay, 5-20 s; ^{1}H and ^{19}F decoupling power, 56 kHz; spin rate, 3.0 kHz; number of transients, 256.

At room temperature, as in previous studies, a single set of resonances was observed in the single-pulse ^{13}C spectrum acquired with ^{1}H decoupling only (Figure 6.17a) since the ring inversion rate is rapid on this timescale.
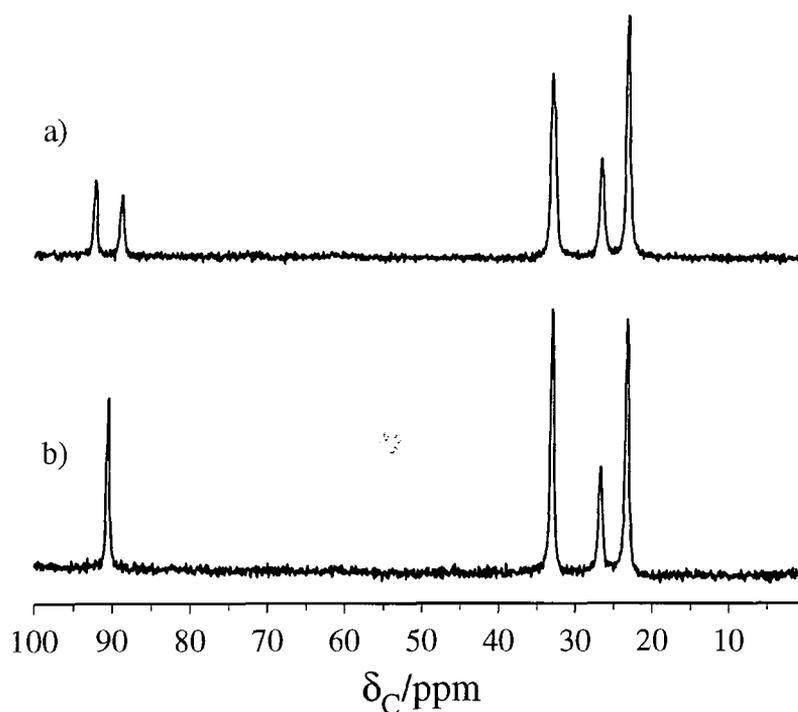
Figure 6.17. Single-pulse ^{13}C spectra (guest region only) obtained at room temperature with a spin rate of 3 kHz with a) ^{1}H decoupling only, and b) ^{1}H and ^{19}F decoupling.

Therefore, as expected, the ^{13}C chemical shifts (Table 6.4) are a weighted average, depending upon the relative populations of the two conformations, of the shifts observed at low temperature in solution for the axial and equatorial conformations.[10]

		Thiourea inclusion compound		Solution
Carbon	conformation	δ_C/ppm (133 K)	δ_C/ppm (25 °C)	δ_C/ppm
1	axial	88.6	90.6	88.8
	equatorial	92.1		92.2
2, 6	axial	31.3	33.0	30.8
	equatorial	33.7		33.2
3, 5	axial	20.9	23.2	20.5
	equatorial	24.8		24.3
4	axial	26.4	26.7	25.6
	equatorial	25.8		25.1

Table 6.4. Assignment of ^{13}C chemical shifts, with solution-state data taken from reference 10 shown for comparison.

However, unlike in a previous study,[8] it was possible to see a doublet for the ^{13}C resonance bonded to the ^{19}F suggesting that the ^{13}C-^{19}F dipolar interaction is less than 3 kHz. The reason for the differing observation may lie in how the spectrum was acquired rather than in the dipolar interaction. The same spinning speeds were used in both cases, so it cannot be attributed to possible averaging of the ^{13}C-^{19}F dipolar interaction by MAS. However, in comparison to this work, the room temperature spectrum of reference 8 was acquired using $^{1}H \rightarrow {}^{13}C$ cross polarisation. Given the dynamics of fluorocyclohexane, the $^{1}H \rightarrow {}^{13}C$ cross-polarisation matching profile for this less protonated carbon may have broken up into sidebands.[74] Hence cross polarisation to this carbon may be much poorer than to other CH_2 carbons, particularly at the Hartmann-Hahn matching condition. If insufficient ^{1}H decoupling powers were used, although this experimental parameter is not cited in reference 8, then this could also account for the absence of the ^{13}C resonance bonded to the ^{19}F in the spectrum (see Chapters 3 and 5).[75] It is also noticeable that the two peaks which make up the doublet appear to be of differing intensities. However, within the S/N limits of the spectrum, they are in fact of the same intensity but the higher frequency component of the doublet has a smaller linewidth. However to check that there was not a stretching and contraction of the two components of the dipolar powder pattern

due to the interplay of dipolar and shielding tensors (see Chapter 7),[44,75] another experiment was run with a spin rate of 5 kHz. However, as expected due to the lack of spinning sidebands in the slower spinning experiment, the same phenomenon was observed. At the higher spin rate, it was also possible to detect a peak at 32.8 ppm which appeared as a shoulder in the spectrum obtained at 3 kHz. This presumably arises from $^2J_{CF}$ coupling. On applying both ^1H and ^{19}F decoupling (Figure 6.17b), only four resonances were now observable in the guest region of the spectrum, due to the removal of both indirect and dipolar ^{19}F-^{13}C couplings.

Unless otherwise stated, all low-temperature spectra discussed in the following section were acquired using both ^1H and ^{19}F decoupling. On lowering the temperature to 133 K, two sets of resonances are observable (Table 6.4) which arise from the axial and equatorial conformations (Figure 6.18). However, it is noticeable that the resonances attributed to the equatorial conformation are more intense than the axial resonances. The intensities in this spectrum (and indeed in all the low-temperature spectra) are not quantitative due to the fact that cross polarisation was used. Unless a detailed study of the cross-polarisation dynamics has been performed, which was not so in this case, such experiments cannot be relied upon to yield quantitative results. However, this is not too important in this case as the guest dynamics and conformational preference are already known from solid-state ^{19}F NMR experiments. As the temperature is increased, it is noticeable that the relative intensities of the axial and equatorial resonances become more or less equal, although for reasons already explained this should be interpreted with caution. With increasing temperature, the chemical shift separation between the axial and equatorial peaks for each carbon decreases. Then, as the chemical shift separations become of the order of the exchange rate, the resonances broaden, and as the temperature is further increased the peaks coalesce and sharpen to give a single set of conformationally averaged peaks. One comparison with the variable-temperature ^{19}F spectra is that the coalescence temperature is lower for ^{13}C due to the smaller chemical shift separation between the two conformations, and differs from one carbon to another.
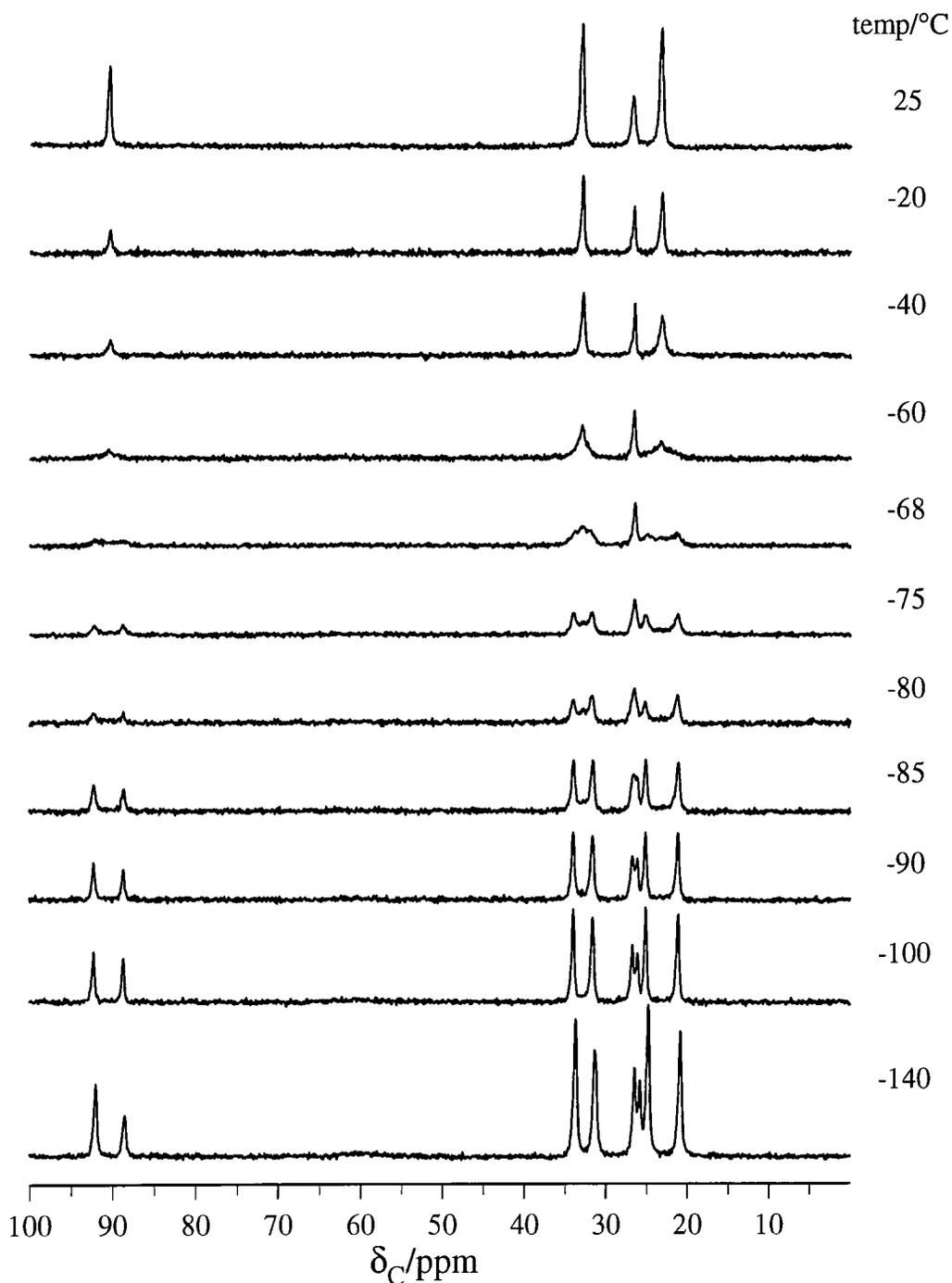
Figure 6.18. Variable-temperature $^1H \rightarrow$ ^{13}C *CP spectra, acquired with both* ^1H *and* ^{19}F *decoupling, (guest region only) of the fluorocyclohexane/thiourea inclusion compound. The spectrum at 25 °C was acquired using single pulse rather than CP.*

It is particularly noticeable that many of the doublets in spectra in the vicinity of the coalescence temperature do not undergo the classical broadening and coalescence behaviour typically observed for exchanging systems. Instead, as the

temperature increases a central peak appears at the expense of the two outer peaks (Figure 6.18). This observation can be attributed to motions occurring at more than one particular exchange rate. There are several possible reasons for this effect which can broadly be ascribed to two sources, experimental and chemical. Experimental reasons include the sample being in a non-equilibrium thermal state at the start of acquisition of data at a particular temperature. Thus, as data are accumulated, the sample temperature would change and so a range of exchange rates would be observed. However, this reason was dismissed after spectra obtained allowing twenty and sixty minutes for sample temperature equilibration were the same. Another possible experimental reason is that a range of temperatures can exist simultaneously across the sample if there is a temperature gradient[76] along the rotor. A preliminary investigation into the possible existence of a temperature gradient across a Chemagnetics 'Pencil' rotor (7.5 mm) has been previously been performed[77] using lead nitrate.[78] The results suggest that there is a temperature gradient across the sample which is in line with other studies that have estimated the existence of temperature gradients in the range of 2-4 °C.[76,78,79] However, to determine whether the existence of a temperature gradient across the rotor is responsible for the effects observed in Figure 6.18, further experiments are necessary in which the sample is confined to only the central part of the rotor thus reducing the temperature gradient. To obtain a reasonable signal-to-noise spectrum for a smaller sample volume, such experiments would obviously demand much more time. Other variable-temperature studies, of compounds showing conformational exchange,[80] using the same Chemagnetics 'Pencil' rotors, do not show the same effects, so perhaps the existence of a temperature gradient as the cause can be ruled out.

The effect observed may be due to properties of the fluorocyclohexane/thiourea rather than 'external' experimental effects. As the temperature is increased from the slow-exchange regime where two peaks are observed, a central peak consistent with the conformationally averaged resonance seen in the fast-exchange limit is observed. Such an observation has previously been identified as being typical of an inhomogeneous distribution of correlation times such as might be expected in a motionally disordered system.[81-83] When there is a broad distribution of correlation times, the lineshape can be simulated by a weighted sum of

the doublet seen in the slow-exchange regime and the conformationally averaged peak seen in the fast-exchange regime. The existence of a broad range of correlation times at a particular temperature is not impossible for the fluorocyclohexane/thiourea inclusion compound. At low temperatures, the lineshapes in the ^{19}F spectra (Figure 6.2) were asymmetric in shape, with a possible explanation for this being due to the disordered nature of the system. However, the nature of the disorder could be either or both spatial and dynamic. It is also worth noting that the detailed effects were not observed with ^{19}F NMR, which could be as a result of the broader ^{19}F lines (fwhh ~ 130 Hz at 177 K) in comparison to ^{13}C lines (fwhh ~ 20 Hz). If the distribution of correlation times was due to the existence of a temperature gradient along the rotor, then as rotors of differing size were used in the ^{19}F (4 mm) and ^{13}C (7.5 mm) NMR experiments, this could also explain differences between the two variable-temperature experiments. For a more definite idea of whether there is inhomogeneous line broadening in the ^{13}C spectra or not, possible temperature gradient effects would have to be accounted for first. However, due to problems with probe operation at low temperatures and a lack of time, it has not been possible to perform the appropriate experiments.

6.4.2 Selective polarisation inversion

The selective polarisation inversion experiment can be used in the same way for ^{13}C as it was used in ^{19}F NMR studies[19] to obtain rate constants below the coalescence temperature. The pulse sequence used is exactly the same as described earlier, but in this case it is necessary to apply double-channel decoupling during both t_1 and t_2, and the transverse magnetisation was created via $^1H \rightarrow ^{13}C$ cross polarisation (Figure 6.19). Another important difference between the ^{19}F and ^{13}C SPI experiments is that the transmitter offset has to be much smaller for ^{13}C and only one pair of peaks can be analysed at a time. Due to the smaller transmitter offset required to achieve selective inversion for ^{13}C, then t_1 is inevitably longer and hence T_2 effects may need to be considered.
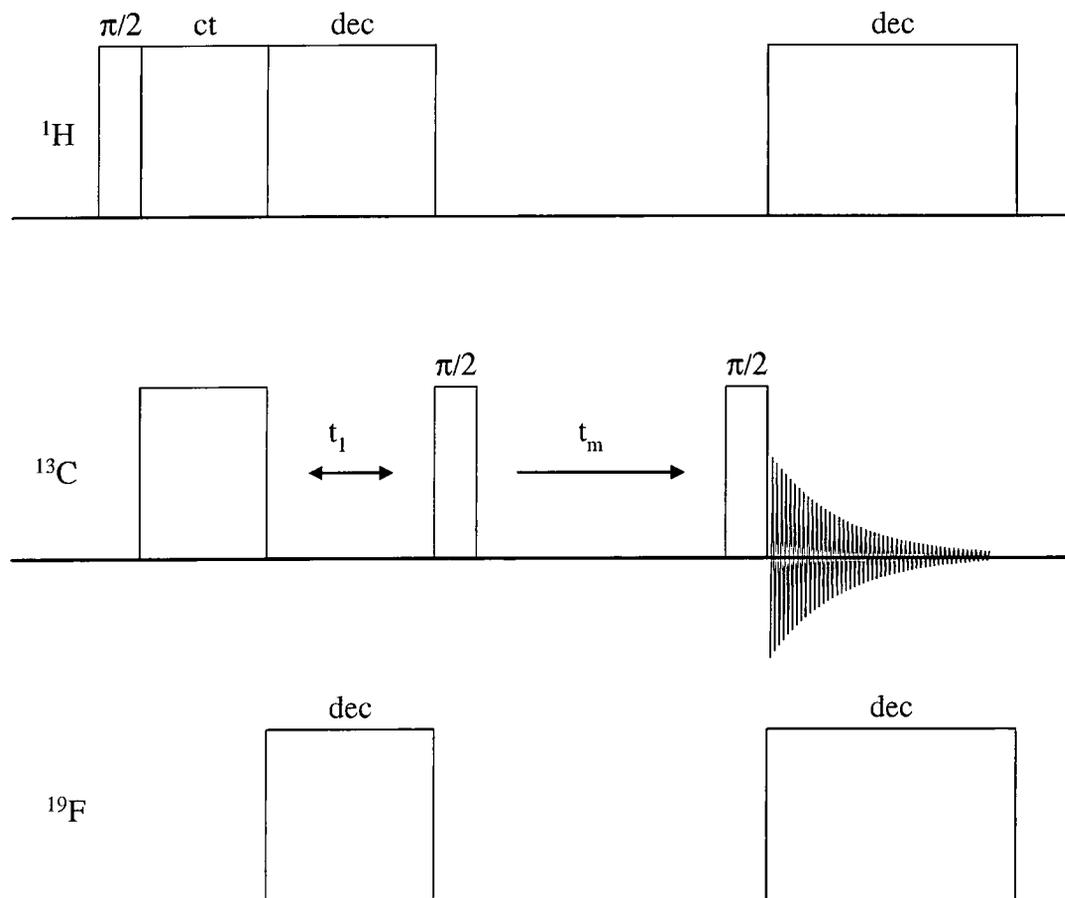
Figure 6.19. Triple-channel selective polarisation inversion pulse sequence with
$^1H \rightarrow {}^{13}C$ *cross polarisation.*

Typical spectral conditions were: $\pi/2$ pulse duration, 5.0 μs; contact time, 1.0 ms; recycle delay, 5 s; ^{1}H and ^{19}F decoupling power, 56 kHz; spin rate, 3.23 kHz; t_1 time, 2483.6 μs; acquisition time, 102.4 ms; number of transients per mixing time, 256. Ten experiments were performed at -90 °C, with mixing times ranging from 0.001-500 ms. As the chemical shift separation between the two conformations is greatest for the C3, C5 peaks, which equates to a frequency separation of 201 Hz, this pair of peaks was selected to monitor the ring inversion process. The transmitter was placed in between the two peaks,[34] i.e., at 23.2 ppm, and hence the time (t_1) used to create a 180° phase difference between the two peaks was 2483.6 μs. Therefore, to ensure refocusing of chemical shift at the end of t_1, a spin rate of 3.23 kHz was used, which meant that t_1 corresponds to eight rotor periods. A typical slice of the SPI

experiment is shown in Figure 6.20. All peaks in the spectrum other than the C3, C5 peaks were ignored.
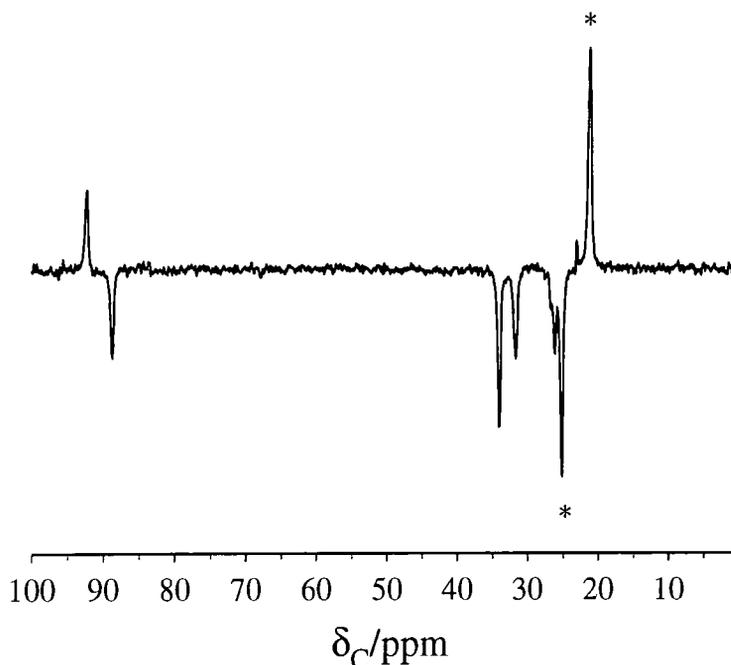
Figure 6.20. Slice from ^{13}C SPI experiment obtained using a mixing time of 0.001 ms. Exchange between the C3, C5 resonances (asterisked) was monitored.

As the ^{13}C T_1 was deemed to be long relative to the timescale upon which exchange occurs, the SPI data were fitted to Equation 6.8 to determine an average exchange rate of 3.6 Hz. The effect of T_2 relaxation during t_1 was considered also, but its influence was negligible on the value obtained for the exchange rate.

An estimate of the actual sample temperature was obtained from variable-temperature calibration data of the HX probe, which uses the same size rotors (7.5 mm) as the HFX probe. The actual sample temperature was estimated to be about -80 °C, which upon comparison with data obtained via ^{19}F SPI experiments gives a slower exchange rate than expected. However, without an accurate temperature calibration of this probe and SPI experiments performed at other temperatures, the validity of this result cannot really be commented on. It is clear, though, that in comparison to the ^{19}F SPI experiments, the ^{13}C experiment took nearly three times longer and the S/N obtained was inferior.
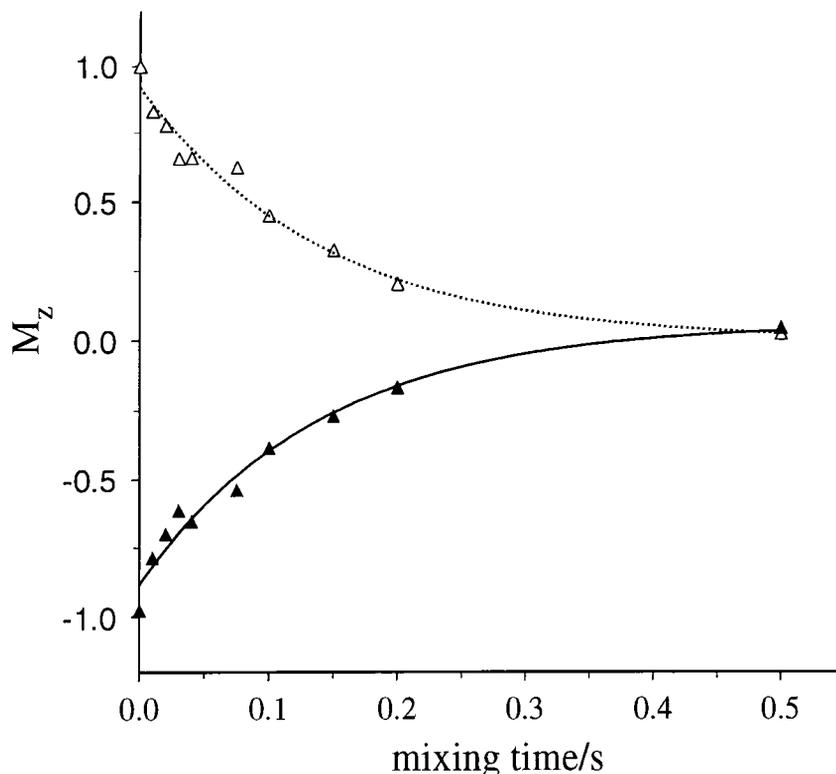
Figure 6.21. Graph plotting ^{13}C signal intensity of the C3, C5 resonances as a function of mixing time.

6.4.3 Off-resonance ^{19}F decoupling

In the section on variable-temperature ^{13}C spectra, with the exception of the room temperature results, only the spectra acquired with both ^{1}H and ^{19}F decoupling have been considered. However, a spectrum has also been obtained at -100 °C with only ^{1}H decoupling (Figure 6.22d). It can be seen that the two C1 peaks in Figure 6.22a, change to be what appears to be a 1:2:1 triplet when no ^{19}F decoupling is applied. On removing ^{19}F decoupling, those ^{13}C resonances which are either dipolar or scalar coupled to ^{19}F can either disappear if the dipolar interaction broadens the peak to such an extent or split to form multiplets due to scalar coupling. In this case from the position of the C1 peaks in the ^{13}C spectrum acquired with both ^{1}H and ^{19}F decoupling, and $^{1}J_{CF}$ data from solution-state studies, it is obvious that the 'triplet' is in fact two overlapping doublets. The $^{1}J_{CF}$ value obtained for the axial and equatorial carbons at -100 °C is -174 Hz, which compares to solution-state values of -168 Hz

and -172 Hz. It is worth noting that $^1J_{CF}$ values are always negative, due to the fact that fluorine bonds predominately via its p orbitals. In Figure 6.22d, the C2, C6 carbons appear as doublets due to $^2J_{CF}$, which incidentally is usually positive in sign. The values obtained for the axial and equatorial carbons are 10 Hz and 9 Hz respectively. Unfortunately it is not possible to see any $^3J_{CF}$ couplings. However, the equatorial C3, C5 peak is broader (fwhh = 25 Hz) than the axial C3, C5 peak (fwhh = 18 Hz) as a result of the larger $^3J_{CF}$ expected for the equatorial carbon (11.0 Hz) than the axial carbon (<0.8 Hz).[84]
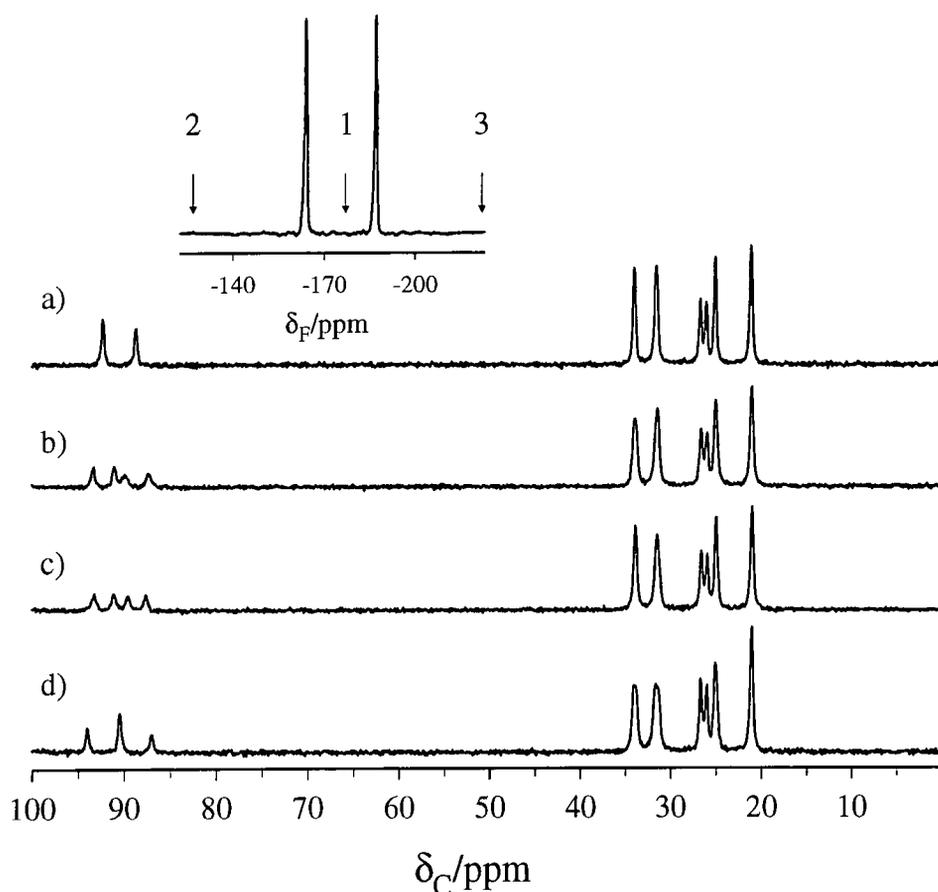
Figure 6.22. Carbon-13 spectra obtained at 173 K using a spin rate of 3.8 kHz with a) on-resonance ^{19}F decoupling (56 kHz), b) ^{19}F off-resonance decoupling (8 kHz) at 3, c) ^{19}F off-resonance decoupling (8 kHz) at 2 and d) no decoupling. The inset shows the position of the transmitter in relation to the ^{19}F spectrum with 1, 2 and 3 being at frequencies of 188.277 MHz, 188.287 MHz and 188.267 MHz respectively.

For further proof, if indeed it is needed, that the 'triplet' is in fact two doublets, the ^{19}F transmitter was placed off-resonance[85] for decoupling (Figure 6.22b and c). In solution-state NMR, the study of off-resonance decoupling effects is

frequently used to provide a rough idea of the decoupling field.[86] This is possible because of the fact that as the decoupler is moved away from being positioned on resonance, the effect of J coupling is scaled. The relationship between the decoupling field and the 'residual' J coupling (i.e. the observed splitting) is given by:

$$B_1 = \frac{\delta v \sqrt{J^2 - |J_r|^2}}{|J_r|} \qquad \text{Equation 6.19}$$

where $|J_r|$ is the reduced J coupling and δv is the transmitter offset from resonance. The position of the ^1H transmitter was kept fixed and a decoupling power of 56 kHz was used. In Figure 6.22b, $|J_r|$ for the axial and equatorial carbon is 126 Hz and 110 Hz respectively, which corresponds to a ^{19}F decoupling power of 8 kHz and 15 kHz. In Figure 6.22c, $|J_r|$ for the axial and equatorial carbon is 100 Hz and 103 Hz respectively, which corresponds to a ^{19}F decoupling power of 16 kHz and 10 kHz. Since a decoupling field of 8 kHz was actually used these values may seem at first sight to be quite inaccurate. However, considering the S/N, the quite small J_{CF} values and also the difficulties associated with measuring such low decoupling fields, then the values obtained are quite respectable. It is also possible to see in Figure 6.22b and Figure 6.22c that $^2J_{CF}$ coupling constants are scaled. However, because of the fact that $^2J_{CF}$ are much smaller in magnitude in comparison to $^1J_{CF}$, then the effect is not as easy to see. In cases where J is larger, such large offsets and low decoupling powers are not required to see a scaling of the J coupling.[87]

6.5 ^1H CRAMPS

Obviously, due to the small chemical shift range of ^1H and the large ^1H homonuclear dipolar couplings, solid-state ^1H NMR does not lend itself readily to variable-temperature studies of systems where only small chemical shift changes are expected. However, a series of ^1H CRAMP spectra was obtained, with and without ^{19}F multiple-pulse decoupling, at temperatures shown in Figure 6.23.
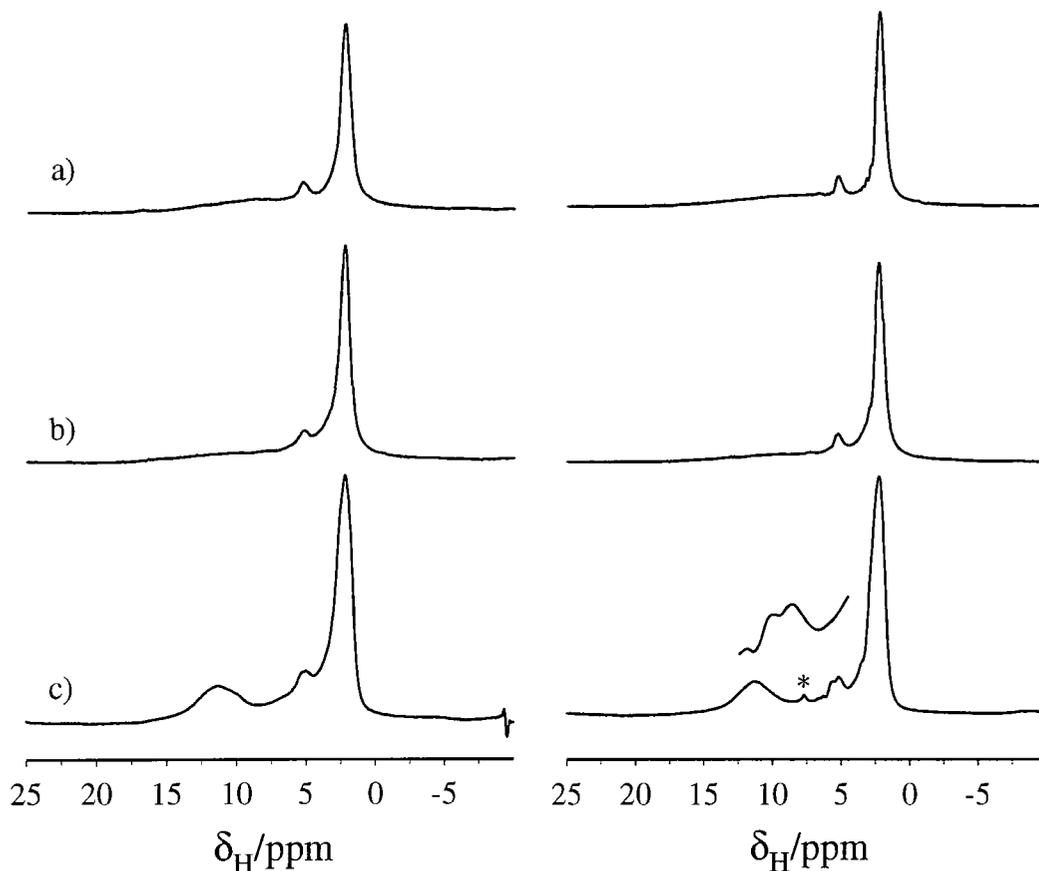
Figure 6.23. Proton CRAMP spectra with (right) and without ^{19}F decoupling (left) at a) room temperature, b) 243 K and c) 193 K. The asterisk in the lower right spectrum indicates a spectral artefact.

From solution-state studies,[17] the peaks evident in the room temperature spectrum at 5.2 ppm and 2.3 ppm can be assigned as ^1H α to ^{19}F and the other fluorocyclohexane ^1H respectively. Upon applying ^{19}F decoupling, the α-^1H, particularly at low temperatures, is better resolved. It is possible to see the α-^1H in the axial (5.1 ppm) and equatorial (5.6 ppm) conformations in the ^{19}F decoupled spectrum at -80 °C. The observed difference in ^1H chemical shift for the two conformations, 0.5 ppm, compares to that of 0.46 ppm in solution.[17] However, the most noticeable feature of the spectra is that as the temperature is decreased, a broad peak at ~11 ppm becomes evident. Upon closer inspection of the room temperature spectrum, it is apparent that there is a very broad peak underlying the entire spectral region shown. This peak can be attributed to thiourea after work on inclusion compounds made from h_4-urea and d_4-urea (see Chapter 4). The chemical shift of the thiourea protons is consistent with

the fact that the host structure is extensively hydrogen bonded. In a previous ^{1}H CRAMPS study of compounds containing NH_3^+ groups,[31] molecular motions on the 100s of kHz to MHz timescale were shown to result in broadened CRAMPS signals. In a study of the 1,4-ditertbutylbenzene/thiourea inclusion compound,[88] ^{2}H NMR studies of the d_4-thiourea version showed that the host molecules undergo 180° flips about the C=S bond. Therefore, it can be assumed that the motion of the host gives rise to broadened CRAMPS signals. As in the study of compounds containing NH_3^+ groups, it appears that dynamic broadening is more dominant that broadening arising from ^{1}H-^{14}N quadrupolar/dipolar interactions.

6.6 Conclusions

Using the superior sensitivity of ^{19}F NMR, in comparison to that of ^{13}C, it has been possible to obtain kinetic and thermodynamic parameters, over a temperature range that spans 120 K, for the 'chair-chair' ring inversion of fluorocyclohexane in thiourea. A number of methods, predominantly bandshape analysis and selective polarisation inversion experiments, have been used to examine the dynamics of fluorocyclohexane. Due to the larger chemical shift difference between the axial and equatorial resonances in ^{19}F spectra, compared to in ^{13}C spectra, more accurate rate constants can be determined from bandshape analysis over a wider temperature range. In the slow-exchange region, where bandshape analysis becomes less accurate, the selective polarisation inversion experiment has been used to obtain rate constants. Hence, improved thermodynamic parameters have been determined using this 'multi-experiment' approach. A ^{19}F two-dimensional exchange experiment has also been performed to clearly illustrate the conformational exchange process.

Triple-channel ^{13}C NMR experiments have also been performed which confirm the results obtained using ^{19}F NMR. However, it is clearly evident that a conformational analysis of fluorocyclohexane performed using ^{13}C NMR would take significantly longer than that utilising ^{19}F NMR. The variable-temperature ^{13}C spectra obtained, particularly in the temperature region at which coalescence occurs, exhibit possible evidence of inhomogeneous broadening. However, for conclusive

evidence of this phenomenon further experiments are needed in which the effects of temperature gradients along the rotor length are investigated. Limited structural information is attainable using ^{1}H NMR in the solid state. Nevertheless, from variable-temperature ^{1}H CRAMP spectra, acquired with ^{19}F heteronuclear decoupling, sufficient resolution was obtained so that the axial and equatorial protons could be distinguished. As for the urea inclusion compounds (see Chapter 4), there is dynamic broadening of the host molecule resonance in the ^{1}H CRAMP spectrum at room temperature. Again the results presented in this chapter, clearly demonstrate the advantages of ^{19}F NMR in terms of sensitivity. This enables spectra to be acquired in a shorter time and with improved signal-to-noise in comparison to ^{13}C, thus increasing the scope of NMR in the elucidation of solid-state structures.

6.7 References

1. A.E. Aliev and K.D.M. Harris, *J. Am. Chem. Soc.*, 1993, **115**, 6369.

2. M.D. Hollingsworth and K.D.M. Harris, *Comprehensive Supramolecular Chemistry*, ed. D.D. MacNicol, F. Toda and R. Bishop, Pergamon, 1996, vol. 6, p. 177.

3. K.D.M. Harris, *J. Mol. Struct.*, 1996, **374**, 241.

4. K.D.M. Harris and J.M. Thomas, *J. Chem. Soc., Faraday Trans.*, 1990, **86**, 1095.

5. J.E. Gustavsen, P. Klæboe and H. Kvila, *Acta Chem. Scand. A*, 1978, **32**, 25.

6. I.J. Shannon, M. J. Jones, K.D.M. Harris, M.R.H. Siddiqui and R.W. Joyner, *J. Chem. Soc., Faraday Trans.*, 1995, **91**, 1497.

7. O.A. Subbotin and N.M. Sergeyev, *J. Am. Chem. Soc.*, 1975, **97**, 1080.

8. M.S. McKinnon and R.E. Wasylishen, *Chem. Phys. Lett.*, 1986, **130**, 565.

9. K. Müller, *Magn. Reson. Chem.*, 1992, **30**, 228.

10. K. Müller, *Magn. Reson. Chem.*, 1995, **33**, 113.

11. A.E. Aliev, K.D.M. Harris and R.C. Mordi, *J. Chem. Soc., Faraday Trans.*, 1994, **90**, 1323.

12. P.A. Schofield, K.D.M. Harris, I.J. Shannon and A.J.O. Rennie, *Chem. Commun.*, 1993, 1293.

13. A.J.O. Rennie and K.D.M. Harris, *Proc. R. Soc. Lond. A*, 1990, **430**, 615.

14. S.D. Christian, J. Grundnes, P. Klæboe, E. Tørneng and T. Woldbæk, *Acta Chem. Scand. A*, 1980, **34**, 391.

15. E.F. Mooney, *An Introduction to ^{19}F NMR Spectroscopy*, Heyden/Sadtler, 1970.

16. P.-S. Chu and N.S. True, *J. Phys. Chem.*, 1985, **89**, 5613.

17. F.A. Bovey, E.W. Anderson, F.P. Hood and R.L. Kornegay, *J. Chem. Phys.*, 1964, **40**, 3099.

18. U. Scheler, P. Holstein, S.A. Carss and R.K. Harris, *Chemagnetics Application Note*, May 1995.

19. A. Nordon, R.K. Harris, L. Yeo and K.D.M. Harris, *Chem. Commun.*, 1997, 962.

20. R.K. Harris, *Nuclear Magnetic Resonance Spectroscopy*, Longman, 1987, p.148.

21. C.-G. Hoelger, B. Wehrle, H. Benedict and H.-H. Limbach, *J. Phys. Chem.*, 1994, **98**, 843.

22. V.J. McBrierty and D.C. Douglass, *J. Polymer Sci.: Macromolecular Rev.*, 1981, **16**, 295.

23. K.D.M. Harris and A.E. Aliev, *Chem. Br.*, 1995, 132.

24. A.E. Aliev, S.P. Smart, I.J. Shannon and K.D.M. Harris, *J. Chem. Soc., Faraday Trans.*, 1996, **92**, 2179.

25. R. Poupko, E. Furman, K. Müller and Z. Luz, *J. Phys. Chem.*, 1991, **95**, 407.

26. F.G. Riddell, S. Arumugam, K.D.M. Harris, M. Rogerson and J.H. Strange, *J. Am. Chem. Soc.*, 1993, **115**, 1881.

27. L. Frydman, A.C. Olivieri, L.E. Diaz, B. Frydman, I. Kustanovich and S. Vega, *J. Am. Chem. Soc.*, 1989, **111**, 7001.

28. J.R. Long, B.Q. Sun, A. Bowen and R.G. Griffin, *J. Am. Chem. Soc.*, 1994, **116**, 11950.

29. J.M. Twyman and C.M. Dobson, *Chem. Commun.*, 1988, 786.

30. W.P. Rothwell and J.S. Waugh, *J. Chem. Phys.*, 1981, **74**, 2721.

31. P. Jackson and R.K. Harris, *J. Chem. Soc., Faraday Trans.*, 1995, **91**, 805.

32. D. Suwelack, W.P. Rothwell and J.S. Waugh, *J. Chem. Phys.*, 1980, **73**, 2559.

33. J. Jeener, B.H. Meier, P. Bachmann and R.R. Ernst, *J. Chem. Phys.*, 1979, **71**, 4546.

34. N.M. Szeverenyi, A. Bax and G.E. Maciel, *J. Am. Chem. Soc.*, 1983, **105**, 2579.

35. C. Connor, A. Naito, K. Takegoshi and C.A. McDowell, *Chem. Phys. Lett.*, 1985, **113**, 123.

36. J. Sandström, *Dynamic NMR Spectroscopy*, Academic Press, Chapter 2, 1982.

37. S. Forsén and R.A. Hoffman, *J. Chem. Phys.*, 1963, **39**, 2892.

38. H.M. McConnell, *J. Chem. Phys.*, 1958, **28**, 430.

39. M.T. Rogers and J.C. Woodbrey, *J. Phys. Chem.*, 1962, **66**, 540.

40. Mathcad, Mathsoft Inc., USA.

41. G. McGeorge, *Ph.D. Thesis*, University of Durham, 1996.

42. J.J. Titman, Z. Luz and H.W. Spiess, *J. Am. Chem. Soc.*, 1992, **114**, 3765.

43. J. Keeler and D. Neuhaus, *J. Magn. Reson.*, 1985, **63**, 454.

44. K. Müller, H. Zimmermann, C. Krieger, R. Poupko and Z. Luz, *J. Am. Chem. Soc.*, 1996, **118**, 8006.

45. G. Bodenhausen, H. Kogler and R.R. Ernst, *J. Magn. Reson.*, 1984, **58**, 370.

46. R.R. Ernst, G. Bodenhausen and A. Wokaun, *Principles of Nuclear Magnetic Resonance in One and Two Dimensions*, Clarendon Press, Oxford, 1991, chapter 6, p 292.

47. D.I. Hoult, *Prog. NMR Spectrosc.*, 1978, **12**, 41.

48. D.J. States, R.A. Haberkorn and D.J. Ruben, *J. Magn. Reson.*, 1982, **48**, 286.

49. U. Scheler, personal communication.

50. H-H. Limbach, B. Wehrle, M. Schlabach, R. Kendrick and C.S. Yannoni, *J. Magn. Reson.*, 1988, **77**, 84.

51. P. Caravatti, G. Bodenhausen and R.R. Ernst, *J. Magn. Reson.*, 1983, **55**, 88.

52. R. Freeman, *A Handbook of Nuclear Magnetic Resonance*, Longman, 1991, p. 207.

53. R. Freeman, *Spin Choreography*, Spektrum, Oxford, 1997, chapter 5.

54. G.A. Morris and R. Freeman, *J. Magn. Reson.*, 1978, **29**, 433.

55. L.D. Field, N. Bampos and B.A. Messerle, *Magn. Reson. Chem.*, 1991, **29**, 36.

56. G. Robinson, P.W. Kuchel, B.E. Chapman, D.M. Doddrell and M.G. Irving, *J. Magn. Reson.*, 1985, **63**, 314.

57. J.A. Shaw, personal communication.

58. G.E.H. Reuter, *Elementary Differential Equations and Operators*, Routledge and Kegan Paul Ltd., London, p 23, 1966.

59. Axum, Mathsoft Inc., USA.

60. D.W. Marquardt, *Journal of the Society for Industrial and Applied Mathematics*, 1963, **2**, 431.

61. W.H. Press, B.P. Flannery, S.A. Teukolsky and W.T. Vetterling, *Numerical Recipes*, Cambridge University Press, 1986, p. 550.

62. T. Grabias and N. Pislewski, *Solid State NMR*, 1994, **3**, 299.

63. F.G. Riddell, M. Bremner and J.H. Strange, *Magn. Reson. Chem.*, 1994, **32**, 118.

64. F.G. Riddell and M. Rogerson, *Magn. Reson. Chem.*, 1997, **35**, 333.

65. E.R. Andrew and R.G. Eades, *Proc. Roy. Soc. A*, 1953, **218**, 537.

66. N. Bloembergen, E.M. Purcell and R.V. Pound, *Phys. Rev.*, 1948, **73**, 679.

67. C.P. Slichter and D.C. Ailion, *Phys. Rev. A*, 1964, **135**, 1099.

68. D.C. Ailion and C.P. Slichter, *Phys. Rev. A*, 1965, **137**, 235.

69. D.C. Douglass and G.P. Jones, *J. Chem. Phys.*, 1966, **45**, 956.

70. G.P. Jones, *Phys. Rev.*, 1966, **148**, 332.

71. P.W. Atkins, *Physical Chemistry*, Oxford University Press, 4th edition, 1990.

72. B.E. Mann, *Prog. NMR Spectrosc.*, 1977, **11**, 95.

73. F.R. Jensen, C.H. Bushweller and B.H. Beck, *J. Am. Chem. Soc.*, 1969, **91**, 344.

74. E.O. Stejskal, J. Schaefer and J.S. Waugh, *J. Magn. Reson.*, 1977, **28**, 105.

75. S.A. Carss, *Ph.D. Thesis*, University of Durham, 1995.

76. F. Aguilar-Parrilla, B. Wehrle, H. Bräunling and H-H. Limbach, *J. Magn. Reson.*, 1990, **87**, 592.

77. G. McGeorge, Summer school on NMR of solids, University of Durham, 1996.

78. A. Bielecki and D.P. Burum, *J. Magn. Reson. A*, 1995, **116**, 215.

79. T. Mildner, H. Ernst and D. Freude, *Solid State NMR*, 1995, **5**, 269.

80. G. McGeorge, R.K. Harris, A.M. Chippendale and J.F. Bullock, *J. Chem. Soc. Perkin Trans. II*, 1996, 1733.

81. D. Casarini, R.K. Harris and A.M. Kenwright, *Magn. Reson. Chem.*, 1992, **30**, 434.

82. P. Tekely, *Mol. Phys.*, 1992, **75**, 747.

83. J.P. Kaplan and A.N. Garroway, *J. Magn. Reson.*, 1982, **49**, 464.

84. H-O. Kalinowski, S. Berger and S. Braun, *Carbon-13 NMR Spectroscopy*, Wiley, 1988.

85. E.W. Hagaman, *J. Magn. Reson. A*, 1993, **104**, 125.

86. A.E. Derome, *Modern NMR Techniques for Chemistry Research*, Pergamon Press, Oxford, 1987, p. 158.

87. J.C. Cherryman and R.K. Harris, *J. Magn. Reson.*, 1997, **128**, 21.

88. G.H. Penner, J.M. Polson, C. Stuart, G. Ferguson and B. Kaitner, *J. Phys. Chem.*, 1992, **96**, 5121.

Chapter 7

Measurement of intermolecular ^{19}F-^{19}F distances in inclusion compounds

7.1 Introduction

The study of intermolecular distances between guest molecules is of particular interest in relation to urea and thiourea inclusion compounds. However, due to the static and/or dynamic disordered nature of these compounds, crystallographic techniques are unable to access this information.[1,2] In the case of substituted cyclohexane/thiourea inclusion compounds, the questions of conformation[3] and both intramolecular and intermolecular distances between guest substituents have been addressed. Bromine K-edge EXAFS has proved to be a useful tool in the elucidation of conformational preferences exhibited by bromocyclohexane derivatives in thiourea. For example, in bromocyclohexane/thiourea, a value of 3.27 Å was obtained for the Br---C3(5) distance,[4] thus supporting the solid-state ^{13}C NMR results which indicated a predominance for the axial conformation.[5-7] In the trans-1-bromo-2-chlorocylohexane/thiourea inclusion compound,[4] again a value of 3.27 Å was obtained for the Br---C3(5) distance, implying that the Br substituent is axial. Moreover, from the value obtained for the intramolecular Br---Cl distance, 4.50 Å, it was then possible to deduce that the guest molecules are in the diaxial conformation. In both compounds, at 80 K, it was possible to detect an intermolecular Br---Br distance, suggesting a head-to-head ordering of the guest molecules. In a synchrotron X-ray powder diffraction study, at 85 K, chlorocyclohexane molecules in thiourea were found to be ordered head to head/tail to tail, with an intermolecular Cl---Cl distance of 4.6 Å.[8]

Bromine K-edge EXAFS has also been used to examine the local structural properties of urea inclusion compounds containing α,ω-dibromoalkanes. However, due to dynamic disorder at high temperatures and static disorder at low temperatures,

a Br---Br distance was unmeasurable both at room temperature and 77 K.[2] In a molecular dynamics simulation of the 1,10-dibromodecane/urea inclusion compound, the bromine radial distribution function was shown to indicate a broad distribution of intermolecular Br---Br distances (~ 3.2-5.5 Å).[9] However, there has been a number of studies which have focused on the conformational properties of α,ω-dihalogenoalkane and alkane guests in urea tunnels. Single-crystal Raman studies have been performed on dichloro-, dibromo- and diiodo-alkane/urea inclusion compounds.[10] It was concluded that as the halogen substituent decreases in size, the proportion of end-groups in the gauche conformation increases (Cl, 51 %, Br, 7 % and I, 1 %). However, there exists a dynamic equilibrium between end-groups in the trans and gauche conformations, which is slow with respect to the Raman timescale (ps). The conformation of n-alkanes has also been examined using CH dipolar switching-angle sample spinning (SASS) NMR, which suggested the existence of various dynamic conformations.[11] Using ^{2}H NMR, trans/gauche conformational exchange was shown to occur near the ends of n-alkanes which is fast on the NMR timescale (μs).[12,13] Dynamic conformational disorder was also found to exist in the 2-^{13}C decane/d_4-urea inclusion compound from the examination of ^{13}C-^{1}H J coupling constants in solid-state ^{13}C NMR.[14]

Hence, it can be seen that the disordered nature of the inclusion compounds, has considerably hampered the study of the local structure exhibited by the guest molecules. As already proved in the previous chapters, solid-state NMR can yield structural information which is difficult to obtain via crystallographic techniques. In order to determine intermolecular distances using NMR, it is particularly desirable for there to exist a homonuclear spin pair, which is sensitive and can be rendered isolated, for example, by the application of ^{1}H decoupling. In this chapter, the possibility of using solid-state ^{19}F NMR to determine ^{19}F-^{19}F distances in the fluoroalkane/urea and fluorocyclohexane/thiourea inclusion compounds has been examined.

7.2 NMR methods for obtaining homonuclear dipolar coupling constants[15-18]

From a sensitivity point of view, ^1H and ^{19}F are the most favourable choice of nuclei in NMR experiments. However, in many organic systems, such as in the urea and thiourea inclusion compounds, due to the high abundance of protons it is not possible to use ^1H NMR to determine intermolecular distances. Of course, if the inclusion compounds were deuterated, such that only the end-groups contained a proton, i.e., CD_2H, then it would be possible to obtain a distance via the ^1H-^1H dipolar interaction. Due to the low natural abundance of nuclei such as ^{13}C and ^{15}N, it is not possible to obtain distance measurements from such nuclei without isotopic labelling. Labelling of samples is not always easy and can also be expensive, and therefore ^{13}C enrichment of the end-groups, to obtain a ^{13}C-^{13}C isolated spin pair, is not often a viable option. Many studies have examined halogen-substituted guest molecules within urea and thiourea. However, due to the quadrupolar nature of Cl, Br and I, information regarding the homonuclear dipolar interaction would be difficult to extract from their spectra. To determine intermolecular distances between unlike spins such as in the dibromoalkane/urea inclusion compounds, techniques which measure heteronuclear dipolar interactions cannot be used, since the directly-bonded interaction will dominate. Therefore, the study of inclusion compounds which contain ^{19}F substituted guest molecules, via ^{19}F NMR, is particularly promising.

The use of ^{19}F NMR, with high-power ^1H decoupling, in the study of solids has only recently become viable with commercial equipment.[19-21] Therefore, in compounds containing isolated ^{19}F-^{19}F spin pairs, ^{19}F NMR now provides the ideal tool for the determination of structural information. Fluorine-19 NMR can be used to measure larger distances than for example, ^{13}C NMR due to the dependence of the dipolar coupling constant on γ^2/r_{IS}^3. Carbon-13 NMR can be used to determine distances up to 7 Å, whereas ^{19}F NMR has been used to measure distances of up to 16 Å.[22] In order to use a homonuclear dipolar interaction, such as ^{19}F-^{19}F, to yield structural information, it is necessary to consider the effect of MAS on this interaction and also the effects of not applying MAS on this and other interactions which may be present.

7.2.1 Static methods

The homonuclear dipolar interaction between relatively isolated ^{1}H-^{1}H spin pairs in gypsum[23] was determined via single-crystal NMR studies. From the variation of splitting observed in the two doublets as a function of the angle between the internuclear vector and B_0, it was possible to determine a ^{1}H-^{1}H distance of 1.58 Å. In a study of the powder lineshape of the same compound, the now characteristic Pake doublet was observed from which it was possible to obtain the ^{1}H-^{1}H distance via the separation of the 'horns'. However, for many powder samples, such an observation is rare due to the observation of many chemical shifts in the relevant spectrum and line broadening arising from SA. Hence, the extraction of a distance measurement between two specific spins may be difficult from a typically broad, relatively featureless peak. However, in samples containing relatively isolated spin pairs, such information may be more accessible. Spin pairs can be rendered isolated, for example, by incorporation in an inert matrix, as was the case for the determination of ^{13}C-^{13}C distances for doubly labelled molecules such as C_2H_4.[24] The Carr-Purcell[25] sequence and various improved versions[26-29] of the original sequence have been used to determine ^{13}C-^{13}C distances in acetic acid at 80 K[26] and in species absorbed on metal surfaces.[16] The distance between doubly labelled ^{15}N-^{15}N spin pairs has been determined in azobenzenes[30,31] and 3,5-substituted pyrazoles[32] by extraction of such information from dipolar/chemical shift powder patterns. The theory behind the extraction of distance information from such spectra is discussed in the relevant experimental section.

7.2.2 MAS methods

MAS is used in solid-state NMR to remove line broadening interactions such as SA. However, the homonuclear dipolar interaction between two isolated spins can also be averaged by MAS. This is in marked contrast with homonuclear dipolar interactions between protons in multi-spin systems, where MAS has little if no effect on this homogeneous interaction.[33] Hence, for systems in which there is more than

one chemical shift in the respective spectrum, and so MAS is needed to yield sufficient spectral resolution, a method for reintroducing the homonuclear dipolar interaction is required. This can be achieved via multi-pulse sequences, which interfere with the modulation imparted by MAS on the spatial term in the expression for the homonuclear dipolar interaction, or via mechanical means. A number of experiments have been proposed, which can be grouped into two broad classes; those which are sensitive to and those which rely upon SA and chemical shift differences.

Experiments which require a chemical shift difference to exist between the two dipolar coupled spins include rotational resonance (R^2),[34,35] simple excitation for the dephasing of rotational echo amplitudes (SEDRA)[36,37] and rf-driven dipolar recoupling (RFDR).[38,39] However, unlike SEDRA and RFDR, R^2 is not a practical method for determining a number of homonuclear dipolar couplings over a broad spectral width, i.e. it is not a broad-band recoupling technique. This is due to the requirement for matching the chemical shift difference between the two coupled spins with a multiple of the MAS rate. Other experiments, such as dipolar recovery at the magic angle (DRAMA),[40] are very sensitive to SA and chemical shift differences and hence work best when the chemical shift difference between the two coupled spins is zero or very small. To overcome the extreme sensitivity of this experiment to SA and offset effects, variations of this sequence have been proposed.[41,42] In fact, one of these compensated DRAMA sequences[42] has been used to determine ^{31}P-^{31}P internuclear distances in a complex of 5-enolpyruvylshikimate-3-phosphate synthase[43] and in phosphine-sulphide disubstituted peptides.[44] The DRAMA sequence can be used as a multiple quantum filter and hence has application as a spectral editing technique.[41,45,46] Other sequences, based on DRAMA, have been developed that are less sensitive to SA and offset effects such as dipolar recoupling via rotor synchronised spin locking (MELODRAMA)[47] and dipolar recoupling with a windowless sequence (DRAWS).[48,49] However, both of these sequences have poor dipolar recoupling efficiency for powder samples, due to the orientation dependence of recoupling. The recoupling efficiency of sequences such as the double-quantum homonuclear rotary resonance (HORROR)[50] experiment is less orientation dependent, but is more sensitive to SA and offset effects. However, a sequence called C7,[51,52] has been developed which has a recoupling efficiency which is less sensitive

to orientation than MELODRAMA and DRAWS, but is also very insensitive to SA and offset effects.

In order to obtain accurate distance measurements using such homonuclear recoupling sequences, it is necessary to consider the effect of other experimental factors. For many of the sequences, their application has been considered with respect to intramolecular homonuclear dipolar interactions for an isolated spin pair. Hence, particularly in the case of nuclei with a high magnetogyric ratio, intermolecular and multi-spin interactions may need to be considered. During the period in which the homonuclear dipolar interaction is recoupled, typically high-power ^{1}H decoupling is also applied. Thus, the powers on the two relevant channels must be mismatched to ensure that signal losses due to cross polarisation are minimised. It is also necessary to be able to quantify losses such as those from magnetic field inhomogeneities, finite field strengths, offset effects and low recoupling efficiency. An estimation of their possible effects can usually be incorporated into simulations for comparison with experimental data by considering higher-order correction terms in the theoretical approximation used.

7.3 Intermolecular ^{19}F-^{19}F distance measurements in fluoroalkane/urea inclusion compounds

The smallest distance that two end-groups, within the same tunnel, can be separated by will be given by the van der Waals radii of the two closest atoms. For example, for two fluorines, the smallest separation that can exist between the two nuclei is 2.7 Å.[53] However, it is known that positional ordering can exist between guests in neighbouring tunnels (described by a parameter Δ_g) in urea inclusion compounds despite the fact that they are separated by at least 8 Å.[1,2] Nevertheless, from the range of Br---Br intermolecular distances in the 1,10-dibromodecane/urea inclusion compound, ~ 3.2-5.5 Å, that were implied from the bromine radial distribution function in a molecular dynamics study,[9] it can be assumed that in the fluoroalkane/urea inclusion compounds, intrachannel interactions between guests are significantly stronger than those between guests in adjacent channels, i.e.

interchannel. Hence, in the difluoroalkane/urea inclusion compounds, there will exist isolated ^{19}F-^{19}F spin pairs. From the ^{19}F MAS spectra, acquired with ^{1}H decoupling, of the fluoroalkane/urea inclusion compounds presented in Chapter 5, it can be concluded that the chemical shift for two fluorines, which are in adjacent CH_2F end-groups, is the same. Hence, a series of static ^{19}F experiments was performed on two of the fluoroalkane/urea inclusion compounds; the 1,10-difluorodecane/urea inclusion compound, in which all the fluorines are dipolar coupled to other fluorines and the 1-fluorotetradecane/urea inclusion compound, in which it is known that approximately half of the fluorines are homonuclear dipolar coupled, whereas the other half experience no homonuclear dipolar interaction as a consequence of the random ordering of guest molecules in the urea tunnels.[54] In the following section, effective dipolar coupling constants have been obtained as a result of the rapid molecular motion undergone by the guest molecules. Due to the complexity of the interpretation of such results in the light of the motional models that have to be considered, discussion of this part of the results will be reserved for a later section.

7.3.1 Static ^{19}F experiments

7.3.1.1 1,10-difluorodecane/urea inclusion compound

In the ^{19}F spectrum acquired for 1,10-difluorodecane/urea (Figure 7.1a), there exist the following interactions: ^{19}F SA, ^{19}F-^{1}H heteronuclear and ^{19}F-^{19}F homonuclear dipolar interactions. As can be seen from the broad, relatively featureless peak, it would be impossible to obtain any structural information from such a spectrum. However, upon applying ^{1}H decoupling (Figure 7.1b), a spectrum arises which now only contains information regarding the ^{19}F SA and the ^{19}F-^{19}F homonuclear dipolar interaction. Both spectra were acquired using a quadrupole echo pulse sequence,[55] which refocuses the homonuclear dipolar interaction, and also ensures that the first few points of the FID are acquired. Typical spectral conditions were: ^{19}F $\pi/2$ pulse duration, 3 µs; ^{1}H decoupling power, 100 kHz (Figure 7.1b); recycle delay, 5 s; pre-echo time, 20 µs; post-echo time, 7 µs; number of transients,

128; acquisition time, 10.2 ms. It is noticeable that with the post- and pre-echo times used, acquisition will start before the top of the echo. This is to ensure that the top of the echo is not missed, as might be the case if the post- and pre-echo times were the same and an 'imperfect' $\pi/2$ pulse was set. Therefore, when processing such data it is necessary to left shift the points acquired before the top of the echo. To determine the number of points which need to be left shifted, it is first necessary to display both the real and imaginary data and then apply a zero-order phase correction on the FID so as to put all the data into the real channel. In this case, it was necessary to left shift the data by two points before Fourier transforming the FID.
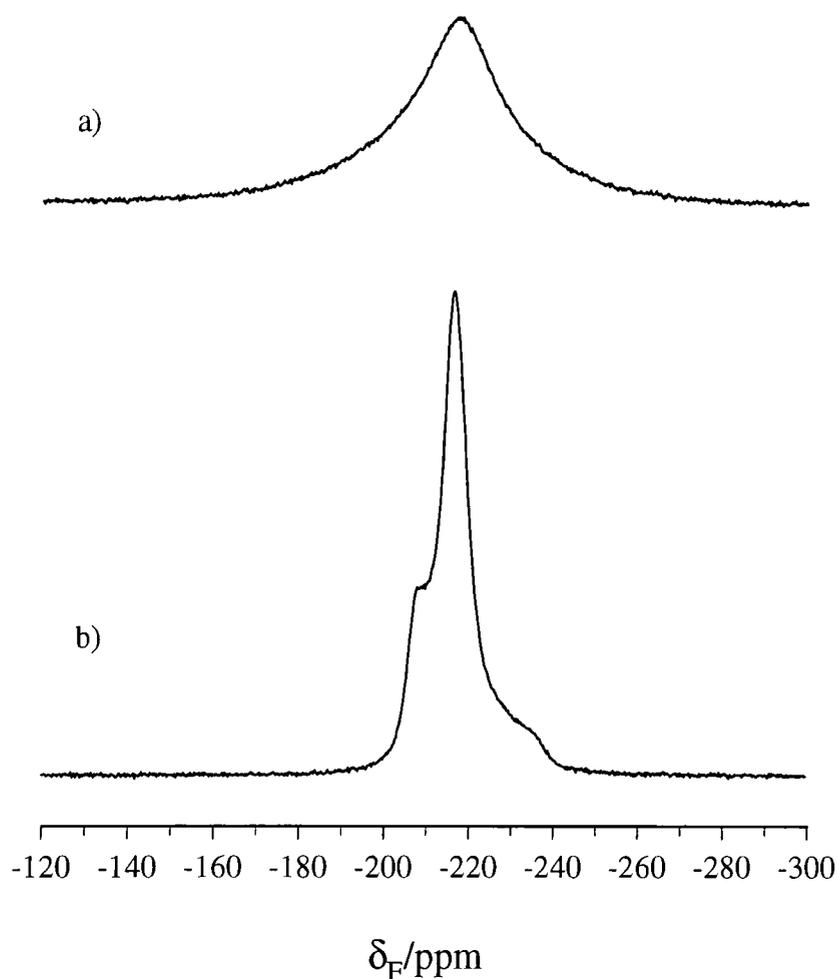
Figure 7.1. Fluorine-19 spectra of the 1,10-difluorodecane/urea inclusion compound acquired a) without and b) with ^{1}H decoupling.

The ultimate aim of the work presented in this chapter, was to obtain a ^{19}F-^{19}F intermolecular distance for fluoroalkane molecules confined within urea tunnels. Two complementary methods have been used to determine the ^{19}F-^{19}F dipolar interaction. In the first method adopted, the ^{19}F-^{19}F dipolar interaction of interest was observed indirectly. Experiments were performed in which both homonuclear and heteronuclear dipolar interactions were removed so that information regarding the ^{19}F shielding could be accessed. From this information, it was then possible to use the combined SA/dipolar powder spectrum (Figure 7.1b) to obtain a homonuclear dipolar coupling constant. In the second approach, experiments have been performed in which all interactions other than the ^{19}F-^{19}F dipolar interaction were removed, and thus involved direct observation of the interaction of interest.

7.3.1.1.1 Determination of the ^{19}F-^{19}F dipolar coupling constant from SA/dipolar powder spectra

7.3.1.1.1.1 Fluorine-19 multiple-pulse experiments

Figure 7.1b contains information regarding both the ^{19}F SA and the ^{19}F-^{19}F homonuclear dipolar interaction. However, it is possible to remove all interactions, other than ^{19}F shielding, by performing a ^{19}F multiple-pulse experiment with ^{1}H decoupling (Figure 7.2). The pulse sequence used was MREV-8 with quadrature detection,[56] to ensure that the spectral width would be sufficient to contain a static ^{19}F spectrum. The spectral conditions were: ^{19}F $\pi/2$ pulse duration, 1.48 μs; ^{1}H π pulse duration, 2.68 μs; tau, 2.65 μs; number of points acquired, 512; recycle delay, 8 s; number of transients, 512. Several experiments were performed with transmitter frequencies that were above, below and on the resonance frequency. As expected, the ability of the pulse sequence to average the homonuclear dipolar interactions deteriorates at larger offsets and so a spectrum obtained with the transmitter set to a slightly higher frequency than the peak was chosen.
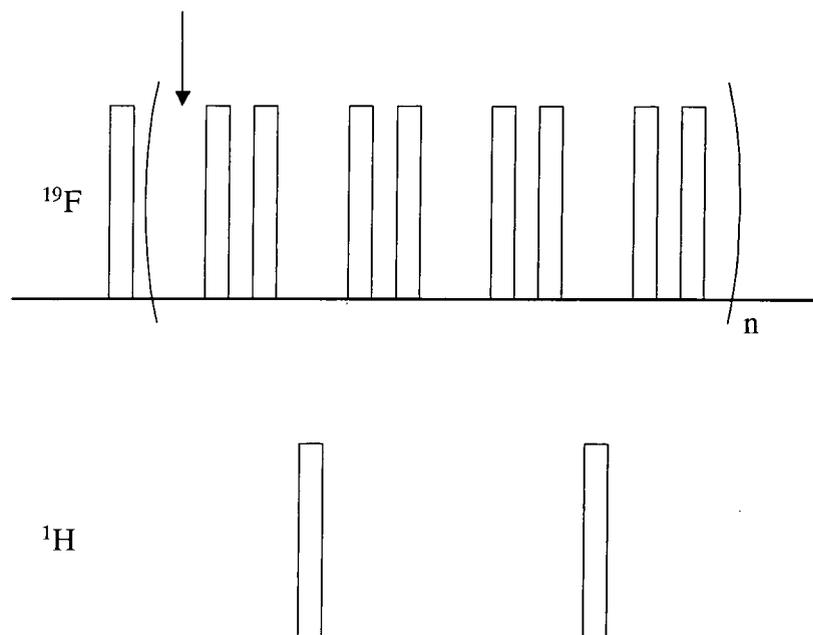
Figure 7.2. Fluorine-19 MREV-8, with ^{1}H decoupling, pulse sequence. The arrow indicates the sampling point.

δ_F/ppm
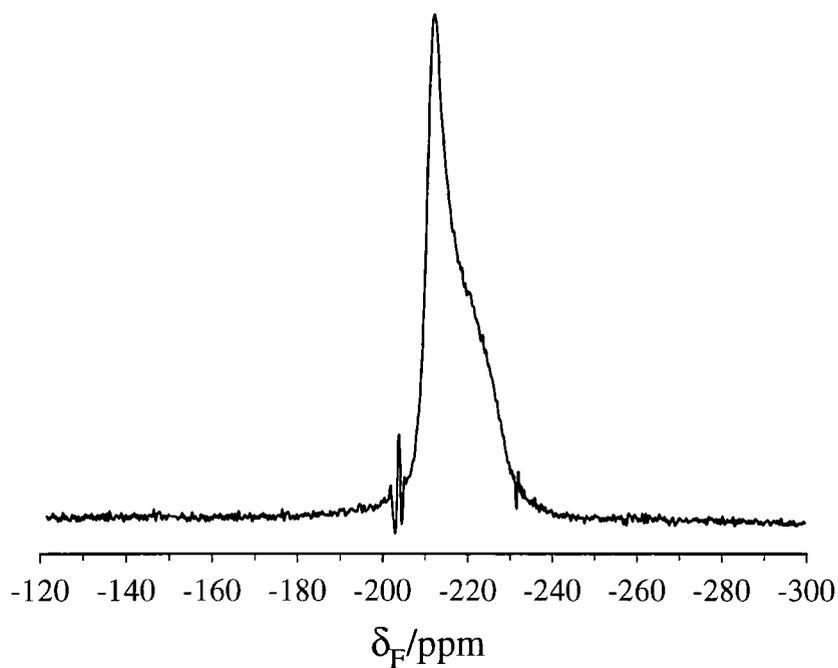
Figure 7.3. Fluorine-19 multiple-pulse spectrum acquired using MREV-8 with ^{1}H decoupling.

The spectrum obtained appears to consist of an axially symmetric shielding powder pattern (Figure 7.3). The principal components of the shielding tensor were

obtained by comparison of simulated spectra, which were created using GAMMA[57] (see Appendix), with the spectrum obtained experimentally. The values obtained for σ_{xx}, σ_{yy} and σ_{zz} (relative to $CFCl_3$ (0 ppm)) are 210.8 ppm, 211.5 ppm and 228.5 ppm, respectively and so, within experimental error, the shielding tensor is confirmed to be axially symmetric. Therefore, it must be assumed that the two fluorines are equivalent and that rapid molecular motion about the tunnel axis renders the shielding axially symmetric. Hence, it can be concluded that the unique tensor orientation, given by σ_{zz}, is parallel to the tunnel axis. The implication of such a result is that the ^{19}F-^{19}F internuclear vector must also be along the tunnel axis and thus must be coincident with σ_{zz}.

7.3.1.1.1.2 Fluorine-19 single-crystal experiments

When the internuclear vector and σ_{zz} are oriented at an identical angle, θ, with respect to the static magnetic field, B_0, the relative orientations of the shielding and dipolar principal axis systems do not need to be considered. The shielding, σ, of a nucleus is given by,

$$\sigma = \sigma_{iso} + \frac{1}{3}\left(3\cos^2\theta - 1\right)\Delta\sigma \qquad \textit{Equation 7.1}$$

where σ_{iso} and $\Delta\sigma$ define the isotropic shielding and the shielding anisotropy, respectively. As the internuclear vector is coincident with σ_{zz}, then the dipolar splitting, R (in units of Hz), is also dependent on the angle θ, and thus is given by,

$$R = \frac{3}{2}\frac{\mu_0\hbar\gamma^2}{8\pi^2 r^3}\left(3\cos^2\theta - 1\right) \qquad \textit{Equation 7.2}$$

where μ_0 is the vacuum permeability, r is the internuclear distance, γ is the magnetogyric ratio of the nucleus and $2\pi\hbar$ is the Planck constant. Hence, if θ is 54.7°, $\left(3\cos^2\theta - 1\right) = 0$ and so $\sigma = \sigma_{iso}$ and R = 0. Therefore, one would expect a single resonance in a spectrum at σ_{iso}, with no dipolar splitting, for a single crystal oriented at the magic angle.

Unfortunately, the 1,10-difluorodecane/urea sample had been ground to a powder and hence single-crystal experiments on this particular sample were impossible without further synthetic work. However, a crystalline sample of the 1,12-difluorododecane/urea inclusion compound was available, which contained single crystals that were approximately 5-7 mm long and 0.5-1.0 mm wide. Such crystals were packed into capillary tubes which had a sufficient cross section to allow more than one crystal to be placed side by side. It was also possible to stack crystals on top of one another within the capillary tube. The capillary tubes, typically four, were inserted into a specially made glass holder with dimensions comparable to that of a standard 4 mm rotor. To ensure that the crystals were in the most homogeneous part of the coil when the glass holder was inserted into the probe, a stop was made at the appropriate position in the glass holder. Such careful packing of the crystals was to ensure that their long axes were all aligned parallel to one another. Therefore, this meant that all the crystals and hence the tunnel axes, were oriented at a specific angle, θ, with respect to the static magnetic field, B_0.

$$\delta_F/ppm$$
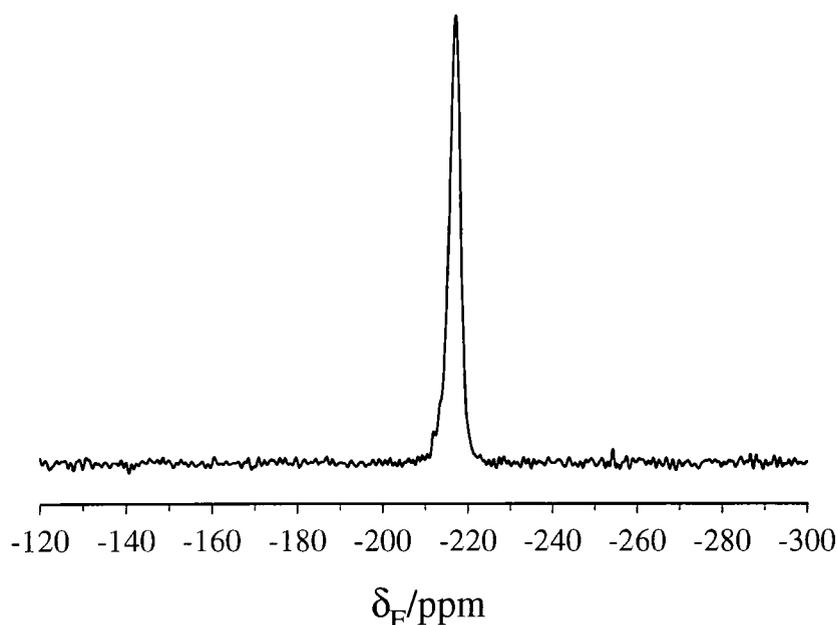
Figure 7.4. $^1H \rightarrow ^{19}F$ CP spectrum, acquired with ^1H decoupling, of single crystals of the 1,12-difluorododecane/urea inclusion compound oriented at 54.7° with respect to B_0.

From the appearance of only a single peak (fwhh ~ 540 Hz) in Figure 7.4, it can be concluded that both the internuclear vector and σ_{zz} are oriented at the same angle with respect to the static magnetic field, B_0. This fact arises because of motional averaging, about the tunnel axis, of the shielding and dipolar interactions. The spectral conditions used were: ^1H $\pi/2$ pulse duration, 3 μs; contact time, 1 ms; recycle delay, 10 s; acquisition time, 5.1 ms; number of transients, 256. It is worth pointing out that this spectrum was acquired using cross polarisation rather than single-pulse operation, purely to remove the background ^{19}F signal, which becomes more obvious in the spectrum as the sample volume is decreased.

7.3.1.1.1.3 Fluorine-19 SA/dipolar spectra

From comparison with the ^{19}F multiple-pulse spectrum (Figure 7.3), Figure 7.1b can be considered as being the superimposition of a ^{19}F-^{19}F dipolar powder pattern and a ^{19}F axially symmetric SA powder pattern. The chemical shift Hamiltonian for a nucleus with axial symmetry can be described by,

$$h^{-1}\hat{H}_{CS} = -v_0[1-\sigma]\hat{I}_z \qquad \textit{Equation 7.3}$$

where $\hat{I}_z$ is the z-component spin operator and v_0 describes the Larmor frequency. Similarly, the Hamiltonian for the homonuclear dipolar interaction (including the Zeeman terms) for an isolated spin pair can be described by,

$$h^{-1}\hat{H}_{II} = -v_0(\hat{I}_{1z} + \hat{I}_{2z}) - D(3\cos^2\theta - 1)\left(\hat{I}_{1z}\hat{I}_{2z} - \frac{1}{4}(\hat{I}_{1+}\hat{I}_{2-} + \hat{I}_{1-}\hat{I}_{2+})\right)$$

Equation 7.4

where D is the dipolar coupling constant, θ is the angle between B_0 and the internuclear vector and the subscripts 1 and 2 denote the two spins. Hence, the Hamiltonian for the SA/dipolar spectrum is given by,

$$h^{-1}\hat{H} = -v_0\left[(1-\sigma_1)\hat{I}_{1z} + (1-\sigma_2)\hat{I}_{2z} - (3\cos^2\theta - 1)\left(\frac{\Delta\sigma_1}{3}\hat{I}_{1z} + \frac{\Delta\sigma_2}{3}\hat{I}_{2z} - \frac{D}{v_0}\left(\hat{I}_{1z}\hat{I}_{2z} - \frac{1}{4}(\hat{I}_{1+}\hat{I}_{2-} + \hat{I}_{1-}\hat{I}_{2+})\right)\right)\right]$$

Equation 7.5

where $\left(\hat{I}_{1+}\hat{I}_{2-} + \hat{I}_{1-}\hat{I}_{2+}\right)$ is the flip-flop term. This term mixes the degenerate $\alpha\beta$ and $\beta\alpha$ states, and hence the combined state can be described by symmetric and antisymmetric combinations of the two. As the antisymmetric state has a total nuclear spin quantum number (I) of zero, this state is not involved in any transitions. The energy levels relating to Equation 7.5 can be described by,

$$h^{-1}U = -v_0\left[\left(1-\sigma_1\right)m_I(1) + \left(1-\sigma_2\right)m_I(2) - \left(3\cos^2\theta - 1\right)\left(\frac{\Delta\sigma_1}{3}m_I(1) + \frac{\Delta\sigma_2}{3}m_I(2) - \frac{D}{v_0}m_I(1)m_I(2)\right)\right]$$

Equation 7.6

where m_I is the nuclear spin quantum number defining orientation. Hence, if $\Delta\sigma_1 = \Delta\sigma_2 = \Delta\sigma$ and $\sigma_1 = \sigma_2 = \sigma$, the energy levels of the $\alpha\alpha$, $\beta\beta$ and $\alpha\beta+\beta\alpha$ states are given by,

$\alpha\alpha \qquad h^{-1}U = -v_0\left[\left(1-\sigma\right) - \left(3\cos^2\theta - 1\right)\left(\frac{\Delta\sigma}{3} - \frac{D}{4v_0}\right)\right]$ \qquad *Equation 7.7*

$\beta\beta \qquad h^{-1}U = v_0\left[\left(1-\sigma\right) - \left(3\cos^2\theta - 1\right)\left(\frac{\Delta\sigma}{3} + \frac{D}{4v_0}\right)\right]$ \qquad *Equation 7.8*

$\alpha\beta+\beta\alpha \qquad\qquad h^{-1}U = v_0\left[\left(3\cos^2\theta - 1\right)\left(\frac{D}{2v_0}\right)\right]$ \qquad *Equation 7.9*

Therefore, the frequencies which make up the two subspectra of the dipolar/SA spectrum are given by,

$$v = v_0(1-\sigma) - v_0\left[\left(3\cos^2\theta - 1\right)\left(\frac{\Delta\sigma}{3} - \frac{3D}{4v_0}\right)\right]$$ \qquad *Equation 7.10*

$$v = v_0(1-\sigma) - v_0\left[\left(3\cos^2\theta - 1\right)\left(\frac{\Delta\sigma}{3} + \frac{3D}{4v_0}\right)\right]$$ \qquad *Equation 7.11*

where the effective anisotropy can be defined by $\left(\frac{\Delta\sigma}{3} \pm \frac{3D}{4v_0}\right)$.[24,58,59] Hence, when $\sigma_{||}$ is at higher shielding than $\sigma_{\perp}$, then as $\Delta\sigma$ is given by $\sigma_{||}$-$\sigma_{\perp}$, Equation 7.10 describes the 'squashed' subspectrum and Equation 7.11 describes the 'stretched'

subspectrum. As expected for a homonuclear dipolar interaction, the dipolar splitting as a function of θ is given by $\dfrac{3D}{2}\left(3\cos^2\theta - 1\right)$.

Using the principal components of the shielding tensor obtained from Figure 7.3, it was possible to simulate combined SA/dipolar spectra for comparison with that obtained experimentally. Simulated spectra were created using GAMMA (see Appendix), with the internuclear vector and σ_{zz} coincident, and a value of 1005 Hz was obtained for the dipolar coupling constant. Because this is reasonably small, it was not possible to obtain such a value from the splitting of the two 'horns'.

7.3.1.1.2 Direct measurement of the ^{19}F-^{19}F dipolar coupling constant

7.3.1.1.2.1 CPMG experiments

To further complement the data obtained, a CPMG[25,26] experiment was performed on the 1,10-difluorodecane/urea inclusion compound, which enabled all interactions other than the ^{19}F-^{19}F dipolar interaction to be removed. The pulse sequence used is that shown in Figure 7.5. Although in principle, the ^{19}F-^1H dipolar interaction is removed by the 180° pulses on ^{19}F (as are chemical shifts), a previous study suggested that ^1H decoupling via continuous irradiation was more effective and hence this method was adopted here.[27]
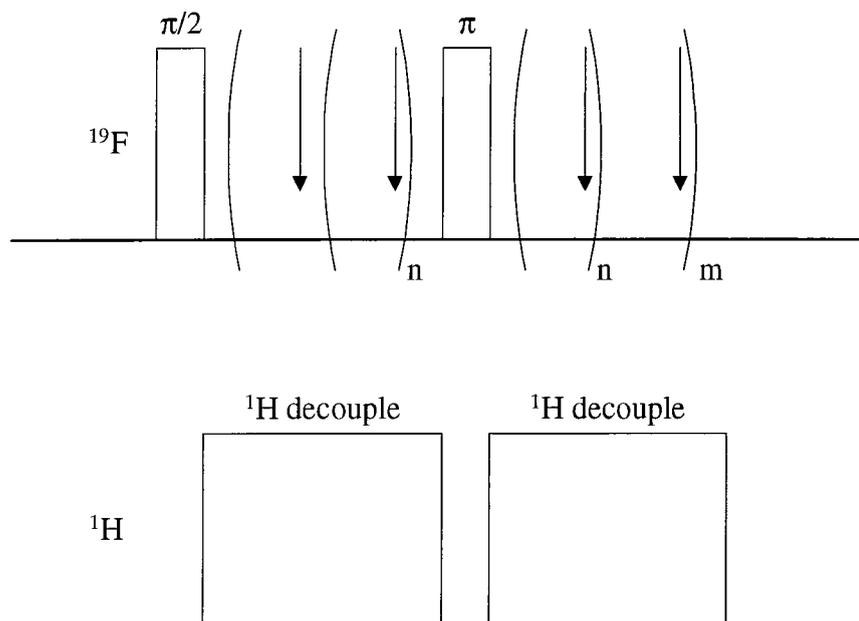
Figure 7.5. CPMG pulse sequence. The arrows denote the sampling points with n and m denoting loop counter parameters in the pulse program which enable the time, tau, between pulses to be altered.

First a 90° pulse is applied to ^{19}F to create transverse magnetisation. The evolution of the ^{19}F spins is monitored by point-wise acquisition of the FID for a time given by (n+1)×dwell, where the dwell is the time interval between data points. A 180° pulse is then applied with a phase shift of 90° with respect to the initial excitation pulse.[26] The phase shift is required to refocus, at even-numbered echoes, any imperfections in the 180° pulses which may attenuate or modulate the echo amplitudes.[60] For the duration of the 180° pulse applied to ^{19}F, no ^1H decoupling is applied (to prevent cross polarisation from occurring between the two types of spins). At a time given by (n+1)×dwell after the 180° pulse, an echo is observed and at this point all interactions other than the homonuclear dipolar interaction are absent. The subsequent decay of the echo, application of a 180° pulse and echo formation is repeated m times. Thus, after the preparation pulse, m×180° pulses are applied and a total of 2m×(n+1) points are collected. As all interactions, other than the ^{19}F-^{19}F dipolar interaction, are only absent at the top of an echo, the point at the echo maximum is extracted from the FID using the 'decimate' command in the Spinsight processing panel. For example, if n+1 points are acquired in the time denoted 'tau',

then the 'decimate' parameter required is 2×(n+1). This gives rise to an FID which contains information regarding the evolution of ^{19}F spins under only the homonuclear dipolar interaction.

A number of CPMG experiments were performed with typical spectral conditions of: ^{19}F π/2 pulse duration, 1.49 μs; ^{19}F π pulse duration, 2.66 μs; dwell, 8 μs; recycle delay; 5 s; ^1H decoupling power, ~100 kHz; number of transients, 528. The parameter denoted n in Figure 7.5, was varied from 1 to 15, to give a range of 'tau' values from 16 μs to 128 μs. Obviously, the maximum value of 'tau' possible is limited by the spectral width required. It is also worth mentioning that as n was increased, m was decreased accordingly, by using the 'double array' facility in Spinsight, so that the overall acquisition time was constant. The ^{19}F CPMG spectrum obtained with a 'tau' time of 56 μs is shown in Figure 7.6. The large central spike, which has been heavily truncated in Figure 7.6, is an artefact which arises from partial spin locking of magnetisation as a result of imperfect 180° pulses.[27,28]
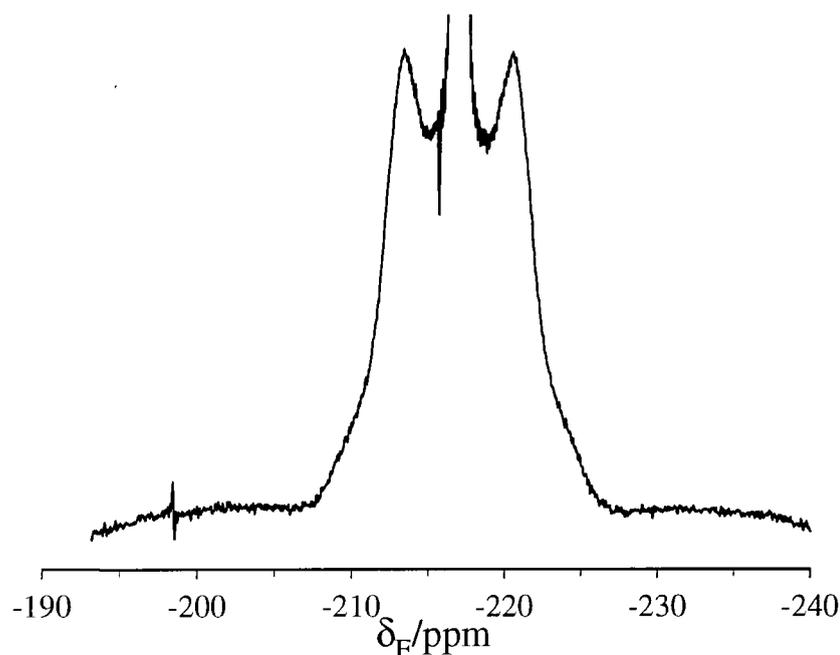
Figure 7.6. Fluorine-19 CPMG spectrum, obtained with a 'tau' time of 56 μs, of the 1,10-difluorodecane/urea inclusion compound.

The reason for performing a number of experiments with different 'tau' values was to see how 'tau' affects the homonuclear dipolar coupling constant. It has

been shown that under 'ideal' circumstances, the observed dipolar splitting, Δ, is linearly dependent upon the duty factor, DF,[27] which is given by,

$$DF = \frac{t_w}{(2\tau + t_w)} \qquad \text{\textit{Equation 7.12}}$$

where t_w is the 180° pulse duration and 2τ is the time between the end of one 180° pulse and the beginning of another. The observed dipolar splitting is then given by,

$$\Delta = R(1 - DF) \qquad \text{\textit{Equation 7.13}}$$

where R is the theoretical dipolar splitting (given by the separation of the 'horns' in a powder spectrum, which corresponds to $\theta=90°$ in Equation 7.2) in the δ pulse limit, where $\Delta=R$. With the pulse duration and 2τ times used, the duty factor ranged from 0.04 to 0.01 and so scaling from this factor will be negligible in comparison to other sources which will now be discussed. For the homonuclear dipolar interaction to be unaffected by chemical shift, the latter must be absent at all times and not just at the top of the echo. Therefore, the echo time, given by 2×tau, must be short compared to the chemical shift dephasing time.[27-29] This arises from the fact that the homonuclear dipolar and chemical shift Hamiltonians do not commute. If tau is short, then clearly a larger number of 180° pulses, will be required which then means that pulse errors become more critical. It is also clear that the shorter 2τ is, then shorter pulse durations are required in order to keep the duty factor low. However, if the duty factor is kept low by increasing 2τ, then $\Delta \neq R$ due to chemical shift dephasing effects.

At longer tau times, the observed dipolar splitting was found to decrease, which can be attributed to dephasing due to chemical shift. Therefore, taking into account the limits of the experimental data, i.e. ignoring those obtained with large tau values, an average value of 1005 Hz was determined for the ^{19}F-^{19}F dipolar coupling constant. This was obtained by comparison of experimental and simulated spectra, which were created using GAMMA (see Appendix).

7.3.1.1.2.2 Single-crystal experiments

In order to provide further corroboration for the value of the dipolar coupling constant obtained, a ^{19}F single-pulse experiment, with ^1H decoupling, was performed on single crystals of the 1,12-difluorododecane/urea inclusion compound. It is possible to obtain the dipolar coupling constant from a single crystal by orientating the sample at an angle other than the magic angle. When θ has a value other than 54.7°, both the isotropic and anisotropic terms in Equation 7.1 contribute to the shielding of the nucleus, with the shielding anisotropy and the dipolar coupling constant (Equation 7.2) both being scaled by $\left(3\cos^2\theta-1\right)$. Therefore, if the angle at which the crystals are oriented at with respect to B_0 is known, then the observed dipolar splitting can be used to calculate the dipolar coupling constant.

The probe used for this experiment, HF, is designed for MAS use and so only minor offsets from the magic angle are possible using the adjustment rod situated at the base of the probe. Therefore, in order to take the spinning module significantly away from the magic angle, it was necessary to remove a pin holding the spinning module and magic-angle adjustment rod together. The largest angle that it was possible to orient the spinning module at with respect to B_0, without having to completely dismantle the probe, was 71°. The angle was actually measured by inserting a rod into the stator and then projecting onto a piece of card, the angle that the rod made with respect to the vertical direction. Measurement of the angle was then made, using a protractor, from the lines drawn on the card. It is vital that the rod diameter is as close as possible to that of a standard rotor, in order to prevent lateral movement of the rod during measurement of the angle. The ^{19}F single-pulse spectrum, acquired with ^1H decoupling, of single crystals of the 1,12-difluorododecane/urea inclusion compound oriented at 71° is shown in Figure 7.7. The spectral conditions used were: ^{19}F $\pi/2$ pulse duration, 3 µs; recycle delay, 15 s; ^1H decoupling power, ~ 100 kHz; acquisition time, 25.6 ms; number of transients, 4000. The splitting of the doublet is 1096 Hz, although the reason why one component of the doublet is more intense than the other is unclear. Given that the

sample is oriented at 71° with respect to B_0, the scaling factor is -0.682 which gives a dipolar coupling constant of 1071 Hz. The shielding is also scaled by the same factor which means that $\sigma = 213.0$ ppm, with respect to $CFCl_3$ (0 ppm). Hence, when the sample is oriented at an angle of 71° to B_0, the resonance is shifted to a higher frequency in comparison to when the sample is oriented at the magic angle. Therefore, the values obtained for the dipolar coupling constant via the single-crystal and CPMG experiments are in reasonable agreement.

δ_F/ppm
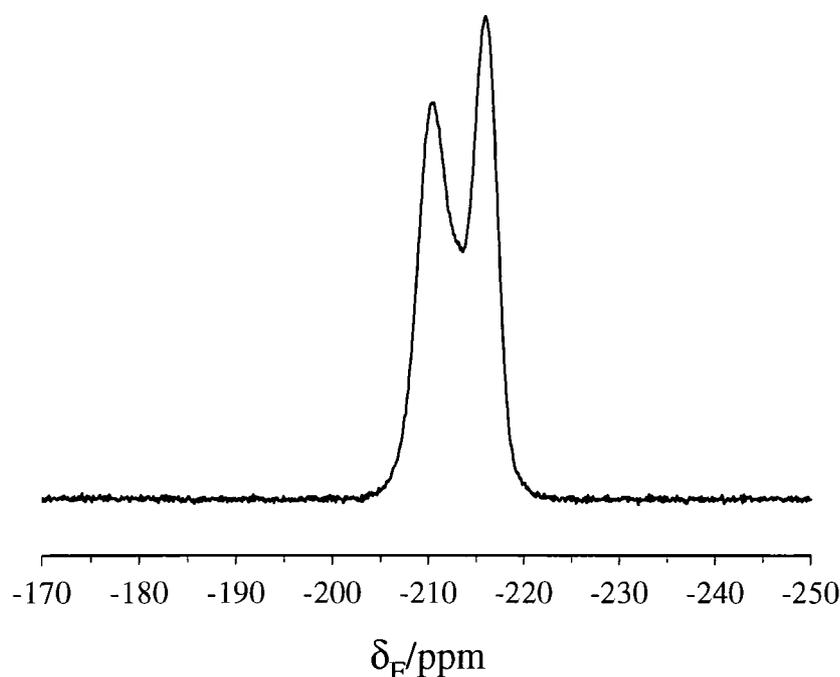
Figure 7.7. Fluorine-19 single-pulse spectrum, acquired with ^1H decoupling, of single crystals of the 1,12-difluorododecane/urea inclusion compound oriented at 71° with respect to B_0.

A summary of experimental and simulated powder spectra is shown in Figure 7.8. Hence, via a combination of experiments which selectively remove certain interactions while retaining others, it is possible to obtain an effective dipolar coupling constant of 1.01 kHz for two fluorines on adjacent guest molecules.
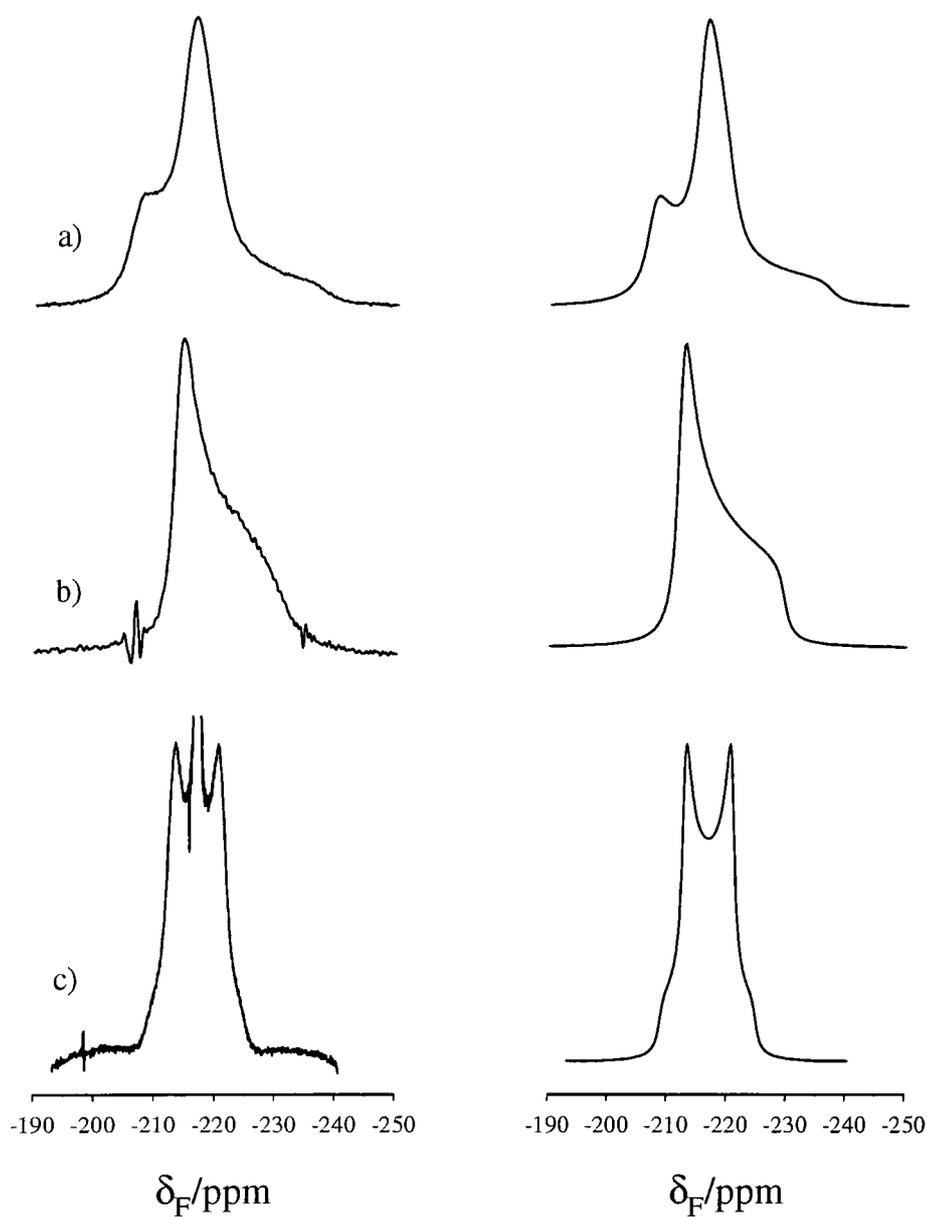
Figure 7.8. Summary of static ^{19}F spectra obtained which 'contain' the following interactions, a) SA and dipolar, b) SA and c) dipolar. The experimentally obtained spectra are those on the left, with the corresponding 'best fit' simulations displayed on the right.

7.3.1.2 1-fluorotetradecane/urea inclusion compound

In the 1-fluorotetradecane/urea inclusion compound, there is a random distribution of end-group interactions. The number of fluorines oriented head to tail (HT) is twice the number oriented head to head (HH), but the number of fluorines contributing to the head-to-head peak is twice the number of actual head-to-head end-group interactions. Therefore, one would expect half of the fluorines to be dipolar coupled and the other half to be essentially isolated. The $^1H \rightarrow ^{19}F$ CP spectrum, acquired with ^1H decoupling, of the 1-fluorotetradecane/urea inclusion compound is shown in Figure 7.9. The spectral conditions used were: ^1H $\pi/2$ pulse duration, 3 μs; contact time, 1 ms; recycle delay, 5 s; acquisition time, 5.1 ms; number of transients, 1024. It is clear that there is an extra 'shoulder' (indicated by the arrow on the left) in between the two 'horns' of the SA/dipolar spectrum in Figure 7.1b. There is also an extra 'shoulder' (indicated by the arrow on the right) in between what corresponds to the perpendicular orientation, with respect to B_0, of the 'squashed' subspectrum and the parallel orientation of the 'stretched' subspectrum of Figure 7.1b.

This can easily be explained if one considers the distribution of end-group interactions in a compound containing unsymmetric guest molecules. Those fluorines that are in head-to-head oriented CH_2F end-groups, will give rise to a SA/dipolar spectrum as in Figure 7.1b. In comparison, those fluorines that are in head-to-tail oriented CH_2F end-groups, will give rise to a SA spectrum as in Figure 7.3. Hence, the spectrum in Figure 7.9 is a superimposition of an axially symmetric SA powder pattern and a SA/dipolar powder spectrum. Therefore, it is possible to obtain the ^{19}F-^{19}F dipolar coupling constant between adjacent guest molecules in the 1-fluorotetradecane compound in the same way as it was for the 1,10-difluorodecane/urea inclusion compound.

-120   -140   -160   -180   -200   -220   -240   -260   -280   -300

δ_F/ppm
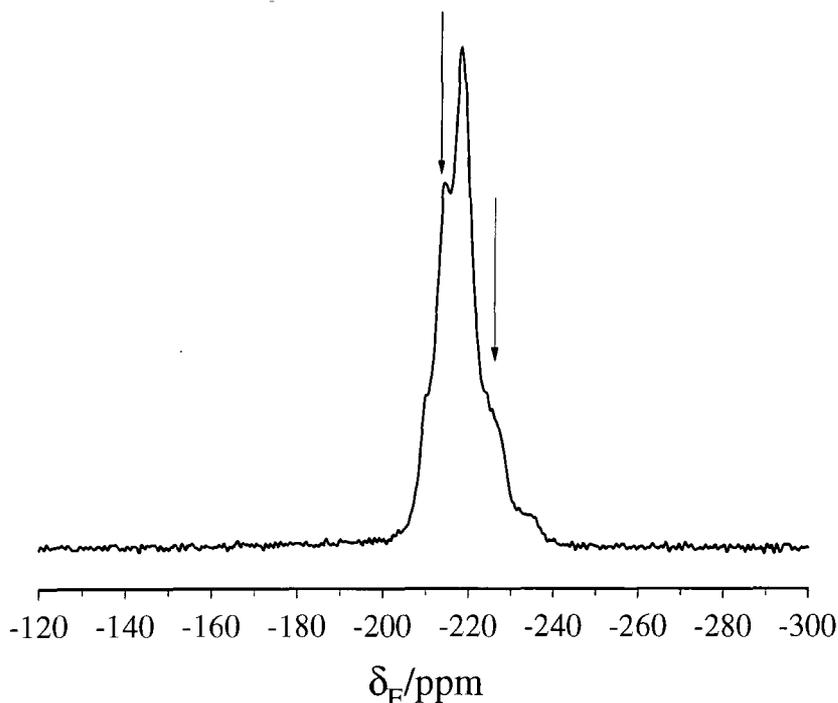
Figure 7.9. $^1H \rightarrow ^{19}F$ CP spectrum, acquired with ^1H decoupling, of the 1-fluorotetradecane/urea inclusion compound. The arrows indicate 'extra' features, that were not present in the analogous spectrum of the 1,10-difluorodecane/urea inclusion compound (Figure 7.1b).

7.3.1.2.1 Determination of the ^{19}F-^{19}F dipolar coupling constant

7.3.1.2.1.1 Fluorine-19 multiple-pulse experiments

For further verification of the symmetry of the shielding tensor, a ^{19}F multiple-pulse spectrum, acquired using MREV-8 and ^{1}H decoupling, was obtained. The spectral conditions used were: ^{19}F $\pi/2$ pulse duration, 1.5 µs; ^{1}H π pulse duration, 2.47 µs; tau, 3.0 µs; recycle delay, 15 s; number of points, 512; number of transients, 640. As can be seen from Figure 7.10, upon removing the ^{19}F-^{19}F dipolar interaction, the SA/dipolar component of Figure 7.9 reduces to an approximately axially symmetric SA powder pattern. Due to the fact that the ^{19}F chemical shift of a head-to-head CH$_2$F is indistinguishable from that for a head-to-tail CH$_2$F, it is possible to see only a single axially symmetric SA powder pattern. Two spectra were

acquired with the transmitter positioned to low (Figure 7.10a) and high (Figure 7.10b) frequency with respect to the signal, the reason for this being that the resolution of the spectra obtained is reduced as the offset from the transmitter increases. Therefore, in order for the σ_{zz} and σ_{xx}/σ_{yy} components of the SA powder pattern to be as clearly resolved as possible, σ_{xx} and σ_{yy} were obtained from Figure 7.10b and σ_{zz} was obtained from Figure 7.10a. The principal components of the shielding tensor were obtained by comparison of simulated spectra, which were created using GAMMA,[57] with the spectra obtained experimentally. The values obtained for σ_{xx}, σ_{yy} and σ_{zz} (relative to CFCl$_3$ (0 ppm)) are 210.8 ppm, 211.5 ppm and 228.7 ppm, respectively and so, within experimental error, the shielding tensor can be considered to be axially symmetric. As for the 1,10-difluorodecane/urea inclusion compound, rapid rotation of the CH$_2$F group renders the shielding tensor axially symmetric for the 1-fluorotetradecane/urea inclusion compound. Therefore, σ_{zz} coincides with the ^{19}F-^{19}F internuclear vector.
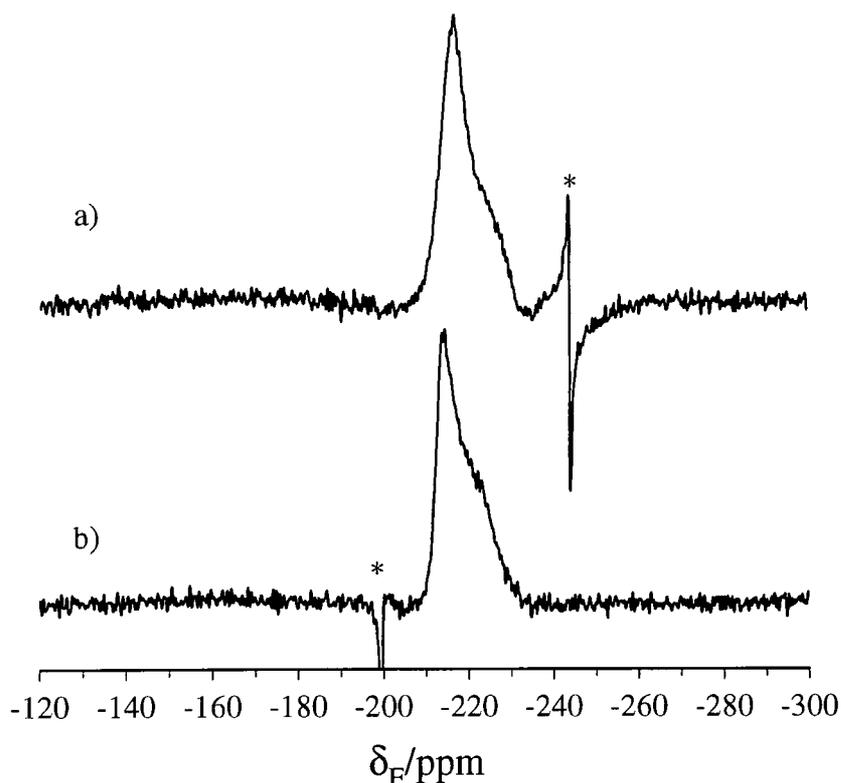
Figure 7.10. Fluorine-19 multiple-pulse spectra acquired using MREV-8 with ^1H decoupling and the transmitter (denoted by the asterisk) positioned a) to low and b) to high frequency with respect to the signal.

7.3.1.2.1.2   Fluorine-19 single-crystal experiments

As for the 1,12-difluorodecane/urea inclusion compound, experiments were also performed on single crystals of the 1-fluorotetradecane/urea inclusion compound. The procedure for the packing of the crystals was the same as that used for the 1,12-difluorodecane/urea inclusion compound. Experiments were performed with the 1-fluorotetradecane/urea single crystals oriented at 54.7° (Figure 7.11a) and 71° (Figure 7.11b), with respect to B_0. The spectral conditions used were: ^1H $\pi/2$ pulse duration, 3 μs; contact time, 1 ms; recycle delay, 10 s; acquisition time, 25 ms; number of transients, 256 (54.7°) and 4000 (71°). When oriented at the magic angle, a single peak was obtained (fwhh ~ 417 Hz), thus confirming that σ_{zz} is coincident with the internuclear vector. The shielding of the resonance is given by σ_{iso}, which has a value of 216.9 ppm with respect to $CFCl_3$. However, when the sample is oriented at 71° to B_0, three peaks are obtained in comparison to the two that were obtained for the 1,12-difluorododecane/urea inclusion compound (Figure 7.7).

This can readily be explained by the fact that half of the fluorines contributing to the spectrum have no dipolar interaction and therefore will give rise to a single resonance with a shielding, σ, given by $\sigma_{iso} + \frac{1}{3}(3\cos^2 71° - 1)\Delta\sigma$. Hence, with $\Delta\sigma = 17.6$ ppm and the sample oriented at 71°, then the resonance will be at a lower shielding ($\sigma = 212.9$ ppm), i.e. higher frequency, than when oriented at the magic angle. The remaining fluorines contributing to the spectrum are dipolar coupled and so a doublet is observed, which is positioned at the same chemical shift as for those fluorines which are not dipolar coupled, given the fact that head-to-head fluorines have the same shielding as head-to-tail fluorines. The splitting of the two 'horns' in Figure 7.11b, although not clearly resolved, is ~ 1000 Hz, which equates to a dipolar coupling constant, D, of ~ 975 Hz.
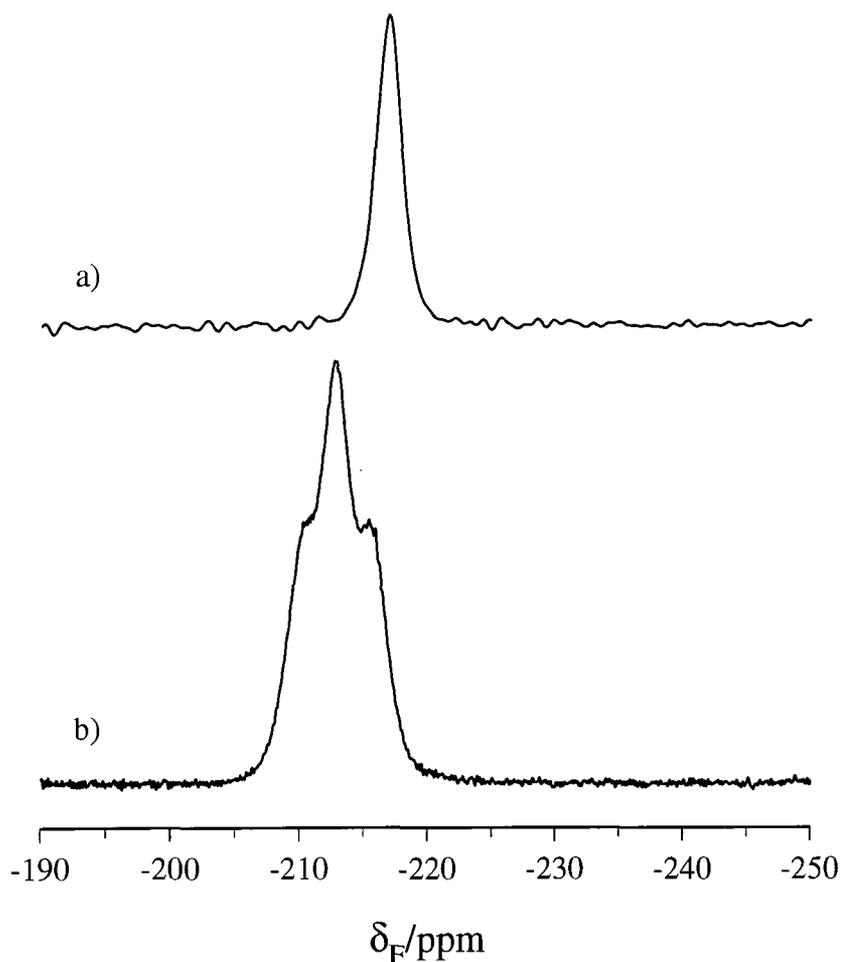
Figure 7.11. $^{1}H \rightarrow {}^{19}F$ CP spectra, acquired with ^{1}H decoupling, of single crystals of the 1-fluorotetradecane/urea inclusion compound oriented at a) 54.7° and b) 71° with respect to B_0.

7.3.1.2.1.3 CPMG experiments

In an attempt to obtain a more resolved dipolar splitting, a CPMG experiment (Figure 7.12) was performed on the 1-fluorotetradecane/urea inclusion compound (powder). The spectral conditions used were: ^{1}H $\pi/2$ pulse duration, 3 µs; ^{19}F π pulse duration, 6 µs; contact time, 1 ms; tau, 72 µs; dwell, 8 µs; recycle delay; 10 s; ^{1}H decoupling power, ~100 kHz; number of transients, 3600. In the experimental spectrum, Figure 7.12a, the first data point was missing and so for simulation (using GAMMA) of Figure 7.12b, the first data point in the FID was omitted. The best fit,

obtained by comparison of the experimental and simulated spectra 'by eye', gave a dipolar coupling constant, D, of 1059 Hz.
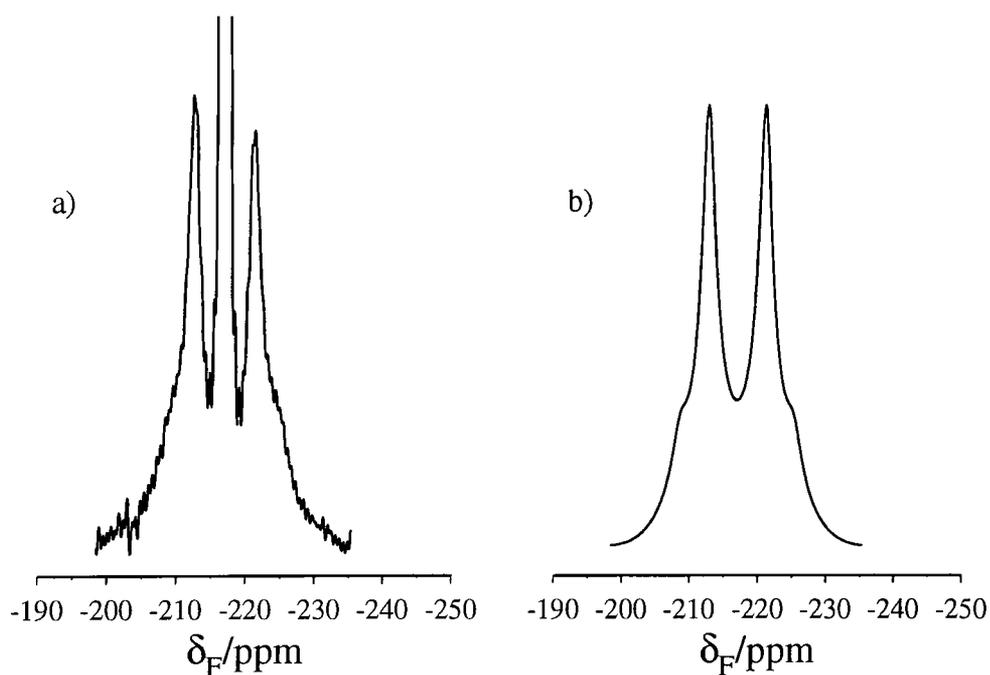
Figure 7.12. $^{1}H \rightarrow ^{19}F$ CPMG spectrum, acquired with ^{1}H decoupling and with a 'tau' time of 72 μs, of the 1-fluorotetradecane/urea inclusion compound, with a) showing the experimental and b) the simulated data.

Having obtained the principal components of the shielding tensor, the relative orientation of the internuclear vector and the dipolar coupling constant, such parameters were then used to 'fit' the combined SA and SA/dipolar spectrum obtained in Figure 7.9.
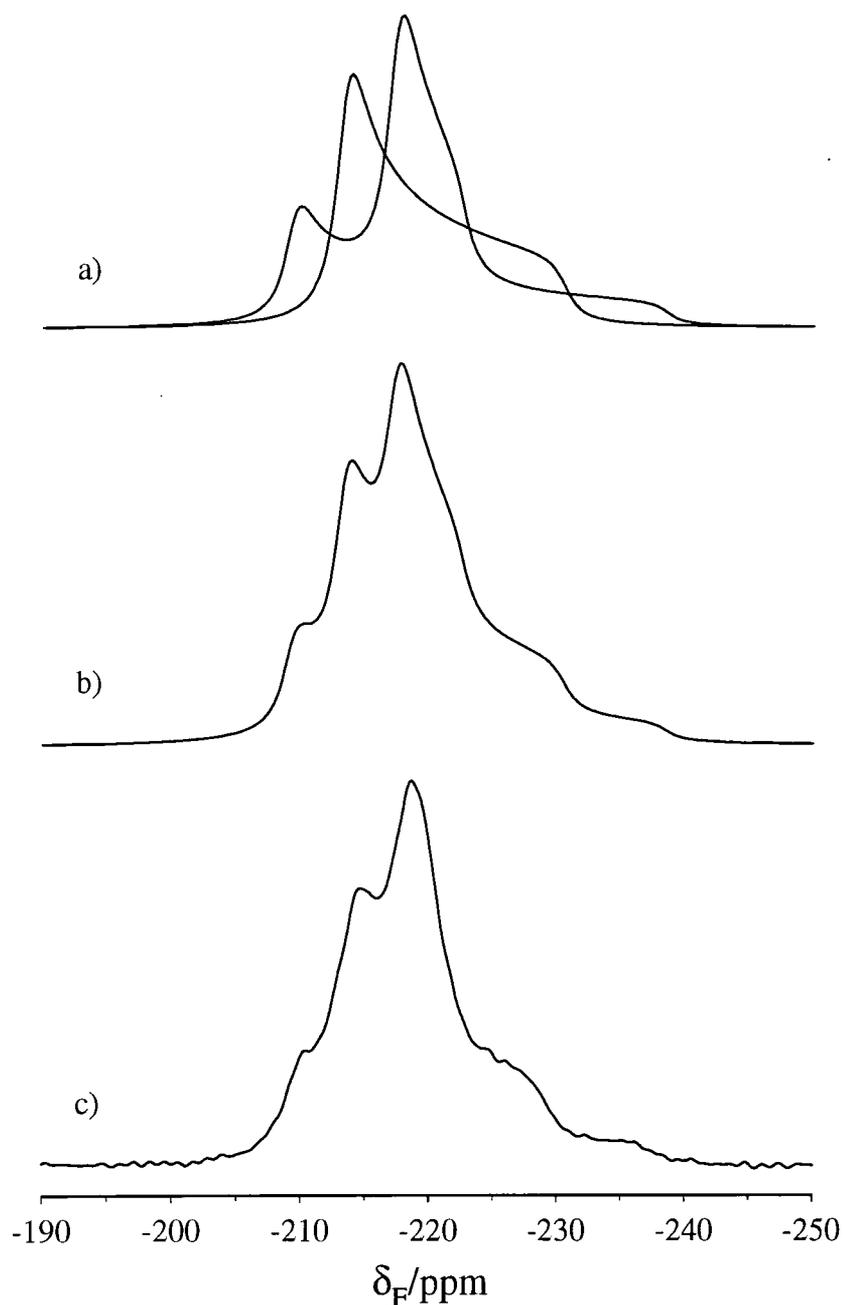
Figure 7.13. Composition of $^1H \rightarrow ^{19}F$ CP spectrum, acquired with ^1H decoupling of the 1-fluorotetradecane/urea inclusion compound, with a) showing the SA and SA/dipolar components which make up the b) simulated and c) experimental spectra.

Figure 7.13 illustrates how a combination of a SA spectrum and a SA/dipolar spectrum make up the overall observed lineshape. The parameters used to simulate the SA spectrum were those obtained from the analysis of Figure 7.10. Such parameters were then used in combination with the dipolar coupling constant obtained from the CPMG and single-crystal experiments (1.06 kHz), to simulate a

combined SA/dipolar powder spectrum. The resultant lineshape, after combination of the two spectra in Figure 7.13a in equal proportions, is shown in Figure 7.13b, with the experimentally obtained data shown in Figure 7.13c. The relative contribution of the SA and SA/dipolar spectra to the overall spectrum further corroborates the results obtained via ^{13}C NMR,[54] which showed that the 1-fluorotetradecane molecules are oriented randomly in the urea tunnels.

7.3.2 *Effect of molecular motion upon the dipolar interaction*

Low-temperature (at 133 K) ^{19}F experiments have also been performed, although due to the comparable appearance of spectra obtained at both ambient and low temperatures, it can be concluded that motional averaging of the SA and dipolar interactions cannot be halted given the present low-temperature capabilities of the equipment. Hence, a model is required in which the alignment of the effective dipolar vector along the tunnel axis can be interpreted in terms of motional averaging of possible end-group conformations. It is known that the guest molecules undergo rapid reorientation, i.e. at $\geq 10^7$ Hz, of the whole molecule about its long molecular axis and torsional libration about the penultimate C-C bond. There is also rapid methyl group rotation for linear alkanes and the guest molecules can move in a direction which is parallel to the tunnel axis.[2] In this case, a model has been adopted which allows reorientation of the whole molecule along its long axis, CH_2F end-group rotation and movement of the whole molecule along the urea tunnels. The model is best explained, if one initially considers two guest molecules within the urea tunnel with the fluorines adopting trans conformations. The CH_2F end-groups can rotate about the C-CH_2F bond, but from consideration of the most and least energetically favourable conformations that alkanes can adopt, it is only necessary to rotate the CH_2F end-groups in 120° steps. Reorientation about the long molecular axis is allowed in 180° steps so that the CH_2F end-groups can be staggered or eclipsed with respect to one another. The minimum separation between the two guest molecules is given by the van der Waals radii of the two atoms which are closest to one another, given the conformational restrictions just outlined. Initially, the two

molecules are separated by a variable distance depending on their mutual conformations. Thus, when rotation about the long molecular axis and/or rotation of the CH_2F end-group(s) is performed, the molecules either move closer together or further apart until their separation is given by the sum of the van der Waals radii of the two atoms which are closest to one another.

If one considers the fact that a fluorine in each CH_2F end-group can be in one of three positions, then for two adjacent CH_2F end-groups, there are nine different conformations which the two end-groups could adopt in the model used. Assuming for now that the end-groups can be either staggered or eclipsed with respect to one another, this then means that there is a total of eighteen ^{19}F-^{19}F conformations to be considered. Figure 7.14 and Figure 7.15 represent all the possible conformations of the two end-groups in the form of Newman projections, with the end-groups staggered and eclipsed, respectively, with respect to one another. The conformation of end-groups is described with respect to the alkyl chain. A computer program, written using GAMMA,[61] has been used to simulate all the possible conformations for the model described. Each possible conformation is defined by four angles, with two describing one end-group conformation and two describing that of the adjacent end-group. These angles define the rotation from an initial position of the whole molecule and of the CH_2F end-group to adopt the conformation required. The program then gives the ^{19}F-^{19}F internuclear distance for each conformation and the angle of the internuclear vector with respect to the tunnel axis. Host-guest interactions have not been included in the simulation, although the presence of the urea tunnel is implied in the simulation, in so far as rotation of the guest molecules is only allowed about the tunnel axis. Some translational motion perpendicular to the tunnel axis is permitted for the staggered conformations (Figure 7.14), so that the atoms on adjacent end-groups, which are trans with respect to the alkyl chains, can 'touch'.
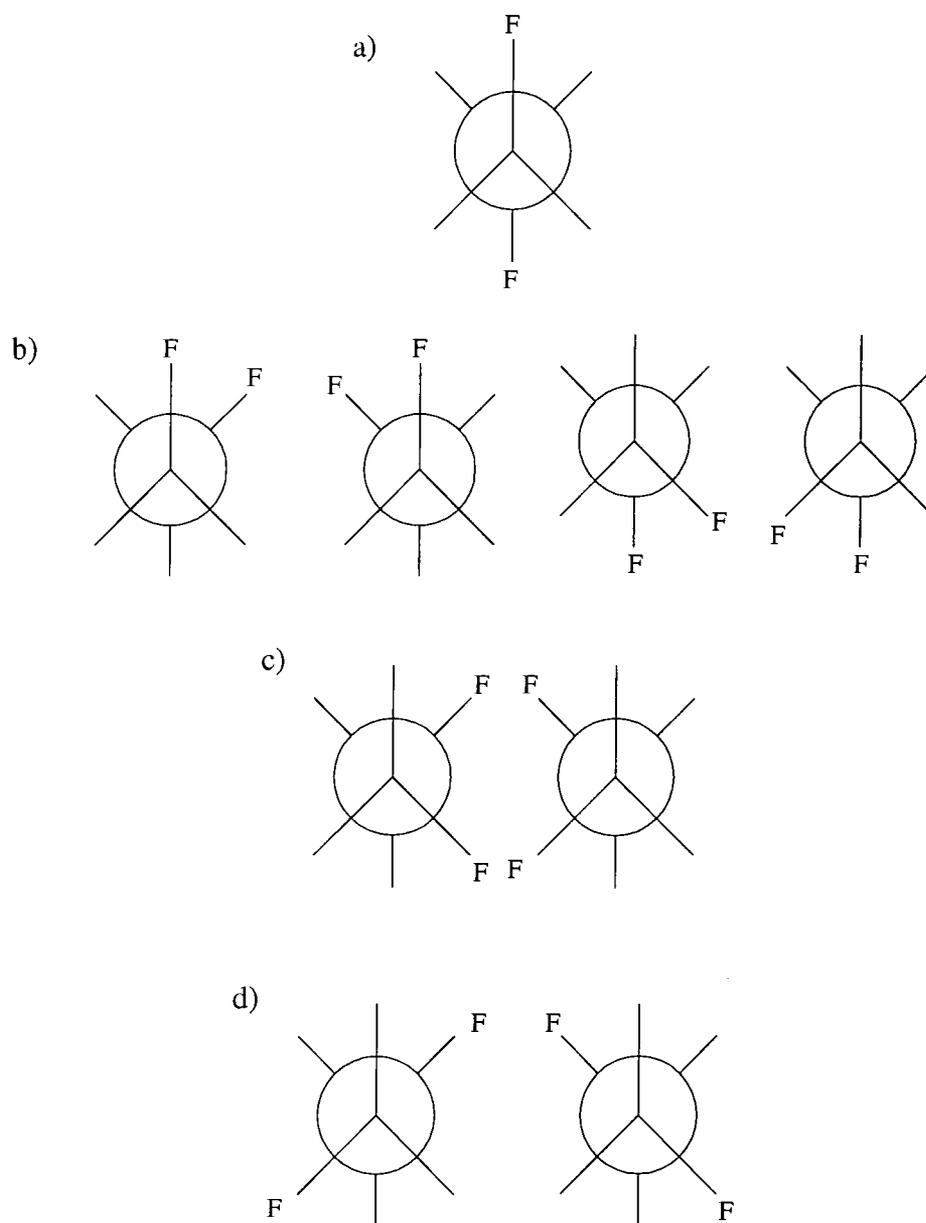
Figure 7.14. The possible conformations for two adjacent CH_2F end-groups, which are staggered with respect to one another, and the fluorines are a) trans/trans, b) trans/gauche, c) gauche/gauche (with a dihedral angle of 120°) and d) gauche/gauche (with a dihedral angle of 180°). The atoms on adjacent end-groups, which are trans with respect to the alkyl chains, are in fact touching.
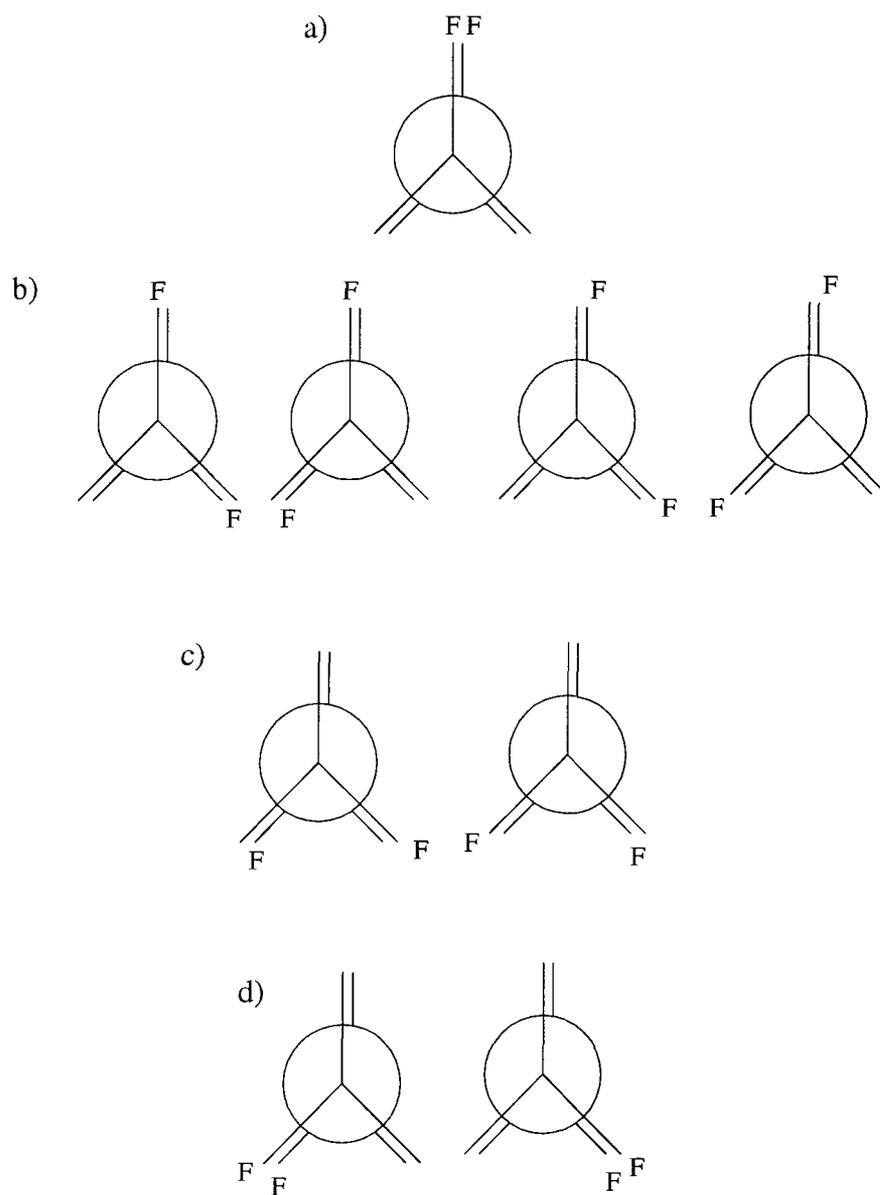
Figure 7.15. The possible conformations for two adjacent CH_2F end-groups, which are eclipsed with respect to one another, and the fluorines are a) trans/trans, b) trans/gauche, c) gauche/gauche (with a dihedral angle of 120°) and d) gauche/gauche (with a dihedral angle of 0°).

To understand how the ^{19}F-^{19}F internuclear distance for each 'static' conformation and the angle of the internuclear vector with respect to the tunnel axis can be used to calculate an effective (aligned along the tunnel axis) dipolar coupling constant, the relative orientations of the relevant frames of reference have been considered. Figure 7.16 describes the relative orientations of the laboratory frame of reference, a molecular frame of reference, in which the z axis is oriented along the tunnel axis, and ^{19}F-^{19}F dipolar reference frame.
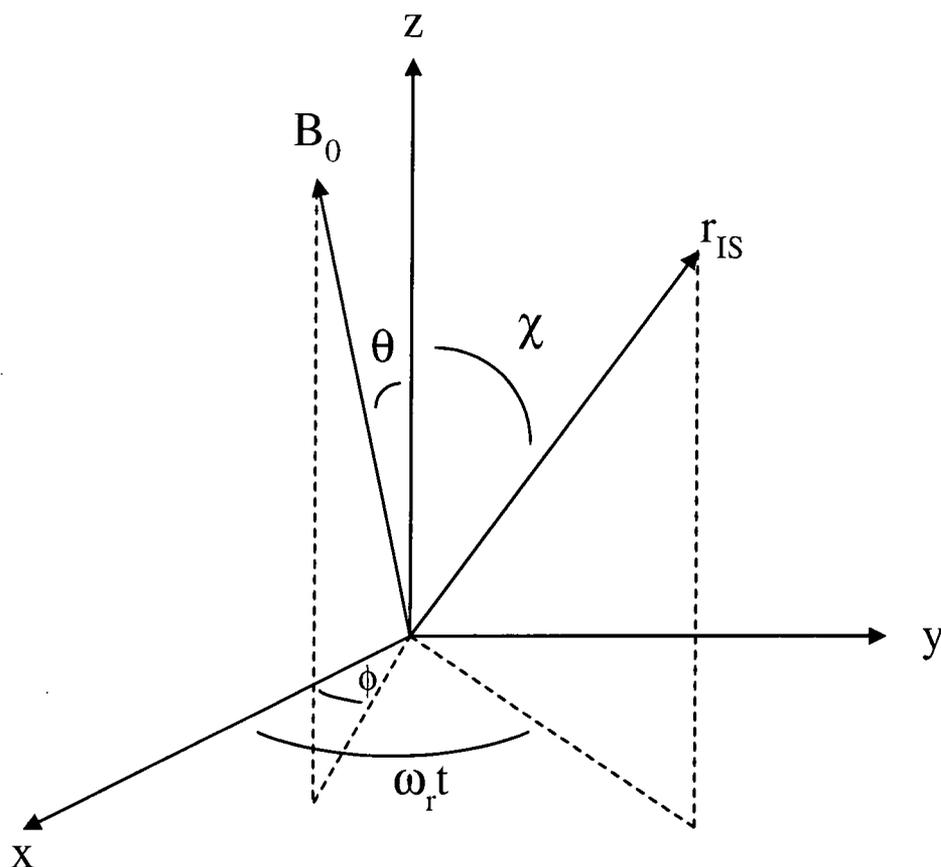
Figure 7.16. Orientation of internuclear vector, r_{IS} (coincident with D_{zz}), with respect to the molecular axis system and B_0 (static magnetic field). The z axis of the molecular axis system is parallel to the urea tunnel.

The definitions of the angles used to describe the relative orientations of the reference frames are: χ is the angle between the tunnel axis and the ^{19}F-^{19}F internuclear vector, $\omega_r t$ is the polar projection angle between the internuclear vector and the x axis, ϕ is the polar projection angle between B_0 and the x axis and θ is the

angle between the tunnel axis and B_0. These definitions will now be used in a rigorous derivation of an expression to be used to calculate the dipolar coupling constant for a particular ^{19}F-^{19}F orientation, undergoing rapid motion about the tunnel axis. When transforming from one reference frame to another, it is easier if the dipolar tensor is expressed in spherical tensor notation and hence rotations can be described using Wigner rotation matrices.[62-64]

For a dipolar vector oriented at angles of χ and $\omega_r t$ with respect to the molecular axis system, which in turn is oriented at angles of ϕ and θ with respect to the laboratory frame of reference, the following transformations are required,

$$DIP_{PAS} \xrightarrow{(0,\chi,\omega_r t)} MOL \xrightarrow{(\phi,\theta,0)} LAB$$

where DIP_{PAS}, MOL and LAB are the dipolar, molecular and laboratory frames of reference, respectively. It is noticeable that only two out of the three Euler[65] angles are required to describe each transformation due to the axial symmetry of the dipolar tensor and the static magnetic field. The Hamiltonian for the homonuclear dipolar interaction, H_D, expressed in spherical tensor notation is given by,

$$H_D = C^D \sum_1 \sum_{m=-1}^{1} (-1)^m R_{lm}^D T_{lm}^D \qquad \textit{Equation 7.14}$$

where C^D contains constants relevant to the dipolar interaction (see later), R_{lm} and T_{lm} describe the spatial and spin terms, respectively, in the LAB and, l and m denote the rank and row, respectively of the tensor. The spatial term in the DIP_{PAS}, $\rho_{lm'}$, is related to its components expressed in the LAB (i.e. R_{lm}) by,

$$R_{lm}^D = \sum_{m'} D_{m'm}^l (\alpha^D, \beta^D, \gamma^D) \rho_{lm'}^D \qquad \textit{Equation 7.15}$$

where $D_{m'm}^l (\alpha^D, \beta^D, \gamma^D)$ are the Wigner rotation matrices and, α^D, β^D and γ^D denote the Euler angles, which describe the rotation of the DIP_{PAS} into the LAB. As R_{lm}^D is derived from a symmetric 2nd-rank Cartesian tensor, only terms with l=0, 2 will be nonzero. The dipolar tensor is both axially symmetric and traceless in the DIP_{PAS}, and so all components other than ρ_{20}^D can be ignored.

In this case it is necessary to perform two transformations, with the first transforming the DIP_{PAS} into the MOL,

$$\rho_{2m'}^D(MOL) = D_{0m'}^2(\phi,\theta,0)\rho_{20}^D(DIP) \qquad \text{Equation 7.16}$$

where ϕ and θ are equivalent to the Euler angles α^D and β^D in Equation 7.15. In the second rotation, the MOL is transformed into the LAB,

$$R_{20}^D(LAB) = \sum_{m'} D_{m'0}^2(0,\chi,\omega_r t)\rho_{2m'}^D(MOL) \qquad \text{Equation 7.17}$$

where χ and $\omega_r t$ are equivalent β^D and γ^P. Therefore, substituting Equation 7.16 into Equation 7.17 gives,

$$R_{20}^D(LAB) = \sum_{m'} D_{m'0}^2(0,\chi,\omega_r t)\left[D_{0m'}^2(\phi,\theta,0)\rho_{20}^D(DIP)\right] \qquad \text{Equation 7.18}$$

which on expansion of the m′ summation (m′=0, ±1, ±2) gives,

$$R_{20}^D(LAB) = D_{20}^2(0,\chi,\omega_r t)\left[D_{02}^2(\phi,\theta,0)\rho_{20}^D\right] + D_{10}^2(0,\chi,\omega_r t)\left[D_{01}^2(\phi,\theta,0)\rho_{20}^D\right]$$

$$+ D_{00}^2(0,\chi,\omega_r t)\left[D_{00}^2(\phi,\theta,0)\rho_{20}^D\right] + D_{-10}^2(0,\chi,\omega_r t)\left[D_{0-1}^2(\phi,\theta,0)\rho_{20}^D\right]$$

$$+ D_{-20}^2(0,\chi,\omega_r t)\left[D_{0-2}^2(\phi,\theta,0)\rho_{20}^D\right]$$

Equation 7.19

Substituting in the Wigner rotation matrices for $D_{0m'}^2$ gives,

$$R_{20}^D(LAB) = D_{20}^2(0,\chi,\omega_r t)\left[\sqrt{\frac{3}{8}}\sin^2\theta\exp(2i\phi)\rho_{20}^D\right]$$

$$+ D_{10}^2(0,\chi,\omega_r t)\left[-\sqrt{\frac{3}{8}}\sin 2\theta\exp(i\phi)\rho_{20}^D\right] + D_{00}^2(0,\chi,\omega_r t)\left[\frac{1}{2}(3\cos^2\theta - 1)\rho_{20}^D\right]$$

$$+ D_{-10}^2(0,\chi,\omega_r t)\left[\sqrt{\frac{3}{8}}\sin 2\theta\exp(-i\phi)\rho_{20}^D\right] + D_{-20}^2(0,\chi,\omega_r t)\left[\sqrt{\frac{3}{8}}\sin^2\theta\exp(-2i\phi)\rho_{20}^D\right]$$

Equation 7.20

The Wigner rotation matrices for $D_{m'0}^2$ can subsequently be substituted into Equation 7.20 to give,

$$R_{20}^{D}(LAB) = \sqrt{\frac{3}{8}}\sin^2\chi\exp(2i\omega_r t)\left[\sqrt{\frac{3}{8}}\sin^2\theta\exp(2i\phi)\rho_{20}^{D}\right]$$

$$+\sqrt{\frac{3}{8}}\sin 2\chi\exp(i\omega_r t)\left[-\sqrt{\frac{3}{8}}\sin 2\theta\exp(i\phi)\rho_{20}^{D}\right]$$

$$+\frac{1}{2}(3\cos^2\chi - 1)\left[\frac{1}{2}(3\cos^2\theta - 1)\rho_{20}^{D}\right] - \sqrt{\frac{3}{8}}\sin 2\chi\exp(-i\omega_r t)\left[\sqrt{\frac{3}{8}}\sin 2\theta\exp(-i\phi)\rho_{20}^{D}\right]$$

$$+\sqrt{\frac{3}{8}}\sin^2\chi\exp(-2i\omega_r t)\left[\sqrt{\frac{3}{8}}\sin^2\theta\exp(-2i\phi)\rho_{20}^{D}\right]$$

Equation 7.21

As motion of the ^{19}F-^{19}F dipolar vectors about the tunnel axis is rapid on the NMR timescale, Equation 7.21 can be integrated with respect to the polar angle, $\omega_r t$, between 2π and 0 to give,

$$R_{20}^{D}(LAB) = \frac{1}{2}(3\cos^2\chi - 1)\left[\frac{1}{2}(3\cos^2\theta - 1)\rho_{20}^{D}\right] \qquad \text{Equation 7.22}$$

This expression can then be substituted into Equation 7.14 to give,

$$H_D = C^D T_{20}^{D}\frac{1}{2}\left(3\cos^2\chi - 1\right)\frac{1}{2}\left(3\cos^2\theta - 1\right)\rho_{20}^{D}(DIP) \qquad \text{Equation 7.23}$$

where,

$$T_{20}^{D} = \frac{2}{\sqrt{6}}\left[I_z I_z - \frac{1}{4}(I_+ I_- + I_- I_+)\right],$$

(I_z, I_+, I_- are the z component and, raising and lowering spin operators, respectively),

$$\rho_{20}^{D}(DIP) = \frac{1}{\sqrt{6}}[3D_{zz}],$$

(D_{zz} is the z principal component of the dipolar tensor),

and $C^D = \dfrac{-2\gamma^2\hbar\mu_0}{8\pi^2}$,

(μ_0 is the vacuum permeability, γ is the magnetogyric ratio of the nucleus and $2\pi\hbar$ is the Planck constant). Substitution of the above into Equation 7.23 gives,

$$H_D = -\frac{1}{2}D\left(3\cos^2\chi - 1\right)\left(3\cos^2\theta - 1\right)\left[I_z I_z - \frac{1}{4}(I_+ I_- + I_- I_+)\right] \qquad \text{Equation 7.24}$$

where $D = \dfrac{\gamma^2 \hbar \mu_0}{8\pi^2 r^3}$ and r is the internuclear distance.

The expression for the energy levels corresponding to Equation 7.24 is given by,

$$h^{-1}U = -v_0 m_I(1) - v_0 m_I(2) - \frac{D}{2}(3\cos^2\theta - 1)(3\cos^2\chi - 1)m_I(1)m_I(2)$$

Equation 7.25

which can then be used to derive the theoretical dipolar splitting, R (see section 7.3.1.1.1.3), for a ^{19}F-^{19}F vector oriented at an angle χ with respect to the tunnel axis, and with the tunnel axis oriented at an angle θ with respect to B_0,

$$R = \frac{3D}{4}(3\cos^2\theta - 1)(3\cos^2\chi - 1) \qquad \textit{Equation 7.26}$$

However, rapid motion about the tunnel axis means that the ^{19}F-^{19}F vector is effectively aligned parallel to the tunnel axis, and so $\chi_{eff} = 0$. Therefore, the dipolar splitting observed for a particular orientation of the tunnel axis (described by an angle θ) with respect to B_0 is given by,

$$R = \frac{3D_{eff}}{2}(3\cos^2\theta - 1) \qquad \textit{Equation 7.27}$$

where D_{eff} is the motionally averaged (about the tunnel axis) dipolar coupling constant. To calculate the effective (as a result of rapid motion) dipolar coupling constant, D_{eff} from the dipolar coupling constant, D for a 'static' ^{19}F-^{19}F vector,

$$\frac{3D}{4}(3\cos^2\theta - 1)(3\cos^2\chi - 1) = \frac{3D_{eff}}{2}\left(3\cos^2\theta - 1\right)$$

and thus it can be seen that rapid molecular motion about the tunnel axis will scale the 'static' dipolar interaction by $\dfrac{1}{2}(3\cos^2\chi - 1)$.

Conformation	dihedral angle	$r_{F\text{-}F}$/Å	$D_{F\text{-}F}$/kHz	χ
trans/trans (s)	180°	2.72	5.29	14.9°
trans/trans (e)	0°	2.71	5.35	0°
gauche/trans (s) (×4)	60°	3.68	2.14	22.9°
gauche/trans (e) (×4)	120°	4.00	1.66	29.5°
gauche/gauche (s) (×2)	120°	4.86	0.93	30.7°
gauche/gauche (s) (×2)	180°	5.36	0.69	38.7°
gauche/gauche (e) (×2)	120°	4.76	0.99	28.2°
gauche/gauche (e) (×2)	0°	4.20	1.44	0°

Table 7.1. Internuclear ^{19}F-^{19}F distance, dipolar coupling constant and angle, χ, (between the tunnel axis and the ^{19}F-^{19}F vector) for different end-group conformations. In the column denoting the conformation of adjacent end-groups, s and e refer to staggered and eclipsed, respectively.

Table 7.1 gives the ^{19}F-^{19}F distance for the eighteen possible conformations of two adjacent end-groups, illustrated in Figure 7.14 and Figure 7.15, and the angle χ which the internuclear vector makes with the tunnel axis. If all eighteen conformations are present in equal populations, then

$$R = \frac{1}{18}\sum_{i=1}^{18} \frac{3D_i}{4}(3\cos^2\theta - 1)(3\cos^2\chi_i - 1) \qquad \textit{Equation 7.28}$$

which is equal to (in units of kHz),

$$R = \frac{1}{18}(3\cos^2\theta - 1)(7.15 + 8.03 + 2(0.85) + 2(0.43) + 2(2.16) + 2(0.99) + 4(2.48) + 4(1.59))$$

$$R = 2.24(3\cos^2\theta - 1)$$

However, for rapid motion of the ^{19}F-^{19}F internuclear vectors about the tunnel axis, χ_{eff} is equal to zero and thus,

$$\frac{3D_{eff}}{2}(3\cos^2\theta - 1) = 2.24(3\cos^2\theta - 1)$$

Therefore, if all eighteen conformations are possible and with rapid molecular motion about the tunnel axis, then $D_{eff} = 1.49$ kHz. Using the same method, D_{eff} has

been calculated for different combinations of conformations, with the values obtained shown in Table 7.2. In the calculations, where the possibility of more than one conformation has been considered, it has been assumed that the respective conformations are all equally probable.

Conformations	D_{eff}/kHz
tt/s, tg/s, gg/s, tt/e, tg/e, gg/e	1.49
tt/s, tg/s, gg/s	1.45
tt/e, tg/e, gg/e	1.53
gt/s, gg/s, gt/e, gg/e	1.05
gt/s, gt/e	1.36
gg/s, gg/e	0.74
gg/s, gt/s	1.04
gg/e, gt/e	1.05
gg/s	0.43
gg/e	1.05
tt/s	4.77
tt/e	5.35
gt/s	1.65
gt/e	1.06

Table 7.2. Effective dipolar coupling constants for different combinations of the possible conformations. gg, gt and tt denote gauche/gauche, gauche/trans and trans/trans conformations while e and s refer to whether the end-groups are eclipsed or staggered, respectively.

From comparison of the values for D_{eff} given in Table 7.2, with the experimentally obtained value of 1.01 kHz, certain conformations can be ruled out. It is important to note at this stage that it has been assumed that all the conformations are equally probable from a thermodynamic point of view, and so it is only the dipolar coupling constant which is being used to rule out, or include certain conformations. Clearly, the trans/trans conformation is not present, either on its own or in substantial amount in combination with other conformations, as the resultant

effective dipolar coupling constant is much larger than that obtained experimentally. The most probable conformations of adjacent end-groups, based purely on the magnitude of D_{eff}, are: i) gauche/gauche (s) and gauche/trans (s), ii) gauche/gauche (e) and gauche/trans (e), iii) gauche/gauche (s and e) and gauche/trans (s and e), iv) gauche/gauche (e) and v) gauche/trans (e). However, these conformations are not all equally favoured from a thermodynamic point of view. Attempts were made to calculate the different conformational energies using CAChe,[66] but it was not possible to mimic the restrictions in movement imposed by the urea tunnels.

However, if one considers the simpler system of 1,2-difluoroethane, the least energetically favourable conformations are when the two CH_2F groups are eclipsed. Although the interatomic distances are different to those calculated for two fluoroalkane guest molecules, it is possible to assume that the eclipsed conformations will be far less energetically favourable than those in which the end-groups are staggered. Therefore, from the experimentally observed D_{eff} of 1.01 kHz, it can be deduced that the end-groups are gauche/gauche and gauche/trans which gives rise to a value of 1.04 kHz for D_{eff}. This would seem sensible if one considers the fact that when the end-groups are trans/trans the two fluorines are required to be in direct contact, which will be a highly repulsive interaction. On the other hand, when the end-groups are gauche/gauche and gauche/trans, there is the possibility of ^{1}H---^{19}F interactions which could be attractive. It is also worth noting that the urea could also influence the conformational preferences of end-groups. In single-crystal Raman experiments performed on dihalogen-alkane/urea inclusion compounds,[10] it was found that as the halogen substituent decreases in size, the proportion of end-groups in the gauche conformation increases (Cl, 51 %, Br, 7 % and I, 1 %). Therefore, the predominance of the gauche conformation in the fluoroalkane/urea compounds, fits in with these Raman results. However, the results obtained in the present study are also in agreement with preliminary results obtained from Raman experiments performed on fluoroalkane/urea inclusion compounds.[67]
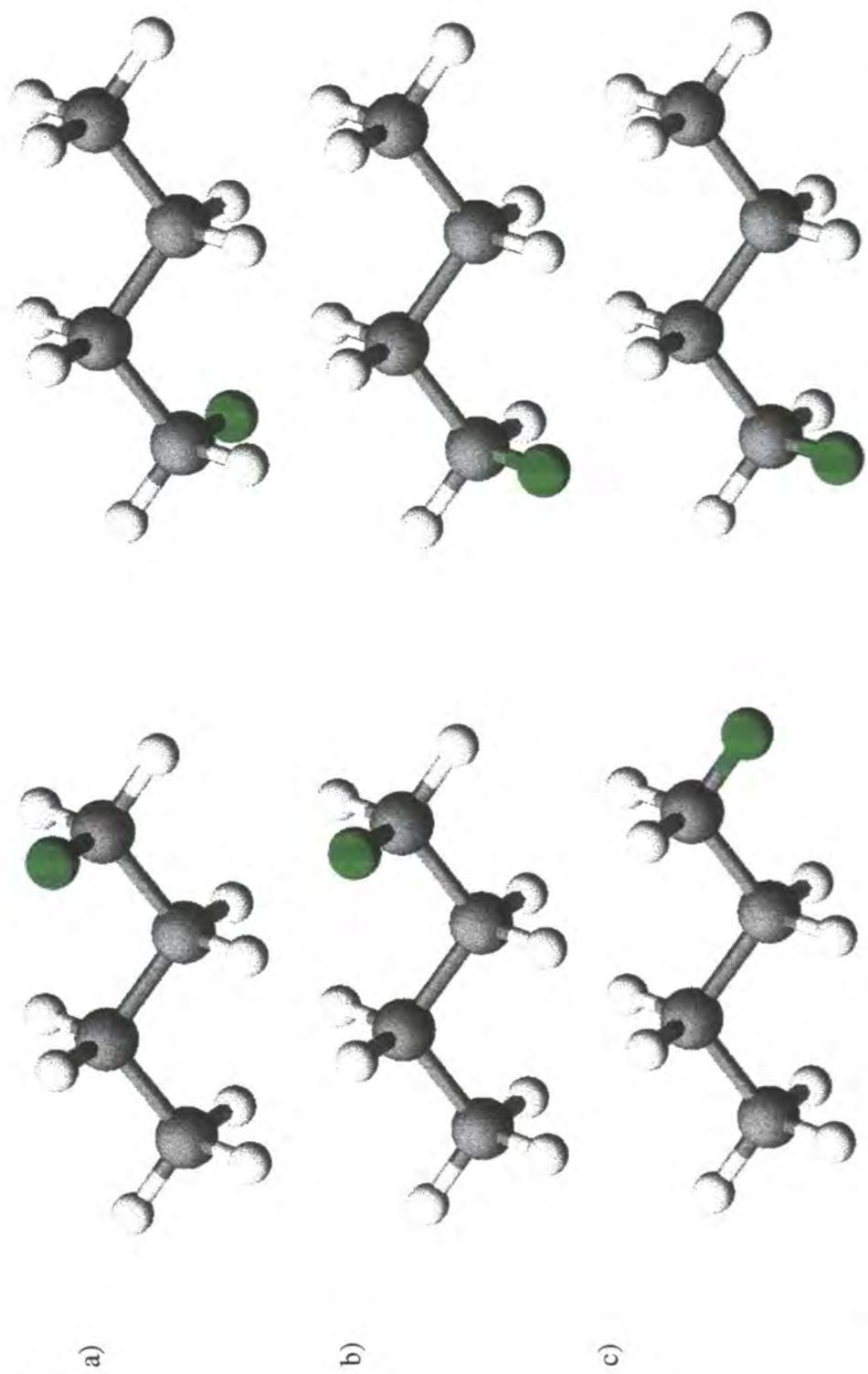
Figure 7.17. Favoured conformations of two fluoroalkane molecules adjacent to one another in a urea tunnel with the ^{19}F-^{19}F internuclear distance in a) 5.36 Å (g/g, dihedral angle 180°), b) 4.86 Å (g/g, dihedral angle 120°) and c) 3.68 Å (t/g).

7.3.3 MAS ^{19}F experiments

As already stated in an earlier section, MAS is used in solid-state NMR to remove line broadening interactions such as SA. However, it also averages the homonuclear dipolar interaction between two isolated spins, which is obviously undesirable in experiments where the interaction needs to be retained in order to yield distance information. A summary of the experiments developed to reintroduce the homonuclear dipolar interaction under MAS conditions was presented in an earlier section. From the ^{19}F results presented in Chapter 5, which showed only a 'single' peak in the MAS spectra of the 1,10-difluorodecane/urea inclusion compound, it is obvious that those experiments which rely on the existence of a chemical shift difference between the two coupled spins cannot be used in this case. Therefore the type of experiment that is required, where the chemical shifts of the two dipolar coupled spins are indistinguishable, is one based on the DRAMA[40] sequence. However, due to the known sensitivity of this particular experiment to pulse imperfections and offset effects, the sequence actually used was dipolar recoupling via rotor synchronised spin locking (MELODRAMA).[47] Although this sequence also suffers from some drawbacks, experiments have been performed to investigate its limitations.

7.3.3.1 MELODRAMA[47] experiments performed on the 1,10-difluorodecane/urea inclusion compound

The MELODRAMA pulse sequence is shown in Figure 7.18. First, a π/2 pulse with a phase of ±x is applied to ^1H in order to create transverse magnetisation. However, due to the extreme sensitivity of the signal obtained to the matching condition, the ramped cross-polarisation sequence was used. A π/2 pulse is then applied to ^{19}F to rotate the magnetisation such that it is parallel to the z axis. Then the MELODRAMA sequence is applied during a 'mixing time', in which the homonuclear dipolar interaction is recoupled. Another π/2 pulse is then applied to ^{19}F

to rotate the magnetisation into the transverse plane where the spins are then allowed to evolve under their chemical shifts. The mixing time is incremented via a loop counter parameter, denoted n in Figure 7.18, such that the signal obtained during t_2 is modulated by the evolution of the spins under the homonuclear dipolar interaction. The MELODRAMA sequence consists of MLEV[68] supercycles with a duration of four rotor periods. One basic cycle, R (expanded in Figure 7.18), consists of eight pulses. In order for the homonuclear dipolar interaction to be recoupled, $\gamma B_1/2\pi$ of the rf field during the mixing time must be a multiple (N) of the MAS rate and for the version shown in Figure 7.18, N must also be even. MELODRAMA recouples the homonuclear dipolar interaction, as, when viewed in the toggling frame, the modulation imposed by MAS on the spatial term in the Hamiltonian interferes with the modulation imposed by the rf field on the spin term in the Hamiltonian. The effect of the chemical shift term is removed at this condition to a zero-order approximation, and the eight-pulse version also compensates to some extent for B_1 field inhomogeneities.
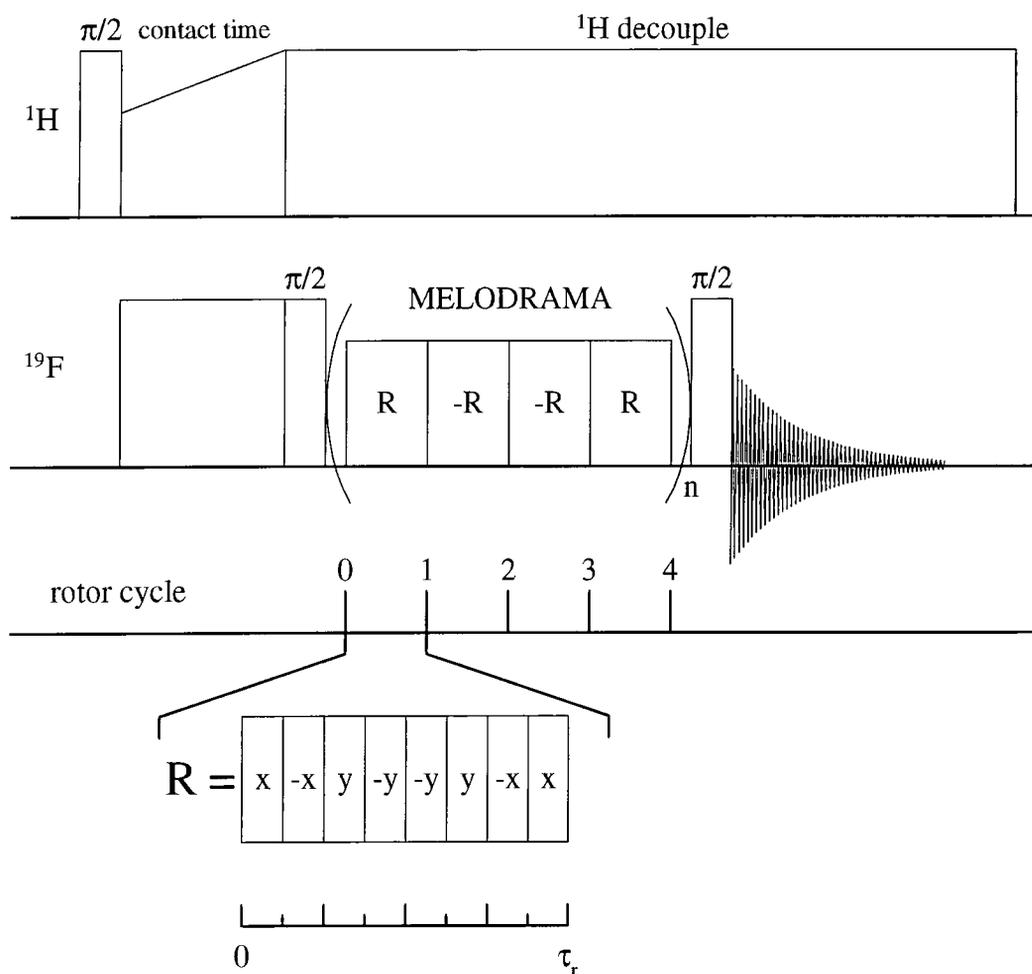
Figure 7.18. MELODRAMA pulse sequence. The expansion of 'R' (denotes a basic cycle) gives the phases of the MELODRAMA pulses and τ_r denotes a rotor period.

Before using MELODRAMA to obtain dipolar coupling constants, experiments were performed in which the limitations of the sequence were tested. The compound used to test the sequence was the actual sample of interest, i.e., the 1,10-difluorodecane/urea inclusion compound. The reason for this choice was that the dipolar coupling constant is known from the static experiments. Furthermore, the ^{19}F MAS spectra contain only one peak so that off-resonance effects can be ignored. As the MELODRAMA experiment relies upon the appropriate matching of the rf field with the MAS rate to achieve recoupling of the dipolar interaction, experiments were performed in which the precision with which this condition needs to be set was explored. In this particular set of experiments, the transmitter was set on resonance so that offset effects can be neglected. For the MELODRAMA experiments, the CE

amplifier in class A/B mode was used for ^{1}H and the Bruker amplifier was used for ^{19}F. The Bruker amplifier was used rather than the AMT amplifier for ^{19}F primarily because the former performs better than the latter for multiple-pulse sequences. To set the MELODRAMA pulse durations, the x and xx CRAMPS tune-up sequences were performed on C_6F_6. Had the AMT been used, in order to set accurate pulse durations using this method, significant changes would have been required to the tune-up pulse sequences as a result of the noise produced by this amplifier in the rest state. This would have involved inserting blanking during the acquisition of a point, which would have to be carefully timed in order to avoid distorting the pulse and/or 'missing' the acquisition point. Another limitation with the AMT amplifier is that the maximum pulse duration is 20 ms and hence the sum of the contact time, 2×90° pulses and the MELODRAMA mixing time cannot exceed this value. However, there is no software control with the Bruker amplifier, and so the ^{19}F CP power and the 2×90° pulses must have the same B_1 field as that used for the MELODRAMA pulses. In the ramped CP experiments discussed in Chapter 3, the ramp was applied on the observe channel, but in this case, due to the lack of software control on the observe channel, the ramp was applied on the ^{1}H channel. However, the performance of the ramped CP experiment is unaffected by the choice of channel for the application of the ramp.[69]

To explore the dependency of the recoupling efficiency upon N, it is possible to vary the MAS rate or the B_1 field. In this case, the MAS rate was varied as it is significantly quicker and easier to change than the B_1 field. Because of the minimum power that can be delivered by the Bruker amplifier and the maximum attainable MAS rates, a matching condition with N equal to 4 was chosen. At the N = 4 matching condition, the spectral parameters used were: ^{1}H $\pi/2$ pulse duration, 3.0 μs; ^{19}F $\pi/2$ pulse duration, 7.4 μs; contact time, 2.0 ms; MAS rate, 8.446 kHz; recycle delay, 5 s, number of transients, 4. It is important to emphasise the necessity for a mismatch in the ^{1}H and ^{19}F powers (~ 100 kHz and 33.784 kHz respectively) during the mixing time to prevent cross polarisation from occurring. The mixing time was varied via a loop counter in the pulse program which has a value equal to the total number of pulses in the mixing time. The initial loop counter parameter, and hence the number of pulses in the first slice of the MELODRAMA experiment, was 8 and

for subsequent slices this value was incremented by the number of pulses in R, i.e. 8, typically up to a value of 320 for the 'test' experiments. Due to the requirement for the duration of R to be equal to one rotor period, this meant that the total time of one MELODRAMA pulse train was 14.8 µs when N = 4. As the MAS rate was altered to vary the value of N from 3.50 to 4.50, the duration, but not the power, of a MELODRAMA pulse was adjusted accordingly. Hence, by this procedure it is possible to see how far B_1 can be mismatched with respect to the MAS rate, before the dipolar recoupling efficiency is significantly affected.
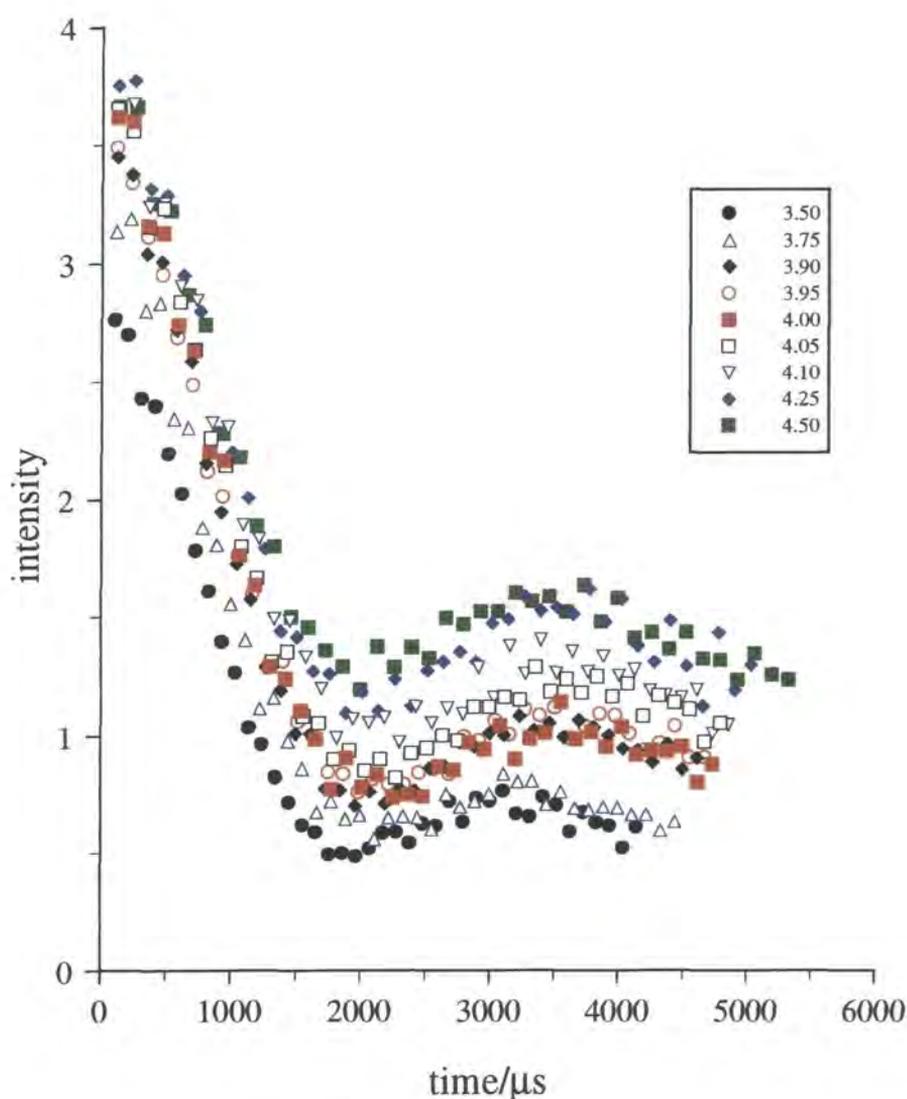
Figure 7.19. Graph plotting variation in signal intensity as a function of time for different N values.

It is clear from Figure 7.19 that when the N = 4 matching condition is mismatched by more than ± 0.1, the signal obtained significantly deviates from that obtained at the exact match. However, at ± 0.05 from N = 4, the signal obtained is comparable. In order to see how these results affect the precision with which the matching condition must be set, it is necessary to consider the pulse durations which correspond to N = 3.95 and N = 4.05. The corresponding pulse durations are 7.3 µs and 7.5 µs, respectively, which means that it must be possible to set the pulse duration to within ± 0.1 µs of the desired value, 7.4 µs in this case. The MELODRAMA pulse duration is set using the CRAMPS tune-up sequences and hence the effect of mis-setting the pulse duration by as little as 0.01 µs is detectable. However, the sample used for the tune up is C_6F_6 (in a glass insert) and so the tip angle achieved with a pulse of a given duration may differ when the actual sample is used. On the other hand, considering the fact that a similar set-up is used for CRAMPS experiments and reasonable resolution is still achieved, it is possible to set pulse durations with an accuracy greater than ± 0.1 µs. Hence, with the experimental set-up employed, the possibility of a mismatch existing between the MAS rate and B_1 which significantly affects the results, can be discounted.

Experiments were then performed at the N = 4 condition, with the transmitter positioned at offsets from +3.0 kHz to -3.0 kHz, with respect to the signal frequency. The spectral conditions used were the same as those described for the previous experiment. Figure 7.20 shows the signal intensity obtained as a function of time with different transmitter offsets. It is immediately clear that even at relatively small offsets, i.e. 0.5 kHz, the signal intensity is significantly affected. This can be interpreted in terms of a reduction in recoupling efficiency at off-resonance conditions, i.e. the signal decays slower. Therefore, to be able to obtain a reasonable estimate of the homonuclear dipolar coupling constant, it is vital that the transmitter is positioned on resonance. However, the reason as to why the signal decays faster with an offset of -0.5 kHz, than when the transmitter is positioned 'on resonance', is not clear.
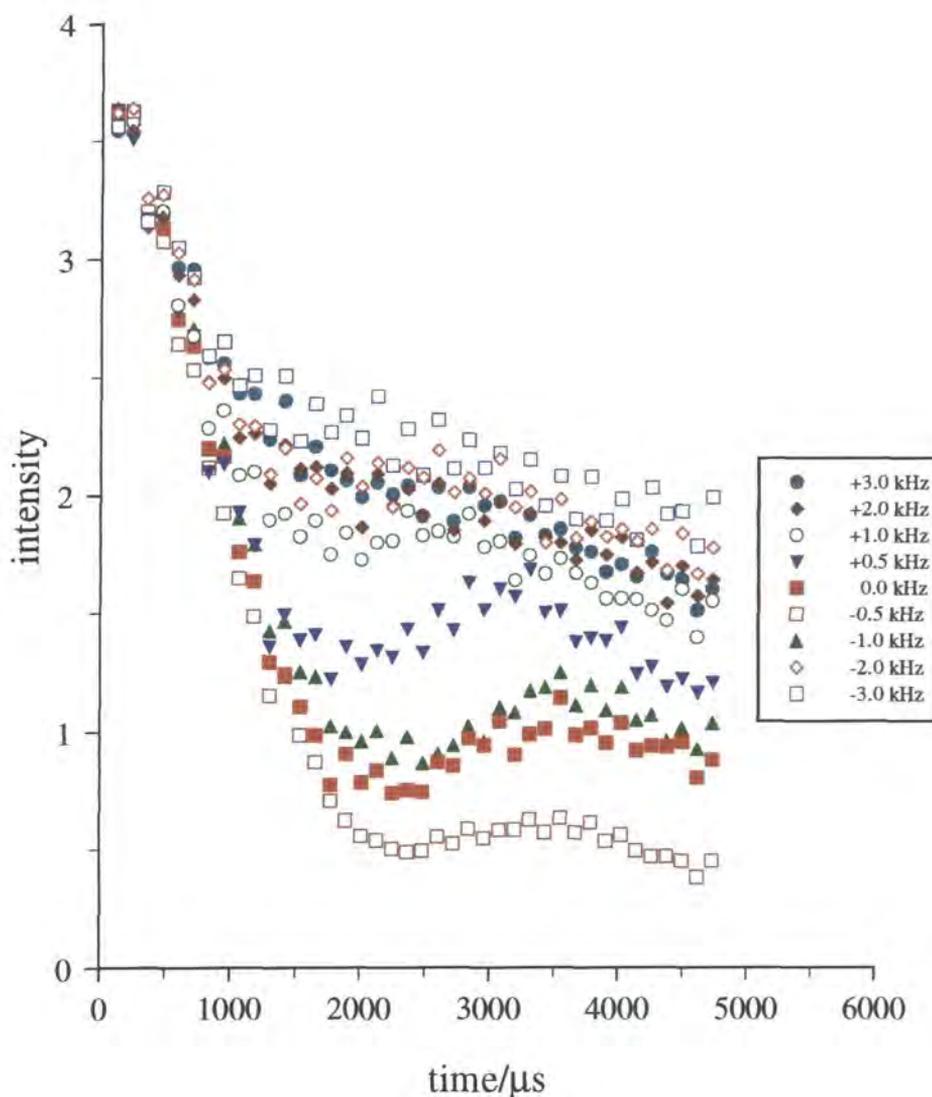
Figure 7.20. Variation in signal intensity as a function of time at different offsets.

A ^{19}F MELODRAMA experiment was then performed on the 1,10-difluorodecane/urea inclusion compound at the N = 4 matching condition. The same spectral conditions were used as before, except that 48 transients were acquired per slice and the number of slices obtained was 192. The initial slice was acquired with 8 MELODRAMA pulses and in subsequent slices the number of pulses was incremented by 8. The t_2 dimension was first Fourier transformed, with the signal intensity as a function of mixing time (Figure 7.21), obtained by integration of each slice using the 'create xy' option in the integration panel of Spinsight. It is of course possible to Fourier transform t_1, after replacing the imaginary part of the data with

zeros (see Chapter 3), to yield a homonuclear dipolar powder pattern in F_1 (Figure 7.22). However, analysis of data is often easier to perform on the FID rather than the spectrum and so discussion will evolve around Figure 7.21.
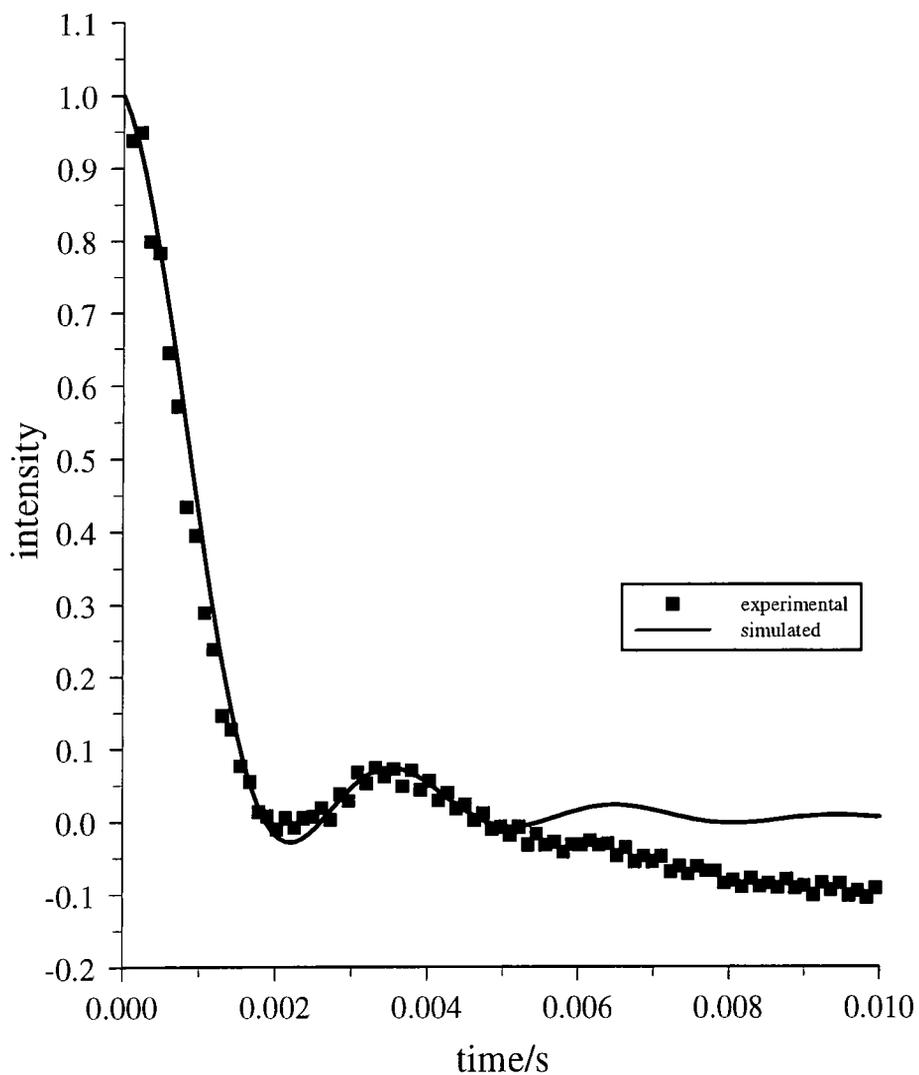
Figure 7.21. Graph plotting ^{19}F signal intensity against MELODRAMA time for the 1,10-difluorodecane/urea inclusion compound at N = 4.
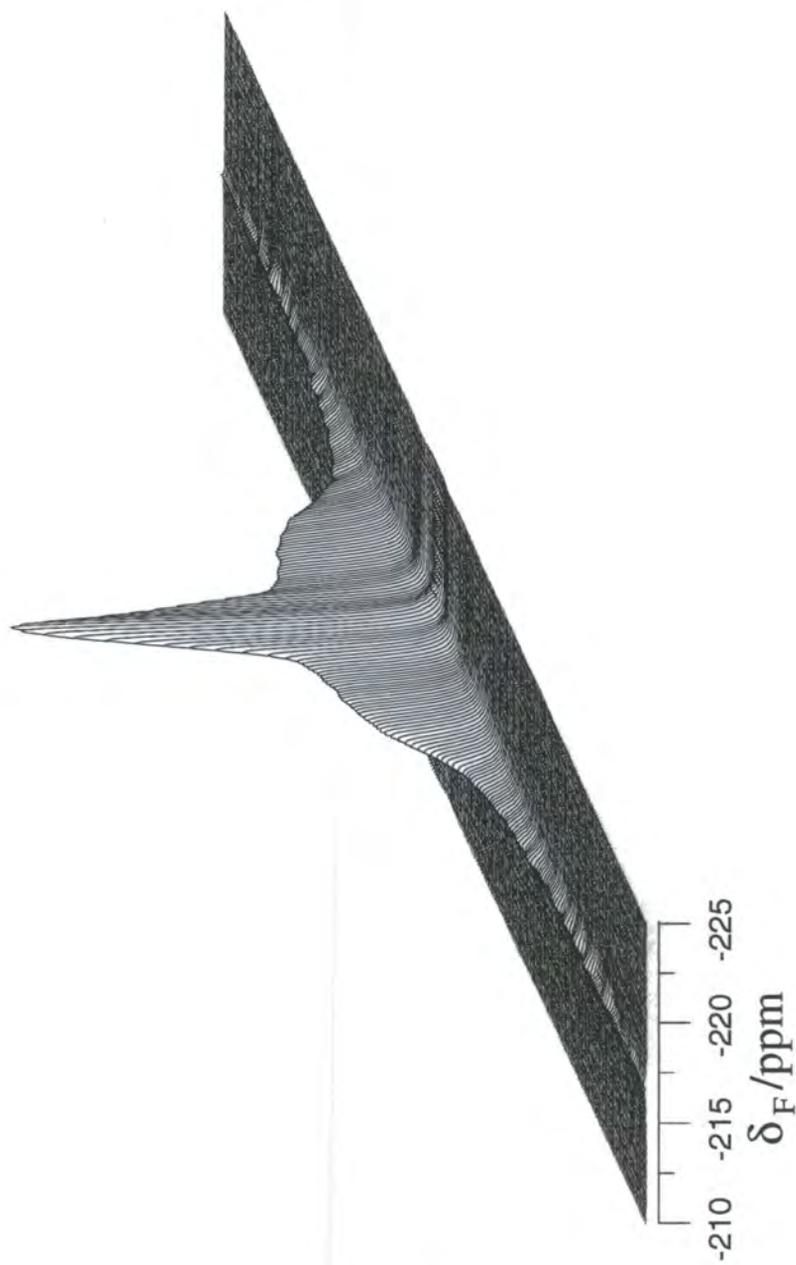
Figure 7.22. Fluorine-19 MELODRAMA (F_1, F_2) spectrum of the 1,10-difluorodecane/urea inclusion compound.

The simulated curve can be given by,

$$\langle I_z + S_z \rangle(t) = \frac{1}{4\pi^2} \int\limits_0^\pi \sin(\beta)d\beta \int\limits_0^{2\pi} d\gamma \cos[D_N(\beta,\gamma)t]$$ *Equation 7.29*

which describes the evolution of magnetisation under the MELODRAMA sequence as a function of time, t, and the angles β and γ which describe the orientations of the internuclear vectors in a powder with respect to the rotor frame of reference. The dipolar coupling at a matching condition of N, D_N, for a particular orientation of the internuclear vector is given by,

$$D_N = \frac{6\omega_D N^2}{\sqrt{2}\pi(4N^2 - 1)} \sin(2\beta)\cos(\gamma)$$ *Equation 7.30*

where ω_D, the dipolar coupling constant in angular frequency units is given by,

$$\omega_D = \frac{\gamma_I \gamma_S \hbar^2}{r_{IS}^3}$$ *Equation 7.31*

The derivation of Equation 7.29, using the average Hamiltonian approximation, can be found in the literature.[47] The actual simulated curve was created with a computer program, written in C (see Appendix), using the equations above. Subsequently, the experimental and simulated data were input into a Mathcad sheet, in which it was possible to compare the two 'by eye' to obtain a value for the homonuclear dipolar coupling constant. It was not possible to 'fit' the entire experimental curve to the simulated one, although, as can be seen from Figure 7.21, a reasonable 'fit' can be obtained for mixing times up to ~ 5.0 ms. The value obtained for the ^{19}F-^{19}F dipolar coupling constant was 995 Hz which is in reasonable agreement with that obtained from the static experiments.

It is known that the recoupling efficiency of the MELODRAMA sequence is dependent upon the orientation of the dipolar vector with respect to the rotor.[47,51] However, it has been suggested that by performing the experiment using two different versions of the MELODRAMA sequence,[47] one which recouples components modulated at the MAS rate and the other which recouples components modulated at twice the MAS rate, the overall recoupling efficiency will be improved. It has also been demonstrated that the MELODRAMA sequence is still sensitive to

chemical shift and offset effects.[51] Hence, simulations of the theoretical dependence of the signal intensity as a function of mixing time will tend to deviate, particularly at longer mixing times, from the experimental data. For the simulated and experimental data to fit better, factors such as the orientation dependence of the dipolar recoupling efficiency, offset effects and relaxation rates would have to be taken into account. Alternatively, sequences such as the C7 sequence[51] which are much less dependent upon such effects could be used to obtain data and hence, simulation of the experimental data should be easier and more accurate.

7.4 Intermolecular ^{19}F-^{19}F distance measurements in the fluorocyclohexane thiourea inclusion compound

In the bromocyclohexane,[4] chlorocyclohexane[8] and trans-1-bromo-2-chlorocyclohexane[4] thiourea inclusion compounds, it has been possible to detect internuclear distances (at ~ 80 K) between the halogen substituents. Although with the equipment available, it is only feasible to perform experiments at a minimum temperature of ~130 K, the possible existence of a ^{19}F-^{19}F homonuclear dipolar interaction has been investigated for the fluorocyclohexane/thiourea inclusion compound.

7.4.1 Static ^{19}F experiments

First a number of static ^{19}F experiments were performed, with ^1H decoupling, at temperatures ranging from 297 K to 133 K (Figure 7.23). It is worth pointing out that the temperatures quoted in this section have not been calibrated as, for the method used (see Chapter 2), MAS is required. As can be seen from Figure 7.23, at temperatures ranging from 297 K to 233 K, the behaviour of the relatively narrow, Gaussian lineshapes is comparable to the spectra obtained using MAS (Chapter 6), in that they show one signal, coalescence and then two signals. Such lineshapes arise as a result of the averaging of SA and ^{19}F-^{19}F dipolar interactions due to the significant motion of the guest molecules. However, at 173 K, the linewidth for the axial

fluorine (-187.0 ppm) is significantly broader than that of the equatorial fluorine (-163.9 ppm). In such spectra, ^{19}F SA and ^{19}F-^{19}F homonuclear dipolar interactions may be present and hence either or both could affect the linewidths and lineshapes obtained. However, on lowering the temperature to 133 K, both peaks exhibit dramatic broadening and a change in lineshape is observed.
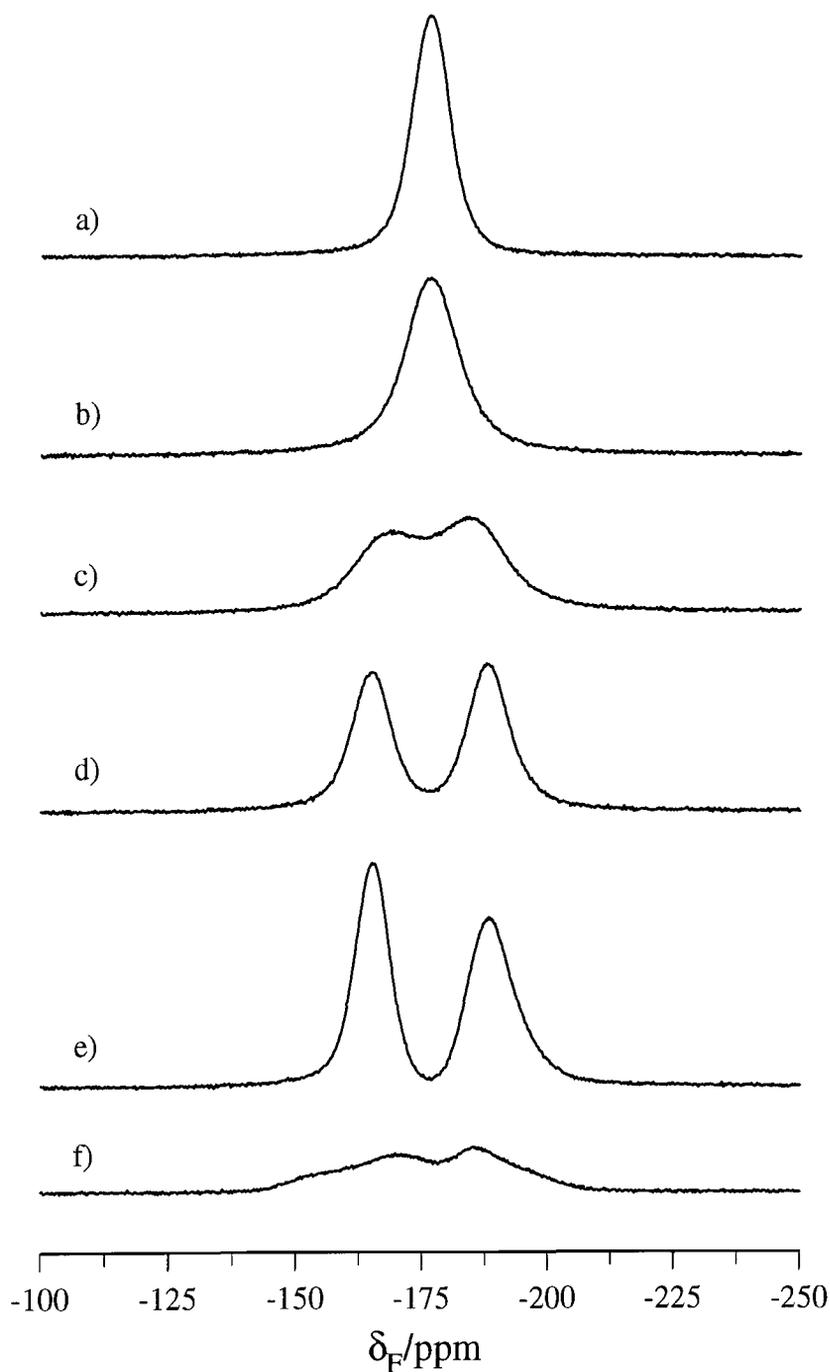
Figure 7.23. Fluorine-19 static spectra of fluorocyclohexane/thiourea at a) 297 K, b) 273 K, c) 253 K, d) 233 K, e) 173 K and f) 133 K.

It is known that cyclohexane/thiourea inclusion compounds can undergo a phase change in the 129-149 K range. This particular fact may account for the dramatic broadening in the static spectrum on going from 173 K to 133 K. To complement the static ^{19}F spectrum obtained at 133 K (Figure 7.23f), a spectrum was obtained with a MAS rate of 1.75 kHz. The static and MAS spectra are shown in Figure 7.24, and it can clearly be seen that the overall static lineshape is approximately mirrored by the spinning sideband intensities in the MAS spectrum.
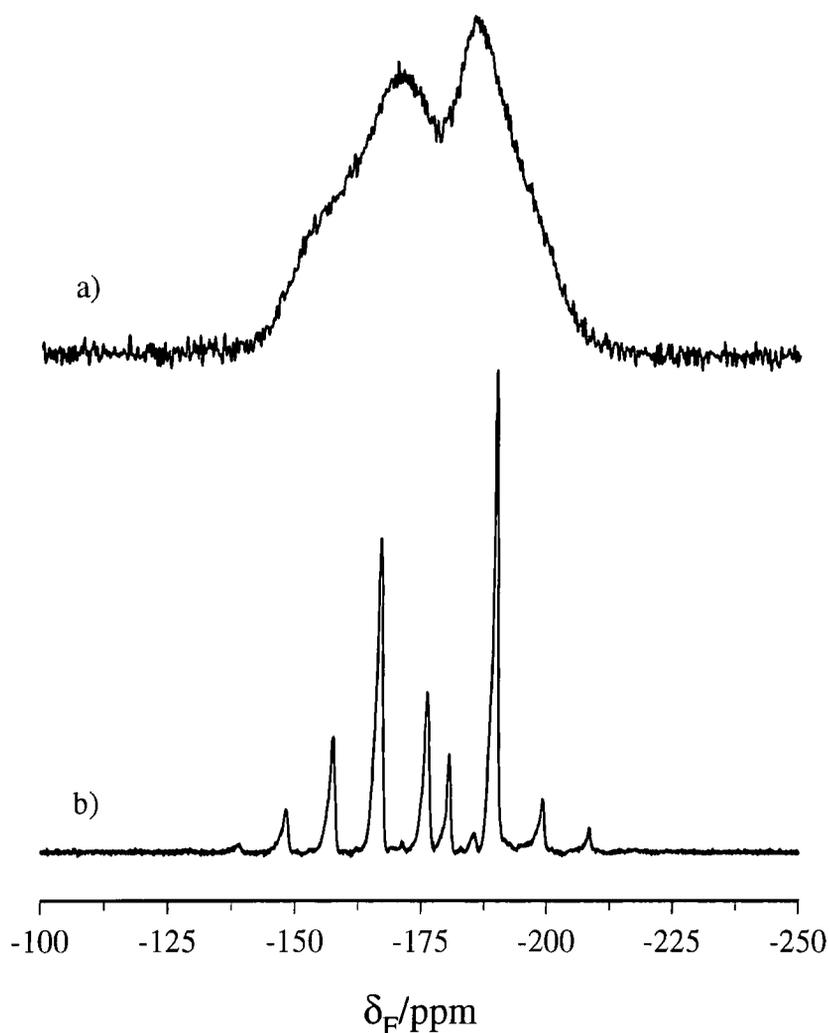
Figure 7.24. Fluorine-19 spectra, acquired with ^{1}H decoupling, of the fluorocyclohexane/thiourea inclusion compound at 133 K under a) static conditions and b) MAS at 1.75 kHz.

Previous distance measurements obtained for similar compounds[4,8] would translate to a dipolar coupling constant of the order of 1 kHz if a similar internuclear distance

(~4.6 Å) exists in the fluorocyclohexane/thiourea inclusion compound. However, it is worth pointing out that the internuclear distances measured in other halogen-substituted cyclohexane/thiourea inclusion compounds have been for axial-axial conformations. Clearly, from the results presented in Chapter 6, in the fluorocyclohexane/thiourea inclusion compound it is also possible that equatorial-equatorial and axial-equatorial conformations could exist. However, with a MAS rate of 1.75 kHz, it has been assumed that this spin rate is sufficient to average any homonuclear dipolar coupling between fluorines and so only the ^{19}F SA is present in Figure 7.24b. A spinning sideband analysis was then performed, using a program based on the method of Herzfeld and Berger,[70,71] in order to obtain the principal components of the axial and equatorial shielding tensors.

Fluorine	σ_{xx}/ppm	σ_{yy}/ppm	σ_{zz}/ppm	σ_{iso}/ppm	$\Delta\sigma$/ppm	η
axial	175.7	185.1	200.2	187.0	19.8	0.71
equatorial	180.0	167.3	144.4	163.9	-29.3	0.65

Table 7.3. Shielding parameters for the axial and equatorial fluorines in the fluorocyclohexane/thiourea inclusion compound. All parameters are quoted relative to $CFCl_3$ (0 ppm).

The most noticeable feature in Table 7.3 is that the shielding anisotropy ($\Delta\sigma$) for the equatorial ^{19}F is bigger than and also of the opposite sign to that observed for the axial ^{19}F. Hence, it can be deduced that, unlike the fluoroalkane/urea inclusion compounds, there is not motional averaging of the SA about the tunnel axis. A possible reason for this could be the cage-like structure of the thiourea, which allows for more general reorientation of guest molecules than in the case of the urea tunnels where the guest motion is anisotropic. These results also mean that if there is a ^{19}F-^{19}F dipolar interaction between two axial fluorines or two equatorial fluorines, the internuclear vector will not be coincident with σ_{zz} and so two angles (denoted χ and $\omega_r t$ in Figure 7.16) are needed to describe the orientation of this vector with respect to the shielding PAS. If there exists a dipolar interaction between an axial and an equatorial ^{19}F, it would also be necessary to determine the orientation of the shielding PAS for an axial ^{19}F with respect to that for an equatorial ^{19}F as well as the

relative orientation of the dipolar vector. Hence, it can be seen that on moving from a system in which the shielding PAS of one nucleus is coincident with that of the other and the internuclear vector is oriented parallel to the σ_{zz} axis, the simulation of static SA/dipolar spectra quickly becomes far from trivial. In fact, more often that not it is impossible, other than in the most simple case, to obtain a unique orientation of the dipolar vector with respect to the shielding PAS.[72,73]
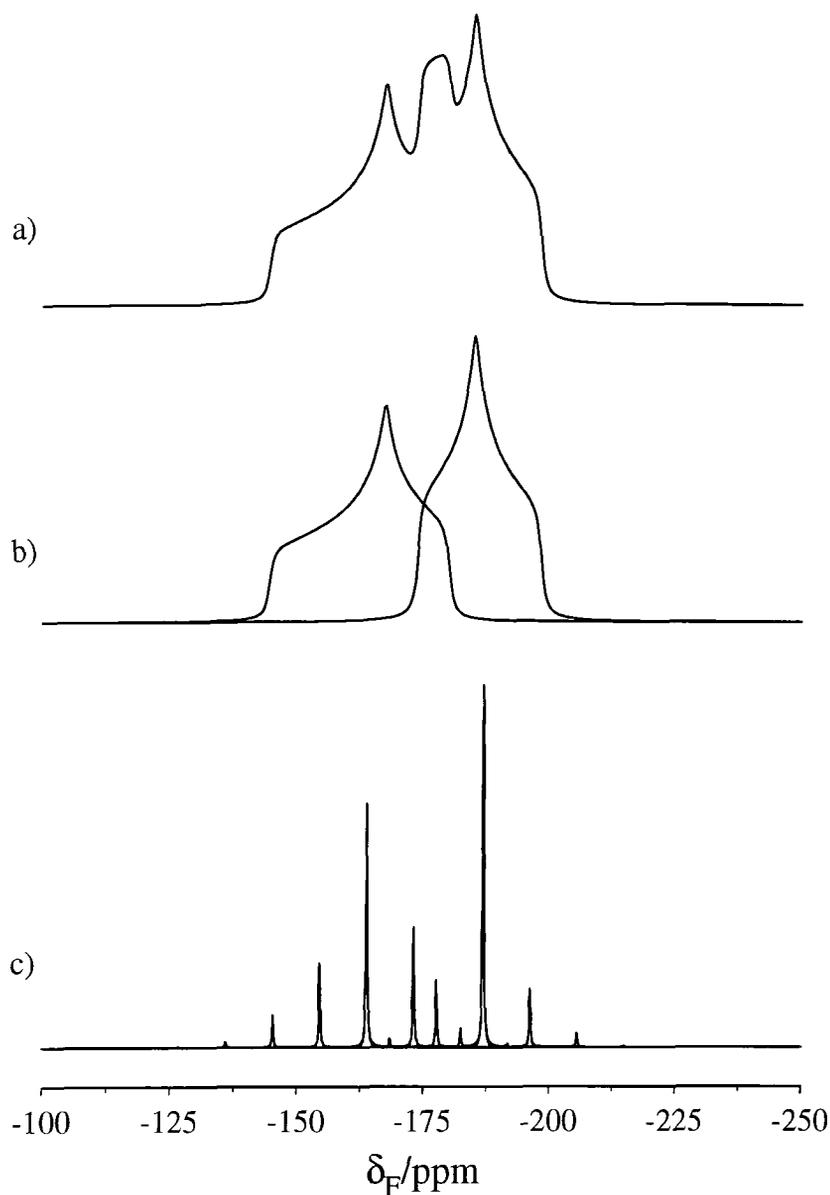
Figure 7.25. Simulation of ^{19}F static and MAS spectra for fluorines in axial and equatorial sites, with a) showing the sum of the two powder patterns b) showing their individual powder patterns and, c) is the MAS spectrum, at 1.75 kHz.

Using the shielding parameters obtained from Figure 7.24b, both static (using GAMMA - see Appendix) and MAS simulations[74] were performed, assuming that there is no dipolar interaction present and that exchange between the two sites is negligible (Figure 7.25). Figure 7.25a shows the sum of the static SA powder patterns for the axial and equatorial fluorines. Although the general overall shape is comparable to that obtained experimentally, there is an extra 'central' peak in between the two σ_{yy} components in the simulated spectrum. This suggests that there is some homonuclear dipolar contribution to Figure 7.24a, but due to the complexities outlined in the previous paragraph, it is not easy to include the effects from the possible existence of a homonuclear dipolar interaction. Hence, in order to be able to extract distance information from Figure 7.24, it would be necessary to perform a series of experiments, as for the 1,10-difluorodecane/urea inclusion compound, in which specific interactions can be systematically removed. Unfortunately, due to time restrictions and problems with the operation of the probe at temperatures in the region required, ~133 K, it has not been possible to perform such experiments.

7.4.2 Rotational resonance (R^2)

For homonuclear dipolar coupled spins with different chemical shifts, it is possible to use the rotational resonance[17,34,35] experiment to obtain a dipolar coupling constant. The homonuclear dipolar interaction for an isolated spin pair with different chemical shifts is given only by term A, i.e., $\hat{I}_{1z}\hat{I}_{2z}$, in Equation 7.4 as the difference in chemical shift of the two spins truncates the flip-flop term (term B). Hence, transitions between the $\alpha\beta$ and $\beta\alpha$ states are inefficient as the chemical shift difference renders the two energy levels non-degenerate. However, in the rotor frame of reference, when the MAS rate is a multiple of the energy difference between the two spins, transitions (flip-flop) between the two energy levels can then occur. Hence, at the so-called rotational resonance condition, the homonuclear dipolar interaction is reintroduced. The rotational resonance experiment has been used to obtain dipolar coupling constants in ^{13}C and ^{15}N doubly-labelled samples such as

zinc acetate[34] and a diazonium cation,[75] respectively. In such cases, prominent splittings were observed in the peaks at rotational resonance and it was then possible to simulate such lineshapes from knowledge of the principal components and relative orientations of the relevant tensors. Rotational resonance has also been observed between two dipolar-coupled ^{19}F spins,[76] although a broadening of the lines was only observed as opposed to a splitting and so a distance measurement could not be extracted from such data. Usually, due to the complexity of the information contained within the lineshape and the subsequent difficulties in extracting the desired information, the rotational resonance spin-exchange experiment[34] is preferred.

From the ^{19}F spectra obtained of the fluorocyclohexane/thiourea inclusion compound at 133 K, it appears that the static spectrum 'contains' a homonuclear dipolar contribution. However, as previously mentioned, the conformation of the fluorines in such an interaction is unknown. A homonuclear dipolar interaction may exist between one or more of the following possible conformational combinations; $^{19}F(ax)$-$^{19}F(ax)$, $^{19}F(eq)$-$^{19}F(eq)$ and $^{19}F(eq)$-$^{19}F(ax)$. In previous studies of bromocyclohexane,[4] chlorocyclohexane[8] and trans-1-bromo-2-chlorocylohexane[4] thiourea inclusion compounds, there was a well-defined head-to-head ordering of the guest molecules. However, the axial conformation is preferred in all three of these cases and hence, the issue of interactions between substituents oriented axial and equatorial did not need to be considered. In the fluorocyclohexane case, as the populations of the two conformations are approximately equal at 133 K, then one might expect either a random distribution of dipolar interactions between different conformers or there may be a preference for a dipolar interaction between particular conformers. Due to the lack of knowledge concerning the orientation of the $^{19}F(eq)$ shielding PAS with respect to that of $^{19}F(ax)$, and then the subsequent necessity to determine the relative orientation of the internuclear vector, the rotational resonance experiment was used to selectively probe for $^{19}F(eq)$-$^{19}F(ax)$ dipolar interactions. Although such information is also required if a value for the dipolar coupling constant is to be determined, at this stage the purpose of the rotational resonance experiment was just to assess the possible existence of a dipolar interaction.

The spectral conditions used were: ^{19}F $\pi/2$ pulse duration, 3.0 μs; recycle delay, 60 s; ^{1}H decoupling power ~ 100 kHz; acquisition time, 41.0 ms; number of

transients, 4. Due to problems with the operation of the probe at lower temperatures, all the experiments were performed at a temperature of 173 K. The fact that the rotational resonance experiments were performed at a higher temperature than the static spectra may mean that the two sets of results are not directly comparable. Experiments were performed at three different MAS rates, 5.50 kHz, 4.35 kHz and 3.00 kHz (Figure 7.26). With a MAS rate of 4.35 kHz, the ^{19}F spectrum obtained is broader than that obtained at the lower and higher MAS rates. Although one might expect linewidths to increase with lower MAS rates, it is clear from the spectrum obtained at 3.00 kHz, that this is not applicable here. The reason for this must be that the MAS rate of 4.35 kHz is equal to the chemical shift difference between the axial and equatorial fluorines. Hence, due to the existence of a $^{19}F(eq)$-$^{19}F(ax)$ dipolar interaction, at the rotational resonance condition, i.e. when the MAS rate is 4.35 kHz, such an interaction is reintroduced, which results in spectral broadening.
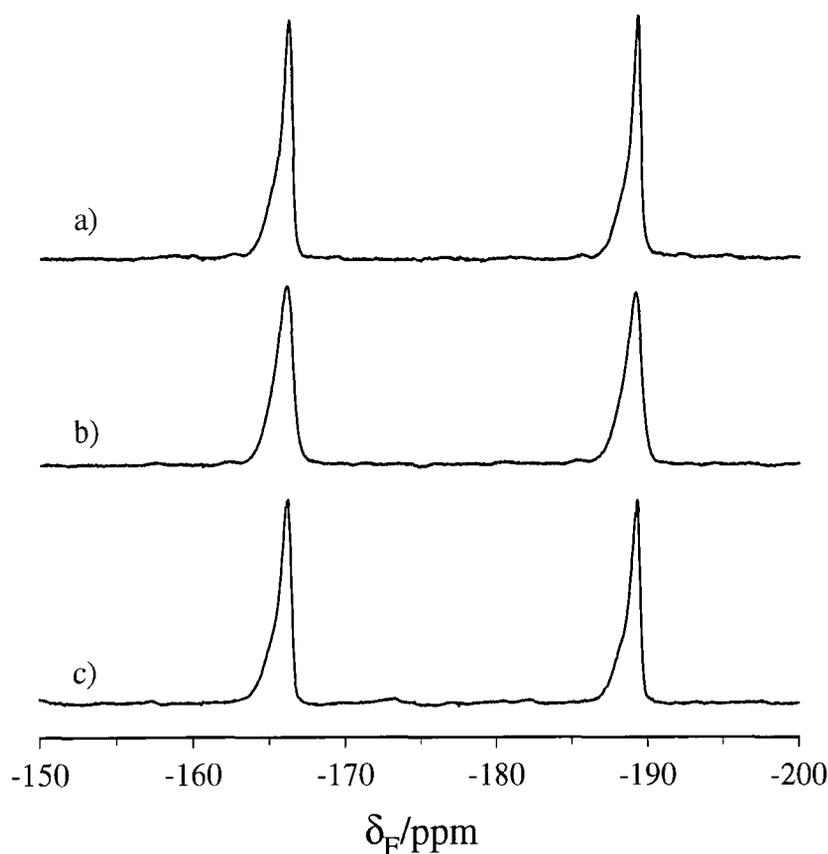
Figure 7.26. Fluorine-19 spectra of the fluorocyclohexane/thiourea inclusion compound acquired at 173 K with a MAS rate of a) 5.50 kHz, b) 4.35 kHz and c) 3.00 kHz.

The linewidths (fwhh) of the ^{19}F peaks at the three MAS rates used are given in Table 7.4. Unfortunately, it is not possible to obtain a dipolar coupling constant from such a spectrum, although this experiment has, at the very least, proved the existence of dipolar interactions between axial and equatorial fluorines.

MAS rate/kHz	linewidth (fwhh)/Hz	
	axial ^{19}F	equatorial ^{19}F
5.50	135	152
4.35	223	239
3.00	143	164

Table 7.4. ^{19}F linewidth as a function of MAS at 173 K.

7.5 Conclusions

The high sensitivity of ^{19}F NMR enabled good signal-to-noise static spectra to be acquired in a relatively short period of time. An intermolecular ^{19}F-^{19}F distance has been determined between two difluoroalkane molecules included within urea tunnels. This was obtained from a series of static experiments in which specific interactions were either selectively removed or observed. Due to the rapid motion of the fluoroalkane molecules about the urea tunnel axis, the effective internuclear vector was found to be aligned parallel to the tunnel. Corroboration of this was obtained from single-crystal experiments, which were also used to obtain an effective dipolar coupling constant. Single-pulse and CPMG experiments, acquired with ^{1}H decoupling, were performed on powder samples, which gave dipolar/SA and dipolar powder patterns, respectively. It was then possible to extract the dipolar coupling constant from such spectra, with the value obtained from each, and that from the single-crystal experiment, in excellent agreement. Static experiments were also performed on the 1-fluorotetradecane/urea inclusion compound, in which it was possible to see both the dipolar coupled and isolated ^{19}F sites. From consideration of all possible conformations for two adjacent CH_2F end-groups, it was concluded that such end-groups prefer to be oriented gauche/gauche and gauche/trans. Hence, it was

then possible to obtain ^{19}F-^{19}F distances for two adjacent guest molecules confined within urea tunnels, in the absence of rapid motion. A ^{19}F MELODRAMA experiment was also performed to measure the ^{19}F-^{19}F dipolar coupling constant. Although the result obtained was in reasonable agreement with the value from the static experiments, the experiment in its present form has limited application in systems with more than one ^{19}F chemical shift, due to its extreme sensitivity to resonance offset effects.

The fluorocyclohexane/thiourea inclusion compound has also been examined. It was deduced from low-temperature static and MAS ^{19}F experiments, that motional averaging of the dipolar interaction about the tunnel axis does not occur in such systems. This is in marked contrast with the urea inclusion compounds, which presumably can be attributed to the cage-like structure present in thiourea that allows more general (as opposed to rotation about the tunnel axis) reorientation of the guest molecules. Hence, it is in fact much more difficult to extract information from the static spectra acquired, although from comparison with a MAS spectrum it was possible to detect the existence of an intermolecular ^{19}F-^{19}F distance. However, because fluorocyclohexane is present as both the axial and equatorial conformations at low temperatures, it is not known whether there are dipolar interactions between conformations only of the same type or between both. It was possible to detect the existence of a ^{19}F-^{19}F dipolar interaction between axial and equatorial conformations in a rotational resonance experiment.

It has been clearly demonstrated by the work presented in this chapter, that ^{19}F NMR can be an extremely powerful tool in the elucidation of solid-state structures. This statement is particularly true for systems which exhibit dynamic and/or static disorder, as is the case for the fluorocyclohexane/thiourea and fluoroalkane/urea inclusion compounds. Although attempts have been made to obtain distance measurements in the bromoalkane/urea inclusion compounds,[2] this is the first time that a direct measurement of the distance between atoms in adjacent guest molecules in an incommensurate urea inclusion compound has been reported.

7.6 References

1. M.D. Hollingsworth and K.D.M. Harris, *Comprehensive Supramolecular Chemistry*, ed. D.D. MacNicol, F. Toda and R. Bishop, Pergamon, 1996, vol. 6, p. 177.

2. K.D.M. Harris, *J. Mol. Struct.*, 1996, **374**, 241.

3. A.E. Aliev and K.D.M. Harris, *J. Am. Chem. Soc.*, 1993, **115**, 6369.

4. I.J. Shannon, M. J. Jones, K.D.M. Harris, M.R.H. Siddiqui and R.W. Joyner, *J. Chem. Soc., Faraday Trans.*, 1995, **91**, 1497.

5. M.S. McKinnon and R.E. Wasylishen, *Chem. Phys. Lett.*, 1986, **130**, 565.

6. K. Müller, *Magn. Reson. Chem.*, 1992, **30**, 228.

7. K. Müller, *Magn. Reson. Chem.*, 1995, **33**, 113.

8. M.J. Jones, I.J. Shannon and K.D.M. Harris, *J. Chem. Soc., Faraday Trans.*, 1996, **92**, 273.

9. A.R. George and K.D.M. Harris, *J. Mater. Chem.*, 1994, **4**, 1731.

10. S.P. Smart, A. El Baghdadi, F. Guillaume and K.D.M. Harris, *J. Chem. Soc., Faraday Trans.*, 1994, **90**, 1313.

11. F. Imashiro, D. Kuwahara, T. Nakai and T. Terao, *J. Chem. Phys.*, 1989, **90**, 3356.

12. G.M. Cannarozzi, G.H. Meresi, R.L. Vold and R.R. Vold, *J. Phys. Chem.*, 1991, **95**, 1525.

13. A. El Baghdadi, E.J. Dufourc and F. Guillaume, *J. Phys. Chem.*, 1996, **100**, 1746.

14. A. Kubo, F. Imashiro and T. Terao, *J. Phys. Chem.*, 1996, **100**, 10854.

15. J.M. Griffiths and R.G. Griffin, *Anal. Chim. Acta*, 1993, **283**, 1081.

16. W.P. Power and R.E. Wasylishen, *Annual Reports NMR Spectroscopy*, 1991, **23**, 1.

17. J.R. Garbow and T. Gullion, *Carbon-13 NMR Spectroscopy of Biological Systems*, (Editor: N. Beckmann), Academic Press, London, 1995, Chapter 3.

18. J.M. Griffiths, A.E. Bennett and R.G. Griffin, 'Homonuclear Recoupling Schemes in MAS NMR', *Encylopedia of NMR*, (Editors: D.M. Grant and R.K. Harris), Wiley, London, 1996, **4**, 2390.

19. S.A. Carss, U. Scheler, R.K. Harris, P. Holstein and R.A. Fletton, *Magn. Reson. Chem.*, 1996, **34**, 63.

20. A. Nordon, R.K. Harris, L. Yeo and K.D.M. Harris, *Chem. Commun.*, 1997, 962.

21. S.C. Campbell, R.K. Harris, M.J. Hardy, D.C. Lee and D.J. Busby, *J. Chem. Soc., Perkin Trans. 2*, 1997, 1913.

22. Y. Tomita, K. Monde, K. Nakanishi and A. McDermott, *ENC Poster*, Asilomar, California, USA, March 1996.

23. G.E. Pake, *J. Chem. Phys.*, 1948, **16**, 327.

24. K.W. Zilm and D.M. Grant, *J. Am. Chem. Soc.*, 1981, **103**, 2913.

25. H.Y. Carr and E.M. Purcell, *Phys. Rev.*, 1954, **94**, 630.

26. S. Meiboom and D. Gill, *Rev. Sci. Instrum.*, 1958, **94**, 688.

27. M. Engelsberg and C.S. Yannoni, *J. Magn. Reson.*, 1990, **88**, 393.

28. M.J. Lizak, T. Gullion and M.S. Conradi, *J. Magn. Reson.*, 1991, **91**, 254.

29. T. Gullion, D.B. Baker and M.S. Conradi, *J. Magn. Reson.*, 1990, **89**, 479.

30. R.E. Wasylishen, W.P. Power, G.H. Penner and R.D. Curtis, *Can. J. Chem.*, 1989, **67**, 1219.

31. R.D. Curtis, J.W. Hilborn, G. Wu, M.D. Lumsden, R.E. Wasylishen and J.A. Pincock, *J. Phys. Chem.*, 1993, **97**, 1856.

32. C.G. Hoelger, F. Aguilar-Parrilla, J. Elguero, O. Weintraub, S. Vega and H.H. Limbach, *J. Magn. Reson., A*, 1996, **120**, 46.

33. M.M. Maricq and J.S. Waugh, *J. Chem. Phys.*, 1979, **70**, 3300.

34. D.P. Raleigh, M.H. Levitt and R.G. Griffin, *Chem. Phys. Lett.*, 1988, **146**, 71.

35. M.H. Levitt, D.P. Raleigh, F. Creuzet and R.G. Griffin, *J. Chem. Phys.*, 1990, **92**, 6347.

36. O. Weintraub, S. Vega, Ch. Hoelger and H.H. Limbach, *J. Magn. Reson., A*, 1994, **109**, 14.

37. O. Weintraub, S. Vega, Ch. Hoelger and H.H. Limbach, *J. Magn. Reson., A*, 1994, **110**, 12.

38. A.E. Bennett, J.H. Ok, R.G. Griffina and S. Vega, *J. Chem. Phys.*, 1992, **96**, 8624.

39. D.K. Sodickson, M.H. Levitt, S. Vega and R.G. Griffin, *J. Chem. Phys.*, 1993, **98**, 6742.

40. R. Tycko and G. Dabbagh, *Chem. Phys. Lett.*, 1990, **173**, 461.

41. R. Tycko and S.O. Smith, *J. Chem. Phys.*, 1993, **98**, 932.

42. C.A. Klug, W. Zhu, M.E. Merritt and J. Schaefer, *J. Magn. Reson., A*, 1994, **109**, 134.

43. L.M. McDowell, C.A. Klug, D.D. Beusen and J. Schaefer, *Biochemistry*, 1996, **35**, 5395.

44. C.A. Klug, D.R. Studelska, G. Chen, S.R. Gilbertson and J. Schaefer, *Solid State NMR*, 1996, **7**, 173.

45. R.H.P. Francisco and H. Eckert, *J. Solid State Chem.*, 1994, **112**, 270.

46. R. Tycko and G. Dabbagh, *J. Am. Chem. Soc.*, 1991, **113**, 9444.

47. B.-Q. Sun, P.R. Costa, D. Kocisko, P.T. Lansbury and R.G. Griffin, *J. Chem. Phys.*, 1995, **102**, 702.

48. D.M. Gregory, D.J. Mitchell, J.A. Stringer, S. Kiihne, J.C. Shiels, J. Callahan, M.A. Mehta and G.P. Drobny, *Chem. Phys. Lett.*, 1995, **246**, 654.

49. M.A. Mehta, D.M. Gregory, S. Kiihne, D.J. Mitchell, M.E. Hatcher, J.C. Shiels and G.P. Drobny, *Solid State NMR*, 1996, **7**, 211.

50. N.C. Nielsen, H. Bildsøe, H.J. Jakobsen and M.H. Levitt, *J. Chem. Phys.*, 1994, **101**, 1805.

51. Y.K. Lee, N.D. Kurur, M. Helmle, O.G. Johannessen, N.C. Nielsen and M.H. Levitt, *Chem. Phys. Lett.*, 1995, **242**, 304.

52. H. Geen, J. Gottwald, R. Graf, I. Schnell, H.W. Spiess and J.J. Titman, *J. Magn. Reson.*, 1997, **125**, 224.

53. P.W. Atkins, *Physical Chemistry*, Oxford University Press, 4th edition, 1990.

54. A. Nordon, R.K. Harris, L. Yeo and K.D.M. Harris, *Chem. Commun.*, 1997, 2045.

55. J.G. Powles and J.H. Strange, *Proc. Phys. Soc.*, 1963, **82**, 60.

56. D.P. Burum, D.G. Cory, K.K. Gleason, D. Levy and A. Bielecki, *J. Magn. Reson., A*, 1993, **104**, 347.

57. S.A. Smith, T.O. Levante, B.H. Meier and R.R. Ernst, *J. Magn. Reson., A*, 1994, **106**, 75.

58. R.K. Harris, K.J. Packer and A.M. Thayer, *J. Magn. Reson.*, 1985, **62**, 284.

59. H. Bai and R.K. Harris, *J. Magn. Reson.*, 1992, **96**, 24.

60. R. Freeman, *Spin Choreography: Basic Steps in High Resolution NMR*, Spektrum, Oxford, 1997.

61. E. Hughes, unpublished work.

62. M. Mehring, 'Internal Spin Interactions & Rotations in Solids', *Encylopedia of NMR*, (Editors: D.M. Grant and R.K. Harris), Wiley, London, 1996, **4**, 2585.

63. U. Haeberlen, *High Resolution NMR in Solids*, Academic Press, New York, 1976.

64. M. Mehring, *High Resolution NMR in Solids*, (Editors: P.Diehl, E. Fluck and R. Kosfeld), Springer-Verlag, New York, 1976.

65. A.R. Edmonds, *Angular Momentum in Quantum Mechanics*, Princeton Univ. Press, Princeton, New Jersey, 1957.

66. CAChe, Oxford Molecular Group, Oxford.

67. L. Elizabe, F Guillaume and K.D.M. Harris, personal communication.

68. M.H. Levitt, R. Freeman and T. Frenkiel, *Advances in Magnetic Resonance*, 1983, **11**, Academic Press, New York, 1983.

69. G. Metz, X. Wu and S.O. Smith, *J. Magn. Reson., A*, 1994, **110**, 219.

70. J. Herzfeld and A.E. Berger, *J. Chem. Phys.*, 1980, **73**, 6021.

71. K. Eichele, 'HBA' v1.0, Dalhousie University, Canada, 1996.

72. K. Eichele and R.E. Wasylishen, *J. Magn. Reson., A*, 1994, **106**, 46.

73. P.L. Stewart, K.G. Valentine and S.J. Opella, *J. Magn. Reson.*, 1987, **71**, 45.

74. J.M. Koons, E. Hughes, P.D. Ellis, *Anal. Chim. Acta*, 1993, **283**, 1045.

75. R. Challoner and R.K. Harris, *Chem. Phys. Lett.*, 1994, **228**, 589.

76. S.A. Carss, *Ph.D. Thesis*, University of Durham, 1995.

Appendix

Research conferences attended

NMR of solids and solid-like materials, NMR discussion group meeting, University College, London, 19 December, 1995.

Summer school on NMR of solids, University of Durham, 16-20 September, 1996.

Chemistry research for Britain meeting, The Royal Society, London, 7 February, 1997.

NMR of inclusion and molecular recognition phenomena in solids and liquids, NMR discussion group meeting, University of Birmingham, 15 April, 1997.

Oral presentations

Solid-state NMR studies of inclusion compounds, Final year graduate symposium, University of Durham, 2 July, 1997.

Fluorine-19 and triple-channel carbon-13 studies probing structural properties of inclusion compounds and polymers, 13th International Meeting on NMR Spectroscopy, The Royal Society of Chemistry, University of Exeter, 6-11 July, 1997.†

Poster presentations

Solid-state NMR studies of inclusion compounds, ICI poster competition, University of Durham, 18 December, 1996.

Solid-state NMR studies of fluorine-containing inclusion compounds, Chemistry research for Britain meeting, The Royal Society, London, 7 February, 1997.

Solid-state NMR studies of inclusion compounds, Polar solids group meeting, Mansfield College, University of Oxford, 26 March, 1997.†

Publications

Solid-state electronic absorption, fluorescence and ^{13}C CPMAS NMR spectroscopic study of thermo- and photo-chromic aromatic Schiff bases,

S.H. Alarcón, A.C. Olivieri, A. Nordon and R.K. Harris, *J. Chem. Soc., Perkin Trans. 2*, 1996, 2293.

Fluorocyclohexane ring inversion in a solid thiourea inclusion compound studied by fluorine-19 magic-angle spinning NMR with high-power proton decoupling,

A. Nordon, R.K. Harris, L. Yeo and K.D.M. Harris, *Chem. Commun.*, 1997, 961.

Application of triple-channel ^{13}C{^{1}H, ^{19}F} NMR techniques to probe structural properties of disordered solids,

A. Nordon, R.K. Harris, L. Yeo and K.D.M. Harris, *Chem. Commun.*, 1997, 2045.

Direct measurement of the distance between adjacent guest molecules in a disordered solid inclusion compound using solid-state ^{19}F-{^{1}H} NMR spectroscopy,

A. Nordon, E. Hughes, R.K. Harris, L. Yeo and K.D.M. Harris, submitted for publication.

Research conducted outside the Department

Worked with members of the structural chemistry research group, under the supervision of Prof. Kenneth D.M. Harris, Department of Chemistry, University of Birmingham, 18-21 March, 1996.

---

† Presented by Prof. Robin K. Harris

Research colloquia, seminars and lectures given by invited speakers

<u>1994</u>

October 5   Prof. N.L. Owen, Brigham Young University, Utah, USA

Determining molecular structure - the INADEQUATE NMR way‡

October 19   Prof. N. Bartlett, University of California

Some aspects of Ag(II) and Ag(III) chemistry

November 2   Dr P.G. Edwards, University of Wales, Cardiff

The manipulation of electronic and structural diversity in metal

complexes - new ligands‡

November 3   Prof. B.F.G. Johnson, Edinburgh University

Arene-metal clusters

November 9   Dr G. Hogarth, University College, London

New vistas in metal-imido chemistry

November 10   Dr M. Block, Zeneca Pharmaceuticals, Macclesfield

Large-scale manufacture of ZD 1542, a thromboxane antagonist

synthase inhibitor

November 16   Prof. M. Page, University of Huddersfield

Four-membered rings and β-lactamase‡

November 23   Dr J.M.J. Williams, University of Loughborough

New approaches to asymmetric catalysis

December 7   Prof. D. Briggs, ICI and University of Durham

Surface mass spectrometry‡

<u>1995</u>

January 11   Prof. P. Parsons, University of Reading

Applications of tandem reactions in organic synthesis

January 18   Dr G. Rumbles, Imperial College, London

Real or imaginary third order non-linear optical materials‡

January 25   Dr D.A. Roberts, Zeneca Pharmaceuticals

The design and synthesis of inhibitors of the renin-angiotensin system

February 1   Dr T. Cosgrove, Bristol University

Polymers do it at interfaces‡

February 8   Dr D. O'Hare, Oxford University

Synthesis and solid-state properties of poly-, oligo- and multidecker

metallocenes‡

February 22   Prof. E. Schaumann, University of Clausthal

Silicon- and sulphur-mediated ring-opening reactions of epoxide

March 1   Dr M. Rosseinsky, Oxford University

Fullerene intercalation chemistry

March 22   Dr M. Taylor, University of Auckland, New Zealand

Structural methods in main-group chemistry

April 26   Dr M. Schroder, University of Edinburgh

Redox-active macrocyclic complexes : rings, stacks and liquid crystals

May 4   Prof. A.J. Kresge, University of Toronto

The Ingold Lecture Reactive intermediates : Carboxylic-acid enols

and other unstable species‡

October 11   Prof. P. Lugar, Frei Univ Berlin, Germany

Low temperature crystallography‡

October 13   Prof. R. Schmutzler, Univ Braunschweig, Germany

Calixarene-phosphorus chemistry: A new dimension in phosphorus chemistry‡

October 18   Prof. A. Alexakis, Univ. Pierre et Marie Curie, Paris,

Synthetic and analytical uses of chiral diamines‡

October 25   Dr Martin Davies, University of Northumbria

Chemical reactions in organised systems‡

November 1   Prof. W. Motherwell, UCL London

New reactions for organic synthesis

November 3   Dr B. Langlois, University Claude Bernard-Lyon

Radical anionic and psuedo cationic trifluoromethylation

November 8   Dr D. Craig, Imperial College, London

New stategies for the assembly of heterocyclic systems

November 15   Dr Andrea Sella, UCL, London

Chemistry of lanthanides with polypyrazoylborate ligands

November 17   Prof. David Bergbreiter, Texas A&M, USA

Design of smart catalysts, substrates and surfaces from simple polymers

November 22   Prof. I. Soutar, Lancaster University

A water of glass? Luminescence studies of water-soluble polymers‡

November 29   Prof. Dennis Tuck, University of Windsor, Ontario, Canada

New indium coordination chemistry

December 8   Professor M.T. Reetz, Max Planck Institut, Mulheim

                Perkin regional meeting

1996

January 10   Dr Bill Henderson, Waikato University, NZ

                Electrospray mass spectrometry - a new sporting technique‡

January 17   Prof. J.W. Emsley, Southampton University

                Liquid crystals: more than meets the eye‡

January 24   Dr Alan Armstrong, Nottingham University

                Alkene oxidation and natural product synthesis

January 31   Dr J. Penfold, Rutherford Appleton Laboratory,

                Soft soap and surfaces

February 7   Dr R.B. Moody, Exeter University

                Nitrosations, nitrations and oxidations with nitrous acid

February 12   Dr Paul Pringle, University of Bristol

                Catalytic self-replication of phosphines on platinum(0)

February 14   Dr J. Rohr, Univ Gottingen, Germany

                Goals and aspects of biosynthetic studies on low molecular weight

                natural products

February 21   Dr C.R. Pulham, Univ. Edinburgh

                Heavy metal hydrides - an exploration of the chemistry of stannanes

                and plumbanes

February 28   Prof. E.W. Randall, Queen Mary & Westfield College

                New perspectives in NMR imaging‡

March 6   Dr Richard Whitby, Univ of Southampton

New approaches to chiral catalysts: Induction of planar and metal centred asymmetry

March 7   Dr D.S. Wright, University of Cambridge

Synthetic applications of Me2N-p-block metal reagents

March 12   Prof. V. Balzani, Univ of Bologna

RSC endowed lecture - Supramolecular photochemistry‡

March 13   Prof. Dave Garner, Manchester University

Mushrooming in chemistry

April 30   Dr L.D. Pettit, Chairman, IUPAC Commission of Equilibrium Data

pH-metric studies using very small quantities of uncertain purity

October 9   Professor G. Bowmaker, University of Aukland, NZ

Coordination and materials chemistry of the Group 11 and Group 12 metals: Some recent vibrational and solid-state NMR studies‡

October 14   Professor A.R. Katritzky, University of Gainesville, University of Florida, USA

Recent advances in benzotriazole mediated synthetic methodology

October 16   Professor Ojima, Guggenheim Fellow, State University of New York at Stony Brook

Silylformylation and silylcarbocyclisations in organic synthesis

October 22   Professor Lutz Gade, Univ. of Wurzburg, Germany

Organic transformations with early-late heterobimetallics: Synergism and selectivity

October 22   Professor B.J. Tighe, Department of Molecular Sciences and Chemistry, University of Aston

(Joint lecture with the Institute of Materials)

Making polymers for biomedical application - can we meet nature's challenge?

October 23   Professor H. Ringsdorf (Perkin Centenary Lecture), Johannes Gutenberg-Universitat, Mainz, Germany

Function based on organisation

October 29   Professor D.M. Knight, Department of Philosophy, University of Durham.

The purpose of experiment - A look at Davy and Faraday

October 30   Dr Phillip Mountford, Nottingham University

Recent developments in Group IV imido chemistry

November 6   Dr Melinda Duer, Chemistry Department, Cambridge

Solid-state NMR studies of organic solid to liquid-crystalline phase transitions‡

November 12   Professor R.J. Young, Manchester Materials Centre, UMIST

(Joint Lecture with Zeneca & RSC)

New materials - Fact or fantasy?

November 13   Dr G. Resnati, Milan

Perfluorinated oxaziridines: Mild yet powerful oxidising agents

November 18   Professor G.A. Olah, University of Southern California, USA

Crossing conventional lines in my chemistry of the elements‡

November 19   Professor R.E. Grigg, University of Leeds

Assembly of complex molecules by palladium-catalysed queueing processes

November 20 Professor J. Earnshaw, Deptartment of Physics, Belfast

Surface light scattering: Ripples and relaxation‡

November 27 Dr Richard Templer, Imperial College, London

Molecular tubes and sponges

December 3 Professor D. Phillips, Imperial College, London

"A little light relief"

December 4 Professor K. Muller-Dethlefs, York University

Chemical applications of very high resolution ZEKE photoelectron spectroscopy

December 11 Dr Chris Richards, Cardiff University

Sterochemical games with metallocenes

1997

January 15 Dr V.K. Aggarwal, University of Sheffield

Sulfur mediated asymmetric synthesis

January 16 Dr Sally Brooker, University of Otago, NZ

Macrocycles: Exciting yet controlled thiolate coordination chemistry

January 21 Mr D. Rudge, Zeneca Pharmaceuticals

High speed automation of chemical reactions

January 22 Dr Neil Cooley, BP Chemicals, Sunbury

Synthesis and properties of alternating polyketones‡

January 29 Dr Julian Clarke, UMIST

What can we learn about polymers and biopolymers from computer-generated nanosecond movie-clips?

February 4   Dr A.J. Banister, University of Durham

From runways to non-metallic Metals - A new chemistry based on sulphur

February 5   Dr A. Haynes, University of Sheffield

Mechanism in homogeneous catalytic carbonylation

February 12   Dr Geert-Jan Boons, University of Birmingham

New developments in carbohydrate chemistry

February 18   Professor Sir James Black, Foundation/King's College London

My dialogues with medicinal chemists

February 19   Professor Brian Hayden, University of Southampton

The dynamics of dissociation at surfaces and fuel cell catalysts‡

February 25   Professor A.G. Sykes, University of Newcastle

The synthesis, structures and properties of blue copper proteins

February 26   Dr Tony Ryan, UMIST

Making hairpins from rings and chains‡

March 4   Professor C.W. Rees, Imperial College

Some very heterocyclic chemistry

March 5   Dr J. Staunton FRS, Cambridge University

Tinkering with biosynthesis: towards a new generation of antibiotics

March 11   Dr A.D. Taylor, ISIS Facility, Rutherford Appleton Laboratory

Expanding the frontiers of neutron scattering

March 19   Dr Katharine Reid, University of Nottingham

Probing dynamical processes with photoelectrons

‡ denotes attendance

Computer programs

Spinsight 2D processing macro

```
/* states2d */

/* macro for processing 2 separately acquired datasets */
/* AN 7/8/96 */

/* display 4 viewports */
/* process panel displayed to speed up processing */
panel_process;
format "2x2";
dis;

info "Click in top left viewport";
info "Read x dataset into top left viewport";
bufnamex = query "name of buffer for xdata?";
xdata = copy bufnamex;
dis xdata;

info "Click in top right viewport";
info "Read y dataset into top right viewport";
bufnamey = query "name of buffer for ydata?";
ydata = copy bufnamey;
dis ydata;

/* parameters and definitions required for processing */
al = get_acq_val al -b xdata;
aldouble = al*2;
al2 = get_acq_val al2 -b xdata;

info "Click in top left viewport";
/* zero fill xdata dataset -> twice original al */
zf xdata aldouble;
dis xdata;
info "xdata zero filled -> 2xal";

info "Click in top right viewport";
/* zero fill ydata dataset -> twice original al */
/* shift ydata dataset al points to the right */
/* -> first al points zero */
zf ydata aldouble;
dsr ydata al;
dis ydata;
info "ydata shifted al points to right";

info "Click in bottom left viewport";
/* add xdata and ydata */
addxy = xdata + ydata;
dis addxy;
info "xdata and ydata combined";

/* set number of data points back to original al */
setsize addxy al;
dis addxy;
```

```
info "size of addxy -> a1";

/* processing of t2 dimension */

/* apodization */
apod = query "Type of line broadening required?" -m gborlb;
if (apod == 1) {
        gb = query "Enter Gaussian broadening required (Hz)";
        gm addxy gb;
}
if (apod == 2) {
        lb = query "Enter line broadening required (Hz)";
        em addxy lb;
}
dis addxy;
info "apodization applied";

/* Complex FT of t2 */
size = query "Enter number of points for FT";
zf addxy size;
ft addxy;
dis addxy;
info "Complex FT applied to t2";

/* Phase first row of F2 */
view -d1 addxy;
dis addxy;
info "When phase panel appears, select first row only";
panel_phase;
info "Click OK when phasing applied to F2 dimension";

/* Phase sensitive sort */
phasesort = query "psort or psort -i?" -m psorttype;
if (phasesort == 1) {
        psort addxy;
}
if (phasesort == 2) {
        psort -i addxy;
}
dis addxy;
info "Phase sensitive sort applied";

/* processing of t1 dimension */
view -d2 addxy;
dis addxy;

/* apodization */
apod = query "Type of line broadening required?" -m gborlb;
if (apod == 1) {
        gb = query "Enter Gaussian broadening required (Hz)";
        gm addxy gb;
}
if (apod == 2) {
        lb = query "Enter line broadening required (Hz)";
        em addxy lb;
}
dis addxy;
info "apodization applied";
```

/* multiplication of first point in t1 by 0.5 */
view -d2 addxy;
mult_first_pt 0.5;
dis addxy;
info "first point multiplication applied";

/* Complex FT of t1 */
size = query "Enter number of points for FT";
zf addxy size;
ft addxy;
dis addxy;
info "Complex FT applied to t1";

/* Phase F1 dimension */
view -d2 addxy;
dis addxy;
info "When phase panel appears, select any row(s)";
panel_phase;
info "Click OK when phasing applied to F1 dimension";

/* Displays F2 dimension parallel to horizontal axis */
view -d1 addxy;
dis addxy;
panel_twod;
info "Processing finished";

Additional files needed to use 2D processing macro (~/menufiles)

/* gborlb */
1 Gaussian
2 Exponential

/* psorttype */
1 psort
2 psort -i

MELODRAMA simulation program

```
/* mdrama.c */
/* Prog. to simulate magnetisation exchange trajectories */
/* B.Q.Sun, P.R.Costa, D.Kocisko, P.T.Lansbury and R.G. Griffin */
/* J.Chem.Phys.,102,1995,702 */

#include <stdio.h>
#include <math.h>

void main(void){
        double  find_max(double *p, int i);
        double  st[1025];
        double  pi;
        int     k, j;
        double  gam, bet;
        int     N;
        int     pmax;
        double  w;
        double  D, D1, D2;
        double  t, t1, tmax;
        double  Dsum, sum, full, st_max;
        FILE    *fp;
        char    filename[20];

pi=4.0*atan(1.0);

/* getting parameters */
printf("input w(rad/s) ??\n");
scanf("%lf",&w);
printf("input max t(s) ??\n");
scanf("%lf",&tmax);
printf("input no. of points (<1024) ??\n");
scanf("%d",&pmax);
printf("input N ??\n");
scanf("%d",&N);
printf("input filename ??\n");
scanf("%s",&filename);

printf("%f", w);
printf("\n%f", tmax);
printf("\n%d", pmax);
printf("\n%d", N);

/* definitions */
D1=(6.0*w*N*N)/((sqrt(2.0))*pi*((4.0*N*N)-1.0));
printf("\n%f", D1);
t1=tmax/pmax;
printf("\n%f", t1);

/* calculation */
for (k=0; k<=(pmax-1); k++){
        sum=0.0;
        st[k]=0.0;
        for (bet=0; bet<180; bet+=0.5){
                Dsum=0.0;
```

```
                    for (gam=0; gam<360; gam+=1){
                            D2=D1*cos((pi*gam)/720)*sin((2*bet*pi)/180);
                            D=cos(D2*k*t1);
                            Dsum = Dsum + D;
                            }
                    full=(4*Dsum)*sin((pi*bet)/180)*((pi*pi)/(720*360));
                    sum = sum + full;
            }
          st[k]=sum/(4.0*pi*pi);
}

for (k=0; k<=(pmax-1);k++){
printf("\n%d",k);
printf("\n%f",st[k]);
}
/* Normalise FID */

st_max=find_max(st, pmax);
printf("\n%f",st_max);
          for (k=0; k<=(pmax-1); k++){
                    st[k]=st[k]/st_max;
          }
for (k=0; k<=(pmax-1);k++){
printf("\n%f",st[k]);
}

/* save data file */

fp=fopen(filename,"w");
for (k=0; k<=(pmax-1); k++){
          t=k*t1;
          fprintf(fp, "%10.8f %10.8f\n", t, st[k]);
}
fclose(fp);

printf("\nCalculation completed !!!\n");
}

double find_max(double *p, int i){
          double   max;
          int      h;

          max=0.0;
for (h=0; h<i; h++){
          if (max < *(p+h))
          max=*(p+h);
          }
          return max;
}
```

GAMMA programs for the simulation of static lineshapes

Simulation of SA powder pattern

```
/* 1pstatic.cc */
/* Effect of ideal 90 pulse on a single spin occupying all orientations */
/* Static */

#include <gamma.h>

main( int argc, char **argv)
{
//        CONSTANTS AND SPIN SYSTEM

spin_system A(1);                             //single spin system
coord B(0,0,1);                               //Define magnetic field along +z axis
double theta = 0.0;                           //rotation angle
double phi = 0.0;                    //rotation angle
int thetainc = 360;                           //no. of angle increments
int phiinc = 360;                    //no. of angle increments
const t2pts = 512;                   //no. of points in FID
double dw2 = 0.005;                           //dwell
double Az, Ax, Ay;                            //

sscanf( argv[1], "%lf", &Az );
sscanf( argv[2], "%lf", &Ay );
sscanf( argv[3], "%lf", &Ax );

double iso_cs;
double delta_cs;
double eta_cs;
iso_cs = (Az + Ay + Ax)/3;                    //
delta_cs = Az - iso_cs;                       //definitions
eta_cs = (Ay - Ax)/delta_cs;                  //
double phidel;
ofstream ofp;

//        SPIN TENSORS

spin_T TTCS = T_CS2(A,0,B);                   //SA tensor for spin A

//        SPATIAL TENSORS

space_T CS = A2(iso_cs, delta_cs, eta_cs, 0.0, 0.0, 0.0);
space_T CSr;                                  //rotated spatial shift tensors

//        VARIABLES

gen_op sigma0;                                //equilibrium density operator
gen_op sigma1;                                //working density operator
gen_op H;                                     //Hamiltonian
gen_op detect;                                //detection operator
block_1D data(t2pts);                         //data storage of single FID
block_1D datasum(t2pts);             //data storage of all FIDs
```

```
detect = Fp(A);                          //set detection operator to F+
sigma0 = sigma_eq(A);                    //set up equilibrium density operator
```

```
//      PULSE SEQUENCE
```

```
sigma1 = Iypuls(A, sigma0, 90);          //apply a 90 pulse
```

```
//      POWDER AVERAGE
```

```
for (int j=1; j<thetainc; j++)           //loop over theta = (0,180)
        {
        theta = double(180*j)/double(thetainc);
        phidel = phiinc*sin(theta*PI/180.0);     //scaling factor

        for (int i=0; i<=phidel; i++)            //loop over phi = (0,360)
                {
                phi = double(360*i)/double(phidel);

                CSr = T_rot(CS,phi,theta,0.0);        //rotate spatial shift tensor
                H = T_prod(TTCS, CSr, 0) + T_prod(TTCS, CSr, 2,0);      //Hamiltonian
                FID(sigma1, detect, H, dw2, t2pts, data);     //FID after pulse
                datasum += data;                      //sum all FIDs
                }
        }
```

```
//      PROCESS DATA
```

```
exponential_multiply (datasum, -10);                     //apply apodization
datasum = FFT (datasum);                                 //Fourier transform FID
```

```
ofp.open(argv[4]);
```

```
int k=t2pts/2;
for (int m=0; m<t2pts; m++)
        ofp << ((1/dw2) * k--)/(t2pts) << " " << Re(datasum(m)) << endl;
```

```
ofp.close();
```

```
}
```

Simulation of dipolar powder pattern

```
/* 1pdipole.cc */
/* Effect of ideal 90 pulse on two spins (dipolar coupled) */
/* Static */
```

```
#include <gamma.h>
```

```
main( int argc, char **argv)
{
//      CONSTANTS AND SPIN SYSTEM
```

```
spin_system AB(2);                       //two spin system
coord B(0,0,1);                          //Define magnetic field along +z axis
double theta = 0.0;                      //rotation angle
```

```
double phi = 0.0;                       //rotation angle
int thetainc = 360;                         //no. of angle increments
int phiinc = 360;                       //no. of angle increments
const t2pts = 512;                      //no. of points in FID
double dw2 = 0.005;                         //dwell
double phidel;
double dipole_D;
double delta_di;
ofstream ofp;

sscanf( argv[1], "%lf", &dipole_D );
delta_di = (2*2*dipole_D)/3;


//      SPIN TENSORS

spin_T TTD = T_D(AB,0,1);               //dipolar tensor


//      SPATIAL TENSORS

space_T DIP = A2(0.0, delta_di, 0.0, 0.0, 0.0, 0.0);
space_T DIPr;                           //rotated dipolar tensor


//      VARIABLES

gen_op sigma0;                          //equilibrium density operator
gen_op sigma1;                          //working density operator
gen_op H;                               //Hamiltonian
gen_op detect;                          //detection operator
block_1D data(t2pts);                   //data storage of single FID
block_1D datasum(t2pts);            //data storage of all FIDs
detect = Fp(AB);                    //set detection operator to F+
sigma0 = sigma_eq(AB);                  //set up equilibrium density operator


//      PULSE SEQUENCE

sigma1 = Iypuls(AB, sigma0, 90);    //apply a 90 pulse



//      POWDER AVERAGE

for (int j=1; j<thetainc; j++)          //loop over theta = (0,180)
        {
        theta = double(180*j)/double(thetainc);
        phidel = phiinc*sin(theta*PI/180.0);    //scaling factor

        for (int i=0; i<=phidel; i++)       //loop over phi = (0,360)
                {
                phi = double(360*i)/double(phidel);

                DIPr = T_rot(DIP,phi,theta,0.0);    //rotate spatial shift tensor
                H = T_prod(TTD, DIPr, 2,0);                     //Hamiltonian
                FID(sigma1, detect, H, dw2, t2pts, data);   //FID after pulse
                datasum += data;                    //sum all FIDs
                }
        }


//      PROCESS DATA
```

```
exponential_multiply (datasum, -10);          //apply apodization
datasum = FFT (datasum);                       //Fourier transform FID

ofp.open(argv[2]);

int k=t2pts/2;
for (int m=0; m<t2pts; m++)
        ofp << ((1/dw2) * k--)/(t2pts) << " " << Re(datasum(m)) << endl;

ofp.close();


}
```

Combined SA/dipolar powder pattern

```
/* 1pcsdip.cc */
/* Effect of ideal 90 pulse on two spins (dipolar coupled) occupying all orientations */
/* Static */

#include <gamma.h>

main( int argc, char **argv)
{
//        CONSTANTS AND SPIN SYSTEM

spin_system AB(2);                    //two spin system
coord B(0,0,1);                       //Define magnetic field along +z axis
double theta = 0.0;                   //rotation angle
double phi = 0.0;             //rotation angle
int thetainc = 360;                   //no. of angle increments
int phiinc = 360;            //no. of angle increments
const t2pts = 512;           //no. of points in FID
double dw2 = 0.005;                   //dwell
double Az, Ax, Ay;                    //
double Bz, Bx, By;                    //
double dipole_D;
double delta_di;
double alpha1, beta1, gamma1;
double alpha2, beta2, gamma2;

sscanf( argv[1], "%lf", &Az );
sscanf( argv[2], "%lf", &Bz );
sscanf( argv[3], "%lf", &Ay );
sscanf( argv[4], "%lf", &By );
sscanf( argv[5], "%lf", &Ax );
sscanf( argv[6], "%lf", &Bx );
sscanf( argv[7], "%lf", &alpha1 );
sscanf( argv[8], "%lf", &alpha2 );
sscanf( argv[9], "%lf", &beta1 );
sscanf( argv[10], "%lf", &beta2 );
sscanf( argv[11], "%lf", &gamma1 );
sscanf( argv[12], "%lf", &gamma2 );
sscanf( argv[13], "%lf", &dipole_D );
delta_di = (2*2*dipole_D)/3;

double iso_cs1;
```

```
double iso_cs2;
double delta_cs1;
double delta_cs2;
double eta_cs1;
double eta_cs2;
iso_cs1 = (Az + Ay + Ax)/3;              //
iso_cs2 = (Bz + By + Bx)/3;              //
delta_cs1 = Az - iso_cs1;                //definitions
delta_cs2 = Bz - iso_cs2;                //definitions
eta_cs1 = (Ay - Ax)/delta_cs1;           //
eta_cs2 = (By - Bx)/delta_cs2;           //
double phidel;
ofstream ofp;
```

```
//       SPIN TENSORS
```

```
spin_T TTCS1 = T_CS2(AB,0,B);            //SA tensor for spin A
spin_T TTCS2 = T_CS2(AB,1,B);            //SA tensor for spin B
spin_T TTD = T_D(AB,0,1);                //dipolar tensor
```

```
//       SPATIAL TENSORS
```

```
space_T CS1 = A2(iso_cs1, delta_cs1, eta_cs1, 0.0, 0.0, 0.0);  //PAS of SA spin A
space_T CS2 = A2(iso_cs2, delta_cs2, eta_cs2, 0.0, 0.0, 0.0);  //PAS of SA spin B
space_T DIP = A2(0.0, delta_di, 0.0, 0.0, 0.0, 0.0);           //PAS of dipolar AB
space_T CSDIP1 = T_rot(CS1,alpha1,beta1,gamma1);               //rotate from CS1 PAS -> DIP PAS
space_T CSDIP2 = T_rot(CS2,alpha2,beta2,gamma2);               //rotate from CS2 PAS -> DIP PAS
space_T CS1r;                            //rotated spatial shift tensors
space_T CS2r;                            //rotated spatial shift tensors
space_T DIPr;                            //rotated dipolar tensors
```

```
//       VARIABLES
```

```
gen_op sigma0;                           //equilibrium density operator
gen_op sigma1;                           //working density operator
gen_op H;                                //Hamiltonian
gen_op detect;                           //detection operator
block_1D data(t2pts);                    //data storage of single FID
block_1D datasum(t2pts);          //data storage of all FIDs
detect = Fp(AB);                  //set detection operator to F+
sigma0 = sigma_eq(AB);                   //set up equilibrium density operator
```

```
//       PULSE SEQUENCE
```

```
sigma1 = Iypuls(AB, sigma0, 90);         //apply a 90 pulse
```

```
//       POWDER AVERAGE
```

```
for (int j=1; j<thetainc; j++)           //loop over theta = (0,180)
        {
        theta = double(180*j)/double(thetainc);
        phidel = phiinc*sin(theta*PI/180.0);      //scaling factor

        for (int i=0; i<=phidel; i++)             //loop over phi = (0,360)
                {
                phi = double(360*i)/double(phidel);
```

```
                    CS1r = T_rot(CSDIP1,phi,theta,0.0);        //rotate spatial shift tensor
                    CS2r = T_rot(CSDIP2,phi,theta,0.0);        //rotate spatial shift tensor
                    DIPr = T_rot(DIP,phi,theta,0.0);     //rotate spatial shift tensor
                    H = T_prod(TTCS1, CS1r, 0) + T_prod(TTCS2, CS2r, 0)     //Hamiltonian
                      + T_prod(TTCS1, CS1r, 2,0) + T_prod(TTCS2, CS2r, 2,0)
                      + T_prod(TTD, DIPr, 2,0);
                    FID(sigma1, detect, H, dw2, t2pts, data);     //FID after pulse
                    datasum += data;                             //sum all FIDs
                    }
            }

//        PROCESS DATA

exponential_multiply (datasum, -10);                          //apply apodization
datasum = FFT (datasum);                                      //Fourier transform FID

ofp.open(argv[14]);

int k=t2pts/2;
for (int m=0; m<t2pts; m++)
        ofp << ((1/dw2) * k--)/(t2pts) << " " << Re(datasum(m)) << endl;

ofp.close();

}
```

Simulation of CPMG lineshapes

```
#include <gamma.h>

main( int argc, char **argv )
{
 spin_system AA(2);                // A two spin system
 AA.isotope(0, "19F");
 AA.isotope(1, "19F");

 gen_op     sigma0 = sigma_eq(AA);
 gen_op     sigma;
 gen_op     H;
 gen_op     detect = Fm(AA);

 int        num_pts = 200;

 double     hplanck = 6.626208e-27;        // Plancks Constant erg s

 double     sw = 1.0e5;        // Spectral width in Hz


 if( argc != 11 )
   exit(1);

//   get field strength in Tesla

 double  field;

 sscanf( argv[1], "%lf", &field );
 field *= 1.0e4;                    // Convert to gauss
```

```
// get frequency in MHz

   double freq1;

   sscanf( argv[2], "%lf", &freq1 );
   freq1 *= 1.0e6;                      // Convert to Hz

// get bond distance in Angstroms

   double    rcc;

   sscanf( argv[3], "%lf", &rcc );
   rcc *= 1.0e-8;                       // Convert to cm

   sscanf( argv[4], "%d", &num_pts );

// get tau in microseconds

   double  tau;

   sscanf( argv[5], "%lf", &tau );

   tau *= 1.0e-6;                       // convert to usecs
   sw = 1.0 / (2.0*tau);

// get size of fid

   int  sizeb;

   sscanf( argv[6], "%d", &sizeb );
   block_1D    fid(sizeb);
   block_1D    fidsum(sizeb);

// get pulse width in microseconds

   double  time;
   double  time1;

   sscanf( argv[7], "%lf", &time );
   sscanf( argv[8], "%lf", &time1 );

   time *= 1.0e-6;                      // convert to usecs
   time1 *= 1.0e-6;                     // convert to usecs

// get pulse angle in degrees

   double  beta;
   double  beta1;

   sscanf( argv[9], "%lf", &beta );
   sscanf( argv[10], "%lf", &beta1 );


// calculate gyro in Hz-1 Gauss-1

   double   gyro1;
```

```
    gyro1 = freq1 / field;

    double  C_di;                    // -2 h gamma gamma hbar
    double  delta_di;                // 1/r^3

    C_di = -gyro1 * gyro1 * hplanck;

    delta_di = 1.0 / ( rcc*rcc*rcc );

// Define spin part

    gen_op T20 = 3.0*Iz(AA,0)*Iz(AA,1)-
            (Ix(AA,0)*Ix(AA,1)+Iy(AA,0)*Iy(AA,1)+Iz(AA,0)*Iz(AA,1));



    for( int i=0; i<num_pts; i++ )
    {
      double theta = i*PI/num_pts;
      H = C_di*delta_di*T20*(3.0*cos(theta)*cos(theta)-1.0)/2.0;
      sigma = Sypuls( AA, sigma0, H, "19F", 0, time, beta );

//    fid(0)=trace( detect, sigma );

      sigma = evolve( sigma, H, tau );

      for( int j=0; j<sizeb; j++ )
      {
        sigma = Sxpuls( AA, sigma, H, "19F", 0, time1, beta1 );
        sigma = evolve( sigma, H, tau );
        fid(j)=trace(detect,sigma);
        sigma = evolve( sigma, H, tau );
      }

      fidsum += fid*sin(theta);
    }

    exponential_multiply( fidsum, -40 );
    fidsum = FFT( fidsum );

    for( int i=0; i<sizeb; i++ )
      cout << (sw/2.0-i*sw/sizeb) << " " << Re(fidsum(i)) << endl;
}
```

SIDE program

```
Program Side;
{ ----------------------------------------------- }
{ Simulated Interrupted Decoupling Experiment    }
{ Converted to Turbo Pascal:  14 October 1989    }
{ R H Newman        Revised 17 November 1989     }
{ ----------------------------------------------- }
uses wincrt;
const
   calpha = 0.577350269;  {cosine of the magic angle}
   salpha = 0.816496581;  {sine of the magic angle}
type
   circle = array[1..16] of real;
   sphere = array[1..16] of circle;
   zip = array[1..32] of integer;
   zap = array[1..256] of zip;
var
   x, sbeta, cbeta, psi : circle;
   phi : sphere;
   pipulse : zip;
   pattern : zap;
   sums : array[1..256] of real;
   pimaxa : array[1..256] of integer;
   tag : string[32];
   file2, file3, pimark : string[12];
   r, rch, d, y, t, delt, sum, scale : real;
   freq, angle, delpsi, cphi : real;
   i, j, n, numb, ix, numrun, irun, istep : integer;
   jstep, pimax, item, tick, ding, dong: integer;
   buf1, buf2, buf3  : text;
{ ----------------------------------------------- }
{ Procedure Setup is called for initialisation of }
{ arrays prior to each simulation run.          }
{ ----------------------------------------------- }
Procedure Setup;
var
   zeros : circle;
   ia, ib : integer;
begin
   writeln('Initialisation for a new run...');
   scale := 0.0;
   angle := pi/64.0;
   for ia := 1 to 16 do begin
     psi[ia] := 4.0*angle;
     cbeta[ia] := cos(angle);
     sbeta[ia] := sin(angle);
     scale := scale+16.0*sbeta[ia];
     angle := angle+pi/32.0;
     zeros[ia] := 0.0;
   end;
   for ib := 1 to 16 do begin
     phi[ib] := zeros;
   end;
end;
{ ----------------------------------------------- }
{ Procedure Newstep computes incremental changes  }
```

```
{ in signal dephasing then rotates the sample in }
{ preparation for the next step.            }
{ --------------------------------------------- }
Procedure Newstep;
var
   ctheta, cpsi, wt : real;
   ic, id : integer;
begin
   sum := 0.0;
   for ic := 1 to 16 do begin
      angle := psi[ic];
      cpsi := cos(angle);
      angle := angle+delpsi;
      psi[ic] := angle;
      x := phi[ic];
      for id := 1 to 16 do begin
         wt := sbeta[id];
         ctheta := salpha*wt*cpsi;
         ctheta := ctheta+calpha*cbeta[id];
         y := 1.0-3.0*ctheta*ctheta;
         angle := x[id];
         x[id] := angle+delt*y*d;
         sum := sum+wt*cos(angle);
      end;
      phi[ic] := x;
   end;
end;
{ --------------------------------------------- }
{ Procedure Pulse changes the sign of the dipolar }
{ interaction if the table of events calls for a }
{ pi pulse.                           }
{ --------------------------------------------- }
Procedure Pulse;
var
   ie : integer;
begin
   for ie := 1 to pimax do begin
      item := pipulse[ie];
      if istep = item then begin
         d := -d;
         pimark := ' pi';
      end;
   end;
end;
{ --------------------------------------------- }
{ Main body of the program Side.            }
{ All input data are read from file SIDE.TXT    }
{ Parameters calculated from the input are:     }
{ d = dipolar coupling constant,              }
{ delpsi = rotation angle per step.           }
{ --------------------------------------------- }
begin
   assign(buf1, 'side.txt');
   reset(buf1);
   writeln;
   readln(buf1);          { skip the header line }
   readln(buf1, file3);
   readln(buf1, rch);
```

```
    writeln('Bond length (picometres) = ', rch:8:1);
    r := rch*rch*rch;
    d := 95102.0/r;
    readln(buf1, freq);
    writeln('MAS frequency (Hertz)   = ', freq:8:1);
    readln( buf1, delt);
    writeln('Time step (microseconds) = ', delt:8:1);
    delpsi := pi*freq*delt;
    delpsi := 0.000002*delpsi;
    readln(buf1, numb);
    writeln('Number of steps to do   = ', numb:6);
    readln(buf1, ding);
    readln(buf1, numrun);
    if numrun < 1 then begin
       tag := 'No pi pulses in this run';
       Writeln(tag);
    end;
    if numrun > 0 then begin
       writeln('Number of runs to add   = ', numrun:6);
       readln(buf1, file2);
       assign(buf2, file2);
       reset(buf2);
       readln(buf2, tag);
       writeln('Table of events labelled ', tag);
       readln(buf2, item);
       if item < numrun then begin
          writeln('contains insufficient data');
          halt;
       end;
       for irun := 1 to numrun do begin
          read(buf2, pimax);
          pimaxa[irun] := pimax;
          if pimax > 0 then begin
             for j := 1 to pimax do begin
                read(buf2, item);
                pipulse[j] := item;
             end;
          end;
          pattern[irun] := pipulse;
          readln(buf2);
          readln(buf2);
       end;
       close(buf2);
    end;
    close(buf1);
{ ---------------------------------------------- }
{ Results of numrun simulations are accumulated   }
{ in an array called sums.                  }
{ ---------------------------------------------- }
    numb := numb+ding;
    dong := numb div ding;
    for i := 1 to dong do begin
       sums[i] := 0.0;
    end;
{ ---------------------------------------------- }
{ Simulation begins.  Identifiers used:        }
{ irun = index for current simulation run,     }
{ t = elapsed time,                    }
```

```
{ index = step counter within a run          }
{ psi = angle of rotation around the MAS axis,   }
{ theta = angle of CH vector from static field,  }
{ phi = phase angle for carbon-13 magnetisation. }
{ --------------------------------------------- }
  if numrun < 1 then begin
    numrun := 1;
    pimaxa[1] := 0;
  end;
  for irun := 1 to numrun do begin
    Setup;
    t := 0.0;
    tick := ding;
    n := 1;
    pimark := ' ';
    pimax := pimaxa[irun];
    if pimax > 0 then pipulse := pattern[irun];
    for jstep := 1 to numb do begin
      Newstep;
      sum := sum/scale;
      if tick = ding then begin
        writeln(t:8:1,'  ', sum:8:4,pimark);
        tick := 0;
        sums[n] := sums[n]+sum;
        n := n+1;
        t := t+ding*delt;
      end;
      tick := tick+1;
      if pimark = ' pi' thenpimark := ' ';
      if pimax > 0 then begin
        istep := jstep;
        Pulse;
      end;
    end;
  end;
{ --------------------------------------------- }
{ Open a file for output.  The first few lines }
{ echo input.                                  }
{ --------------------------------------------- }
  assign(buf3, file3);
  rewrite(buf3);
  write(buf3, 'Simulated Interrupted');
  writeln(buf3, ' Decoupling Experiment');
  writeln(buf3, 'Program = SIDE/Nov89');
  writeln(buf3);
  write(buf3, 'CH bond ', rch:8:1);
  writeln(buf3, ' picometres' );
  writeln(buf3, 'MAS at ', freq:8:1, ' Hz');
  write(buf3, 'Steps of ', delt:8:2);
  writeln(buf3, ' microseconds');
  write(buf3, 'Header on table of events: ');
  writeln(buf3, tag);
  writeln(buf3);
  writeln(buf3, '  Time    Signal');
  t := 0;
  for i := 1 to dong do begin
    writeln(buf3,t:8:1, '    ',sums[i]:8:4);
    t := t+ding*delt;
```

```
   end;
   writeln(buf3);
   writeln(buf3,'   End of simulation');
   writeln('Results filed in ', file3);
   close(buf3);
end.
```